

# Graph Neural Network Flavour Tagging and Boosted Higgs Measurements at the LHC

Samuel John Van Stroud  
University College London

Submitted to University College London in fulfilment  
of the requirements for the award of the  
degree of **Doctor of Philosophy**

March 23, 2023

## **Declaration**

I, Samuel John Van Stroud confirm that the work presented in this thesis is my own. Where information has been derived from other sources, I confirm that this has been indicated in the thesis.

Samuel Van Stroud

---

# Abstract

This thesis presents investigations into the challenges of, potential improvements to, and the application of  $b$ -jet identification to study the Higgs boson at the ATLAS experiment at the Large Hadron Collider (LHC). A focus is placed on the high transverse momentum regime, which is a critical region in which to study the Standard Model, but within which successful  $b$ -jet identification becomes difficult.

As  $b$ -jet identification relies on the successful reconstruction of charged particle trajectories (tracks), the tracking performance is investigated and potential improvements are assessed. Track reconstruction becomes increasingly difficult at high transverse momentum due to the increased multiplicity and collimation of tracks, and also due to the presence of displaced tracks that may occur as the result of the decay of a long-flying  $b$ -hadron. The investigations revealed that the track quality selections applied during track reconstruction are suboptimal for tracks inside high transverse momentum  $b$ -jets, motivating future studies into the optimisation of these cuts.

To improve  $b$ -tagging performance two novel techniques are employed: the classification of the origin of tracks and the application of graph neural networks. An algorithm has been developed to classify the origin of tracks, which allows a more optimal collection of tracks to be selected for use in other algorithms. A graph neural network (GNN) jet flavour tagger has also been developed. This tagger requires only tracks and jet variables as inputs, making a break from previous algorithms, which relied on the outputs of several other

algorithms. This model is trained to simultaneously predict the jet flavour, track origins, and track-pair compatibility (i.e. vertexing), and demonstrates markedly improvements in  $b$ -tagging performance, both at low and high transverse momenta. The closely related task of c-jet identification also benefits from these methods.

Analysis of high transverse momentum  $H \rightarrow b\bar{b}$  decays, where the Higgs boson is produced in association with a vector boson, was also performed using  $139 \text{ fb}^{-1}$  of 13 TeV proton-proton collision data from Run 2 of the LHC. The analysis is described, with a focus on the detailed modelling studies performed by the author. The analysis measured provided first measurements in this channel of the Higgs boson production in two high transverse momentum regions.

# Impact Statement

This thesis details research in experimental particle physics. The primary contributions are on the improvement of the data analysis algorithms which are used to process proton-proton collisions induced within the ATLAS detector at the Large Hadron Collider (LHC), and the analysis of candidate Higgs boson events.

The primary outcome of the research is an advancement of knowledge about how the Universe works on the most fundamental level, encoded for example in the improved measurement of the fundamental constants for the Standard Model, or in the observation of previously unseen particles or interactions. Although this kind of knowledge doesn't always have an immediate and direct relevance for society, potential applications are impossible to rule out and could have a very large impact further in the future, as has been seen with previous advancements in fundamental science.

The research does find indirect application in the form of associated technological developments that have transferable application within different fields. The cutting-edge techniques developed at CERN for ATLAS and the LHC have found many spin-off applications elsewhere in society, for example the World Wide Web, high-field magnet technology in MRI, touch-screen technology and cloud computing. Fundamental physics, as a proposer of novel and difficult problems, can therefore be seen as a way to generate innovative technologies.

Working in the field also helps to train skilled researchers, which can be redeployed to other areas of society to tackle various problems. In this thesis advanced statistical and data science methods are

deployed. Such methods currently find wide and varied use in many fields. The training of such highly skilled individuals, has a sustained and significant positive economic impact.

Finally, the work carried at ATLAS and the LHC is widely publicised – support of and interest in fundamental physics research helps to generate excitement about science and technology, and educate people about how the Universe works. This in turn attracts people into the area, propagating the benefits described above.

## Acknowledgements

Firstly I give thanks to my supervisor Tim Scanlon for all the guidance and support he has offered over the course of this doctorate. Tim has always been consistent with clear explanations and sound advice throughout the last four years. I would also like to thank everyone I've worked with at ATLAS and at UCL. In particular I have Jonathan Shlomi to thank for the fruitful collaboration on advancements in flavour tagging. I would also like to thank Brian Moser and Hannah Arnold for their patient support during the course of the  $VH$ ,  $H \rightarrow b\bar{b}$  analysis. I'm grateful to everyone I've worked with in the ATLAS Flavour Tagging and Tracking groups, in particular to Gabriel Facini, Valerio Dao, Bingxuan Liu and Francesco Di Bello for their guidance, and Dan Guest for his fastidious merge request reviews. This thesis was made in L<sup>A</sup>T<sub>E</sub>X 2 <sub>$\varepsilon$</sub>  using the “heptesis” class [1].

# Contents

<b>1</b>	<b>Introduction</b>	<b>12</b>
<b>2</b>	<b>Theoretical Framework</b>	<b>14</b>
2.1	The Standard Model . . . . .	14
2.1.1	Quantum Electrodynamics . . . . .	15
2.1.2	Quantum Chromodynamics . . . . .	17
2.1.3	The Electroweak Sector . . . . .	18
2.2	The Higgs Mechanism . . . . .	19
2.2.1	Electroweak Symmetry Breaking . . . . .	20
2.2.2	Fermionic Yukawa Coupling . . . . .	23
2.2.3	Higgs Sector Phenomenology . . . . .	25
<b>3</b>	<b>The Large Hadron Collider and the ATLAS Detector</b>	<b>28</b>
3.1	The Large Hadron Collider . . . . .	29
3.2	Coordinate System & Collider Definitions . . . . .	30
3.2.1	ATLAS Coordinate System . . . . .	31
3.2.2	Track Parameterisation . . . . .	32
3.2.3	Hadron Collider Definitions . . . . .	32
3.3	The ATLAS Detector . . . . .	36
3.3.1	Inner Detector . . . . .	37
3.3.2	Calorimeters . . . . .	40
3.3.3	Muon Spectrometer . . . . .	42
3.3.4	The Trigger . . . . .	43
3.4	Reconstructed Physics Objects . . . . .	44
3.4.1	Tracks . . . . .	44
3.4.2	Vertices . . . . .	48
3.4.3	Jets . . . . .	49
3.4.4	Leptons . . . . .	51

3.4.5	Missing Transverse Momentum . . . . .	53
3.5	Flavour Tagging Algorithms . . . . .	53
3.5.1	Common Definitions . . . . .	54
3.5.2	Low-level Algorithms . . . . .	54
3.5.3	High-level Algorithms . . . . .	55
<b>4</b>	<b>Tracking and Flavour Tagging at High-<math>p_{\text{T}}</math></b>	<b>56</b>
4.1	Datasets . . . . .	56
4.2	$b$ -hadron Reconstruction . . . . .	57
4.2.1	Decay Topology . . . . .	57
4.2.2	Challenges . . . . .	60
4.3	Investigations into High $p_{\text{T}}$ $b$ -hadron Tracking Improvements . . . . .	64
4.3.1	Shared Hits . . . . .	64
4.3.2	Global $\chi^2$ Fitter Outlier Removal . . . . .	64
4.4	Conclusion . . . . .	67
<b>5</b>	<b>Track Classification MVA</b>	<b>69</b>
5.1	Machine Learning Background . . . . .	69
5.1.1	Neural Networks . . . . .	71
5.1.2	Training with Gradient Descent . . . . .	73
5.2	Track Truth Origin Labelling . . . . .	73
5.3	Fake Track Identification Tool . . . . .	74
5.3.1	Model Inputs . . . . .	76
5.3.2	Model Hyperparameters . . . . .	78
5.3.3	Results . . . . .	79
5.4	$b$ -hadron Track Identification . . . . .	80
5.5	Combined Approach . . . . .	80
5.6	Conclusion . . . . .	82
<b>6</b>	<b>Graph Neural Network Flavour Tagger</b>	<b>84</b>
6.1	Motivation . . . . .	84
6.2	Graph Neural Network Theory . . . . .	86
6.3	Experimental Setup . . . . .	88
6.3.1	Datasets . . . . .	88
6.4	Model Architecture . . . . .	89
6.4.1	Model Inputs . . . . .	89

6.4.2	Auxiliary Training Objectives . . . . .	91
6.4.3	Architecture . . . . .	92
6.4.4	Training . . . . .	96
6.5	Results . . . . .	97
6.5.1	<i>b</i> -tagging Performance . . . . .	98
6.5.2	<i>c</i> -tagging Performance . . . . .	100
6.5.3	Ablations . . . . .	103
6.5.4	Inclusion of Low-Level Vertexing Algorithms . . . . .	105
6.5.5	Jet Display Diagrams . . . . .	105
6.5.6	Vertexing Performance . . . . .	107
6.5.7	Track Classification Performance . . . . .	113
6.6	Further Studies . . . . .	115
6.6.1	Looser Track Selection . . . . .	115
6.6.2	High Level Trigger . . . . .	116
6.6.3	High Luminosity LHC . . . . .	116
6.7	Conclusion . . . . .	119
<b>7</b>	<b>Boosted VHbb Analysis</b>	<b>123</b>
7.1	Analysis Overview . . . . .	124
7.1.1	Object Reconstruction . . . . .	125
7.1.2	Event Selection . . . . .	127
7.1.3	Control Regions . . . . .	128
7.1.4	Background Composition . . . . .	128
7.1.5	Data & Simulated Samples . . . . .	131
7.1.6	Overview of Systematic Uncertainties . . . . .	131
7.2	Experimental Uncertainties . . . . .	133
7.3	Background Modelling Uncertainties . . . . .	134
7.3.1	Truth Tagging . . . . .	135
7.3.2	Sources of Systematic Modelling Uncertainties . . . . .	135
7.3.3	Implementation of Variations . . . . .	137
7.3.4	Vector Boson + Jets Modelling . . . . .	138
7.3.5	Diboson Modelling . . . . .	144
7.3.6	$t\bar{t}$ and single-top Modelling . . . . .	147
7.3.7	Signal Modelling . . . . .	148

7.4 Statistical Treatment . . . . .	149
7.4.1 The Likelihood Function . . . . .	149
7.4.2 Background Normalisations . . . . .	152
7.4.3 Asimov Dataset & Expected Results . . . . .	153
7.5 Results . . . . .	153
7.5.1 Post-fit Results . . . . .	154
7.5.2 Observed Signal Strength & Significance . . . . .	158
7.5.3 Impact of Systematics . . . . .	160
7.5.4 STXS Interpretation . . . . .	162
7.6 Conclusion . . . . .	165
<b>8 Conclusion</b>	<b>166</b>
8.1 Summary . . . . .	166
8.2 Future Work . . . . .	167
<b>Bibliography</b>	<b>169</b>
<b>List of figures</b>	<b>184</b>
<b>List of tables</b>	<b>196</b>

# <sup>2</sup> Chapter 1

## <sup>3</sup> Introduction

- <sup>4</sup> This thesis describes various efforts in improving the understanding of the Higgs  
<sup>5</sup> boson and its coupling to heavy flavour quarks, primarily through the improvement  
<sup>6</sup> of the algorithms used to reconstruct and analyse jets. The thesis is structured in  
<sup>7</sup> the following manner:
- <sup>8</sup> Chapter 2 describes the theoretical foundations of the work presented in the rest of  
<sup>9</sup> the thesis.
- <sup>10</sup> Chapter 3 describes the ATLAS detector and the CERN accelerator complex. Details  
<sup>11</sup> of reconstructed physics objects are also provided.
- <sup>12</sup> Chapter 4 provides an overview of the reconstruction of charged particle tracks  
<sup>13</sup> (tracking) and identification of jets containing  $b$ -hadrons ( $b$ -tagging) at ATLAS, and  
<sup>14</sup> studies into the challenges of high transverse momentum  $b$ -tagging.
- <sup>15</sup> Chapter 5 describes the development of an algorithm to predict the origins of tracks.  
<sup>16</sup> The tool is used to improve  $b$ -tagging performance by the identification and removal  
<sup>17</sup> of fake tracks before their input to the  $b$ -tagging algorithms.
- <sup>18</sup> Chapter 6 introduces a novel monolithic approach to  $b$ -tagging using graph neural  
<sup>19</sup> networks and auxiliary training objectives.
- <sup>20</sup> Chapter 7 describes the measurement of the associated production of a Higgs boson  
<sup>21</sup> decaying into a pair of  $b$ -quarks at high transverse momentum.
- <sup>22</sup> Chapter 8 contains some concluding remarks.

<sup>23</sup> The author's contribution to the work presented in this thesis is as follows.

<sup>24</sup> **Tracking:** The author was an active member of the Cluster and Tracking in Dense  
<sup>25</sup> Environments group throughout their PhD, starting with their qualification task  
<sup>26</sup> on the understanding of tracking performance at high transverse momentum. The  
<sup>27</sup> author played a key role in software r22 validation studies for the tracking group,  
<sup>28</sup> including the validation of the quasi-stable particle interaction simulation and the  
<sup>29</sup> radiation damage Monte-Carlo simulation. The author helped design and improve  
<sup>30</sup> several tracking software frameworks, and contributed to heavy flavour tracking  
<sup>31</sup> efficiency studies in dense environments. The author developed a tool to identify  
<sup>32</sup> and reject fake-tracks, which is being investigated for use in the upcoming tracking  
<sup>33</sup> paper.

<sup>34</sup> ***b*-tagging:** The author has been an active member of the Flavour Tagging group  
<sup>35</sup> since September 2014. The author played a key role in investigating the performance  
<sup>36</sup> of the low level taggers at high transverse momentum and led studies into the  
<sup>37</sup> labelling and classification of track origins. Based on work by Jonathan Shlomi [2],  
<sup>38</sup> the author helped develop a new flavour tagging algorithm which offers a large  
<sup>39</sup> performance improvement with respect to the current state of the art. The author  
<sup>40</sup> was the primary editor of a public note associated with this work [3], which will  
<sup>41</sup> also be further developed in an upcoming paper. The author also contributed to  
<sup>42</sup> the proliferation of the new algorithm to the trigger, High Luminosity LHC, and  
<sup>43</sup>  $X \rightarrow bb$  use cases. The author also played a key role in software r22 validation  
<sup>44</sup> studies for the Flavour Tagging group, including the validation of the quasi-stable  
<sup>45</sup> particle interaction simulation. The author maintains and contributes to various  
<sup>46</sup> software frameworks used in the Flavour Tagging group, including as lead developer  
<sup>47</sup> of three packages, to create training datasets, pre-process samples for algorithm  
<sup>48</sup> studies and a framework for training graph neural networks, and contributes to group  
<sup>49</sup> documentation.

<sup>50</sup> **Higgs:** The author was an active member of the Boosted VHbb analysis group. The  
<sup>51</sup> author performed various studies deriving systematic uncertainties for the  $V+jets$   
<sup>52</sup> and diboson backgrounds. The author also produced and maintained samples, ran fit  
<sup>53</sup> studies and cross checks, and gave the diboson unblinding approval talk to the Higgs  
<sup>54</sup> group. The author also contributed to the development of the analysis software.

55 **Chapter 2**

56 **Theoretical Framework**

57 The Standard Model (SM) of particle physics is the theory describing all known  
58 elementary particles and their interactions via three of the four fundamental forces.

59 Developed by merging the successful theories of quantum mechanics and relativity  
60 in the second half of the 20th century, the SM's position today at the centre of our  
61 understanding of the nature of the Universe is firmly established by an unparalleled  
62 level of agreement between the model predictions and experimental results [4, 5].

63 The SM has predicted the discovery of the top and bottom quarks [6–8], the  $W$   
64 and  $Z$  bosons [9], and the tau neutrino [10]. The last missing piece of the SM to be  
65 discovered was the Higgs boson, first theorised in the 1960s [11–13], and eventually  
66 observed at the LHC in 2012 [14, 15]. After its discovery, much ongoing work has  
67 been carried out performing detailed measurements of its mass and interactions with  
68 other particles.

69 In this chapter, an overview of the SM is given in Section 2.1, and a more detailed  
70 discussion of the Higgs sector and Higgs phenomenology is provided in Section 2.2.

71 **2.1 The Standard Model**

72 The SM is formulated in the language of Quantum Field Theory (QFT). In this  
73 framework, particles are localised excitations of corresponding quantum fields, which  
74 are operator-valued distributions across spacetime.

75 Central to QFT is the Lagrangian density which describes the kinematics and  
 76 dynamics of a field. Observations of conserved quantities are linked, via Noether's  
 77 theorem, to symmetries which are expressed by the Lagrangian. Alongside Global  
 78 Poincaré symmetry, the SM Lagrangian observes a local non-Abelian  $SU(3)_C \otimes$   
 79  $SU(2)_L \otimes U(1)_Y$  gauge symmetry. Gauge symmetries leave observable properties of  
 80 the system unchanged when the corresponding gauge transformations are applied  
 81 to the fields. The full Lagrangian of the SM can be broken up into distinct terms  
 82 corresponding to the different sectors, as in Eq. (2.1). An overview of each sector is  
 83 given in the following chapters.

$$\mathcal{L}_{\text{SM}} = \mathcal{L}_{\text{EW}} + \mathcal{L}_{\text{QCD}} + \mathcal{L}_{\text{Higgs}} + \mathcal{L}_{\text{Yukawa}} \quad (2.1)$$

84 The SM provides a mathematical description of how three of the four fundamental  
 85 forces interact with the matter content of the Universe. The particle content of the  
 86 SM consists of spin-1/2 fermions, listed in Table 2.1, and integral spin bosons listed  
 in Table 2.2.

<b>Generation</b>	Leptons			Quarks		
	<b>Flavour</b>	<b>Mass [MeV]</b>	<b>Charge [e]</b>	<b>Flavour</b>	<b>Mass [MeV]</b>	<b>Charge [e]</b>
First	$e$	0.511	-1	$u$	2.16	$2/3$
	$\nu_e$	$< 1.1 \times 10^{-6}$	0	$d$	4.67	$-1/3$
Second	$\mu$	105.7	-1	$c$	$1.27 \times 10^3$	$2/3$
	$\nu_\mu$	$< 0.19$	0	$s$	93.4	$-1/3$
Third	$\tau$	1776.9	-1	$t$	$173 \times 10^3$	$2/3$
	$\nu_\tau$	$< 18.2$	0	$b$	$4.18 \times 10^3$	$-1/3$

**Table 2.1:** The fermions of the SM [16]. Three generations of particles are present. Also present (unlisted) are the antiparticles, which are identical to the particles up to a reversed charge sign.

87

### 88 2.1.1 Quantum Electrodynamics

89 Quantum electrodynamics (QED) is the relativistic quantum theory which describes  
 90 the interactions between the photon and charged matter. Consider a Dirac spinor  
 91 field  $\psi = \psi(x)$  and its adjoint  $\bar{\psi} = \psi^\dagger \gamma^0$ , where  $\psi^\dagger$  denotes the Hermitian conjugate

Name	Symbol	Mass [GeV]	Charge [ $e$ ]	Spin
Photon	$\gamma$	$< 1 \times 10^{-27}$	$< 1 \times 10^{-46}$	1
Charged Weak boson	$W^\pm$	$80.377 \pm 0.012$	$\pm 1$	1
Neutral Weak boson	$Z$	$91.1876 \pm 0.0021$	0	1
Gluon	$g$	0	0	1
Higgs	$H$	$125.25 \pm 0.17$	0	0

**Table 2.2:** The bosons of the SM [16]. The photon, weak bosons and gluons are gauge bosons arising from gauge symmetries, and carry the four fundamental forces of the SM. The recently discovered Higgs boson is the only fundamental scalar particle in the SM.

of  $\psi$ . The field  $\psi$  describes a fermionic spin-1/2 particle, for example an electron. The Dirac Lagrangian density is

$$\mathcal{L}_{\text{Dirac}} = \bar{\psi}(i\cancel{\partial} - m)\psi, \quad (2.2)$$

where  $\cancel{\partial} = \gamma^\mu \partial_\mu$  denotes the contraction with the Dirac gamma matrices  $\gamma^\mu$  (summation over up-down pairs of indices is assumed). Application of the Euler-Lagrange equation on Eq. (2.2) yields the Dirac equation

$$(i\cancel{\partial} - m)\psi = 0. \quad (2.3)$$

Suppose some fundamental symmetry that requires invariance under a local  $U(1)$  gauge transformation

$$\psi \rightarrow \psi' = \psi e^{-iq\alpha(x)}, \quad (2.4)$$

where  $\alpha$  varies over every spacetime point  $x$ . Under this transformation, the Dirac equation transforms as

$$(i\cancel{\partial} - m)\psi e^{-iq\alpha(x)} + q\cancel{\partial}\alpha(x)\psi e^{-iq\alpha(x)} = 0. \quad (2.5)$$

For the Dirac equation to remain invariant under the transformation in Eq. (2.4), a new field  $A_\mu$  which transforms as  $A_\mu \rightarrow A'_\mu = A_\mu + \partial_\mu\alpha(x)$  must be added. The transformed interaction term

$$-q\cancel{A}\psi \rightarrow -q\cancel{A}\psi e^{-iq\alpha(x)} - q\cancel{\partial}\alpha(x)\psi e^{-iq\alpha(x)} \quad (2.6)$$

104 will then cancel the asymmetric term in Eq. (2.5) as required. The  $U(1)$  invariant  
105 Lagrangian can therefore be constructed by adding an interaction between the  $\psi$   
106 and  $A_\mu$  fields to Eq. (2.2). For completeness, the kinetic term for the new field  $A_\mu$   
107 is also added in terms of  $F_{\mu\nu} = \partial_\mu A_\nu - \partial_\nu A_\mu$ , which is trivially invariant under the  
108 transformation in Eq. (2.4). The interaction term is typically absorbed into the  
109 covariant derivative  $D_\mu = \partial_\mu + iqA_\mu$ , thus named as it transforms in the same way as  
110 the field  $\psi$ . Collecting these modifications to Eq. (2.2) yields the QED Lagrangian

$$\mathcal{L}_{\text{QED}} = -\frac{1}{4}F_{\mu\nu}F^{\mu\nu} + \bar{\psi}(iD^\mu - m)\psi. \quad (2.7)$$

111 The quadratic term  $A_\mu A^\mu$  is not invariant and therefore the field  $A_\mu$  must be massless.  
112 Requiring invariance under local  $U(1)$  gauge transformations necessitated the addition  
113 of a new field  $A_\mu$ , interpreted as the photon field, which interacts with charged matter.  
114 In the SM, the QED Lagrangian is absorbed into the electroweak sector, discussed  
115 in Section 2.1.3.

### 116 2.1.2 Quantum Chromodynamics

117 Quantum Chromodynamics (QCD) is the study of quarks, gluons and their interac-  
118 tions. Quarks and gluons carry colour charge, which comes in three kinds, called  
119 red, green and blue. While the  $U(1)$  symmetry group in Section 2.1.1 was Abelian,  
120 the QCD Lagrangian is specified by requiring invariance under transformations from  
121 the non-Abelian  $SU(3)$  group, making it a Yang-Mills theory [17] which requires the  
122 addition of self-interacting gauge fields. The infinitesimal  $SU(3)$  group generators  
123 are given by  $T_a = \lambda_a/2$ , where  $\lambda_a$  are the eight Gell-Mann matrices. These span the  
124 space of infinitesimal group transformations and do not commute with each other,  
125 instead satisfying the commutation relation

$$[T_a, T_b] = if_{abc}T_c, \quad (2.8)$$

126 where  $f_{abc}$  are the group's structure constants. Consider the six quark fields  $q_k = q_k(x)$ .  
127 Each flavour of quark  $q_k$  transforms in the fundamental triplet representation, in  
128 which each component of the triplet corresponds to the colour quantum number  
129 for red, green and blue colour charged respectively.  $G_{\mu\nu}^a$  are the eight gluon field

130 strength tensors, one for each generator  $T_a$ , defined as

$$G_{\mu\nu}^a = \partial_\mu A_\nu - \partial_\nu A_\mu - g_s f^{abc} A_\mu^b A_\nu^c, \quad (2.9)$$

131 where  $A_\mu^a$  are the gluon fields and  $g_s$  is the strong coupling constant. The covariant  
132 derivative is written as

$$D_\mu = \partial_\mu + ig_s T_a A_\mu^a. \quad (2.10)$$

133 The full QCD Lagrangian is then given by

$$\mathcal{L}_{\text{QCD}} = -\frac{1}{4} G_{\mu\nu}^a G_a^{\mu\nu} + q_k (i \not{D} - m_k) q_k. \quad (2.11)$$

134 Cubic and quartic terms of the gauge fields  $A_\mu^a$  appear in the Lagrangian, leading to  
135 the gluon's self interaction.

136 The QCD coupling constant  $g_s$  varies, or “runs”, with energy. At lower energy scales  
137 (and corresponding larger distance scales) the interaction is strong. This leads to  
138 quark confinement, whereby an attempt to isolate individual colour-charged quarks  
139 requires so much energy that additional quark-antiquark pairs are produced. At  
140 higher energy scales (and corresponding smaller distance scales), asymptotic freedom  
141 occurs as the interactions become weaker, allowing perturbative calculations to be  
142 performed. Hadrons are bound states of quarks. They are invariant under  $SU(3)$   
143 gauge transformations (i.e. are colour-charge neutral, or *colourless*).

### 144 2.1.3 The Electroweak Sector

145 The weak and electromagnetic forces are unified in the Glashow-Weinberg-Salam  
146 (GWS) model of electroweak interaction [18–20]. The Lagrangian is specified by  
147 requiring invariance under the symmetry group  $SU(2)_L \otimes U(1)_Y$ , as motivated by a  
148 large amount of experimental data. Here,  $SU(2)_L$  is referred to as weak isospin and  
149  $U(1)_Y$  as weak hypercharge.

150 The generators of  $SU(2)_L$  are  $T_a = \sigma_a/2$ , where  $\sigma_a$  are the three Pauli spin matrices  
151 which satisfy the commutation relation

$$[T_a, T_b] = i\varepsilon_{abc}T_c. \quad (2.12)$$

152 The generator of  $U(1)_Y$  is  $Y = 1/2$ . Each generator corresponds to a gauge field,  
153 which, after symmetry breaking (discussed in Section 2.2), give rise to the massive  
154 vector bosons,  $W^\pm$  and  $Z$ , and the massless photon. The massive vector bosons  
155 are the carriers of the weak force. Due to the mass of the force carriers, the weak  
156 force has a short range and so it appears weak even though its intrinsic strength is  
157 comparable to that of QED.

158 The charge operator  $Q$  can be written as a combination of the third  $SU(2)_L$  generator  
159 and the  $U(1)_Y$  generator as in

$$Q = T_3 + Y. \quad (2.13)$$

160 The weak force violates parity conservation [21–23], i.e. invariance under parity  
161 transformations (mirror reflections). Only left handed fermions participate in the  
162 weak interaction. Since there is no other force through which neutrinos interact with  
163 other particles, there are no right handed neutrinos in the Standard Model.

## 164 2.2 The Higgs Mechanism

165 The Brout-Englert-Higgs mechanism (henceforth just the “Higgs mechanism”) is the  
166 process through which the fundamental particles of the SM acquire mass [11–13].  
167 Experimentally it was known that the weak force had a low effective strength, which  
168 was suggestive of a massive mediating gauge particle. However, directly adding  
169 mass to the weak gauge bosons violates the non-Abelian symmetry of the SM.  
170 Instead, the gauge bosons gain mass through the interaction with a scalar Higgs  
171 field which results from the spontaneous breakdown of symmetry as discussed in  
172 Section 2.2.1. Similarly, the Higgs mechanism gives mass to the fermions, as discussed  
173 in Section 2.2.2. Section 2.2.3 described some basic phenomenology of the Higgs  
174 particle relevant to hadron colliders.

### <sup>175</sup> 2.2.1 Electroweak Symmetry Breaking

<sup>176</sup> Spontaneous symmetry breaking (SSB) is a key part of the Higgs mechanism. It  
<sup>177</sup> is the transition of a physical system from a state of manifest symmetry to a state  
<sup>178</sup> of hidden, or *broken*, symmetry. In particular, this applies to physical systems  
<sup>179</sup> where the Lagrangian observes some symmetry, but the lowest energy vacuum states  
<sup>180</sup> do not exhibit that same symmetry. In other words, the symmetry is broken for  
<sup>181</sup> perturbations around the vacuum state.

<sup>182</sup> Consider the case in which the gauge fields from the local  $SU(2)_L \otimes U(1)_Y$  symmetry  
<sup>183</sup> group (discussed in Section 2.1.3) are coupled to a complex scalar field  $\phi = \phi(x)$ ,  
<sup>184</sup> transforms as a weak isospin doublet. Omitting the kinetic term of the gauge fields,  
<sup>185</sup> and writing  $\phi^2 \equiv \phi^\dagger \phi$ , the Lagrangian is

$$\mathcal{L}_{\text{Higgs}} = (D_\mu \phi)^\dagger (D^\mu \phi) - [\mu^2 \phi^2 + \lambda \phi^4], \quad (2.14)$$

<sup>186</sup> where the covariant derivative is given by

$$D_\mu = \partial_\mu + igA_\mu^a T^a + ig'B_\mu, \quad (2.15)$$

<sup>187</sup> and  $T^a$  are the generators of  $SU(2)$ . The potential term  $V(\phi)$  is made up of a  
<sup>188</sup> quadratic and quartic term in the scalar field  $\phi$ , which each contain an arbitrary  
<sup>189</sup> parameter, respectively  $\lambda$  and  $\mu$ . The quartic term gives the field self-interaction, and  
<sup>190</sup> cannot be negative as this would lead to a potential that was unbounded from below.  
<sup>191</sup> The quadratic term can be positive or negative. In the case where the quadratic term  
<sup>192</sup> is positive, it is interpreted as a mass term for the scalar field. By choosing  $\mu^2 < 0$   
<sup>193</sup> the field becomes unphysical due to its negative mass. The shape of the potential in  
<sup>194</sup> this case is shown in Fig. 2.1. Note that in the case of the Standard Model, the scalar  
<sup>195</sup> field  $\phi$  is a complex doublet, and so the corresponding potential is 5-dimensional.  
<sup>196</sup> In order to obtain a physical interpretation of the Lagrangian in Eq. (2.14) for the  
<sup>197</sup> case where  $\mu^2 < 0$ , the field  $\phi$  is expanded around the vacuum state. The vacuum  
<sup>198</sup> expectation value (VEV) is the expected value of the field  $\phi$  which minimises the  
<sup>199</sup> potential  $V(\phi)$  (equivalently the expected value of the field operator  $\phi$  when the  
<sup>200</sup> system is in a vacuum state,  $|\langle \phi \rangle_0|^2 \equiv |\langle 0 | \phi | 0 \rangle|^2 \equiv \phi_0^2$ ). Minimising the potential

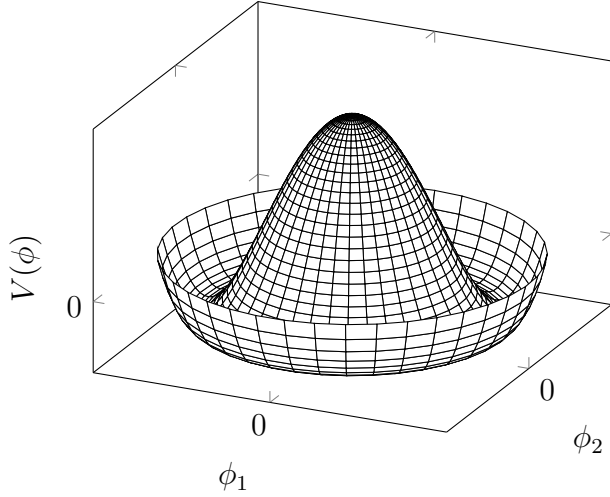


**Figure 2.1:** The Higgs potential  $V(\phi)$  of the complex scalar field singlet  $\phi = \phi_1 + i\phi_2$ , with a choice of  $\mu^2 < 0$  leading to a continuous degeneracy in the true vacuum states. A false vacuum is present at the origin.

201 gives a VEV of

$$\phi_0^2 = -\mu^2/\lambda = v^2. \quad (2.16)$$

202 Due to the shape of the potential in Fig. 2.1, there is a degeneracy in the direction  
203 that the complex doublet  $\phi$  points. As all the different vacuum states minimise  
204 the potential and therefore yield identical physics, one can arbitrarily choose the  
205 state to lie along the second component of the doublet. Application of Eq. (2.13)  
206 shows this choice is manifestly invariant under the charge operator. This allows  
207 the identification of the unbroken subgroup  $U(1)_Q$ , under which the ground state is  
208 invariant. The generator of  $U(1)_Q$  is the charge operator  $Q$ .

209 Adding the particle content back to the theory by expanding the field around the  
210 vacuum state, and making a transformation to the unitary gauge to remove unphysical  
211 Nambu-Goldstone modes (which arise in the context of global symmetries [24, 25]),  
212 yields

$$\phi = \frac{1}{\sqrt{2}} \begin{bmatrix} 0 \\ v + H \end{bmatrix}, \quad (2.17)$$

where  $H$  is a real scalar field, the *true vacuum* Higgs field. Substituting this into Eq. (2.14) and identifying physical fields from the quadratic terms of linear combinations of unphysical fields, one can write the physical fields  $W_\mu^\pm$ ,  $Z_\mu$  and  $A_\mu$  in terms of the original fields  $A_\mu^a$  and  $B_\mu$ . This gives

$$W_\mu^\pm = \frac{1}{\sqrt{2}}(A_\mu^1 \mp iA_\mu^2) \quad \begin{bmatrix} A_\mu \\ Z_\mu \end{bmatrix} = \begin{bmatrix} \cos \theta_W & \sin \theta_W \\ -\sin \theta_W & \cos \theta_W \end{bmatrix} \begin{bmatrix} B_\mu \\ A_\mu^3 \end{bmatrix}. \quad (2.18)$$

where  $\theta_W$  is the weak mixing angle defined by

$$\cos \theta_W = \frac{g}{\sqrt{g^2 + g'^2}}. \quad (2.19)$$

The corresponding masses of the now massive vector bosons can be read off as

$$m_W = \frac{1}{2}gv \quad m_Z = \frac{m_W}{\cos \theta_W}, \quad (2.20)$$

while the photon remains massless. The Higgs mass is  $m_H = v\sqrt{\lambda} = \mu$ .

This is the Higgs mechanism. It maintains the renormalisability and unitarity of the SM whilst allowing the weak vector bosons to acquire mass. In summary, an unphysical complex scalar field  $\phi$  with a nonzero VEV leads to spontaneous symmetry breaking. Due to the non-Abelian symmetry breaking, would-be massless Nambu-Goldstone modes, which arise after expansion around the true vacuum state, are cancelled out by making a local gauge transformation to the unitary gauge, and instead are absorbed by the vector bosons, allowing them to acquire mass.

This sector of the SM contains four fundamental parameters that must be determined from experiment. These can be specified by the Lagrangian parameters  $g$ ,  $g'$ ,  $v$  and  $\lambda$  or the physically measurable parameters  $m_Z$ ,  $\sin \theta_W$ ,  $m_H$  and  $e$ . In the local neighbourhood around the true vacuum, the macroscopic symmetry of the system is not realised, and therefore the physical particles do not obey the original symmetry. However, information about the symmetry is retained through some additional constraints on the parameters of the theory. Prior to symmetry breaking, the potential contained two terms and two constants. After symmetry breaking there are three terms but still only two constants that relate these terms. This is the vestige of the original symmetry.

237 Spontaneous symmetry breaking has modified the original symmetry group of the SM  
238  $SU(2)_L \times U(1)_Y \rightarrow SU(3)_C \otimes U(1)_Q$ . Three broken generators from the symmetry  
239 group  $SU(2)_L \times U(1)_Y$  have been absorbed into the definition of the physical weak  
240 vector bosons, giving them mass. The same methodology can be used to generate  
241 the fermion masses, as shown in the next section.

### 242 2.2.2 Fermionic Yukawa Coupling

243 Adding the masses of the fermions by hand breaks the gauge invariance of the  
244 theory. Instead, we can use a Yukawa coupling between the fermion fields and the  
245 Higgs field in order to generate mass terms after spontaneous electroweak symmetry  
246 breakdown [19]. In this way, the fermion masses are determined by both the respective  
247 couplings to the Higgs field and the VEV of the Higgs field itself, which sets the  
248 basic mass scale of the theory.

249 The Higgs field  $\phi$  transforms as an  $SU(2)$  doublet with  $Y = 1/2$ , as does the left-  
250 handed fermion field  $\psi_L$ . The right-handed fermion field  $\psi_R$  transforms as an  $SU(2)$   
251 singlet.

### 252 Charged Lepton Masses

253 The renormalisable and gauge invariant coupling between a fermionic field  $\psi$  and a  
254 scalar Higgs field  $\phi$  can be written as

$$\mathcal{L}_{\text{Yukawa}} = -g_f(\bar{\psi}_L \phi \psi_R + \bar{\psi}_R \phi^\dagger \psi_L). \quad (2.21)$$

255 where  $\psi_L = (\nu_L, e_L)$  and  $\psi_R = e_R$  for the first generation leptons. After spontaneous  
256 symmetry breaking (see Section 2.2.1), the scalar Higgs field in unitary gauge  
257 Eq. (2.17) consists of a VEV and the true vacuum Higgs field  $H$ . Substituting this  
258 in to Eq. (2.21) yields

$$\mathcal{L}_{\text{Yukawa}} = -\frac{v g_e}{\sqrt{2}} \bar{e} e - \frac{g_e}{\sqrt{2}} \bar{e} H e, \quad (2.22)$$

259 using  $\bar{e} e = (\bar{e}_L + \bar{e}_R)(e_L + e_R) = \bar{e}_L e_R + \bar{e}_R e_L$ . The VEV component of  $\phi$  provides  
260 the first term in Eq. (2.22) which is quadratic in the electron field, and can therefore

261 be identified as the electron mass term. An interaction term between the electron  
 262 field  $e$  and the true vacuum Higgs field  $H$  is also present. Mass is generated for the  
 263 other charged lepton generations in the same way.

264 **Quark Masses**

265 The down-type quarks acquire their mass analogous to the leptons, with  $\psi_L = (u_L, d_L)$   
 266 and  $\psi_R = d_R$  for the first quark generation. Mass is generated for the up-type quarks  
 267 using the conjugate field to  $\phi$  which transforms under  $SU(2)$  as a doublet with  
 268  $Y = -1/2$ . The conjugate field  $\tilde{\phi}$  is constructed as

$$\tilde{\phi} = i\sigma_2 \phi^\dagger = \begin{bmatrix} 0 & 1 \\ -1 & 0 \end{bmatrix} \begin{bmatrix} \phi_1^\dagger \\ \phi_2^\dagger \end{bmatrix} = \frac{1}{\sqrt{2}} \begin{bmatrix} v + H \\ 0 \end{bmatrix}, \quad (2.23)$$

269 and transforms in the same way as  $\phi$ . This field can be used to write an additional  
 270 Yukawa coupling which provides mass for the up-type quarks in a similar way as  
 271 before.

$$\mathcal{L}_{\text{Yukawa}}^{\text{up}} = -g_q (\bar{\psi}_L \tilde{\phi} \psi_R + \bar{\psi}_R \tilde{\phi}^\dagger \psi_L) \quad (2.24)$$

272 Considering the first generation of up-type quarks with  $\psi_L = (u_L, d_L)$  and  $\psi_R = u_R$ ,  
 273 substitution into Eq. (2.24) yields

$$\mathcal{L}_{\text{Yukawa}}^{\text{up}} = -\frac{vg_u}{\sqrt{2}} \bar{u}u - \frac{g_u}{\sqrt{2}} \bar{u}Hu. \quad (2.25)$$

274 The Yukawa terms mix quarks of different generations. Physical particles are detected  
 275 in their mass eigenstates  $q$ , which diagonalise the mass matrix, but interact via the  
 276 weak interaction according to their weak eigenstates  $\tilde{q}$ , which are superpositions  
 277 of the mass eigenstates. This feature of the weak sector leads to mixing between  
 278 different generations of quarks. Quark mixing can be expressed using the Cabibbo-  
 279 Kobayashi-Maskawa (CKM) matrix, which specifies the strength of flavour-changing  
 280 weak currents. The entries in the matrix are enumerated as

$$\begin{bmatrix} \tilde{d} \\ \tilde{s} \\ \tilde{b} \end{bmatrix} = \begin{bmatrix} V_{ud} & V_{us} & V_{ub} \\ V_{cd} & V_{cs} & V_{cb} \\ V_{td} & V_{ts} & V_{tb} \end{bmatrix} \begin{bmatrix} d \\ s \\ b \end{bmatrix}, \quad (2.26)$$

281 where the size of the elements  $|V_{pq}|^2$  measures the probability of a transition between  
282 states  $p$  and  $q$ .

### 283 2.2.3 Higgs Sector Phenomenology

284 As previously discussed in this chapter, the Higgs field plays a key role in the SM  
285 by giving mass to fundamental particles. The strength of the coupling between  
286 the Higgs field and another particle is proportional to that particle's mass. This  
287 fact dictates which production mechanisms and decay modes are dominant at the  
288 LHC. The cross sections for different production mechanisms at a centre of mass  
289 energy  $\sqrt{s} = 13 \text{ TeV}$  are shown as a function of the Higgs mass  $m_H$  in Fig. 2.2. At  
290 leading order in QCD, Higgs boson production occurs mainly through four modes,  
291 shown in Fig. 2.3. The dominant production mode is gluon-gluon fusion ( $pp \rightarrow H$ ),  
292 which is predominantly mediated by a virtual top quark loop. Vector boson fusion  
293 ( $pp \rightarrow qqH$ ) is the second most likely production mechanism, in which a pair of  
294  $W$  or  $Z$  bosons fuse to produce a Higgs after being radiated by two quarks. Next  
295 most common is the associated production of a Higgs boson and a vector boson  
296 ( $pp \rightarrow VH$ ), in which a pair of quarks fuse to produce a single  $W$  or  $Z$  boson which  
297 radiates a Higgs. The final of the four leading production modes is top quark fusion,  
298 in which two gluons each radiate a quark-antiquark pair, and a quark from each pair  
299 fuses to produce a Higgs boson.

300 Although gluon-gluon fusion is the dominant production mode, for hadronic decays  
301 of the Higgs boson the associated production with a vector boson has the advantage  
302 of leading to a more distinct signature due to the likelihood of the vector bosons  
303 decaying leptons. Leptons provide a clean signals to detect and trigger on.

304 Since the Higgs boson couples proportional to mass, decays to heavier particles are  
305 favoured. The branching ratios of different Higgs boson decay modes are shown  
306 as a function of  $m_H$  in Fig. 2.4. Approximately 58% of the time the Higgs boson  
307 decays to a pair of  $b$ -quarks, the dominant decay mode. The next most likely decay  
308 mode is to a pair of  $W$  bosons, which occurs approximately 20% of the time. After  
309 the  $b$ -quark, the next heaviest fermions are the tau lepton and the  $c$ -quark, decays  
310 to pairs of these particles happen approximately an order of magnitude less often.  
311 Decays to pairs of vector bosons are via a virtual off shell Higgs boson only. While  
312 the  $H \rightarrow \gamma\gamma$  and  $H \rightarrow ZZ$  branching ratios are small compared with fermionic decay

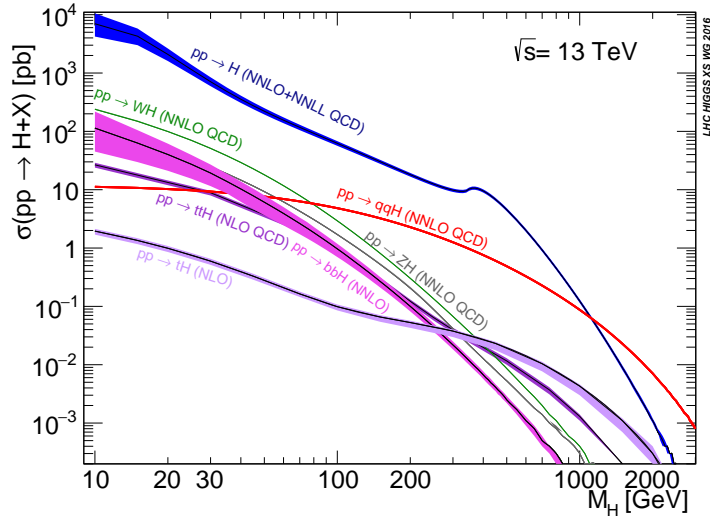


**Figure 2.2:** Higgs boson production cross sections as a function of Higgs mass ( $m_H$ ) at  $\sqrt{s} = 13 \text{ TeV}$  [26]. Uncertainties are shown in the shaded bands. At  $m_H = 125 \text{ GeV}$ , Higgs boson production is dominated by gluon-gluon fusion, vector boson fusion, associated production with vector bosons, and top quark fusion.

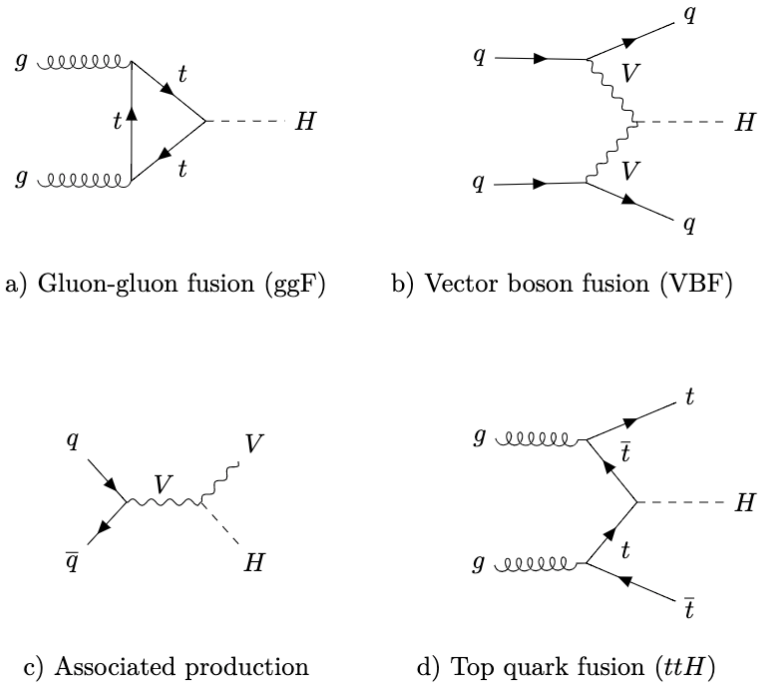


**Figure 2.3:** Diagrams for the four main Higgs boson production modes at the LHC for a Higgs mass  $m_H = 125 \text{ GeV}$  at a centre of mass energy  $\sqrt{s} = 13 \text{ TeV}$ .

<sup>313</sup> modes (around 0.2% for  $H \rightarrow \gamma\gamma$ ), these decay channels were instrumental in the  
<sup>314</sup> initial discovery of the Higgs due to the low level of background processes which  
<sup>315</sup> mimic the final state [14, 15].

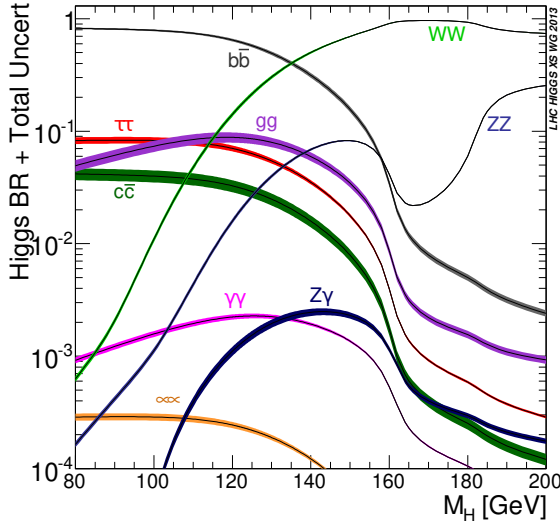


**Figure 2.4:** Higgs boson branching ratios as a function of Higgs mass ( $m_H$ ) at  $\sqrt{s} = 13$  TeV [26]. Uncertainties are shown in the shaded bands. At  $m_H = 125$  GeV, the Higgs predominantly decays to a pair of  $b$ -quarks, around 58% of the time. The leading subdominant decay mode is to a pair of  $W$  bosons.

<sup>316</sup> This thesis presents a measurement of the Higgs bosons production rate using events  
<sup>317</sup> with a Higgs boson produced in association with vector boson and decaying to a pair  
<sup>318</sup> of  $b$ -quarks, i.e.  $pp \rightarrow VH(b\bar{b})$ . The  $H \rightarrow b\bar{b}$  decay mode directly probes the Higgs  
<sup>319</sup> coupling to fermions, and more specifically to the bottom quark. This coupling was  
<sup>320</sup> first observed in 2018 [27, 28]. Ongoing work measuring the coupling strengths, in  
<sup>321</sup> particular in the high energy regime, is the focus of the analysis presented in this  
<sup>322</sup> thesis in Chapter 7.

323 Chapter 3

324 The Large Hadron Collider and the  
325 ATLAS Detector

326 Since the completion of its construction in 2008, the Large Hadron Collider (LHC) [29]  
327 at CERN has extended the frontiers of particle physics through significant increases  
328 in centre of mass energy and luminosity compared with previous collider experiments.  
329 The LHC accelerates bunches of protons around a 27 km ring until they are travelling  
330 just  $3 \text{ m s}^{-1}$  slower than the speed of light, at which point they are made to collide.  
331 The proton bunches travel round the ring 11,000 times per second in two concentric  
332 beams, which are guided by superconducting magnets cooled using liquid helium to  
333  $-271.3^\circ\text{C}$  (1.9 K). The beams travel in opposite directions around the ring and are  
334 crossed at four locations so that collisions between protons can take place. Around  
335 these collision points four specialised detectors, ALICE [30], CMS [31], LHCb [32] and  
336 ATLAS [33], are located to capture information about the products of the collisions.

337 In this chapter, a brief overview of the LHC and the accelerator complex at CERN  
338 is given in Section 3.1. The coordinate system used at the ATLAS detector and  
339 other common definitions are introduced in Section 3.2. An overview of the different  
340 detector systems is provided in Section 3.3, and finally descriptions of various  
341 commonly used reconstructed objects is given in Section 3.4.

### <sup>342</sup> 3.1 The Large Hadron Collider

<sup>343</sup> The LHC is operated in multi-year *runs* during which beams of protons are circulated  
<sup>344</sup> and collided. Between runs there are periods of shutdown while the accelerator and  
<sup>345</sup> detector machinery is maintained and upgraded. Run 1 began in 2010 when the LHC  
<sup>346</sup> collided proton bunches, each containing more than  $10^{11}$  particles, 20 million times  
<sup>347</sup> per second, providing 7 TeV proton-proton collisions at instantaneous luminosities  
<sup>348</sup> of up to  $2.1 \times 10^{32} \text{ cm}^{-2} \text{ s}^{-1}$ . The centre-of-mass energy was increased to 8 TeV  
<sup>349</sup> in 2012. Over the course of Run 1,  $26.4 \text{ fb}^{-1}$  of usable integrated luminosity was  
<sup>350</sup> recorded. Run 2, which spanned 2015–2018, further increased the proton-proton  
<sup>351</sup> collision energy to 13 TeV. During Run 2 the bunch spacing was reduced, leading  
<sup>352</sup> to a collision rate of 40 MHz. Over the course of Run 2 a total usable integrated  
<sup>353</sup> luminosity of  $139 \text{ fb}^{-1}$  was recorded. 2022 marked the beginning of Run 3 which,  
<sup>354</sup> with a higher center of mass energy and peak luminosity, is expected to culminate in  
<sup>355</sup> an approximate tripling of the dataset size. A summary of key information about  
<sup>356</sup> each run is listed in Table 3.1.

Period	Year	$\sqrt{s}$ [TeV]	$\langle \mu \rangle$	Bunch spacing [ns]	Luminosity [ $\text{cm}^{-2} \text{ s}^{-1}$ ]
Run 1	2010–2012	7–8	18	50–150	$8 \times 10^{33}$
Run 2	2015–2018	13	34	25	$1\text{--}2 \times 10^{34}$
Run 3	2022–2025	13.6	50	25	$2 \times 10^{34}$

**Table 3.1:** Overview of the different LHC runs [34,35]. The average number of interactions per bunch-crossing is denoted as  $\langle \mu \rangle$  (see Section 3.2.3), and is here averaged over the entire run. The luminosity is the peak instantaneous luminosity. Numbers for Run 3 are preliminary and are only provided to give an indication of expected performance.

<sup>357</sup> An overview of the accelerator complex at CERN is shown in Fig. 3.1. The LHC is  
<sup>358</sup> at the final stage of a chain of accelerators which incrementally step-up the energy  
<sup>359</sup> of incoming protons. The first accelerator is Linac2 (which has been replaced by  
<sup>360</sup> Linac4 in 2020), a linear accelerator which accelerates negative hydrogen ions to an  
<sup>361</sup> energy of 160 MeV. Upon leaving Linac4, the ions are stripped of both electrons  
<sup>362</sup> and the resulting protons are fed into the Proton Synchrotron Booster (PSB), which  
<sup>363</sup> increases the energy of the protons to 2 GeV. The protons leaving the PSB are passed  
<sup>364</sup> to the Proton Synchrotron (PS), which increases the energy to 26 GeV, and then  
<sup>365</sup> from the PS to the Super Proton Synchrotron (SPS) which further increases the

366 energy to 450 GeV. Finally, the proton beams are injected in the LHC where they  
 367 are accelerated to their final energy of 6.5 TeV (for Run 2).

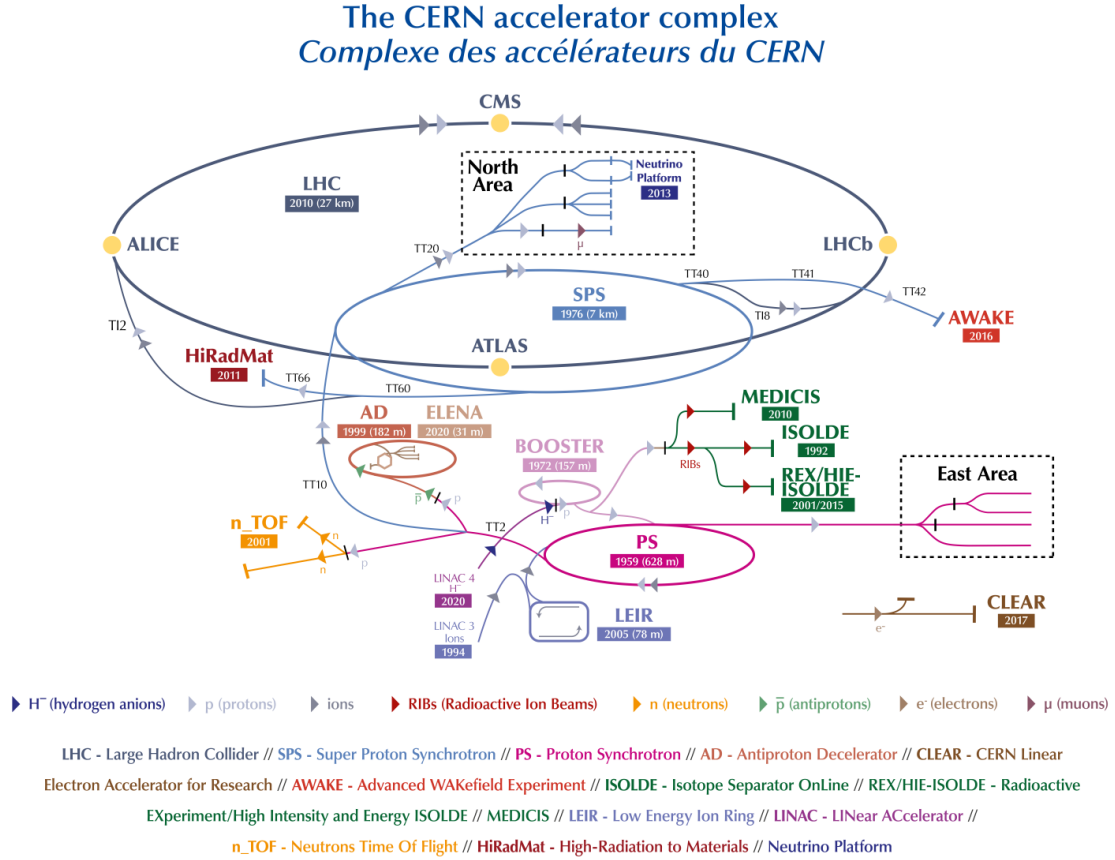


**Figure 3.1:** An overview of the CERN accelerator complex [36]. The LHC is fed by a series of accelerators starting with Linac2 (or Linac4 from 2020). Next are the Proton Synchrotron Booster, the Proton Synchrotron, and finally the Super Proton Synchrotron which injects protons into the LHC.

## 368 3.2 Coordinate System & Collider Definitions

369 In Section 3.2.1, the coordinate system used at ATLAS is introduced. The parame-  
 370 terisation used for specifying the trajectory of charged particle tracks is described in  
 371 Section 3.2.2, and definitions for some frequently occurring concepts and quantities  
 372 is provided in Section 3.2.3.

### <sup>373</sup> 3.2.1 ATLAS Coordinate System

<sup>374</sup> The origin of the coordinate system used by ATLAS is the nominal interaction point  
<sup>375</sup> in the centre of the detector. As shown in Fig. 3.2, the  $z$ -axis points along the  
<sup>376</sup> direction of the beam pipe, while the  $x$ -axis points from the interaction point to the  
<sup>377</sup> centre of the LHC ring, and the  $y$ -axis points upwards. The transverse plane lies  
<sup>378</sup> in  $x$ - $y$  while the longitudinal plane lies along the  $z$ -axis. A cylindrical coordinate  
<sup>379</sup> system with coordinates  $(r, \phi)$  is used in the transverse plane, where  $r$  is the radius  
<sup>380</sup> from the origin and  $\phi$  is the azimuthal angle around the  $z$ -axis.

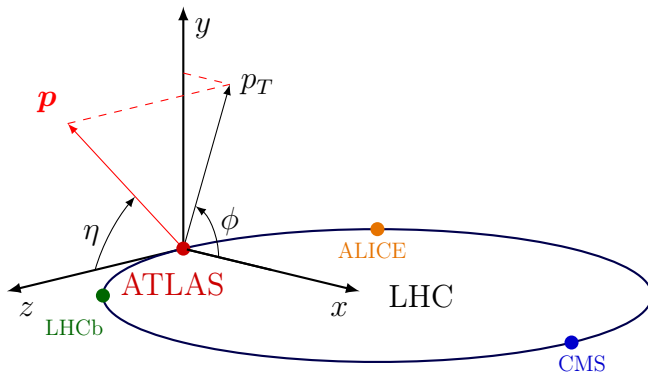


**Figure 3.2:** The coordinate system used at the ATLAS detector, showing the locations of the four main experiments located at various points around the LHC. The 3-vector momentum  $\mathbf{p} = (p_x, p_y, p_z)$  is shown by the red arrow. Reproduced from Ref. [37].

<sup>381</sup> The polar angle  $\theta$  is commonly specified in terms of the pseudorapidity  $\eta$ , defined as

$$\eta = -\ln \left[ \tan \left( \frac{\theta}{2} \right) \right]. \quad (3.1)$$

<sup>382</sup> The pseudorapidity is a convenient quantity to work with as differences in  $\eta$  are  
<sup>383</sup> invariant under Lorentz boosts.

<sup>384</sup> The transverse momentum  $p_T$  of an object is the sum in quadrature of the momenta  
<sup>385</sup> in the transverse plane

$$p_T = \sqrt{p_x^2 + p_y^2}. \quad (3.2)$$

386 Angular distance between two objects is measured in units of  $\Delta R$  and is defined as

$$\Delta R = \sqrt{(\Delta\eta)^2 + (\Delta\phi)^2}, \quad (3.3)$$

387 where  $\Delta\eta$  and  $\Delta\phi$  are the differences in pseudorapidity and azimuthal angle between  
388 the two objects.

### 389 3.2.2 Track Parameterisation

390 The trajectories of charged particle tracks are parameterised as a helix which is fully  
391 specified using five parameters:  $(d_0, z_0, \phi, \theta, q/p)$ . The transverse and longitudinal  
392 impact parameters (IP)  $d_0$  and  $z_0$  specify the closest approach of the trajectory of a  
393 particle to an given origin, where the hard scatter primary vertex (see Section 3.4.2)  
394 is used in this thesis.  $\phi$  and  $\theta$  are the azimuthal and polar angles respectively, and  
395  $q/p$  is the measured charge on the track<sup>1</sup> divided by the scalar 3-momentum. Fig. 3.3  
396 shows each of these parameters diagrammatically.

397 Impact parameter significances are defined as the IP divided by its corresponding  
398 uncertainty,  $s(d_0) = d_0/\sigma(d_0)$  and  $s(z_0) = z_0/\sigma(z_0)$ . When used in flavour tagging  
399 (see Chapter 4), track IP significances are lifetime signed according to the track's  
400 direction with respect to the jet axis and the primary vertex [39]. The signed IP  
401 significances is positive if the track crosses the jet axis in front of the primary vertex  
402 and negative if the crossing is behind the primary vertex.

### 403 3.2.3 Hadron Collider Definitions

#### 404 Cross Section

405 The cross section  $\sigma$  is closely related to the probability of an interaction between  
406 two colliding particles, and is analogous to an effective cross-sectional area of the  
407 particles. The cross section of a process depends on the transition matrix element  
408 and a phase space integral. At hadron colliders such as the LHC, the proton-proton

---

<sup>1</sup>Reconstructed charged particles are assumed to have a charge of  $\pm 1$ .

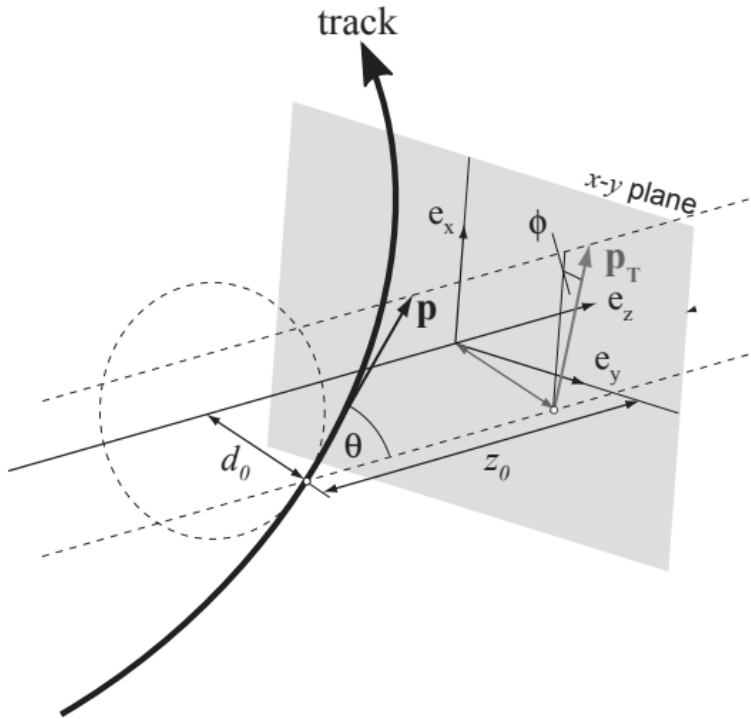


**Figure 3.3:** The track parameterisation used at the ATLAS detector. Five coordinates ( $d_0, z_0, \phi, \theta, q/p$ ) are specified, defined at the track's point of closest approach to the nominal interaction point at the origin of the coordinate system. The figure shows the three-momentum  $\mathbf{p}$  and the transverse momentum  $p_T$  (defined in Eq. (3.2)). The basis vectors  $e_x, e_y$  and  $e_z$  are also shown. Reproduced from Ref. [38].

<sup>409</sup> cross section can be factorised as

$$\sigma(pp \rightarrow X) \approx \text{PDFs} \cdot \text{partonic cross section.} \quad (3.4)$$

<sup>410</sup> The partonic cross section can be calculated at high energies such as those found at  
<sup>411</sup> the LHC, while the parton distribution functions (PDFs) have to be extracted from  
<sup>412</sup> experimental results.

### <sup>413</sup> Luminosity

<sup>414</sup> The total number of proton-proton collisions  $N$  is related to the total  $pp$  cross  $\sigma$   
<sup>415</sup> section by the integrated luminosity  $L$ , as in

$$N = \sigma L = \sigma \int \mathcal{L} dt. \quad (3.5)$$

<sup>416</sup> The instantaneous luminosity  $\mathcal{L}$  relates the cross section to the number of collisions  
<sup>417</sup> per unit time. For two colliding bunched proton beams, it is defined as

$$\mathcal{L} = \frac{1}{\sigma} \frac{dN}{dt} = \frac{fn_1 n_2}{4\pi \sigma_x \sigma_y}, \quad (3.6)$$

<sup>418</sup> where  $n_1$  and  $n_2$  are the number of protons in the colliding bunches,  $f$  is the bunch  
<sup>419</sup> crossing frequency, and  $\sigma_x$  and  $\sigma_y$  are the RMS width of the beam in the horizontal  
<sup>420</sup> and vertical directions.

<sup>421</sup> The total luminosity recorded over the course of Run 2 is shown in Fig. 3.4. In  
<sup>422</sup> total,  $139 \text{ fb}^{-1}$  of usable physics data was collected over the three-year run. The  
<sup>423</sup> uncertainty on the total integrated luminosity is 1.7% [40].

### <sup>424</sup> Pile-up

<sup>425</sup> At the centre of the ATLAS detector, bunches of more than  $10^{11}$  protons are collided.  
<sup>426</sup> Each bunch-crossing is called an *event*. There is generally one hard proton-proton  
<sup>427</sup> scatter per event. Additional interactions are typically relatively soft ( $low-p_T$ ) and  
<sup>428</sup> are known as *pile-up*. Pile-up from interactions within the same bunch-crossing is  
<sup>429</sup> known as *in-time* pile-up while residual signatures from previous bunch-crossings  
<sup>430</sup> is known as *out-of-time* pile-up. The number of pile-up interactions is denoted  $\mu$ ,

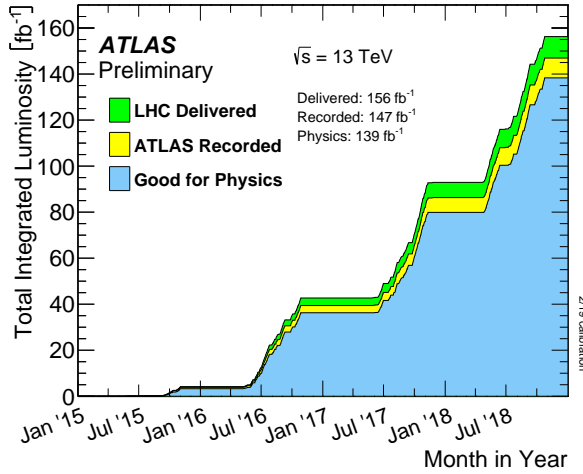


**Figure 3.4:** Delivered, recorded, and usable integrated luminosity as a function of time over the course of Run 2 [35]. A total of  $139 \text{ fb}^{-1}$  of collision data is labelled as good for physics, meaning all sub-detector systems were operating nominally.

431 which is often given as a time-averaged value  $\langle \mu \rangle$ . Histograms showing the number  
of pile-up interactions over the course of Run 2 are shown in Fig. 3.5.

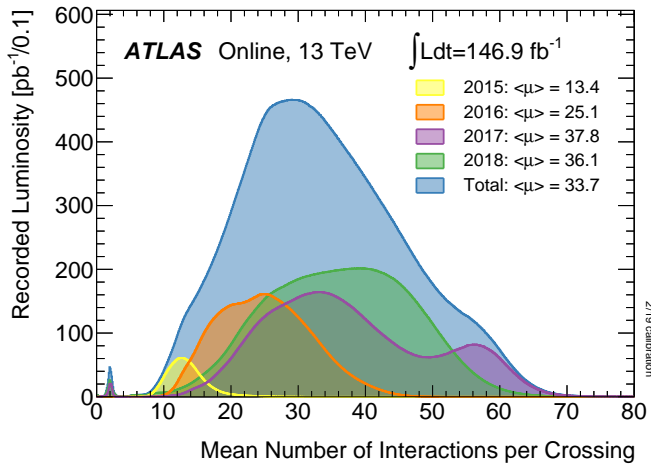


**Figure 3.5:** Average pile-up profiles measured by ATLAS during Run 2 [35].

### <sup>433</sup> 3.3 The ATLAS Detector

<sup>434</sup> The ATLAS<sup>2</sup> detector is made up of several specialised sub-detectors which are  
<sup>435</sup> arranged concentrically around the nominal interaction point at the centre of the  
<sup>436</sup> detector, as shown in Fig. 3.6. The detector is designed to cover nearly the entire solid  
<sup>437</sup> angle around the collision point. In this section a brief overview of each sub-detector  
<sup>438</sup> is given, in order of increasing radial distance from the point of collision. The inner  
<sup>439</sup> tracking detector is described in Section 3.3.1, the electromagnetic and hadronic  
<sup>440</sup> calorimeters in Section 3.3.2, the muon spectrometer in Section 3.3.3, and finally the  
<sup>441</sup> trigger is described in Section 3.3.4. More complete information on the detector can  
<sup>442</sup> be found in Ref. [33], while an overview of physics performance is given in [41].

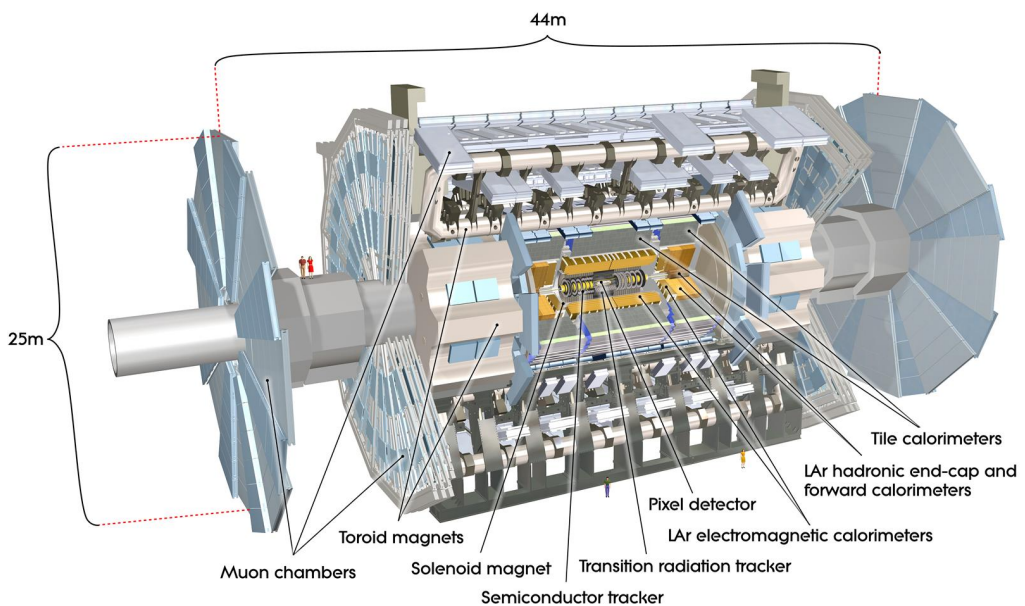


**Figure 3.6:** A 3D model of the entire ATLAS detector [42]. Cutouts to the centre of the detector reveal the different sub-detectors which are arranged in concentric layers around the nominal interaction point.

<sup>2</sup>A Toroidal LHC ApparatuS.

### 443 3.3.1 Inner Detector

444 The inner-detector system (ID) provides high-resolution charged particle trajectory  
445 tracking in the range  $|\eta| < 2.5$ . The ID is immersed in a 2 T axial magnetic field,  
446 produced by a superconducting solenoidal magnet, which enables the measurement  
447 of particle momentum and charge. After Run 3, the ID will be replaced by the  
448 ITk [43, 44].

449 The inner detector is made up of several sub-systems, shown in Figs. 3.7 and 3.8.  
450 The high-granularity silicon pixel detector covers the innermost region and typically  
451 provides four space-point measurements per track. It is followed by the silicon  
452 microstrip tracker (SCT), which usually provides a further four space-point measure-  
453 ments (8 hits) per track. These silicon detectors are complemented by the Transition  
454 Radiation Tracker (TRT), which enables radially extended track reconstruction up  
455 to  $|\eta| = 2.0$  and typically provides 33 (38) additional hits in the barrel (end-cap).

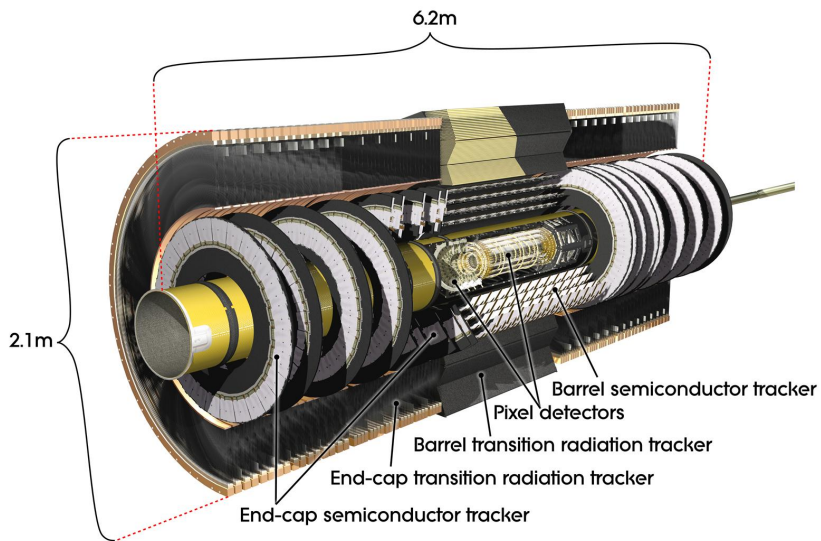


**Figure 3.7:** A 3D model of the ATLAS ID showing the pixel, SCT and TRT sub-detectors [45].

456 The target inverse momentum resolution for the combined ID measurement is  
457 parameterised as a function of the track transverse momentum and polar angle [41].

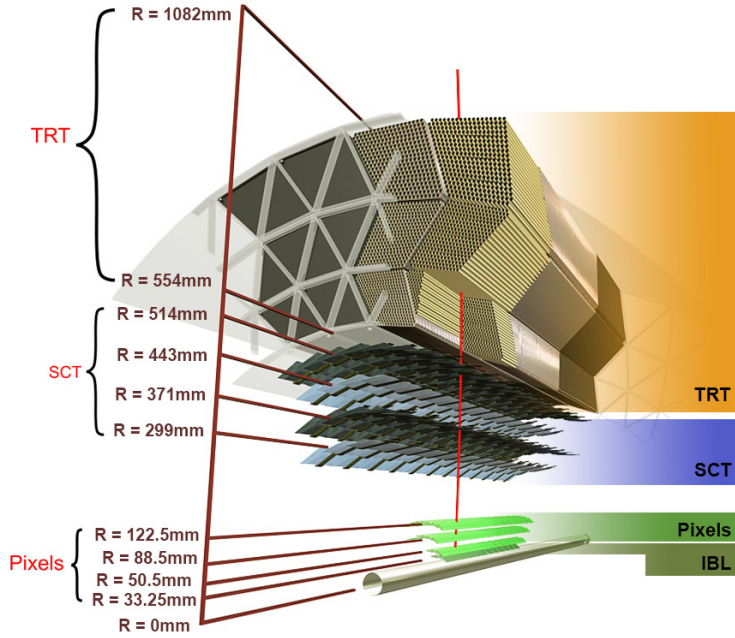


**Figure 3.8:** A cross-sectional view of the ATLAS ID, with the radii of the different barrel layers shown [38].

<sup>458</sup> The parameterisation is given by

$$\sigma(1/p_T) = 0.36 \oplus \frac{13}{p_T \sin \theta} \text{ TeV}^{-1}, \quad (3.7)$$

<sup>459</sup> where  $\oplus$  denotes a sum in quadrature. For low- $p_T$  tracks (e.g.  $p_T \approx 500 \text{ MeV}$ ) in the  
<sup>460</sup> central region this corresponds to a relative error of approximately 0.01%. Meanwhile  
<sup>461</sup> for high- $p_T$  tracks (e.g.  $p_T \approx 100 \text{ GeV}$ ) in the central region this corresponds to  
<sup>462</sup> a relative error of approximately 4%. The momentum resolution generally good  
<sup>463</sup> enough to correctly identify the sign of the charge on particles up to the highest  
<sup>464</sup> energies expected at the LHC. The transverse impact parameter resolution  $\sigma(d_0)$  is  
<sup>465</sup> parameterised similarly as

$$\sigma(d_0) = 11 \oplus \frac{115}{p_T \sin \theta} \mu\text{m}. \quad (3.8)$$

<sup>466</sup> Typical uncertainties for the transverse IP resolution are 230  $\mu\text{m}$  and 11  $\mu\text{m}$  for low  
<sup>467</sup> and high- $p_T$  tracks in the central region, respectively.

#### 468 Pixel Detector

469 The silicon pixel detector is comprised of four cylindrical barrels at increasing radii  
 470 from the beamline, and four disks on each side. The innermost barrel layer is the  
 471 insertable B-layer (IBL), shown in Fig. 3.9. The IBL was installed before Run 2 [46,47]  
 472 and lies approximately just 33 mm from the beam axis. The second-to-innermost layer  
 473 is often referred to as the B-layer. The specification of the pixel detector determines  
 474 the impact parameter resolution and the ability to reconstruct primary and secondary  
 475 vertices. The detector is required to have a high granularity (i.e. resolution) to  
 476 maintain the low occupancy required to resolve nearby particles. Individual pixels  
 477 are  $50\text{ }\mu\text{m}$  in the transverse direction  $R\phi$  and  $400\text{ }\mu\text{m}$  in the longitudinal  $z$  direction  
 478 ( $250\text{ }\mu\text{m}$  for the IBL). Cluster positions have a resolution of approximately  $10\text{ }\mu\text{m}$  in  
 479  $R\phi$  and  $100\text{ }\mu\text{m}$  in  $z$ .

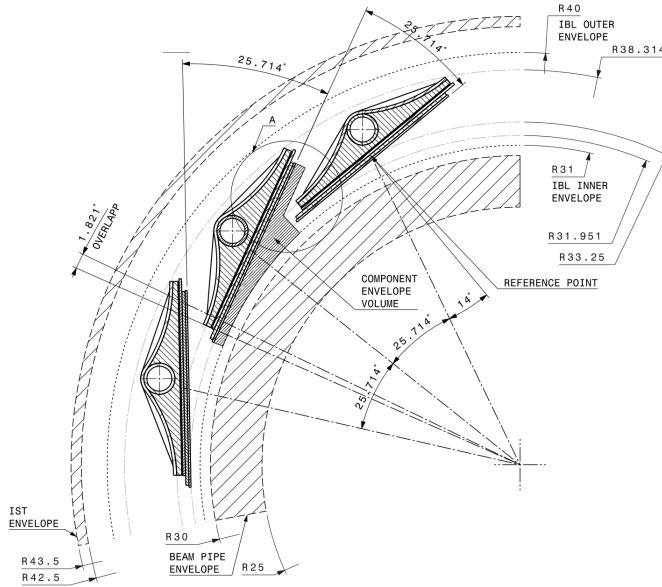


**Figure 3.9:** A schematic cross-sectional view of the ATLAS IBL [46].

#### 480 Semi-Conductor Tracker (SCT)

481 The SCT is made up of four concentric barrel layers in the central region, and nine  
 482 disks in each end-cap. Each layer is itself made of a pair of silicon microstrip layers,  
 483 with a small stereo angle (20 mrad) between the two layers enabling the  $z$ -coordinate

484 to be measured from a pair of strip measurements. The SCT typically provides  
485 four precision space-point measurements (eight strip measurements) per track in  
486 the barrel region. These have intrinsic uncertainties of  $17\text{ }\mu\text{m}$  in the transverse  
487 direction  $R\phi$ , and  $580\text{ }\mu\text{m}$  in the longitudinal direction  $z$  [48]. The measurements  
488 provide a contribution to the measurement of charged particle momentum and impact  
489 parameter.

490 **Transition Radiation Tracker (TRT)**

491 The TRT is a straw-tube tracker which complements the higher-resolution silicon-  
492 based tracks by offering a larger number of hits per track (typically more than 30)  
493 and a long lever arm, which aids the accurate measurement of particle momentum.  
494 It is made up of approximately 300 000 drift tubes with a diameter of 4 mm which  
495 are filled with an argon/xenon gas mixture. The walls of each tube are electrically  
496 charged, and a thin conducting wire runs along the center. When a charged particle  
497 traverses a tube, it ionises the gas and the resulting liberated electrons drift along  
498 the electric field to the wire, where an associated charge is registered. In the barrel  
499 the straws run parallel to the  $z$ -axis and therefore the TRT only provides tracking  
500 information in  $R\phi$ . Straws are arranged radially in the end-caps. The resulting  
501 two-dimensional space-points have a resolution of approximately  $120\text{ }\mu\text{m}$ . The spaces  
502 between the straws are filled with a polymer which encourages the emission of  
503 transition radiation, aiding electron identification.

504 **3.3.2 Calorimeters**

505 The calorimeter system measures the energy of incident particles over the range  
506  $|\eta| < 4.9$ . There are two main sub-systems: the electromagnetic calorimeter (ECal),  
507 which focuses on the measurement of electrons and photons, and the hadronic  
508 calorimeter (HCal), which measures the energy of hadrons. A schematic view of the  
509 calorimeter system is shown in Fig. 3.10. Upon entering the calorimeter, incident  
510 particles will interact with the detector material to produce a shower of secondary  
511 particles with reduced energies. The charge deposited in this process is measured to  
512 reconstruct the energy of the initial incident particle. The two calorimeter sub-systems

513 must provide strong containment of showering particles to prevent punch-through of  
 514 EM and hadronic particles to the HCal and muon systems respectively.

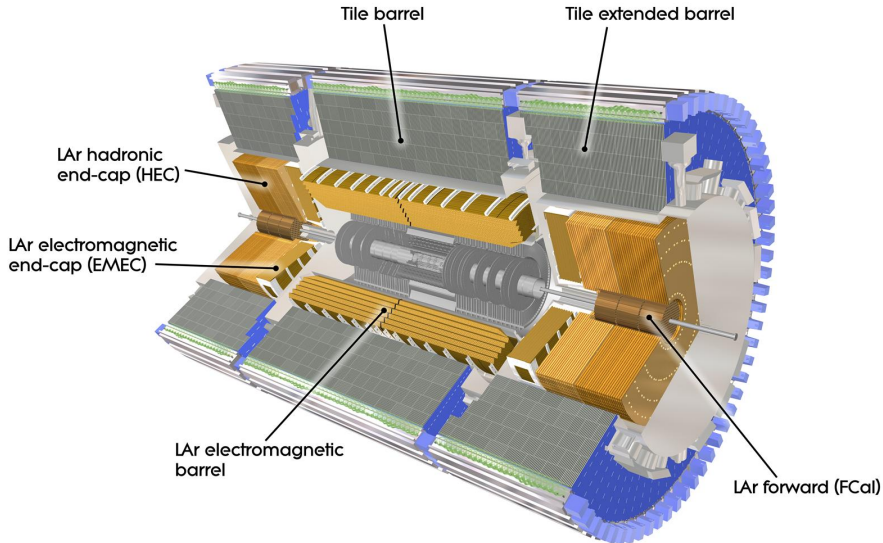


**Figure 3.10:** The ATLAS calorimeters [49]. The ECal uses LAr-based detectors, while the HCal uses mainly scintillating tile detectors. In the forward region the HCal also includes the LAr hadronic end-caps.

### 515 Liquid Argon (LAr) Electromagnetic Calorimeter

516 The more granular lead/liquid-argon ECal covers the region  $|\eta| < 3.2$  and is split  
 517 into barrel (covering  $|\eta| < 1.475$ ) and end-cap (covering  $1.375 < |\eta| < 3.2$ ) regions.  
 518 EM calorimetry works by encouraging electrons and photons to interact with electric-  
 519 cally charged particles in detector material via bremsstrahlung ( $e \rightarrow e\gamma$ ) and pair  
 520 production ( $\gamma \rightarrow e^+e^-$ ). The EM calorimeter uses lead absorber plates to initiate  
 521 EM showers, resulting in secondary particles which ionise the surrounding liquid  
 522 argon. The charge is collected on copper electrodes and read out. The accordion  
 523 geometry of the ECal allows for a full coverage in  $\phi$  without any azimuthal cracks.  
 524 The energy resolution of the LAr calorimeter is made up of a sampling and a constant  
 525 term, which are summed in quadrature to produce the overall energy resolution. The  
 526 sampling term contributes approximately  $10\%/\sqrt{E}$ , while the constant term adds an  
 527 additional 0.7%. Photons with moderate transverse energy  $E_T \approx 50$  GeV have an

528 overall energy resolution of at most 1.6% over most of the pseudorapidity range. At  
 529 lower  $E_T \approx 10 \text{ GeV}$ , the resolution is degraded to approximately 5%. The resolution  
 530 measurements are obtained from test beam data [41].

531 **Hadronic Tile Calorimeter**

532 In the central barrel region with  $|\eta| < 1.7$ , the HCal uses a tile calorimeter with  
 533 steel as an absorbing material, and scintillating tiles as the active material. Two  
 534 copper/liquid-argon calorimeter end-caps are also used. Incident hadrons interact  
 535 via the strong and electromagnetic forces with the absorber material, mainly losing  
 536 energy due to multiple inelastic nuclear collisions. The active material captures the  
 537 resulting electrons and photons to measure the energy of the incident hadron.  
 538 The hadronic energy resolution of the HCal is parameterised as a function of the  
 539 hadron's transverse energy

$$\sigma(E_T)/E_T = 50\%/\sqrt{E_T} \oplus 3\%, \quad (3.9)$$

540 corresponding to a energy resolution of 11% (6.5%) for a hadron with  $E_T$  of approxi-  
 541 mately 10 GeV (50 GeV) [50].

542 **3.3.3 Muon Spectrometer**

543 Due to their higher mass, muons easily pass unimpeded through the ID and calorime-  
 544 ters and therefore require specialised detectors for their measurement. The Muon  
 545 Spectrometer (MS) is made up of dedicated tracking and triggering hardware, as  
 546 shown in Fig. 3.11. The precision tracking system uses three layers of monitored drift  
 547 tubes with a barrel region covering  $|\eta| < 1.2$  and end-caps covering  $1 < |\eta| < 2.7$ .  
 548 The inner layers of the end-caps use cathode strip chambers to better cope with the  
 549 high occupancy in the forward region. The trigger system is comprised of resistive  
 550 plate chambers in the barrel region covering  $|\eta| < 1.0$  and thin gap chambers in  
 551 the end-cap regions covering  $1 < |\eta| < 2.4$ . A set of three superconducting air-core  
 552 toroidal magnets, each made up of eight coils, is used in each of the barrel and  
 553 end-caps to deflect the muons as they pass through the MS, allowing their momentum  
 554 and charge to be measured from the direction and magnitude of curvature. The

555 toroidal magnets generate a field which is largely orthogonal to the muon trajectories  
 556 which allows for maximum deflection. The transverse momentum resolution (mea-  
 557 sured for combined ID and muon tracks, see Section 3.4.4) has been measured to be  
 558 approximately 1.7% in the central region for muons from  $J/\psi$  decays, increasing to  
 2.3% for muons in the forward regions [51].

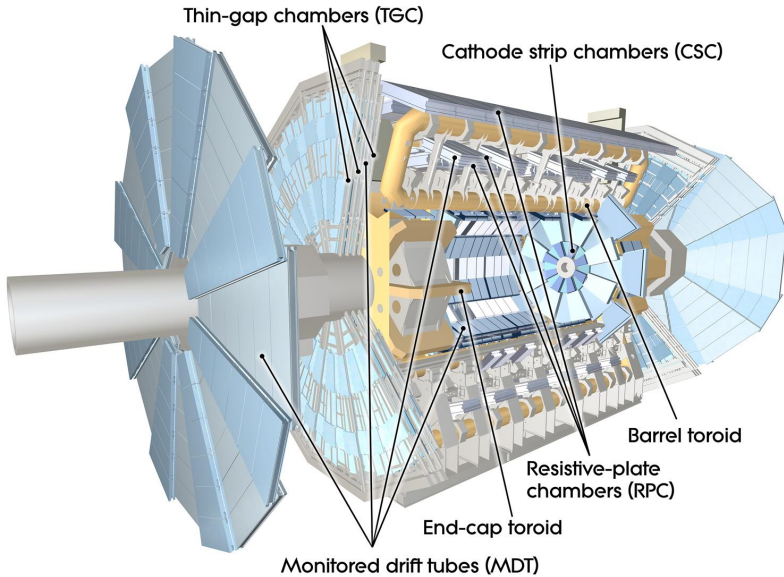


**Figure 3.11:** The ATLAS muon spectrometer [52].

559

### 560 3.3.4 The Trigger

561 The 25 ns bunch spacing used over the course of Run 2 corresponds to a bunch-  
 562 crossing or event rate of 40 MHz (see Table 3.1). If the full information for the  
 563 detector was written out for each event, this would correspond to the generation  
 564 of 60 TB of data each second. This is more than can be feasibly read out from the  
 565 hardware, processed and stored, requiring the use of a trigger system which quickly  
 566 makes a decision about whether or not an event is potentially interesting and should  
 567 be kept for further analysis. The trigger system is comprised of two levels which  
 568 aim to identify various signatures, such as electrons, muons, taus, photons, and jets  
 569 (including  $b$ -jets), as well as events with large total or missing transverse energy. The  
 570 hardware-based Level-1 (L1) trigger uses coarse information from the calorimeters  
 571 and MS to accept events at an average rate of 100 kHz approximately 2.5  $\mu$ s after the

572 event. After the L1 trigger, the software-based High Level Trigger (HLT) makes use  
573 of 40 000 CPU cores to make a final selection on surviving events in approximately a  
574 few hundred milliseconds. The final event read-out rate is approximately 1.2 kHz,  
575 corresponding to  $1.2 \text{ GB s}^{-1}$  of permanent data storage. More information is provided  
576 in [53].

## 577 3.4 Reconstructed Physics Objects

578 Event reconstruction is the process of analysing the output from the detector to  
579 determine the type and properties of particles present in an event. The reconstructed  
580 event provides information about the underlying physics process that led to these  
581 observable final state particles. Events passing the trigger selection (described in  
582 Section 3.3.4) undergo offline reconstruction, which makes use of the full information  
583 from the detector. Reconstruction and analysis of events relies on the extensive  
584 ATLAS software stack, see Ref. [54] for more information.

585 Several different reconstructed objects are used for physics analyses. Objects relevant  
586 to this thesis are described below.

### 587 3.4.1 Tracks

588 The reconstructed trajectories of charged particles are referred to as *tracks*. Tracks  
589 are reconstructed from the energy depositions (called *hits*) left by the particles as  
590 they traverse the inner detector. Tracks are used in the reconstruction of other  
591 objects, including vertices and jets, so their accurate reconstruction is a critical  
592 task. A comprehensive introduction to ATLAS tracking is available in Ref. [55],  
593 while specific optimisations for dense environments are detailed in Refs. [56, 57]. An  
594 overview of track reconstruction is given below.

### 595 Space-point Formation (Clustering)

596 When a charged particle traverses a silicon layer, charge can be collected in more  
597 than one pixel or strip. This is due to the incident angle of the particles with respect  
598 to the sensor, and also the drift of electrons between sensors caused by the magnetic

599 field. Clusters (also called *hits* or *space-points*) are formed by clustering neighbouring  
600 pixels or strips and estimating locations of space-points using the shape and energy  
601 distribution of the clusters.

602 **Track Finding**

603 Space-points are used to build track seeds. These are groups of three hits which  
604 are geometrically compatible with being part of a track segment. A combinatorial  
605 Kalman filter (KF) is used to build track candidates by extending track seeds. The  
606 filter can create multiple track candidates per seed, with bifurcations along the track  
607 occurring when more than one compatible space-point exists on a given layer. In  
608 this way, the KF creates an excess of *track candidates*, which are only required to  
609 satisfy basic quality requirements. Track candidates are allowed to reuse or *share*  
610 hits freely (a single hit may be used by multiple track candidates). Typically, the  
611 presence of shared hits is a predictor of a bad track due to the high granularity of  
612 the ATLAS tracking detectors. At this stage, there can also be a large number of  
613 incorrect hits assigned to otherwise good tracks, and additionally large numbers of  
614 *fake* tracks, which are comprised of a majority of wrong hits and do not correspond  
615 to the trajectory of any one physical particle (*fake* tracks are defined as those where  
616 the majority of associated hits do not originate from one single truth particle, see  
617 Eq. (5.5)). The low quality of tracks at this stage necessitates an ambiguity solving  
618 step, in which candidates are cleaned, and the highest quality track are selected.

619 **Ambiguity Solving**

620 Ambiguity solving was introduced as part of the ATLAS New Tracking effort [55],  
621 which was intended to improve track reconstruction performance in dense envi-  
622 ronments. In the ambiguity solver, track candidates are processed individually in  
623 descending order of a track score. The track score quantifies the likelihood of the  
624 track corresponding to the trajectory of a real particle. Scoring uses a number of  
625 variables, including the number and positions of hits (preferring hits in more precise  
626 regions of the detector), the transverse momentum of the track and the track fit  
627 quality. The track fit quality describes the quality of the track as the  $\chi^2$  divided  
628 by the number degrees of freedom on the track. A preference for high transverse

629 momentum tracks promotes the successful reconstruction of the more physically  
 630 interesting energetic particles, and suppresses the large number of wrong hits assigned  
 631 to low momentum tracks. The ambiguity solver also penalises tracks with missing  
 632 hits on the innermost detector layers.

633 During the processing of a track candidate, the track is cleaned (whereby problematic  
 634 hits are removed), and, if the resulting track satisfies the quality selection criteria, a  
 635 high precision fit of the track parameters using the surviving hits is performed. The  
 636 high precision fit makes full use of all available information, and uses an updated  
 637 position and uncertainty estimate for each cluster obtained from a Neural Network  
 638 (NN) [58]. If the track has reached this stage without being rejected by passing various  
 639 quality requirements, it is re-scored and returned to the list of track candidates. If  
 640 the same track is then processed again without requiring modification, it is added to  
 641 the final track collection. Track candidates that fall below certain quality threshold  
 642 are rejected. This selection does allow for the possibility of a track having small  
 643 number of shared hits, as detailed in Table 3.2.

Parameter	Selection
$p_T$	$> 500 \text{ MeV}$
$ \eta $	$< 2.5$
$ d_0 $	$< 3.5 \text{ mm}$
$ z_0 \sin \theta $	$< 5 \text{ mm}$
Silicon hits	$\geq 8$
Shared silicon hits	$< 2$
Silicon holes	$< 3$
Pixel holes	$< 2$

**Table 3.2:** Quality selections applied to tracks, where  $d_0$  is the transverse IP of the track,  $z_0$  is the longitudinal IP with respect to the PV and  $\theta$  is the track polar angle (see Section 3.2.2 for the IP definitions). Silicon hits are hits on the pixel and SCT layers. Shared hits are hits used on multiple tracks which have not been classified as split by the cluster-splitting neural networks [57]. A hole is a missing hit, where one is expected, on a layer between two other hits on a track.

#### 644 Neural Network Cluster Splitting

645 As part of track cleaning, shared hits are classified by a NN to determine if they are  
 646 compatible with the characteristic features of a merged cluster [56, 58]. A merged  
 647 cluster is one made up of a combination of energy deposits from more than one  
 648 particle, which have become merged due to the closeness of the associated particles  
 649 and the limited resolution of the detector. It is common for clusters to become  
 650 merged in dense environments, as discussed in Section 4.2. If the cluster is predicted  
 651 to be merged it is labelled as being freely shareable, or *split*. Hits not compatible  
 652 with the merged hypothesis can still be shared by a limited number of tracks, but  
 653 come with a penalty for the track which may hinder its acceptance into the final  
 track collection.

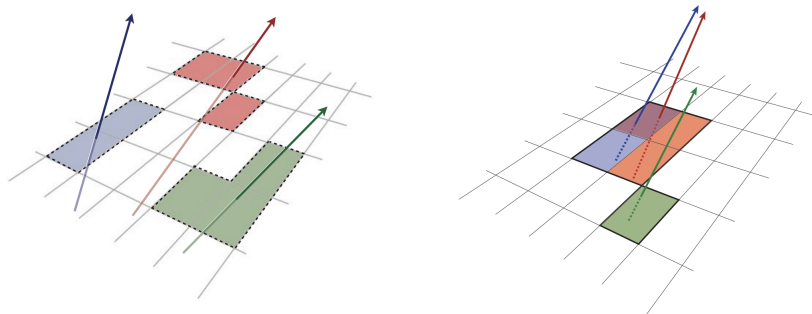


**Figure 3.12:** Particles (left) which have enough separation will leave charge depositions which are resolved into separate clusters. Sufficiently close particles (right) can lead to merged clusters. Their combined energy deposits are reconstructed as a single merged cluster [57].

654

#### 655 Pseudotracking

656 Pseudotracking uses Monte Carlo truth information to group together all the hits  
 657 left by each truth particle. Each collection of hits which, as a unit, satisfies basic  
 658 quality requirements is directly used in a full resolution track fit. If the track fit is  
 659 successful, a “pseudotrack” track is created and stored. If the track fit fails, or the  
 660 collection of hits does not pass the basic quality requirements (for example because  
 661 of a lack of hits) then the particle is said to be un-reconstructable. In this way,  
 662 pseudotracking performance represents the ideal reconstruction performance given

the ATLAS detector, with perfect hit-to-track association and track reconstruction efficiency. The approach was introduced in Ref. [59] as a way to obtain a fast approximation of tracking reconstruction for simulated data, however the technique has become a useful tool for studying tracking performance in general [56].

### 3.4.2 Vertices

Groups of reconstructed tracks can be examined to determine whether the particles originated from a common spatial point of origin. This occurs when proton-proton collisions take place (primary vertices), when a particle decays or radiates, and also as a result of interaction with the detector material (secondary vertices). Vertex reconstruction is made up of two stages. First, vertex finding takes place, which is the process of grouping tracks into compatible vertices. Second, vertex fitting combines information from compatible tracks to reconstruct the physical properties of the vertex, such as mass and position.

#### Primary Vertices

Each proton-proton interaction happens at a *primary vertex* (PV). Primary vertices are iteratively reconstructed with tracks using the iterative vertex finder (IVF) [60]. The *hard scatter vertex* of an event is chosen as the primary vertex whose associated tracks have the largest sum of transverse momentum squared,  $\Sigma(p_T^2)$ .

#### Secondary Vertices

Secondary vertices (SV) occur when a particle radiates or decays at a sufficient distance from the primary vertex to be resolved from the primary vertex (see Section 4.2.1). Two widely used secondary vertexing tools are used within ATLAS: SV1 and JetFitter [61, 62]. Each attempts to reconstruct secondary vertices inside a jet using the tracks associated to that jet (see Section 3.4.3 for more information about track association). SV1 by design attempts to reconstruct only a single inclusive vertex per jet. This inclusive vertex groups all  $b$ -hadron decay products, including tracks from the  $b$ -hadron decay itself and tracks from  $b \rightarrow c$  decays. The second tool, JetFitter attempts to resolve each displaced vertex inside the jet, such

691 that secondary vertices from  $b$ -hadron decays are reconstructed separately to tertiary  
 692 vertices from  $b \rightarrow c$  decay chains.

### 693 3.4.3 Jets

694 Jets are an aggregate reconstructed object corresponding to a collection of collimated  
 695 stable particles which results from the presence of a quark or gluon. Jets are built  
 696 by clustering constituent objects (e.g. tracks or calorimeter clusters) using a jet  
 697 finding algorithm, for example the anti- $k_t$  algorithm [63], which is implemented in  
 698 FASTJET [64].

699 Objects can be associated to jets in one of two ways. The first is via a geometrical  
 700 matching in  $\Delta R$  (see) The second is via a ghost association [65], where the object is  
 701 assigned a negligible momentum and re-clustered into the jet after its formation.

702 Jets from pile-up interactions are suppressed using the Jet Vertex Tagger (JVT)  
 703 algorithm, which uses the transverse momenta of tracks to identify jets from pile-up  
 704 interactions [66].

#### 705 EMTopo Jets

706 EMTopo jets are reconstructed from noise-suppressed topological clusters (topoclus-  
 707 ters) of calorimeter energy depositions [67]. The clustering uses the energy significance  
 708 of each cell, defined as

$$S_{\text{cell}} = \frac{E_{\text{cell}}}{\sigma_{\text{noise, cell}}}, \quad (3.10)$$

709 where  $E_{\text{cell}}$  is the energy measured in a given calorimeter cell, and  $\sigma_{\text{noise, cell}}$  is the  
 710 expected level of noise on the cell (e.g. from pile-up interactions). Topoclusters are  
 711 formed from a seed cell with a large  $S_{\text{cell}}$ , and expanded by iteratively adding neigh-  
 712 bouring cells with a sufficiently large energy significance. Collections of topoclusters  
 713 are then clustered into a jet using the anti- $k_t$  algorithm with a radius parameter of  
 714 0.4 (small- $R$  jets) or 1.0 (large- $R$  jets). More information, including information on  
 715 the calibration of the topocluster jet energy scale, is available in Ref. [67].

## 716 Particle Flow Jets

717 Particle-flow (PFlow) jets are reconstructed from particle-flow objects [68] using  
718 the anti- $k_t$  algorithm with a radius parameter of 0.4. Particle-flow objects integrate  
719 information from both the ID and the calorimeters, improving the energy resolution  
720 at high transverse momenta and reducing pile-up contamination. The PFlow jet  
721 energy scale is calibrated according to Ref. [69].

## 722 Large- $R$ Jets

723 Large- $R$  jets have a radius parameter  $R = 1.0$  and are built by clustering topological  
724 calorimeter clusters using the anti- $k_t$  algorithm [70]. The large radius parameter  
725 is especially useful for containing the decay products of a boosted Higgs boson, as  
726 discussed in Chapter 7. Due to their large size, large- $R$  jets benefit from a grooming  
727 procedure called trimming which remove soft contaminants inside the jet [71, 72].  
728 Trimming aims to remove jet constituents from pile-up and the underlying event,  
729 which helps to improve the jet mass resolution and its robustness to varying levels  
730 of pile-up. The jet mass is computed using a combination of information from the  
731 calorimeters and ID, and a calibration to data is applied [73].

## 732 Track-jets

733 Track-jets are built by clustering tracks using the anti- $k_t$  clustering algorithm. They  
734 are associated to large- $R$  jets as sub-jets and used to identify large- $R$  jets containing  
735  $b$ -hadrons. The radius parameter is allowed to vary with transverse momentum such  
736 that a broader cone (up to  $R = 0.4$ ) is used for low- $p_T$  track-jets and a narrower  
737 cone (down to  $R = 0.02$ ) for high- $p_T$  track-jets [74, 75]. The narrower cone is better  
738 suited to clustering highly collimated jet constituents at high- $p_T$ .

## 739 Jet Flavour Labels

740 Jet flavour labels are assigned to small- $R$  jets according to the presence of a truth  
741 hadron within  $\Delta R(\text{hadron}, \text{jet}) < 0.3$  of the jet axis. If a  $b$ -hadron is found the jet is  
742 labelled a  $b$ -jet. In the absence of a  $b$ -hadron, if a  $c$ -hadron is found the jet is called

<sup>743</sup> a  $c$ -jet. If no  $b$ - or  $c$ -hadrons are found, but a  $\tau$  is found in the jet, it is labelled as a  
<sup>744</sup>  $\tau$ -jet, else it is labelled as a light-jet.

<sup>745</sup> PFlow jets are used to train the algorithms discussed in Chapter 5 and Chapter 6.

#### <sup>746</sup> Jet Track Association

<sup>747</sup> Tracks are associated to small- $R$  jets using a  $\Delta R$  association cone, the width of which  
<sup>748</sup> decreases as a function of jet  $p_T$ , with a maximum cone size of  $\Delta R \approx 0.45$  for jets  
<sup>749</sup> with  $p_T = 20$  GeV and minimum cone size of  $\Delta R \approx 0.25$  for jets with  $p_T > 200$  GeV.  
<sup>750</sup> If a track is within the association cones of more than one jet, it is assigned to the  
<sup>751</sup> jet which has a smaller  $\Delta R(\text{track}, \text{jet})$ .

### <sup>752</sup> 3.4.4 Leptons

<sup>753</sup> Electrons and muons leave characteristic signatures that are picked up in the ECal  
<sup>754</sup> and MS respectively. The reconstruction of both types of charged lepton is briefly  
<sup>755</sup> outlined below.

#### <sup>756</sup> Electrons

<sup>757</sup> A diagrammatic view of electron reconstruction is shown in Fig. 3.13. Electrons  
<sup>758</sup> candidates are reconstructed by matching PV-compatible<sup>3</sup> inner detector tracks  
<sup>759</sup> to topological calorimeter clusters. The track-cluster matching criteria takes into  
<sup>760</sup> account the significant energy loss of the electron due to bremsstrahlung. If a match  
<sup>761</sup> is found, a refit of the track is performed using the Gaussian Sum Filter (GSF) [76],  
<sup>762</sup> which better handles trajectory reconstruction in the presence of bremsstrahlung.  
<sup>763</sup> Various identification criteria are then applied to the candidates using a likelihood-  
<sup>764</sup> based (LH) method to improve purity. These include requirements on the track  
<sup>765</sup> quality and cluster matching, the shape of electromagnetic shower in the ECal,  
<sup>766</sup> leakage into the HCal, and the amount of transition radiation detected in the TRT.  
<sup>767</sup> Isolation criteria with respect to other nearby ID tracks and calorimeter clusters may  
<sup>768</sup> also be applied. A full description can be obtained from Ref. [77].

---

<sup>3</sup>The ID track associated with the electron is required to satisfy  $d_0/s(d_0) < 5$  and  $z_0 \sin \theta < 0.5$  mm.

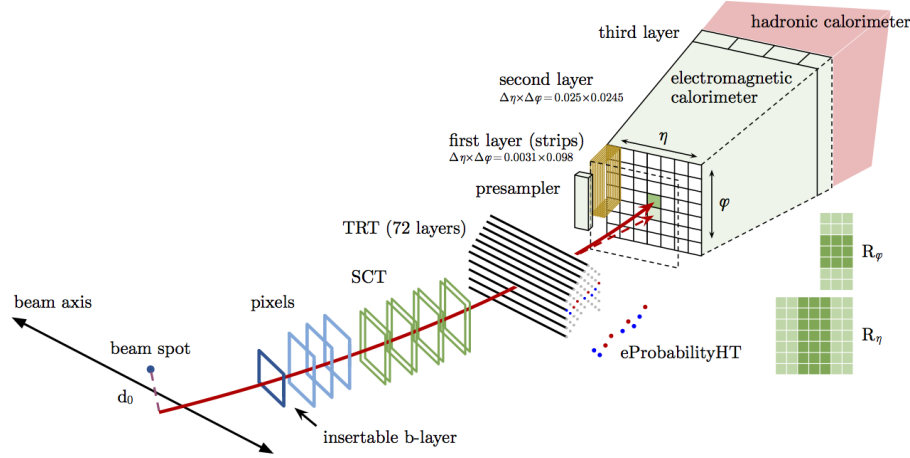


**Figure 3.13:** A sketch of electron reconstruction using the ATLAS detector [77]. Electron reconstruction makes use of the entire ID and the calorimeters.

## 769 Muons

770 Muon reconstruction makes use of the dedicated MS (see Section 3.3.3), the tracks  
 771 from the ID, and the presence of characteristic signatures in the calorimeters. Muon  
 772 tracks (i.e. a track reconstructed in the MS) are reconstructed by connecting straight-  
 773 line track segments, which are identified via a Hough transform, and combined into  
 774 a approximately parabolic trajectory. Finally, a global  $\chi^2$  fit is performed, taking  
 775 into account possible interactions between the muon and the detector material. A  
 776 reconstructed muon is called *combined* if it can be matched successfully to an to  
 777 an ID track. Combined muons undergo a further fit with the combined ID and MS  
 778 hits, with the energy loss due to the traversal of the calorimeters being taking into  
 779 account.

780 After reconstruction, candidate undergo an identification processes which helps to  
 781 efficiently identify prompt muons whilst rejecting background signals (e.g. non-  
 782 prompt muons from pion and kaon decays, the punch-through of a hadron from the  
 783 calorimeter, or the semi-leptonic decay of a heavy flavour hadron). Combined muon  
 784 identification takes into account discrepancies in the  $p_T$  and charge measurements  
 785 in the MS and ID, and the  $\chi^2$  of the combined track fit. Selections on the number  
 786 of hits in the ID and MS are also applied. At the medium identification working  
 787 point, approximately 96% of prompt muons with  $20 \text{ GeV} < p_T < 100 \text{ GeV}$  are

788 successfully identified. On top of the identification requirements, a number of  
789 isolation requirements can also be applied to further suppress background signals.

790 More information on muon reconstruction, identification and isolation can be found  
791 in Ref. [51].

### 792 3.4.5 Missing Transverse Momentum

793 An imbalance in the final state transverse momentum can occur as a result of  
794 incomplete measurement of the final state particles. In particular, neutrinos are  
795 not measured by the detector and contribute to the missing transverse momentum  
796  $\mathbf{E}_T^{\text{miss}}$ . Incomplete detector acceptance and inaccuracies in the reconstruction of the  
797 final state can also contribute to the missing transverse momentum of an event. In  
798 order to calculate the missing transverse momentum, the negative vector sum of  
799 the momentum of all photons, leptons and small- $R$  jets with  $p_T > 20 \text{ GeV}$  is taken.  
800 The momenta of tracks associated to the primary vertex are also taken into account.  
801 The magnitude of  $\mathbf{E}_T^{\text{miss}}$  is written  $E_T^{\text{miss}}$ . More information about missing transverse  
802 momentum reconstruction is provided in [78].

## 803 3.5 Flavour Tagging Algorithms

804 Many ATLAS analyses rely on flavour tagging, which is the identification of jets  
805 containing heavy flavour (HF) hadrons ( $b$ -hadrons and  $c$ -hadrons) as opposed to those  
806 containing only light-flavour hadrons or gluons (collectively referred to as light-jets).  
807 In particular,  $b$ -tagging is the identification of jets originating only from  $b$ -hadrons  
808 (i.e.  $b$ -jets). Flavour tagging is a critical component of the physics programme of the  
809 ATLAS experiment. It is of crucial importance for the study of the Standard Model  
810 (SM) Higgs boson and the top quark, which decay preferentially to  $b$ -quarks [79, 80],  
811 and additionally for several Beyond the Standard Model (BSM) resonances that  
812 readily decay to heavy flavour quarks [81].

813 In this section some common definitions used in flavour tagging are given in Sec-  
814 tion 3.5.1, followed by a description of the various  $b$ -jet identification algorithms  
815 (also called *taggers*) used in ATLAS in Sections 3.5.2 and 3.5.3.

### 816 3.5.1 Common Definitions

817 Each flavour tagging algorithm outputs a discriminant value that can be used to  
 818 select jets of the signal flavour. The efficiency of a flavour tagging algorithm is  
 819 defined as the fraction of signal jets which are correctly identified by the tagger.  
 820 Given  $N^{\text{signal}}$  signal jets,  $N_{\text{tagger}}^{\text{signal}}$  of which have passed the algorithm's selection and  
 821  $N_{\text{untagger}}^{\text{signal}}$  of which have not, the efficiency is given by

$$\varepsilon = \frac{N_{\text{tagged}}^{\text{signal}}}{N_{\text{tagged}}^{\text{signal}} + N_{\text{untagged}}^{\text{signal}}}. \quad (3.11)$$

822 Meanwhile the *fake rate* is defined as the efficiency for a background class to be  
 823 selected, i.e.

$$\text{fake rate} = \frac{N_{\text{tagged}}^{\text{background}}}{N_{\text{tagged}}^{\text{background}} + N_{\text{untagged}}^{\text{background}}}. \quad (3.12)$$

824 The *rejection power* of the model is quantified for a given background as the reciprocal  
 825 of the fake rate, i.e.

$$\text{rejection power} = \frac{1}{\text{fake rate}}. \quad (3.13)$$

826 A *fixed-cut working point* (WP) defines the corresponding selection applied to the  
 827 tagging discriminant in order to achieve a given efficiency on the inclusive  $t\bar{t}$  sample.

### 828 3.5.2 Low-level Algorithms

829 The low-level algorithms are the first step in the  $b$ -tagging process. They take inputs  
 830 information about the jet and its associated tracks and reconstruct distinct features  
 831 of the experimental signature of heavy flavour jets. The low-level algorithms are a  
 832 combination of manually optimised reconstruction algorithms, for example SV1 and

833 JetFitter which reconstruct displaced decay vertices (see Section 3.4.2) and IPxD  
 834 which discriminates based on track IPs, and trained machine learning models such  
 835 as RNNIP and DIPS which use IP and hit information from a variable number of  
 836 tracks [82, 83].

### 837 3.5.3 High-level Algorithms

838 The high-level algorithms combine the outputs of the independently optimised low-  
 839 level algorithms using a multivariate approach to produce a discriminant value for  
 840 each jet. For example the MV2c10 algorithm, used in the analysis described in  
 841 Chapter 7, consists of a boosted decision tree which combines the outputs of IPxD,  
 842 SV1 and JetFitter [61, 84, 85]. The working point is tuned to achieve an average  $b$ -jet  
 843 efficiency of 70% on simulated  $t\bar{t}$  events. At this efficiency working point, rejection  
 844 factors for  $c$ -jets and light-jets are approximately 9 and 304 respectively.

845 The current ATLAS flavour tagger, DL1r [85], is part of a series of taggers that  
 846 use a deep neural network to combine the outputs of the low-level algorithms. The  
 847 low-level algorithms used by the different high-level taggers DL1, DL1r and DL1d is  
 848 shown in Fig. 3.14.

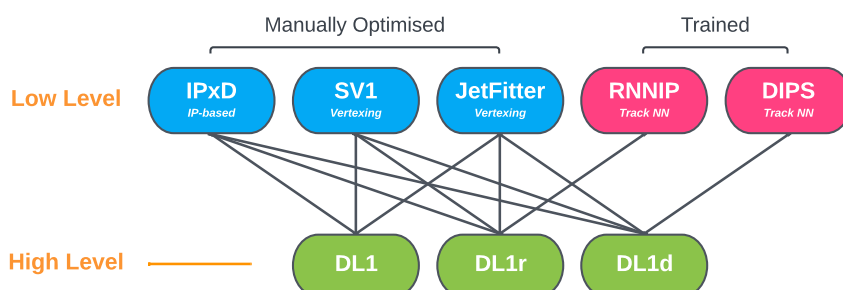


**Figure 3.14:** An overview of different high and low level taggers used in ATLAS. The low level taggers are IPxD, SV1 and JetFitter, and RNNIP and DIPS [61, 62, 82, 83]. The outputs of these taggers are fed into the high-level taggers DL1, DL1r and DL1d [85, 86].

849 **Chapter 4**

850 **Tracking and Flavour Tagging at  
851 High- $p_T$**

852 The various flavour tagging algorithms (introduced in Section 3.5) work by identi-  
853 fying the unique signatures of heavy flavour (HF) jets ( $b$ - and  $c$ -jets). Ultimately,  
854 the tagging algorithms use input information about the reconstructed jet and its  
855 associated tracks. Successful  $b$ -tagging therefore relies on the efficient and accurate  
856 track reconstruction, especially for tracks corresponding to the products of HF decays.  
857 In this chapter studies investigating the challenges facing track reconstruction and  
858 flavour tagging at high- $p_T$  are discussed.

859 The chapter is structured as follows. In Section 4.1 an introduction to the datasets  
860 used in this thesis is given. The unique signatures of  $b$ -jets are outlined in Section 4.2.  
861 A summary of the challenges facing tracking and  $b$ -tagging at high transverse mo-  
862 mentum is provided in Section 4.2.2. Some preliminary investigations into improving  
863 tracking in the high- $p_T$  regime are investigated in Section 4.3. In Section 4.4 the  
864 conclusions of this chapter are given.

865 **4.1 Datasets**

866 This thesis makes extensive use of two simulated datasets which are described in this  
867 section. The datasets are made up of simulated SM  $t\bar{t}$  and BSM  $Z'$  events initiated by  
868 proton-proton collisions at a center of mass energy  $\sqrt{s} = 13$  TeV. The  $Z'$  sample is  
869 constructed in such a manner that it has a relatively flat jet  $p_T$  spectrum up to 5 TeV

and decays democratically to equal numbers of  $b$ -,  $c$ - and light-jets. The generation of the simulated event samples includes the effect of multiple  $pp$  interactions per bunch crossing with an average pile-up of  $\langle \mu \rangle = 40$ , which includes the effect on the detector response due to interactions from bunch crossings before or after the one containing the hard interaction.

The  $t\bar{t}$  events are generated using the POWHEGBox v2 generator [87–90] at next-to-leading order with the NNPDF3.0NLO [91] set of parton distribution functions (PDFs). The  $h_{\mathrm{damp}}$  parameter<sup>1</sup> is set to 1.5 times the mass of the top-quark ( $m_{\mathrm{top}}$ ) [92], with  $m_{\mathrm{top}} = 172.5$  GeV. The events are interfaced to PYTHIA 8.230 [93] to model the parton shower, hadronisation, and underlying event, with parameters set according to the A14 tune [94] and using the NNPDF2.3LO set of PDFs [95].  $Z'$  events are generated with PYTHIA 8.2.12 with the same tune and PDF set. The decays of  $b$ - and  $c$ -hadrons are performed by EVTGEN v1.6.0 [96]. Particles are passed through the ATLAS detector simulation [97] based on GEANT4 [98].

Jets are required to have a pseudorapidity  $|\eta| < 2.5$  and  $p_{\mathrm{T}} > 20$  GeV. Additionally, a standard selection using the JVT tagger (see Section 3.4.3) at the tight working point is applied to jets with  $p_{\mathrm{T}} < 60$  GeV and  $|\eta| < 2.4$  in order to suppress pile-up contamination [66].

## 4.2 $b$ -hadron Reconstruction

This section outlines the typical detector signature of a  $b$ -hadron in Section 4.2.1 and discusses some associated reconstruction difficulties in Section 4.2.2.

### 4.2.1 Decay Topology

$b$ -hadrons are quasi-stable bound states of a bottom quark and one or more lighter quarks. Collectively, these are the  $B$ -mesons (e.g.  $B^+ = u\bar{b}$ ,  $B^0 = d\bar{b}$ ) and baryons (e.g.  $\Lambda_b^0 = udb$ ). After a  $b$ -quark is produced as the result of a proton-proton collision, they quickly hadronise. The hadronisation process is hard – around 70-80% of the  $b$ -quark’s momentum is passed to the  $b$ -hadron, with the rest being radiated

---

<sup>1</sup>The  $h_{\mathrm{damp}}$  parameter is used to limit the effect of resummed higher order corrections. It is used to suppress the transverse momentum of the radiation which the  $t\bar{t}$  system recoils against.

as prompt hadronisation or fragmentation particles. See Ref. [99] for a more in depth discussion on hadronisation and the closely related process of fragmentation. Henceforth the combined hadronisation and fragmentation products will be referred to collectively as fragmentation.

$b$ -hadrons are interesting objects of study due to their relatively long proper lifetimes  $\tau \approx 1.5 \text{ ps}$  [100]. This lifetime corresponds to a proper decay length  $c\tau \approx 450 \mu\text{m}$ . In the rest frame of the detector, the typical  $b$ -hadron travels a distance

$$d = \gamma\beta c\tau \approx \gamma c\tau \quad (4.1)$$

before decaying, where in the high energy limit  $\gamma = E_b/m_b$  and  $\beta = v/c = 1$ .

For a 50 GeV  $b$ -hadron, this gives  $d \approx 4.5 \text{ mm}$ , which is displaced enough to be resolved from the primary vertex. Meanwhile for a 1 TeV  $b$ -hadron,  $d \approx 90 \text{ mm}$  – well beyond the radius of the first pixel layer (the IBL) which is situated at a radius of approximately 33 mm from the center of the detector (the distance varies due to the interleaved structure). Fig. 4.1 shows how the mean decay radius varies as a function of  $b$ -hadron  $p_{\mathrm{T}}$ . This significant displacement is characteristic of  $b$ -jets and makes it possible to reconstruct secondary vertices (SV) at the  $b$ -hadron decay point.

$b$ -hadrons decay weakly to on average four or five collimated stable particles [101]. These particles, along with any other fragmentation particles, are reconstructed in the detector as a jet. A  $b$ -jet has several characteristic features which differentiate it from light-jets. The primary feature is the presence of a high mass secondary vertex that is significantly displaced from the primary vertex. Reconstruction of these vertices from tracks with common points of spatial origin is a common approach used in the identification of  $b$ -jets.

Additional signatures of  $b$ -hadrons are as follows. Associated tracks and SVs can have a large transverse impact parameter  $d_0$  as a result of the  $b$ -hadron displacement (as shown in Fig. 4.2). Furthermore, since it is common for the  $b$ -hadron to decay to a  $c$ -hadron with non-negligible lifetime, tertiary vertices can be found within  $b$ -jets resulting from  $b \rightarrow c$  decay chains. Additionally, as the  $b$ - or  $c$ -hadron decays semileptonically in approximately 40% of cases [16], the presence of a reconstructed electron or muon inside a jet gives information about the jet flavour.

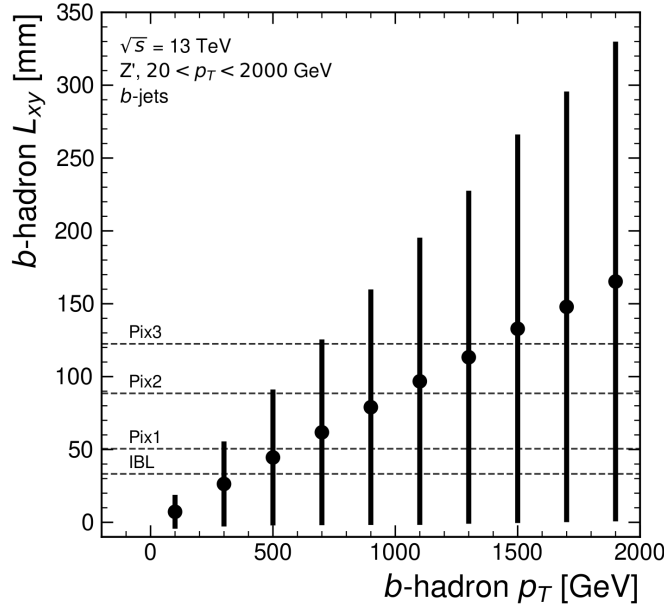


**Figure 4.1:** The truth  $b$ -hadron decay radius  $L_{xy}$  as a function of truth transverse momentum  $p_T$  for reconstructed  $b$ -jets in  $Z'$  events. Error bars show the standard deviation. The pixel layers are shown in dashed horizontal lines.

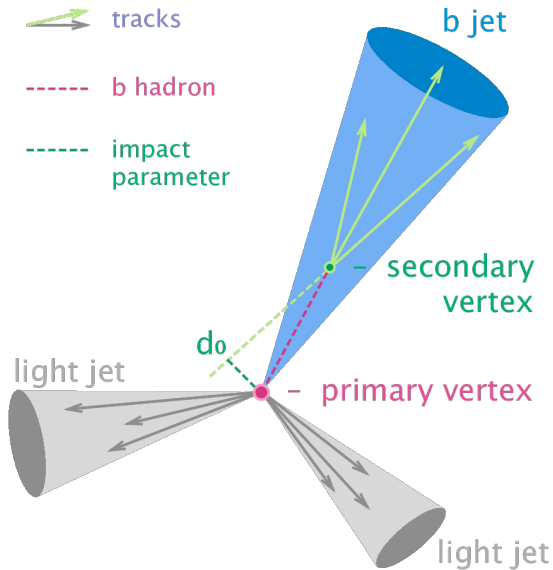


**Figure 4.2:** Diagram of a typical  $b$ -jet (blue) which has been produced in an event alongside two light jets (grey) [102]. The  $b$ -hadron has travelled a significant distance (pink dashed line) from the primary interaction point (pink dot) before its decay. The large transverse impact parameter  $d_0$  is a characteristic property of the trajectories of  $b$ -hadron decay products.

926 These signatures are primarily identified using tracks associated to jets, or using re-  
927 constructed electrons or muons, which also rely on tracks as discussed in Section 3.4.4.  
928 As such, efficient and accurate track reconstruction is essential for high performance  
929 flavour tagging.

930 **4.2.2 Challenges**

931 As discussed, a necessary requirement for successful  $b$ -tagging is the efficient and  
932 accurate reconstruction of the charged particle trajectories in the jet. For high  $p_{\mathrm{T}}$   
933 jets ( $p_{\mathrm{T}} > 250$  GeV) this task becomes difficult due to a combination of effects, which  
934 are described below.

935 As the  $b$ -jet energy increases, the multiplicity of the fragmentation products inside the  
936 jet increases, while the multiplicity of the products of the weak decay remains fixed.  
937 The “signal” tracks (those from the weak decay of the  $b$ -hadron) therefore become  
938 significantly outnumbered. Both fragmentation and  $b$ -hadron weak decay products  
939 also become increasingly collimated as their inherited transverse momentum increases.  
940 This is compounded by the increased decay length of  $b$ -hadrons (and  $c$ -hadrons) at  
941 high- $p_{\mathrm{T}}$ , which means that the decay products have less of an opportunity to diverge  
942 before reaching the first tracking layers of the detector (shown in Fig. 4.3). If the  
943 weak decay of the  $b$ -hadron takes place close enough to a detector layer, or if the  
944 particles are otherwise sufficiently collimated, charge deposits left by nearby particles  
945 may not be resolved individually, instead being reconstructed as merged clusters [57].

946 As discussed in Section 3.4.1, merged clusters are generally rare, and so shared  
947 hits generally predict bad tracks and are correspondingly penalised during track  
948 reconstruction. However, in the core of high  $p_{\mathrm{T}}$   $b$ -jets the density of particles is high  
949 enough that the probability of cluster merging increases dramatically. Successful  
950 reconstruction of such tracks requires the presence of shared hits to be effectively  
951 dealt with, but in the standard reconstruction the presence of these can instead  
952 impair the successfully reconstruction of the track. Furthermore, HF decays may also  
953 take place inside the tracking detectors themselves, which at best leads to missing  
954 measurements on the most sensitive detector layers, and at worst can lead to wrong  
955 inner layer hits being added to displaced tracks, since the reconstruction process  
956 penalises tracks without inner layer hits.

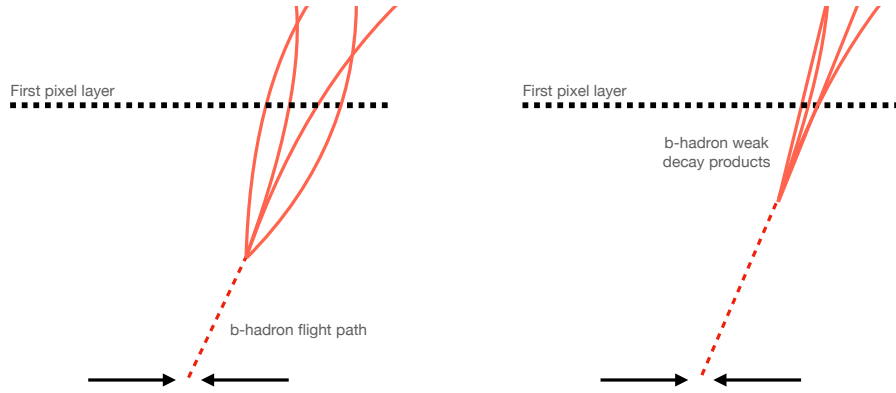


**Figure 4.3:** At lower  $p_T$  (left) the decay length of the  $b$ -hadron is on average reduced, and the decay tracks are less collimated. At higher  $p_T$  (right) the  $b$ -hadron decay length increases and the resulting decay tracks are more collimated and have less distance over which to diverge before reaching detector elements. As a result, the ID may be unable to resolve charged depositions from different particles, resulting merged clusters.

- 957 The above effects create two distinct but related problems for  $b$ -tagging. The first is  
 958 a drop in track reconstruction efficiency. The presence of shared and missing hits  
 959 reduces a track's score in the ambiguity solver meaning that higher ranking, but  
 960 potentially less accurate, track candidates are processed first and take ownership  
 961 of the hits. This can make it difficult for otherwise reasonable  $b$ -hadron decay  
 962 tracks to meet the ambiguity solver's stringent track quality requirements, leading  
 963 to their rejection at this stage and an overall decrease in the  $b$ -hadron decay track  
 964 reconstruction efficiency. As shown in Fig. 4.4, this can result in a large drop in  
 965 reconstruction efficiency for  $b$ -hadron decay products of up to 50% for at  $p_T > 2 \text{ TeV}$ .
- 966 The second part of the problem is that, due to the high multiplicity of clusters  
 967 available for assignment in the vicinity of the typical high- $p_T$   $b$ -hadron decay track,  
 968 and also given the strong positive bias of the ambiguity solver towards those tracks  
 969 with pixel measurements in each layer (especially the innermost IBL measurement),  
 970 many  $b$ -hadron decay tracks are assigned incorrect inner layer hits. This is only a  
 971 problem for those decay products which were produced within the pixel detector  
 972 as a result of a significantly displaced  $b$ -hadron decay, and so do not have a correct  
 973 hit available for assignment. Fig. 4.5 shows the number of hits as a function of the  
 974 reconstructed track  $p_T$  for fragmentation tracks and tracks from the weak decay  
 975 of the  $b$ -hadron. The baseline tracks represent the standard reconstruction setup,

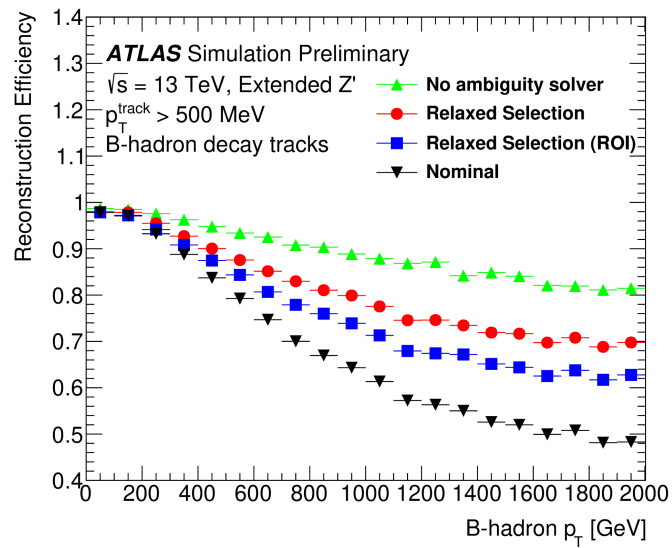


**Figure 4.4:**  $b$ -hadron decay track reconstruction efficiency as a function of truth  $b$ -hadron  $p_T$  [103]. Nominal track reconstruction is shown in black, while the track reconstruction efficiency for track candidates (i.e. the pre-ambiguity solver efficiency) is shown in green. For high- $p_T$   $b$ -hadrons, the ambiguity solver is overly aggressive in its removal of  $b$ -hadron decay tracks. Suggestions for the improvement of the track reconstruction efficiency in this regime by the loosening of cuts in the ambiguity solver are shown in blue and red.

976 while the pseudotracks represent the ideal tracking setup as outlined in Section 3.4.1.  
 977 Hit multiplicities on the pseudotracks decrease at high  $p_T$  due to the flight of the  
 978  $b$ -hadron before its decay. The baseline tracks have more hits than the pseudotracks,  
 979 indicating that they are being incorrectly assigned additional hits on the inner layers  
 980 of the detector.

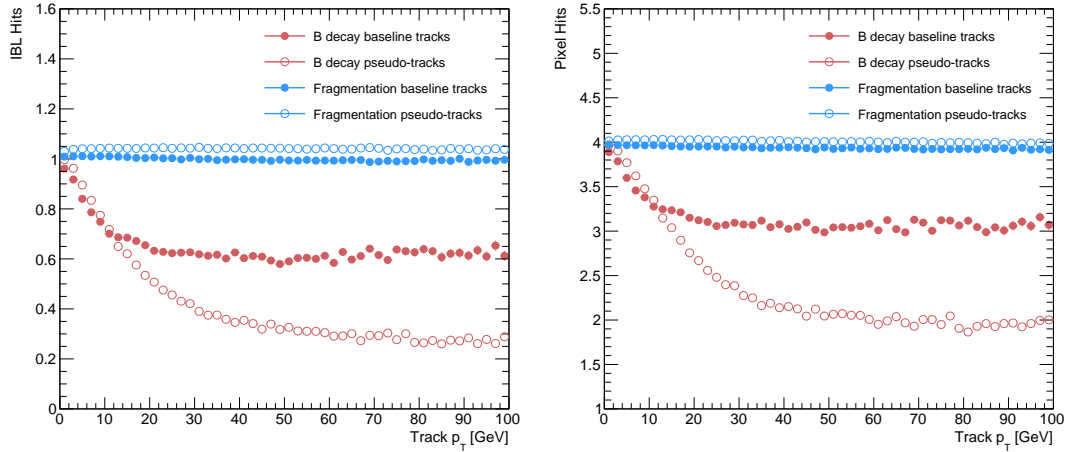


**Figure 4.5:** Hit multiplicities on the IBL (left) and the pixel layers (right) as a function of the  $p_T$  of the reconstructed track for tracks in jets in a  $Z'$  sample at  $\sqrt{s} = 13$  TeV. Tracks from the weak decay of the  $b$ -hadron are shown in red, while fragmentation tracks (which are prompt) are in blue. Baseline tracks are those produced in the standard reconstruction described in Section 3.4.1, while pseudotracks represent the ideal performance of the ATLAS detector and are described in Section 3.4.1.

981 These incorrect hits may skew the parameters of the track, which can in turn lower  
 982 the performance of the downstream  $b$ -tagging algorithms. In particular,  $b$ -tagging  
 983 algorithms rely heavily on the transverse impact parameter significance  $s(d_0)$  of the  
 984 track (see Section 3.2.2). The quality of this measurement is expected to be adversely  
 985 affected by wrong inner-layer hits on the track. Furthermore, multiple tracks sharing  
 986 an incorrect hit can lead to the creation of spurious secondary vertices, which can  
 987 cause further problems for the  $b$ -tagging algorithms.

988 The combination of the effects described makes reconstructing tracks in the core  
 989 of high  $p_T$   $b$ -jets particularly challenging. The reduced reconstruction efficiency of  
 990  $b$ -hadron decay tracks and incorrectly assigned hits is thought to be the primary  
 991 cause of the observed drop in  $b$ -tagging efficiency at high energies, however further  
 992 study is required to determine which effect may dominate.

## 993 4.3 Investigations into High $p_{\mathrm{T}}$ $b$ -hadron Tracking 994 Improvements

995 In Section 4.3.1 pseudotracks, a key tool for studying the ideal tracking performance  
996 of the ATLAS detector, are used to study the shared hit requirements on tracks in  
997 the dense cores of high- $p_{\mathrm{T}}$   $b$ -jets. Section 4.3.2 details a study which investigated  
998 modifying the global track fitter to improve reconstruction performance in this  
999 regime.

### 1000 4.3.1 Shared Hits

1001 The ambiguity solver is not run for pseudotracks. However, if the standard track  
1002 collection is produced alongside the pseudotracks, then cluster splitting neural  
1003 networks will be run for the standard tracks, and the resulting classification of  
1004 clusters will be propagated to hits on pseudotracks. This quirk allows one to study  
1005 the inefficiencies of the cluster splitting process, and relatedly to determine whether  
1006 shared hit cuts in the ambiguity solver are too loose or too tight. The fraction of hits  
1007 that are shared for the IBL and the B-layer is shown in Fig. 4.6. The shared hits on  
1008 pseudotracks represent correctly assigned hits from merged clusters that were not  
1009 able to be classified as split by the cluster splitting neural networks. As such, these  
1010 represent the number of shared hits the ambiguity solver should aim to allow given  
1011 the current performance of the cluster splitting algorithm. For shared hits on the IBL  
1012 for particles produced before the IBL, the baseline selection appears to be successful  
1013 in disallowing excessive numbers of shared hits. However, the ambiguity solver fails to  
1014 limit shared hits for those particles produced after the IBL, reflecting the previously  
1015 discussed problem of displaced tracks picking up incorrect hits. Meanwhile, it is clear  
1016 that for the B-layer, the ambiguity solver is being overly aggressive in its rejection of  
1017 shared hits.

### 1018 4.3.2 Global $\chi^2$ Fitter Outlier Removal

1019 As part of the track fit an outlier removal procedure is run in which suspicious hits  
1020 are identified and removed. This section documents ongoing studies into improving

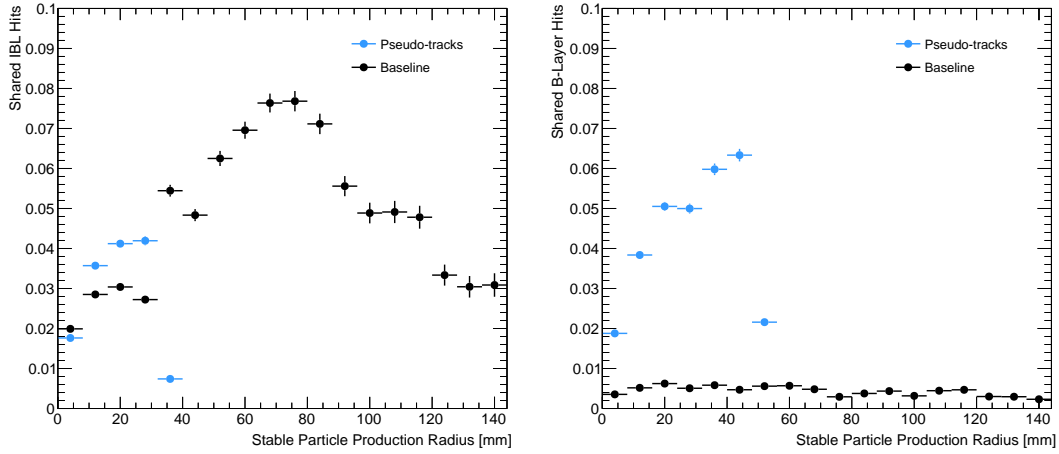


**Figure 4.6:** The fraction of IBL (left) and B-layer (right) hits which are shared on  $b$ -hadron decay tracks as a function of the production radius of the  $b$ -hadron decay product for tracks in jets in a  $Z'$  sample at  $\sqrt{s} = 13$  TeV. Pseudotrack represent the ideal performance given the ATLAS detector, see Section 3.4.1.

hit-to-track assignment by using the Global  $\chi^2$  Fitter (GX2F) to identify and prevent incorrect hits from being assigned to tracks during the track fit. This is in contrast to a previously investigated approach [104] which attempted to identify and remove incorrect hits after the reconstruction of the track.

The GX2F code, as a relatively low-level component of track reconstruction, has not undergone significant modification for several years, and was originally only optimised in the context of prompt, isolated tracks. Since then, a new tracking sub-detector, the IBL, was installed. The motivation for looking at the GX2F is that this change may require the re-optimisation of the GX2F code, and in particular the outlier removal procedure. Further motivation for this approach comes from the low rate of labelled outliers in baseline tracking, in contrast to the relatively higher rate of tracks with an incorrect IBL hit.

### Implementation

The outlier removal procedure for the pixel detector is described in this section. The hits on the track are looped over in order of increasing radial distance to the beam pipe. For each hit, errors  $\sigma(m_i)$  on the measurement of the transverse and longitudinal coordinates are calculated. These errors are dependent on the sub-

1038 detector which recorded the measurement (some sub-detectors are more precise than  
1039 others). Additionally, a residual displacement  $r_i = m_i - x_i$  between the predicted  
1040 position of the track  $x_i$  (inclusive of the current measurement), and the position of  
1041 the hit itself,  $m_i$ , is calculated. The pull  $p_i$  on the track state due to the current  
1042 measurement is calculated according to

$$p_i = \frac{m_i - x_i}{\sqrt{\sigma(m_i)^2 - \sigma(x_i)^2}} \quad (4.2)$$

1043 This pull is computed for the transverse and longitudinal coordinates of the mea-  
1044 surement, and the maximum of the two is selected and checked to see if it exceeds  
1045 a certain selection threshold. If it does, the hit will be removed if the track also  
1046 exceeds a threshold on the total  $\chi^2/n$ , where  $n$  is the number of degrees of freedom  
1047 on the track. The results of varying the outlier selection and  $\chi^2/n$  thresholds are  
1048 described below.

## 1049 Selection Optimisation

1050 A systematic variation of the outlier selection and  $\chi^2/n$  thresholds has been carried  
1051 out. Both thresholds were reduced in fixed step sizes of 0.25 for the outlier selection  
1052 threshold and 1 for the  $\chi^2/n$  threshold. The results for the best performing selections  
1053 are discussed below. The value of the outlier selection threshold was reduced from 4  
1054 down to 1.75, a change which affects the silicon layers (the TRT has separate outlier  
1055 removal logic). Furthermore, a specific cut for the IBL was introduced, and after  
1056 optimisation is set to 1.25. The second threshold on the track  $\chi^2/n$  was also reduced  
1057 from 7 to 4. Finally, instead of taking the maximum of the pulls in the longitudinal  
1058 and transverse directions, a quadrature sum is taken of these two values and used.  
1059 This variation is labelled “Mod GX2F” and was found to improve performance.

1060 The results are shown in Fig. 4.7 and demonstrate a reduction in wrong hit assignment  
1061 whilst also improving slightly the rate at which good hits are assigned to tracks. For  
1062 a 1 TeV track, the rate to assign good hits to the track increases by approximately  
1063 10%, while the rate to assign incorrect hits decreases by approximately 16%. The  
1064 improvements are also observed when looking inclusively in all tracks, which avoids  
1065 the need for a specific  $b$ -jet region-of-interest selection.

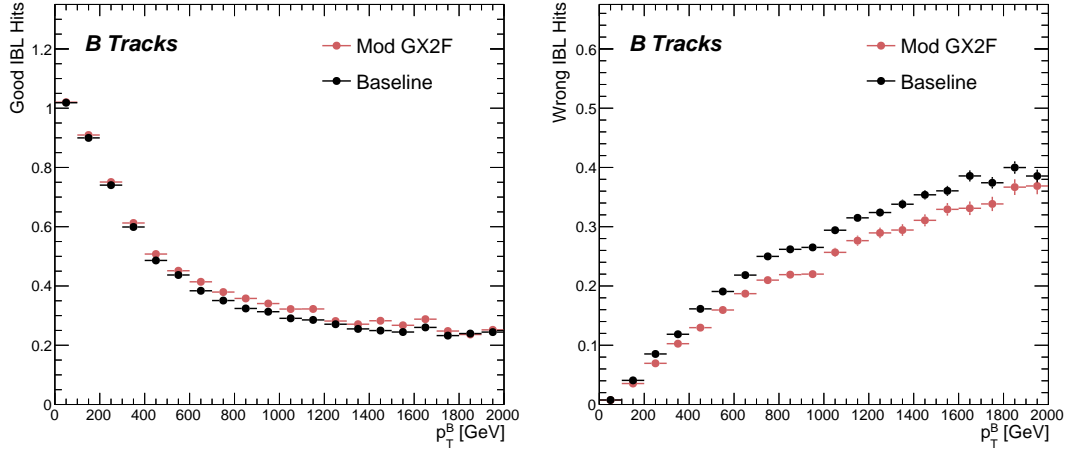


**Figure 4.7:** The average number of good (left) and wrong (right) IBL hits as a function of  $b$ -hadron  $p_T$  for tracks using baseline tracking (black) and the modified version of the outlier removal procedure (red).

1066 An improvement, though modest, of all track parameter resolutions and pulls is  
 1067 observed. The improvement for the transverse impact parameter pull is shown in  
 1068 Fig. 4.8. The results demonstrate an improvement in hit assignment, unchanged  
 1069 reconstruction efficiency, and modest improvement in track parameter resolutions  
 1070 and pulls. In addition, the truth match probability of tracks is unchanged, suggesting  
 1071 that there is no increase in fake track rates. The changes are expected to have a  
 1072 negligible impact on computational resources.

## 1073 4.4 Conclusion

1074 In this section, the difficulties facing efficient and accurate track reconstruction,  
 1075 and hence performant  $b$ -tagging, have been outlined. The ambiguity solver, which  
 1076 attempts to clean or reject tracks which have an excessive number of shared hits,  
 1077 is shown to be overly aggressive in the removal of  $b$ -hadron decay product track  
 1078 candidates. The ambiguity solving process relies on a complicated pre-defined  
 1079 selection which has not been optimised for high transverse momentum  $b$ -hadron  
 1080 track reconstruction. These conclusions have motivated further ongoing studies into  
 1081 the improvement of the track reconstruction in dense environments and the high- $p_T$   
 1082 regime, such as those in Ref. [103].

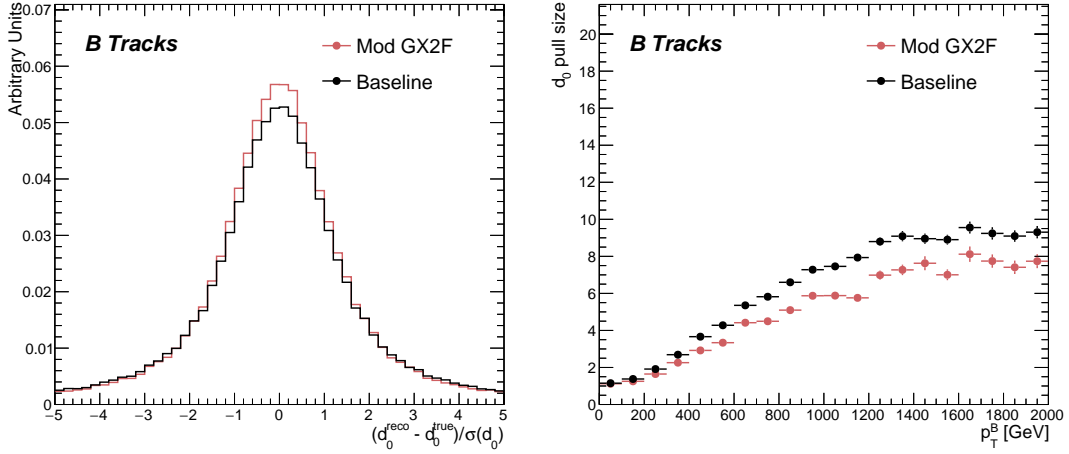


**Figure 4.8:** (left)  $b$ -hadron decay track  $d_0$  pulls ( $d_0/s(d_0)$ ) for baseline and modified GX2F tracks. (right) The absolute value of the  $d_0$  pull as a function of the truth  $b$ -hadron transverse momentum.

1083 An optimisation of the outlier removal process in the global  $\chi^2$  fitter was carried out.  
 1084 The results of the optimisation show that more aggressive removal of outlier hits can  
 1085 lead to fewer wrong hits being assigned to tracks, and improvements in the pulls of  
 1086 the track parameters.

## 1087 Future Work

1088 The studies were carried out in Release 21 of the ATLAS software, and need to be  
 1089 reproduced using the newer Release 22 to confirm the results against other changes  
 1090 in the baseline tracking configuration. It is also necessary to study the impact of  
 1091 the improved outlier removal on the downstream  $b$ -tagging algorithms. Thanks to  
 1092 the all-in-one flavour tagging approach described in Chapter 6, this will in future be  
 1093 easier to study.

1094 As there are some known data-MC discrepancies, fine tuned optimisation such as the  
 1095 work presented here presents an opportunity to over-optimize the tracking algorithms  
 1096 on MC. As such, further studies validating the improved outlier removal procedure  
 1097 on data are required.

1098 **Chapter 5**

1099 **Track Classification MVA**

1100 This chapter details work on implementing a multivariate algorithm (MVA) to predict  
1101 the truth origin of reconstructed tracks. An introduction to formalisms of machine  
1102 learning is given in Section 5.1. In Section 5.2, the truth origin label is defined,  
1103 and in Section 5.3 these labels are used to train a machine learning model that can  
1104 effectively discriminate between good and fake tracks. Several studies motivated this  
1105 work by demonstrating that at high  $p_T$ ,  $b$ -tagging performance was degraded by the  
1106 presence of large numbers of poorly reconstructed or fake tracks. If an algorithm  
1107 could be trained to detect fake tracks, these could be removed before their input to  
1108 the  $b$ -tagging algorithms with the aim of improving performance. In addition, other  
1109 groups that are sensitive to the presence of fake tracks would also benefit from this  
1110 work.

1111 **5.1 Machine Learning Background**

1112 Over the past few decades, machine learning (ML) techniques have become increas-  
1113 ingly popular in High Energy Physics experiments due the increased volumes of  
1114 high-dimensional data and improvements in the techniques used (in particular deep  
1115 learning). Machine learning is the process by which a computer program uses data  
1116 to learn suitable parameters for a predictive model. This is opposed to explicitly  
1117 providing instructions on how to perform a task. A subfield known as *supervised*  
1118 *learning* is used in this work, and consists of exposing a model to a large number of  
1119 labelled examples in order to extract relationships between the input data and their

1120 labels. These relationships are often complex, and explicitly programmed rules can  
 1121 fail to fully capture the relationships between inputs and outputs.

1122 In the simplest case, a set of  $m$  labelled training examples  $S = \{(x_1, y_1), \dots, (x_m, y_m)\}$   
 1123 is collected. Each element  $(x_i, y_i)$  consists of a input vector  $x_i \in \mathbb{R}^{\text{input}}$ , and the  
 1124 corresponding label  $y_i$ . In classification problems, these labels are integer *class labels*  
 1125  $y_i \in \{0, \dots, N - 1\}$ , where  $N$  is the number of classes, which specify which of a  
 1126 pre-determined set of categorical classes the training example belongs to. The rest  
 1127 of the discussion in this chapter is limited to binary classification problems ( $N = 2$ ).  
 1128 The two classes are often referred to as signal ( $y_i = 1$ ) and background ( $y_i = 0$ ),  
 1129 which need to be separated. Collecting sufficient and suitable data is one of the  
 1130 primary challenges of machine learning, as such data is not always readily available.  
 1131 Fortunately, sophisticated tools to simulate particle collisions have already been  
 1132 developed by the scientific community [105, 106]. These tools play a key role in  
 1133 generating a suitably large amount of labelled data which is used to train algorithms.  
 1134 More detail on the input datasets is given in Section 4.1.

1135 After obtaining suitable training data, the next step is to define a model. Given an  
 1136 input domain  $\mathbb{R}^{\text{input}}$  and an output domain  $(0, 1)$ , the model  $f_\theta : \mathbb{R}^{\text{input}} \rightarrow (0, 1)$  is a  
 1137 parameterised functional mapping from input space to output space. Given an input  
 1138 example  $x_i$  and a set of parameters  $\theta$ , the model outputs a prediction  $\hat{y}_i \in (0, 1)$  for  
 1139 the true label  $y_i$ , as in

$$f_\theta(x_i) = \hat{y}_i. \quad (5.1)$$

1140 The output  $\hat{y}_i$  is in the interval  $(0, 1)$  so as to be interpreted as the probability that  
 1141 the input example  $x_i$  belongs to the signal class. The parameters  $\theta$  of the model are  
 1142 randomly initialised, and the model is designed to be expressive enough to correctly  
 1143 map the inputs  $x_i$  to the outputs  $y_i$  given a reasonable optimisation of the parameters.  
 1144 To perform this optimisation, the model is then trained, which amounts to showing  
 1145 the model a series of labelled training examples and modifying the parameters of the  
 1146 model based on its ability to correctly predict the labels.

### 5.1.1 Neural Networks

Neural networks (NNs) are a common choice for the machine learning model  $f$  since they have the ability to approximate any function [107] and are easy to train via backpropagation [108].

#### Artificial Neurons

The basic functional component of a NN is the *artificial neuron* or node, which is loosely inspired by a mathematical model of a biological neuron [109, 110]. A diagram of an artificial neuron is shown in Fig. 5.1. Each neuron is defined by its parameters or *weights*  $\theta$  and a choice of activation function. Each neuron takes a fixed number of inputs and computes the dot product of the input and weight vectors  $x^T\theta$  and additionally adds a constant bias term  $\theta_0$ . This term plays the role of a trainable constant value that is independent of the inputs.

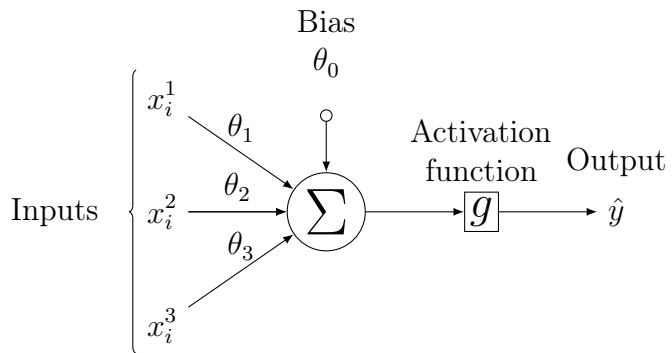


**Figure 5.1:** A diagram displaying the logical flow of a single neuron with three inputs  $x_i^j$ . Each input is multiplied by a weight  $\theta_j$ , and the resulting values are summed. A bias term  $\theta_0$  is added, and the result  $z$  is passed to an activation function. Each neuron can be thought of as a logistic regression model.

The output of the dot product and bias term  $z$  is fed into an activation function  $g(z)$ . The activation function has several uses, most notably acting as a source of non-linearity and bounding the output of the neuron. Some common activation functions (sigmoid, tanh, ReLU and SiLU) [111, 112] are shown in Fig. 5.2. The choice of activation function can have implications for the performance and convergence of the network, since the gradient of  $g(z)$  is used to compute the weight updates during

1165 training. This is also why input data is typically normalised to have zero mean and  
1166 unity variance [113].

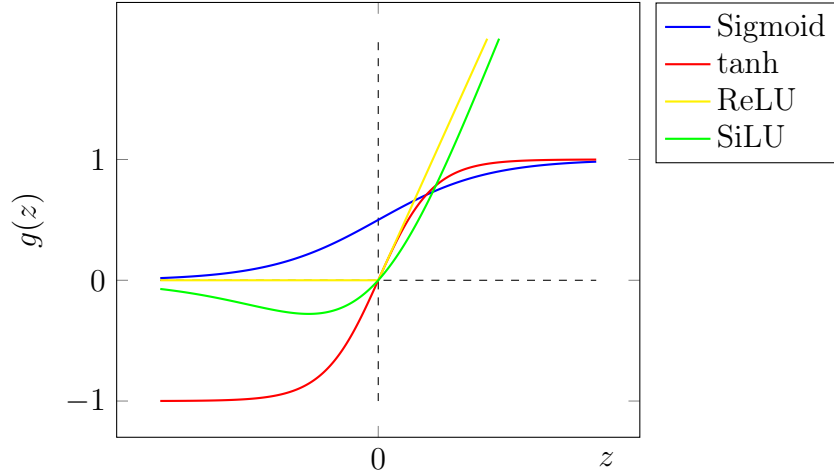


**Figure 5.2:** The output of several common choices for the activation function  $g(z)$  of an artificial neuron. The input  $z$  is the output of the dot product between the activation and the weights, plus a bias term.

1167 **Networks**

1168 Several neurons are linked together in layers to form a neural network. The inputs  
1169 are propagated layer-by-layer through the network until reaching the final output  
1170 layer. The number of layers and neurons per layer are important hyperparameters  
1171 (those parameters which are not optimised as part of the training process) which  
1172 influence the performance of the model. In the case of binary classification, the final  
1173 output layer generally consists of a single neuron with a sigmoid activation

$$g(z) = \frac{1}{1 + e^{-z}}, \quad (5.2)$$

1174 where  $z$  is the output from the dot product of the inputs and the weights, plus the  
1175 bias term. This value is bounded between zero and one allowing the final output to  
1176 be interpreted as the probability that the input sample belongs to the signal class.  
1177 NNs have the crucial property of being differentiable functions, which facilitates the  
1178 training process described in the next section.

### 5.1.2 Training with Gradient Descent

A training algorithm is used to optimise the weights and biases of a NN after exposure to the training data. The training algorithm works by minimising a loss function  $L$ , which quantifies the error in the model's predictions. NNs are commonly trained using backpropagation in combination with a variant of the stochastic gradient descent algorithm to iteratively update the model parameters. In binary classification problems, the binary cross entropy given in Eq. (5.3) loss is often used.

$$L(x_i, \theta) = y_i \ln[f_\theta(x_i)] + (1 - y_i) \ln[1 - f_\theta(x_i)] \quad (5.3)$$

Since the model  $f$  is differentiable, a correction for each parameter  $\theta_i$  can be computed by taking the partial derivative of  $L$  with respect to the parameter. Updated parameters  $\theta'_i$  are calculated by updating the original parameter in the direction which reduces the loss.

$$\theta'_i = \theta_i - \alpha \frac{\partial L}{\partial \theta_i} \quad (5.4)$$

The hyperparameter  $\alpha$  is known as the *learning rate* and dictates the size of the step taken in the direction of the slope. The errors for each parameter are efficiently calculated using the backpropagation algorithm [108]. The process of updating weights is repeated until the weights are judged to have converged, which means the network is trained. In practice, small batches of the input data are shown to the network at a time. For each batch the average loss is calculated and the network's weights are updated. There are many extensions and variations of the gradient descent algorithm. This work uses the Adam optimiser which adds momentum to the weight updates (dampening oscillations) and an adaptive per-parameter learning rate [114].

## 5.2 Track Truth Origin Labelling

Crucial to supervised learning techniques are the ground truth class labels which the machine learning model is trained to predict. A set of track truth labels which a high degree of granularity have been implemented in the ATLAS software stack, and are listed in Table 5.1. The labelling scheme has been designed to be useful beyond

the classification of good and fake tracks. The origins are determined by analysing the simulated record to determine the physical process that led to the creation of the truth (i.e. simulated) particle which is associated with each reconstructed track. Tracks are associated with truth particles by selecting the particle with the highest *truth-matching probability* (TMP), defined in Eq. (5.5). For a given truth particle, the TMP is a weighted sum of the number of hits on a reconstructed track which are matched to the truth particle  $N^{\text{match}}$ , divided the total number of hits on the track  $N^{\text{total}}$ . The weights are sub-detector-dependent and are designed to account for the varying importance of the different ID sub-detectors (based upon their precision) in the reconstruction of a track.

$$\text{TMP} = \frac{10N_{\text{Pix}}^{\text{match}} + 5N_{\text{SCT}}^{\text{match}} + N_{\text{TRT}}^{\text{match}}}{10N_{\text{Pix}}^{\text{total}} + 5N_{\text{SCT}}^{\text{total}} + N_{\text{TRT}}^{\text{total}}} \quad (5.5)$$

For the fake track classification tool, the track truth origins in Table 5.1 are used to construct a binary label by assigning all fake tracks to the background category, and all other tracks as signal. The fake track classifier is then trained to distinguish between these two categories of tracks. Fake tracks are defined using the TMP, with a  $\text{TMP} < 0.75$ <sup>1</sup> giving a track the label of fake. Fake tracks are made up of combinatorial fakes, which are tracks which do not correspond to the trajectory of any truth particle, and poorly reconstructed tracks, which may somewhat resemble the trajectory of a truth particle but due to the presence of some wrong hits on the track will not accurately reproduce the true trajectory. In such cases the fake track can still be identified as having an origin: it is for example possible to have a fake track which is from the decay of a  $b$ -hadron.

### 5.3 Fake Track Identification Tool

The rate of fake tracks increases at high transverse momentum as shown in Fig. 5.3 due to the difficulties in track reconstruction outlined in Section 4.2.2. The performance of  $b$ -tagging algorithms is reduced as a direct result of the presence of these tracks as

---

<sup>1</sup>An alternative definition of a fake track as one with  $\text{TMP} < 0.5$  is also in use within ATLAS, but 0.75 was used for this study.

Truth Origin	Description
Pile-up	From a $pp$ collision other than the primary interaction
Fake	Created from the hits of multiple particles
Primary	Does not originate from any secondary decay
fromB	From the decay of a $b$ -hadron
fromBC	From a $c$ -hadron decay which itself is from the decay of a $b$ -hadron
fromC	From the decay of a $c$ -hadron which is not from the decay of a $b$ -hadron
OtherSecondary	From other secondary interactions and decays

**Table 5.1:** Truth origins which are used to categorise the physical process that led to the production of a track. Tracks are matched to charged particles using the truth-matching probability [57]. A truth-matching probability of less than 0.75 indicates that reconstructed track parameters are likely to be mismeasured and may not correspond to the trajectory of a single charged particle. The “OtherSecondary” origin includes tracks from photon conversions,  $K_S^0$  and  $\Lambda^0$  decays, and hadronic interactions.

1230 shown for SV1 (see Section 3.4.2) in Fig. 5.4, where the efficiency to mistag a light-jet  
 1231 decreases by up to 35% at a  $b$ -jet efficiency of 35% if such tracks are removed.

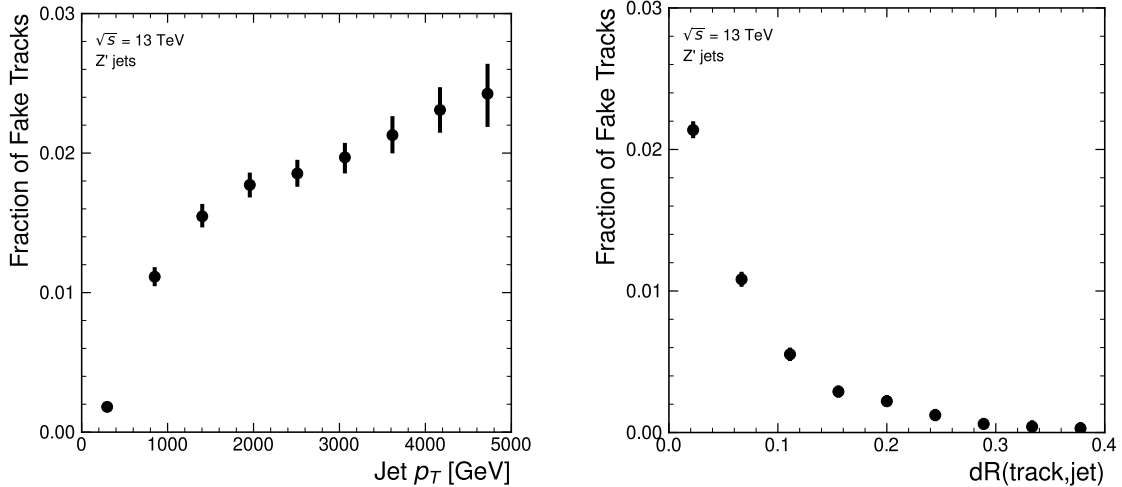


**Figure 5.3:** Rate of fake tracks as a function of jet transverse momentum (left) and  $\Delta R(\text{track},\text{jet})$  (right) for jets in the  $Z'$  sample. The rate of fake tracks increases significantly as a function of  $p_T$ , and also increases as the distance to the jet axis decreases.

1232 To identify and remove fake tracks, a NN classification tool was trained with all  
 1233 non-fake tracks as the signal class and fake tracks as the background class. Inputs to  
 1234 the model are described in Section 5.3.1, while fake track removal performance is

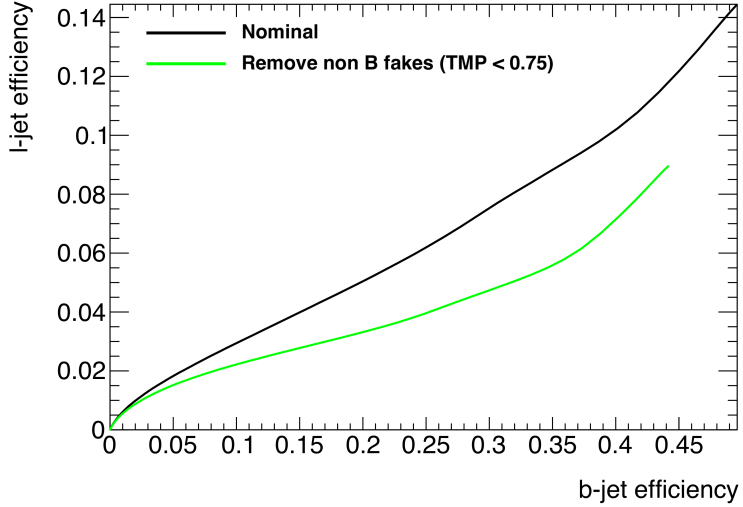


**Figure 5.4:** The light-jet efficiency of the low level tagger SV1 for jets in the  $Z'$  sample with  $250 < p_T < 5000$  GeV, as a function of  $b$ -jet efficiency. The nominal tracking setup (black) is shown alongside the case where fake tracks which are not from the decay of a  $b$ -hadron are removed. The light-jet efficiency is decreased, demonstrating that the presence of fake tracks is detrimental to the algorithm performance.

1235 given in Section 5.3.3. Both models are trained and evaluated using jets from the  $t\bar{t}$   
 1236 and  $Z'$  samples described in Section 4.1

### 1237 5.3.1 Model Inputs

1238 The fake track MVA is given two jet variables and 20 tracking related variables  
 1239 for each track fed into the network. The jet transverse momentum and signed  
 1240 pseudorapidity constitute the jet-level inputs, with the track-level inputs listed in  
 1241 Table 5.2.

1242 The track parameters and hit pattern are key indicators of whether or not a track  
 1243 is fake. The FracRank variable is the ordered index of the tracks that pass the  
 1244 ambiguity solver's selection divided by the total number of successfully reconstructed  
 1245 tracks in the event. The ambiguity solver processes track candidates iteratively  
 1246 in order of an internal score (see Section 3.4.1), and the order in which tracks are  
 1247 accepted is preserved. Since tracks with shared hits have lower scores, tracks which  
 1248 do not require the removal of shared hits are likely to be processed and accepted

Jet Input	Description
$p_T$	Jet transverse momentum
$\eta$	Signed jet pseudorapidity
Track Input	Description
$p_T$	Track transverse momentum
$\Delta R$	Angular distance between the track and jet
$d_0$	Closest distance from the track to the PV in the longitudinal plane
$z_0$	Closest distance from the track to the PV in the transverse plane
nIBLHits	Number of IBL hits
nPixHits	Number of pixel hits
nSCTHits	Number of SCT hits
nTRTHits	Number of TRT hits
nBLHits	Number of B-layer hits
nIBLShared	Number of shared IBL hits
nIBLSplit	Number of split IBL hits
nPixShared	Number of shared pixel hits
nPixSplit	Number of split pixel hits
nSCTShared	Number of shared SCT hits
$r_{\text{first}}$	Radius of first hit
nDOF	Number of degrees of freedom on the track
FracRank	Ambiguity solver ordering variable

**Table 5.2:** Input features to the fake track classification NN. Basic jet kinematics, along with information about the reconstructed track parameters and constituent hits are used. Shared hits, are hits used on multiple tracks which have not been classified as split by the cluster-splitting neural networks [57], while split hits are hits used by multiple tracks which have been identified as merged, and therefore split.

1249 earlier on, whereas tracks with shared hits will be processed later and potentially  
1250 have their shared hits removed. Hence the FracRank variable gives an indication  
1251 of the track quality and how likely it is that hits would have been removed (tracks  
1252 processed later on are more likely to have hits removed).

1253 Track selection follows the loose selection described in Ref. [83] and outlined in  
1254 Table 3.2, which was found to improve the performance compared to previous tighter  
1255 selections, whilst ensuring good resolution of the track’s parameters and a low fake  
1256 rate [57]. Inputs are scaled to have a central value of zero and a variance of unity  
1257 before training and evaluation.

### 1258 5.3.2 Model Hyperparameters

1259 Due to the imbalance between the two classes (with fake tracks being relatively  
1260 uncommon), a weight was added to the loss function for the background class to  
1261 balance their relative weights. The NN was made up of two hidden layers with  
1262 220 nodes per layer. The ReLU activation function was used in conjunction with  
1263 the Adam optimiser with a learning rate of  $1e-3$ . Optimisation of the networks  
1264 architecture was carried out to ensure optimal performance with a relatively small  
1265 number of learnable parameters – 54,000. The model was trained using 40 million  
1266 tracks with a further 4 million tracks each used for validation and testing. A full list  
1267 of the model hyperparameters is given in Table 5.3.

Hyperparameter	Value
Batch size	2048
Activation	ReLU
Optimiser	Adam
Initial learning rate	$1e-3$
Training epochs	20
Training tracks	40m
Validation tracks	4m
Testing tracks	4m

**Table 5.3:** Hyperparameter for the track classification model

### 5.3.3 Results

In order to evaluate the fake track classification tool, a orthogonal test sample of 4 million tracks in jets in the combined  $t\bar{t}$  and  $Z'$  samples was used. The continuous scalar output from the NN model is interpreted as the probability that a given track is a signal track (i.e. not fake). Fig. 5.5 shows the performance of the fake track classification MVA. The signal and background classes are well separated in the output of the tool. Also shown is a receiver operating characteristic (ROC) curve, which plots the rate of true positives against the rate of false positives over a scan of cut points on the NN output ranging from zero to one. The area under the curve (AUC) gives a summary of the aggregate classification power of the model. The fake track classification tool achieves an AUC of 0.935 for all tracks, which is indicative of a well-performing model. Considering only tracks from  $b$ -hadron decays, this value drops slightly to 0.928.

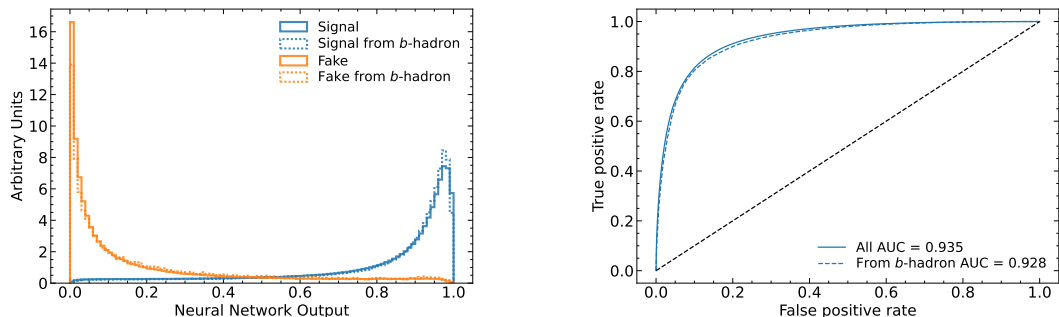


**Figure 5.5:** (left) Normalised histograms of the fake track classification model output separated for signal and fake tracks, and further separated by those tracks which are from the decay of a  $b$ -hadron. (right) The ROC curve for all tracks (solid line) and tracks from the decay of a  $b$ -hadron (dashed line). The plots show tracks in the combined  $t\bar{t}$  and  $Z'$  testing sample. The model is able to successfully discriminate between signal and fake tracks, and shows a very similar performance when looking specifically at tracks from the decay of a  $b$ -hadron.

Signal and fake track efficiencies at two different NN output cut points are shown in Table 5.4. The results demonstrate that the tool is effective in retaining 98.8% of signal tracks, while correctly identifying (and therefore enabling the removal of) 45.6% of fake tracks. Table 5.4 also shows that a significant amount of tracks which are labelled as both fake and from the decay of a  $b$ -hadron are also removed. This can

1286 happen because fake tracks with  $\text{TMP} < 0.75$  are still matched to a truth particle,  
1287 which can be the decay product of a  $b$ -hadron.

MVA Output Cut	Signal Track Efficiency		Fake Track Efficiency	
	All	From $b$	All	From $b$
0.06	98.8%	98.9%	45.6%	39.8%
0.12	97.3%	97.5%	59.4%	53.6%

**Table 5.4:** Good and fake track selection efficiencies for the combined  $t\bar{t}$  and  $Z'$  samples. Two working points are defined, cutting on the NN output at 0.06 and 0.12.

## 1288 5.4 $b$ -hadron Track Identification

1289 After initial tests and investigation, it was found that fake tracks which were the  
1290 result of  $b$ -hadron decays actually aided  $b$ -tagging performance, as demonstrated in  
1291 Fig. 5.7. The application of a single tool which removed all fake tracks was therefore  
1292 not optimal. A second tool was therefore trained in the same manner as the first,  
1293 this one was designed to distinguish between those tracks which were from the decay  
1294 of a  $b$ -hadron (FromB and FromBC in Table 5.1) and those which were not (all other  
1295 truth origins). Fake tracks which were from the decay of a  $b$ -hadron were included in  
1296 the signal class. The  $b$ -hadron decay track MVA was trained using the same setup  
1297 as described above, with the same tracks, input variables, and training procedure.  
1298 The performance of the model to separate  $b$ -hadron decay tracks from other tracks  
1299 is shown in Fig. 5.6. Using a selection WP of 0.1, the model can retain 98.5% of  
1300  $b$ -hadron tracks and reject 46.2% of tracks not from the decay of a  $b$ -hadron. In  
1301 Section 5.5, this model is used in conjunction with the fake track identification MVA  
1302 to identify and remove fake tracks which are not from the decay of a  $b$ -hadron.

## 1303 5.5 Combined Approach

1304 A 2-dimensional cut was then used to only reject those tracks that had a high  
1305 probability of being fake, and also a low probability of being a  $b$ -hadron decay track.  
1306 The results of the combined approach are provided in Table 5.5, which shows that

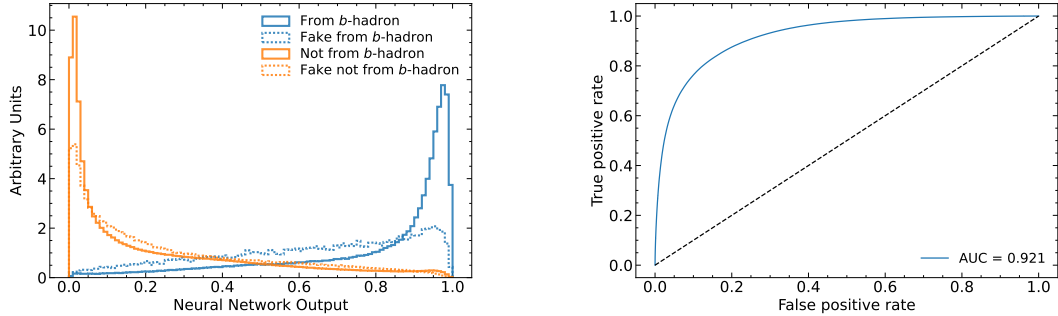


**Figure 5.6:** (left) Normalised histogram of the  $b$ -hadron track identification model output separated for tracks from the decay of a  $b$ -hadron and tracks from other sources. The two groups are further separated into those tracks which are fake. (right) The ROC curve for all tracks (solid line). The plots show tracks in the combined  $t\bar{t}$  and  $Z'$  testing sample.

1307 for the working point “A”, 98.6% of  $b$ -hadron decay tracks (both good and fake) are  
 1308 retained, while 50.7% of fake tracks which are not from  $b$ -hadron decays are rejected.

WP	Fake MVA Cut	$b$ -hadron Decay MVA Cut	Retained $b$ -hadron Tracks	Fake non- $b$ -hadron Tracks Rejected
A	0.5	0.4	98.6%	50.7%
B	0.6	0.5	97.5%	62.0%

**Table 5.5:** Cut values for the fake and  $b$ -hadron decay track MVAs for the two defined working points. Working point “B” cuts more aggressively on the MVA outputs than WP “A”, removing more fake tracks but resulting in an increased loss of signal tracks (which here are all  $b$ -hadron decay tracks).

1309 The light-jet efficiency of SV1 is successfully reduced when using the combined tools  
 1310 to remove fake tracks that are not from a  $b$ -hadron decay, as shown in Fig. 5.7. At a  
 1311  $b$ -jet efficiency of 70%, the light-jet mistag rate for jets with  $250 < p_T < 400$  GeV  
 1312 is reduced from 0.054 to 0.044, a relative improvement of approximately 20%. For  
 1313 jets with  $400 < p_T < 1000$  GeV the mistag rate drops from 0.1 to 0.08 for a similar  
 1314 relative improvement of 20%. The performance of the fake track removal approach  
 1315 was also tested for the other low level vertexing algorithm – JetFitter. A similar level  
 1316 of improvement in the light-jet mistag rate was observed with a reduction of up to a  
 1317 20% reduction for both low- and high- $p_T$  jets in the  $Z'$  sample achieved. Together,  
 1318 these results demonstrate that by identifying and removing fake tracks which are not

the result of the weak decay of a  $b$ -hadron, the performance of the low level tagging algorithms can be improved by an amount which is comparable to the improvement that would be observed if the tracks were selected at truth level1.

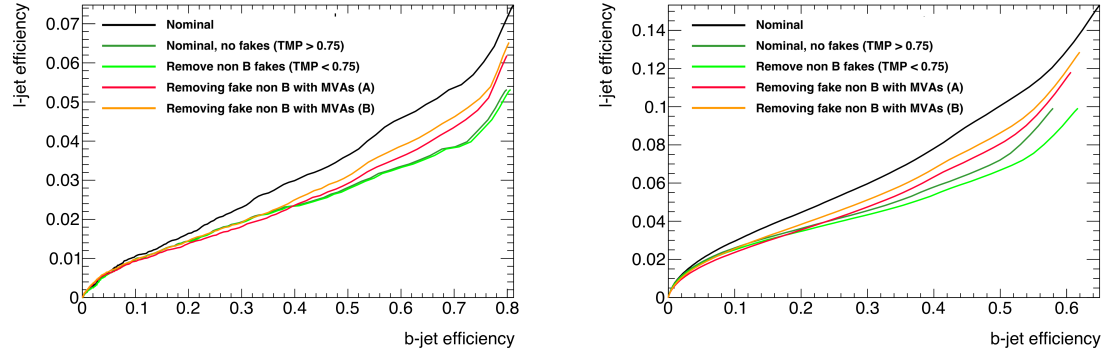


**Figure 5.7:** The effect of applying the fake track identification algorithm together with the  $b$ -hadron decay track identification on the jet tagging performance of SV1 for jets in the  $Z'$  sample with  $250 \text{ GeV} < p_T < 400 \text{ GeV}$  (left) and  $400 \text{ GeV} < p_T < 1 \text{ TeV}$  (right). The nominal SV1 light-jet rejection (black) is compared to two working points of fake track removal, labelled “A” (red) and “B” (orange), which represent two different 2D working points of the track classification tools. Removal of fake tracks based on truth information is shown by the green curves.

## 5.6 Conclusion

Fake tracks, which are prevalent in the core of high  $p_T$  jets, have an adverse impact on  $b$ -tagging performance. A ML tool to identify fake tracks has been developed, which can be used to limit the number of fake tracks being input to the  $b$ -tagging algorithms. An advantage of the approach is that the continuous output of the model allows for the tuning of good and fake track identification efficiencies. Since it was found that  $b$ -hadron decay tracks can also be poorly reconstructed and thus marked as fake, it was deemed necessary also to train a second algorithm to detect  $b$ -hadron decay tracks so that the removal of these tracks could be avoided. Removing fake and non- $b$  decay tracks in this way was found to improve the light-jet mistagging rate of SV1 and JetFitter by up to 20% at high transverse momentum. The improvement achieved using the classification tools was in general comparable with that achieved when using the truth information to remove the fake tracks not from the decay of a  $b$ -hadron.

**1336 Future Work**

1337 While removing tracks prior to their input to the low level tagging algorithms is  
1338 shown here to be beneficial, a more performant alternative might be to keep these  
1339 tracks but label them as being fake (for example using the output of the classification  
1340 tool), and allow the tagging algorithms to take this into consideration. This is not  
1341 straightforward with manually optimised taggers such as SV1 and JetFitter, but is  
1342 possible with more advanced taggers as described in Chapter 6.

1343 Tools which identify the origin of a given track have other potential uses. One  
1344 application is to isolate a relatively pure sample of fake tracks which can be used  
1345 to estimate the fake track rate in data, which would be useful for estimating the  
1346 uncertainty on fake track modelling. Another application is to use the  $b$ -hadron  
1347 track identification tool to improve the track-to-jet association. Both applications  
1348 are currently under investigation.

1349 The approach here works on a track-by-track basis, but a more sophisticated approach  
1350 would consider the correlations between the tracks inside a jet. Also left for future  
1351 work is to simultaneously train a single tool which discriminates between all the  
1352 truth origins listed in Table 5.1. Such a tool would be useful as a general purpose  
1353 multiclass classifier. An algorithm which takes both these aspects into consideration  
1354 is discussed in Chapter 6.

<sub>1355</sub> **Chapter 6**

<sub>1356</sub> **Graph Neural Network Flavour  
Tagger**

<sub>1358</sub> This chapter introduces GN1, a novel ML-based flavour tagging algorithm based on  
<sub>1359</sub> graph neural networks (GNNs). In Section 6.1, an overview of the approach used  
<sub>1360</sub> for GN1 is given. An introduction to the theory of GNNs is provided in Section 6.2.  
<sub>1361</sub> Details of the experimental setup are provided in Section 6.3, while the architecture  
<sub>1362</sub> of GN1 is specified in Section 6.4.3. In Section 6.4.4, the training procedure is  
<sub>1363</sub> described, and in Section 6.5 the results are shown.

<sub>1364</sub> **6.1 Motivation**

<sub>1365</sub> GN1 is a monolithic approach to flavour tagging as illustrated in Fig. 6.1. As opposed  
<sub>1366</sub> to the existing approach to flavour tagging described in Chapter 4, which relies  
<sub>1367</sub> on a two tiered approach requiring the use of both low- and high-level algorithms,  
<sub>1368</sub> GN1 takes as inputs information directly from an unordered variable number of  
<sub>1369</sub> tracks as input, and predicts the jet flavour without requiring outputs from the  
<sub>1370</sub> intermediate low-level algorithms. In addition to predicting the flavour of the jet, the  
<sub>1371</sub> model predicts which physical processes produced the various tracks, and groups the  
<sub>1372</sub> tracks into vertices. These auxiliary training objectives provide valuable additional  
<sub>1373</sub> information about the contents of the jet and enhance the performance of the primary  
<sub>1374</sub> flavour prediction task. The use of GNNs offers a natural way to classify jets with

1375 variable numbers of unordered associated tracks (see Section 6.2), while allowing for  
1376 the inclusion of auxiliary training objectives [2, 115].

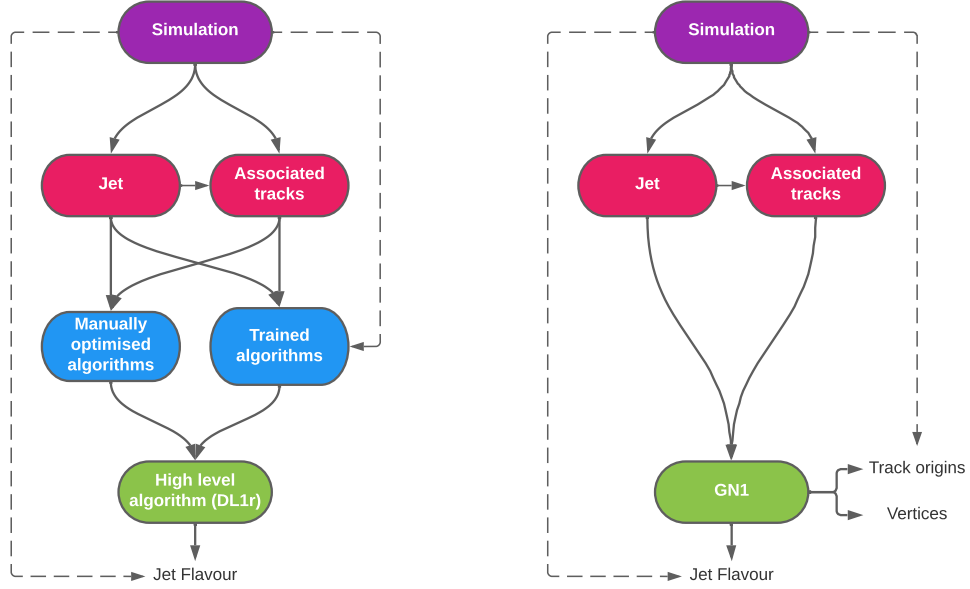


**Figure 6.1:** Comparison of the existing flavour tagging scheme (left) and GN1 (right). The existing approach utilises low-level algorithms (shown in blue), the outputs of which are fed into a high-level algorithm (DL1r). Instead of being used to guide the design of the manually optimised algorithms, additional truth information from the simulation is now being used as auxiliary training targets for GN1. The solid lines represent reconstructed information, whereas the dashed lines represent truth information [3].

1377 The current flavour tagging algorithms utilise a two-tired approach, with five low  
1378 level algorithms feeding intermediate features into the high-level tagger DL1r, which  
1379 outputs variables which discriminate between the different jet flavours. In contrast  
1380 GN1 consists of only a single neural network, which takes the tracks as inputs along  
1381 with some kinematic information about the jet. As a result, it does not depend on  
1382 the outputs of any other flavour tagging algorithm. A simple training of the model  
1383 fully optimises its parameters, representing a significant simplification with respect to  
1384 the optimisation procedure for DL1r. This is particularly important when optimising  
1385 the tagger for new regions of phase space (e.g.  $c$ -tagging or high- $p_T$   $b$ -tagging), or  
1386 when the detector is upgraded or the charged particle reconstruction or selection  
1387 algorithms are re-optimised.

1388 GN1 is trained to learn about the internal structure of the jet through the use of two  
 1389 auxiliary training objectives: the prediction of the underlying physics process from  
 1390 which each track originated, and the grouping of tracks originating from a common  
 1391 spatial position (i.e. a common vertex). These auxiliary objectives are meant to  
 1392 guide the neural network towards a more complete understanding of the underlying  
 1393 physics inside the jet, thereby removing the need for the low-level algorithms, which  
 1394 previously contained information about the underlying physics in their design. The  
 1395 training targets for the primary and auxiliary objectives are extracted from truth  
 1396 information, as opposed to reconstructed quantities available in both collision data  
 1397 and simulation.

1398 In this chapter, the following advantages of the GN1 approach will be demonstrated:

- 1399 1. GN1 boasts improved performance with respect to the current ATLAS flavour  
 1400 tagging algorithms, with significantly larger background rejection rates for a  
 1401 given signal efficiency. Alternatively the rejection rates can be kept fixed for a  
 1402 substantial increase in signal efficiency, in particular at high- $p_T$ .
- 1403 2. The same network architecture can be easily optimised for a wider variety of  
 1404 use cases (e.g.  $c$ -jet tagging and high- $p_T$  jet tagging) since there are no low-level  
 1405 algorithms to retune.
- 1406 3. There are fewer algorithms to maintain.
- 1407 4. Alongside the network's prediction of the jet flavour, the auxiliary vertex and  
 1408 track origin predictions provide more information on why a jet was (mis)tagged  
 1409 or not. This information can also have uses in other applications, for instance  
 1410 to explicitly reconstruct displaced decay vertices or to remove fake tracks.<sup>1</sup>

## 1411 6.2 Graph Neural Network Theory

1412 Graph neural networks are a more sophisticated neural network model (see Sec-  
 1413 tion 5.1.1) that are designed to operate on graph structured data. A brief introduction  
 1414 to GNNs is provided in this section following the formalism in Ref. [116].

---

<sup>1</sup>A fake track is defined in this chapter as a track with a truth-matching probability less than 0.5, where the truth-matching probability is defined in Ref. [57].

1415 A graph  $\mathcal{G}$  consists of a set of  $N^n$  nodes  $\mathcal{N} = \{h_i\}_{i=1:N^n}$ , a set of  $N^e$  edges  $\mathcal{E} =$   
1416  $\{e_i\}_{i=1:N^e}$ , and a global representation  $u$ . Each node represents an individual object,  
1417 and edges are directed connections between two nodes, called the *sender* and *receiver*  
1418 nodes. The connectivity of the graph therefore encodes information about the  
1419 relationships between objects that exist in the graph.

1420 A single graph network layer consists of three separate update functions  $\phi^e$ ,  $\phi^h$  and  
1421  $\phi^u$  one for each of the nodes, edges, and global graph representation, and similarly  
1422 three aggregation functions  $\rho^{e \rightarrow h}$ ,  $\rho^{e \rightarrow u}$  and  $\rho^{h \rightarrow u}$ . The aggregation functions combine  
1423 information across different edges or nodes for input into the update functions,  
1424 which produce new representations for the nodes, edges and global objects based on  
1425 the information in the previous layer and the aggregated information. The update  
1426 functions are typically each implemented as a dense feedforward neural network (as  
1427 described in Section 5.1.1). The edges  $e_i$  are updated by a edge network  $\phi^e$  as in

$$e'_i = \phi^e(e_i, h_s, h_r, u), \quad (6.1)$$

1428 where  $h_s$  and  $h_r$  are the sender and receiver nodes respectively. The nodes are  
1429 updated with a node network  $\phi^h$  as in

$$h'_i = \phi^h(\bar{e}'_i, h_i, u), \quad (6.2)$$

1430 where  $\bar{e}'_i = \rho^{e \rightarrow h}(E'_i)$ , and  $E'_i$  is the set of sender nodes for receiver node  $h_i$ .  $\rho^{e \rightarrow h}$  is  
1431 referred to as the edge aggregation function. The global representation is updated  
1432 using the global network  $\phi^u$  as in

$$u' = \phi^u(\bar{e}', \bar{h}', u), \quad (6.3)$$

1433 where  $\bar{e}'$  is the aggregation  $\rho^{e \rightarrow u}$  over all updated edges  $e'_i$  and  $\bar{h}'$  is the aggregation  
1434  $\rho^{h \rightarrow u}$  over all updated nodes  $h'_i$ .

1435 The graph network layer performs a graph convolution, in an analogous way to a  
1436 convolutional neural network operating on a grid of pixels. The above description  
1437 is general, and not all concrete implementations of GNNs need to implement every  
1438 aspect. For example, the global graph representation need not be present, and  
1439 it is also possible that no dedicated edge features are present. In such cases the  
1440 corresponding update and aggregation functions are not needed. Fig. 6.2 shows two

1441 possible graph network update layers. The layer used in the GN1 model is specified  
1442 in more detail in Section 6.4.3.

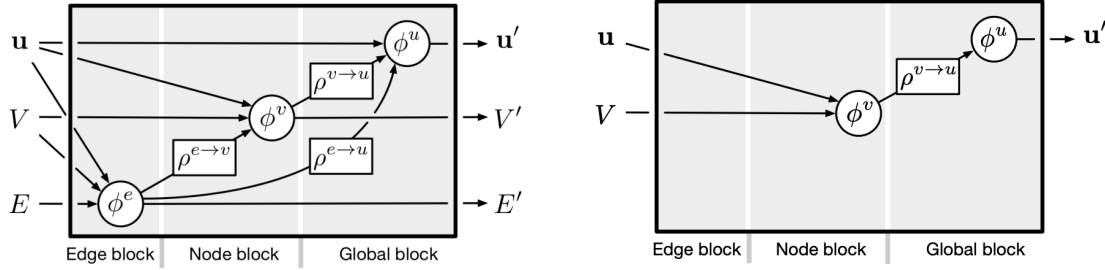


**Figure 6.2:** The flow of information through a graph neural network layer for (left) a full implementation of the layer and (right) a deep sets model [117]. Reproduced from Ref. [116].

### 1443 6.3 Experimental Setup

#### 1444 6.3.1 Datasets

1445 The datasets used to train the GN1 tagger are the same as described in Section 4.1.  
1446 The training dataset contains 30 million jets, 60% of which are  $t\bar{t}$  jets and 40% of  
1447 which are  $Z'$  jets. In order to evaluate the performance of the model during training,  
1448 a statistically independent validation set of 500k jets from both the  $t\bar{t}$  and  $Z'$  samples  
1449 are used. For the testing of the model and the creation of the performance plots,  
1450 a further 1 million independent testing jets from each of the  $t\bar{t}$  and  $Z'$  samples are  
1451 used. Before being fed into the model, the track- and jet-level inputs are normalised  
1452 to have a mean of zero and a variance of unity. The jet flavour labels are assigned  
1453 as described in Section 3.4.3. Truth labelled  $b$ -,  $c$ - and light-jets are kinematically  
1454 re-sampled in  $p_T$  and  $\eta$  to ensure identical distributions in these variables.

## 1455 6.4 Model Architecture

### 1456 6.4.1 Model Inputs

1457 As inputs, GN1 is fed two kinematic jet variables and an unordered set of up to 40  
1458 tracks which have been associated to the jet. If more than 40 tracks are associated  
1459 to a given jet, only the first 40 tracks with the largest transverse IP significance  $s(d_0)$   
1460 (see Section 3.2.2) are fed into the model as inputs. Each track is characterised by 21  
1461 variables as detailed in Table 6.1. The kinematic jet variables are the jet transverse  
1462 momentum and signed pseudorapidity. For each track, variables containing the  
1463 track parameters and uncertainties, and detailed information on the hit content are  
1464 provided as inputs to the model.

1465 Dependence of the model on the absolute value of the azimuthal jet angle  $\phi$  is  
1466 explicitly removed by providing only the azimuthal angle of tracks relative to the jet  
1467 axis. The track pseudorapidity is also provided relative to the jet axis.

1468 Since heavy flavour hadrons can decay semileptonically approximately 40% of the time,  
1469 the presence of a reconstructed lepton in the jet carries discriminating information  
1470 about the jet flavour. To exploit this, a variant of GN1 called GN1Lep is trained in  
1471 addition to the baseline model. The GN1Lep variant is identical to the baseline model,  
1472 except for the inclusion an additional track-level input, leptonID, which indicates  
1473 if the track was used in the reconstruction of an electron, a muon or neither. The  
1474 variable is signed by the charge of the reconstructed lepton. The leptons used in the  
1475 definition of the leptonID variable are required to satisfy basic quality requirements.  
1476 The muons are required to be combined [118], and the electrons are required to pass  
1477 the *VeryLoose* likelihood-based identification working point [119].

1478 The selections applied to the tracks, outlined in Table 3.2, is the same as that used  
1479 for the fake track classification MVA described in Chapter 5. However, Section 6.6.1  
1480 demonstrates that further relaxation of the track selection requirements may be  
1481 warranted.

Jet Input	Description
$p_T$	Jet transverse momentum
$\eta$	Signed jet pseudorapidity
Track Input	Description
$q/p$	Track charge divided by momentum
$d\eta$	Pseudorapidity of the track, relative to the jet $\eta$
$d\phi$	Azimuthal angle of the track, relative to the jet $\phi$
$d_0$	Closest distance from the track to the PV in the longitudinal plane
$z_0 \sin \theta$	Closest distance from the track to the PV in the transverse plane
$\sigma(q/p)$	Uncertainty on $q/p$
$\sigma(\theta)$	Uncertainty on track polar angle $\theta$
$\sigma(\phi)$	Uncertainty on track azimuthal angle $\phi$
$s(d_0)$	Lifetime signed transverse IP significance
$s(z_0)$	Lifetime signed longitudinal IP significance
nPixHits	Number of pixel hits
nSCTHits	Number of SCT hits
nIBLHits	Number of IBL hits
nBLHits	Number of B-layer hits
nIBLShared	Number of shared IBL hits
nIBLSplit	Number of split IBL hits
nPixShared	Number of shared pixel hits
nPixSplit	Number of split pixel hits
nSCTShared	Number of shared SCT hits
nPixHoles	Number of pixel holes
nSCTHoles	Number of SCT holes
leptonID	Indicates if track was used to reconstruct an electron or muon

**Table 6.1:** Input features to the GN1 model. Basic jet kinematics, along with information about the reconstructed track parameters and constituent hits are used. Shared hits, are hits used on multiple tracks which have not been classified as split by the cluster-splitting neural networks [57], while split hits are hits used on multiple tracks which have been identified as merged. A hole is a missing hit, where one is expected, on a layer between two other hits on a track. The track leptonID is an additional input to the GN1Lep model [3].

## 1482 6.4.2 Auxiliary Training Objectives

1483 In addition to the jet flavour classification, two auxiliary training objectives are  
1484 defined. The first auxiliary objective is the prediction of the physical process that  
1485 gave rise to each track within the jet (i.e. the track origin), while the second is the  
1486 prediction of track-pair vertex compatibility. Each auxiliary training objective comes  
1487 with a training target which, similar to the jet flavour label, is a truth labels derived  
1488 from the simulation. The presence of the auxiliary training objectives improves the  
1489 jet classification performance as demonstrated in Section 6.5.3.

1490 For the track origin prediction objective, each track is labelled with one of the  
1491 exclusive categories defined in Table 5.1 of Section 5.2 after analysing the particle  
1492 interaction (or lack thereof) which led to its formation. Since the presence of different  
1493 track origins is strongly related to the flavour of the jet, training GN1 to recognise  
1494 the origin of the tracks provides an additional handle on the classification of the  
1495 jet flavour. This task may also aid the jet flavour prediction by acting as a form of  
1496 supervised attention [120] - in detecting tracks from heavy flavour decays the model  
1497 may learn to pay more attention to these tracks.

1498 The vertexing auxiliary objective makes use of the fact that displaced decays of  $b$ -  
1499 and  $c$ -hadrons lead to secondary and tertiary vertices inside the jet, as described  
1500 in Section 4.2.1. The presence of displaced secondary vertices is not a completely  
1501 clean signal of a heavy flavour jet, as displaced secondary vertices can also occur  
1502 in light-jets as a result of material interactions, conversions, and long-lived particle  
1503 decays (e.g.  $K_S^0$  and  $\Lambda^0$ ). For this objective, GN1 predicts a binary label for each pair  
1504 of tracks in the jet. The label has a value of 1 if the truth particles associated with  
1505 the two tracks in the pair originated from the same spatial point, and 0 otherwise. To  
1506 derive the corresponding truth labels for training, truth production vertices within  
1507 0.1 mm are merged. Track-pairs where one or both of the tracks in the pair have an  
1508 origin label of either Pile-up or Fake are assigned a label of 0. Using the pairwise  
1509 predictions from the model, groups of tracks that have common compatibility can  
1510 be formed, resulting in the identification of vertices. Two existing low-level tagging  
1511 algorithms, SV1 and JetFitter (introduced in Section 3.4.2), are currently used to  
1512 find and reconstruct vertices inside jets and are used as inputs to the existing jet  
1513 flavour tagger DL1r. The addition of this auxiliary training objective removes the  
1514 need for inputs from a dedicated secondary vertexing algorithm.

1515 Both of the auxiliary training objectives described here can be considered as “stepping  
1516 stones” on the way to classifying the flavour of the jet. By requiring the model to  
1517 predict the truth origin of each track and the vertex compatibility of each track-pair,  
1518 the model is guided to learn representations of the jet which are connected to the  
1519 underlying physics and therefore relevant for classifying the jet flavour.

1520 **6.4.3 Architecture**

1521 A coarse optimisation of the network architecture hyperparameters (for example  
1522 number of layers and number of neurons per layer) has been carried out in order  
1523 to maximise the flavour tagging performance, but it is likely that further dedicated  
1524 optimisation studies could lead to further performance improvements.

1525 The model architecture builds on a previous implementation of a GNN-based jet  
1526 tagger [115]. The previous approach was comprised of two separate graph neural  
1527 networks with the auxiliary tasks being performed at an intermediate stage after the  
1528 first and before the second. This two stage approach was found to be unnecessary and  
1529 as such GN1 simplifies the architecture into a single graph neural network with the  
1530 auxiliary tasks being performed at the end, alongside the primary jet classification  
1531 task. GN1 makes use of a more sophisticated graph neural network layer [121],  
1532 which is described in more detail below. The changes significantly improved tagging  
1533 performance and also led to a significant reduction in training time.

1534 As inputs, the model takes information about the jet and a number of associated  
1535 tracks, as detailed in Section 6.4.1. The jet variables are concatenated with the  
1536 variables for each track as shown in Fig. 6.3. The combined jet-track input vectors  
1537 are then fed into a per-track initialisation network with three hidden layers, each  
1538 containing 64 neurons, and an output layer with a size of 64, as shown in Fig. 6.4. The  
1539 track initialisation network is similar to a deep sets model [117], but does not include  
1540 a reduction operation (mean or summation) over the output track representations.  
1541 The initialisation network allows for initial per-track input processing without the  
1542 associated parameter count cost of the graph convolutional layers described below.

1543 The outputs of the track initialisation network are used to populate the nodes of a  
1544 fully connected graph, such that each node in the graph neighbours every other node.  
1545 Each node  $h_i$  in the graph corresponds to a single track in the jet, and is characterised

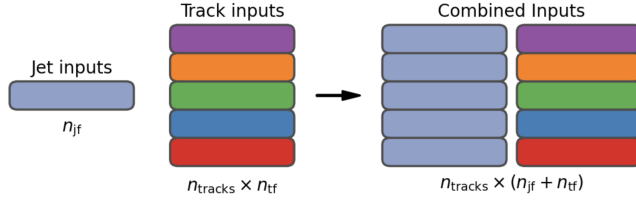


**Figure 6.3:** The inputs to GN1 are the two jet features ( $n_{jf} = 2$ ), and an array of  $n_{tracks}$ , where each track is described by 21 track features ( $n_{tf} = 21$ ). The jet features are copied for each of the tracks, and the combined jet-track vectors of length 23 form the inputs of GN1 [3].

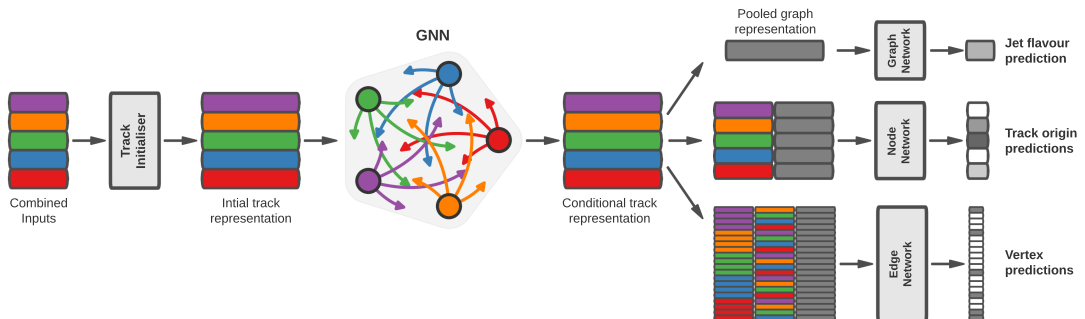


**Figure 6.4:** The network architecture of GN1. Inputs are fed into a per-track initialisation network, which outputs an initial latent representation of each track. These representations are then used to populate the node features of a fully connected graph network. After the graph network, the resulting node representations are used to predict the jet flavour, the track origins, and the track-pair vertex compatibility [3].

1546 by a feature vector, also called a representation. The per-track output representations  
 1547 from the initialisation networks are used as the initial feature vectors of each node  
 1548 in the graph. In each layer of the graph network, output node representations  $h'_i$   
 1549 are computed by aggregating the features of  $h_i$  and neighbouring nodes  $\mathcal{N}_i$  using  
 1550 a multi-head attention mechanism ( $n = 2$ ) as described in Ref. [121, 122]. First,  
 1551 the feature vectors of receiver and sender nodes are fed into two fully connected  
 1552 linear layers  $\mathbf{W}_r$  and  $\mathbf{W}_s$ , to produce an updated representation for each sender and  
 1553 receiver node  $\mathbf{W}_r h_i$  and  $\mathbf{W}_s h_j$ . These updated feature vectors are used to compute  
 1554 edge scores  $e(h_i, h_j)$  for each node pair, as in

$$e(h_i, h_j) = \mathbf{a} \cdot \theta [\mathbf{W}_r h_i + \mathbf{W}_s h_j], \quad (6.4)$$

1555 where,  $\theta$  is a non-linear activation function, and  $\mathbf{a}$  is a learned vector. These edge  
 1556 scores are then used to calculate attention weights  $a_{ij}$  for each pair of nodes using  
 1557 the softmax function over the edge scores

$$a_{ij} = \text{softmax}_j [e(h_i, h_j)]. \quad (6.5)$$

1558 Finally, the updated representations for the receiver nodes  $h'_i$  are computed by taking  
 1559 the weighted sum over each updated node representation  $\mathbf{W}_r h_i$ , with weights  $a_{ij}$

$$h'_i = \sigma \left[ \sum_{j \in \mathcal{N}_i} a_{ij} \cdot \mathbf{W}_r h_j \right]. \quad (6.6)$$

1560 The set of operations described above constitute a single graph network layer. Three  
 1561 such layers are stacked to construct the graph network, representing a balance  
 1562 between achieving good performance in a reasonable time and avoiding overtraining  
 1563 due to inflation of the parameter count of the model. The final output from the graph  
 1564 neural network is a set of per-node (i.e. per-track) feature vectors that are conditional  
 1565 representations of each track given the other tracks in the jet. In order to perform

the jet flavour prediction, a flattened global representation of the jet is needed. To produce this, the output track representations are combined using a weighted sum, where the weights are learned during training and therefore act as a form of attention over the different tracks. The flattened outputs from the sum are then fed into a fully connected feedforward neural network with four layers and three outputs, one for each jet flavour. Two other separate fully connected feedforward neural networks are then also used to independently perform the auxiliary classification objectives of GN1. A summary of the different classification networks used for the various training objectives is shown in Table 6.2.

Network	Hidden layers	Output size	Label
Node classification network	128, 64, 32	7	Track origin
Edge classification network	128, 64, 32	1	Track-pair compatibility
Graph classification network	128, 64, 32, 16	3	Jet flavour

**Table 6.2:** A summary of GN1’s different classification networks used for the various training objectives, adapted from Ref. [3]. The hidden layers column contains a list specifying the number of neurons in each layer. ReLU activation is used through the network [111].

The node classification network predicts the track truth origin as defined in Table 5.1. This network takes as inputs the features from a single output node from the graph network and the global representation of the jet. The node network has three hidden layers containing 128, 64 and 32 neurons respectively, and an output size of seven, corresponding to the seven different truth origins defined in Table 5.1.

The edge classification network is used to predict whether the tracks in the track-pair belong to a common vertex. This network takes as inputs the concatenated representations from each pair of tracks and the global jet representation. Similar to the node network, the edge network has three hidden layers containing 128, 64 and 32 neurons respectively, and a single output, which is used to perform binary classification of the track-pair compatibility. The output predictions for the two auxiliary networks are used for the auxiliary training objectives discussed in Section 6.4.2.

Finally, the graph classification network is used to predict the jet flavour. This network takes only the global jet representation as input. The graph classification

1590 network is comprised of four fully connected hidden layers with 128, 64, 32 and 16  
1591 neurons respectively, and has three outputs corresponding to the  $b$ -,  $c$ - and light-  
1592 jet classes. To obtain probability outputs for each task, the outputs from each  
1593 classification network are passed through a softmax function.

#### 1594 6.4.4 Training

1595 The full GN1 training procedure minimises the total loss function  $L_{\text{total}}$ , defined as

$$L_{\text{total}} = L_{\text{jet}} + \alpha L_{\text{vertex}} + \beta L_{\text{track}}. \quad (6.7)$$

1596 This loss is composed of three terms:  $L_{\text{jet}}$ , the categorical cross entropy loss over the  
1597 different jet flavours;  $L_{\text{vertex}}$ , the binary track-pair compatibility cross entropy loss;  
1598 and  $L_{\text{track}}$ , the categorical cross entropy loss for the track origin prediction.  $L_{\text{vertex}}$  is  
1599 computed via a weighted average over all intra-jet track-pairs in the batch, and  $L_{\text{track}}$   
1600 is computed by a weighted average over all tracks in the batch, where the weights  
1601 are described below.

1602 The different losses converge to different values during training, reflecting differences  
1603 in the relative difficulty of the various training objectives. The values of  $L_{\text{vertex}}$  and  
1604  $L_{\text{track}}$  are weighted by  $\alpha = 1.5$  and  $\beta = 0.5$  respectively to ensure they converge to  
1605 similar values, giving them an equal weighting towards  $L_{\text{total}}$ . The values of  $\alpha$  and  
1606  $\beta$  are chosen to ensure that  $L_{\text{jet}}$  converges to a larger value than either  $L_{\text{vertex}}$  and  
1607  $L_{\text{track}}$ , which reflects the primary importance of the jet classification objective. It  
1608 was found that in practice the overall performance of the model was not sensitive  
1609 to modest changes in the loss weights  $\alpha$  and  $\beta$ . Pre-training using  $L_{\text{total}}$  (i.e. on  
1610 all tasks) and fine tuning on only the jet classification task also did not improve  
1611 performance versus the standard setup, indicating that the auxiliary tasks are not  
1612 in direct competition with the jet classification task. As there was a large variation  
1613 in the relative abundance of tracks of the different origins, the contribution of each  
1614 origin to  $L_{\text{track}}$  was weighted by the inverse of the frequency of their occurrence. In  
1615 vertexing loss  $L_{\text{vertex}}$ , the class weight for track-pairs where both tracks are from  
1616 either a  $b$ - or  $c$ -hadron was increased by a factor of two as compared with other

1617 track-pairs, to encourage the network to focus on correctly classifying heavy flavour  
1618 vertices.

1619 GN1 can be trained with either the node or edge networks (and their corresponding  
1620 auxiliary tasks), or both, removed, as discussed in Section 6.5.3. In such cases,  
1621 the corresponding losses  $L_{\text{vertex}}$  and  $L_{\text{track}}$  are also removed from the calculation  
1622 of the overall loss  $L_{\text{total}}$ . The performance of the resulting models provides a  
1623 useful indication of the benefit of including the auxiliary tasks to the primary jet  
1624 classification objective.

1625 GN1 was trained for 100 epochs on 4 NVIDIA V100 GPUs. Each epoch takes  
1626 approximately 25 mins to complete over the training sample of 30 million jets. The  
1627 Adam optimiser [123] with an initial learning rate of  $1e-3$ , and a batch size of 4000  
1628 jets (spread across the 4 GPUs) was used. Typically the validation loss, calculated  
1629 on 500k jets, became stable after around 60 epochs. The epoch that minimized the  
1630 validation loss was used for evaluation. GN1 has been integrated into the ATLAS  
1631 software [54] using ONNX [124]. The test sample jet flavour predictions scores are  
1632 computed using the ATLAS software stack as a verification of this process.

## 1633 6.5 Results

1634 The GN1 tagger is evaluated both as a  $b$ -tagging and  $c$ -tagging algorithm in Sec-  
1635 tion 6.5.1 and Section 6.5.2 respectively. Evaluation is performed separately on  
1636 jets in the  $t\bar{t}$  sample with  $20 < p_T < 250 \text{ GeV}$  and jets in the  $Z'$  sample with  
1637  $250 < p_T < 5000 \text{ GeV}$ . The performance of the model is compared to the DL1r  
1638 tagger [85, 86], which has been retrained on 75 million jets from the same samples as  
1639 GN1. The input RNNIP tagger [82] to DL1r has not been retrained. As discussed,  
1640 each tagger predicts the probability that a jet belongs to the  $b$ -,  $c$ - and light-classes.  
1641 To use the model for  $b$ -tagging, these probabilities are combined into a single score  
1642  $D_b$ , which is defined as

$$D_b = \log \frac{p_b}{(1 - f_c)p_l + f_c p_c}, \quad (6.8)$$

where  $f_c$  is a free parameter that determines the relative weight of  $p_c$  to  $p_l$  in the score  $D_b$ , controlling the trade-off between  $c$ - and light-jet rejection performance. The choice of  $f_c$  is arbitrary, and is optimised based upon the desired light- vs  $c$ -jet rejection performance. This parameter is set to a value of  $f_c = 0.018$  for the DL1r model, obtained through an optimisation procedure described in Ref. [85]. Based on a similar optimisation procedure, a value of  $f_c = 0.05$  is used for the GN1 models.

A comparison of the  $b$ -tagging discriminant  $D_b$  between DL1r and GN1 is shown in Fig. 6.5. The shapes of the  $D_b$  distributions are generally similar for  $b$ -,  $c$ - and light-jets between both models, however, GN1 shifts the  $b$ -jet distribution to higher values of  $D_b$  in the regions with the greatest discrimination. The GN1  $c$ -jet distribution is also shifted to lower values of  $D_b$  when compared with DL1r, enhancing the separation and indicating that GN1 is improving  $c$ -jet rejection when compared with DL1r.

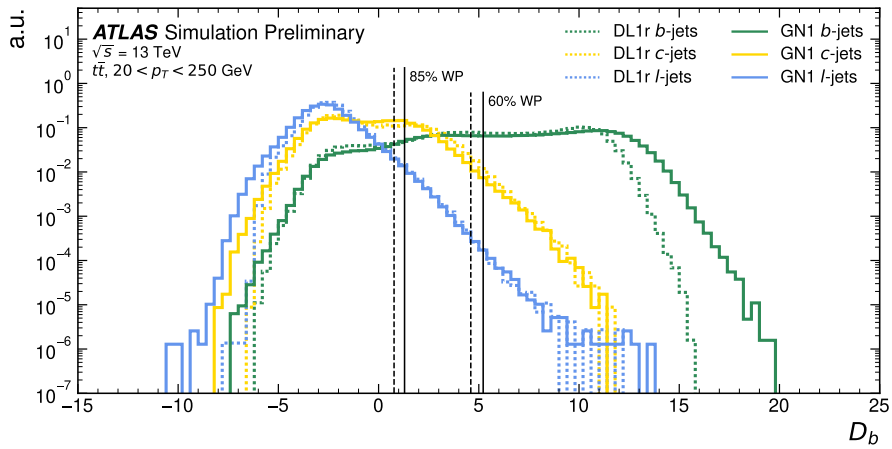


**Figure 6.5:** Comparison between the DL1r and GN1  $b$ -tagging discriminant  $D_b$  for jets in the  $t\bar{t}$  sample. The 85% WP and the 60% WP are marked by the solid (dashed) lines for GN1 (DL1r), representing respectively the loosest and tightest WPs typically used by analyses. A value of  $f_c = 0.018$  is used in the calculation of  $D_b$  for DL1r and  $f_c = 0.05$  is used for GN1. The distributions of the different jet flavours have been normalised to unity area [3].

### 6.5.1 $b$ -tagging Performance

The performance of  $b$ -tagging algorithms is quantified by their ability to reject  $c$ - and light-jets for a given  $b$ -jet selection efficiency WP. In order to compare the  $b$ -tagging performance of the different taggers for the  $b$ -jet tagging efficiencies in the range

1659 typically used by analyses, the corresponding  $c$ - and light-jet rejection rates are  
1660 displayed in Figs. 6.6 and 6.7 for jets in the  $t\bar{t}$  and  $Z'$  samples respectively. Four  
1661 standard WPs are defined with  $b$ -jet tagging efficiencies of 60%, 70%, 77% and 85%  
1662 respectively. These WPs are commonly used by physics analyses depending on their  
1663 specific signal and background requirements. The WPs are defined based on jets in  
1664 the  $t\bar{t}$  sample only. Due to the much higher jet  $p_T$  range in the  $Z'$  sample, and the  
1665 increased difficulty in tagging jets at high- $p_T$  (see Chapter 4), the corresponding  $b$ -jet  
1666 tagging efficiencies for jets in the  $Z'$  sample are lower than the corresponding WPs  
1667 calculated in the  $t\bar{t}$  sample. For instance the WP cut value computed to provide a  
1668 70%  $b$ -jet tagging efficiency on the  $t\bar{t}$  sample results in a  $b$ -jet tagging efficiency of  
1669 just  $\sim 30\%$  on the  $Z'$  sample. In order to account for this, the range of  $b$ -jet tagging  
1670 efficiencies displayed for plots showing the performance for jets in the  $Z'$  sample (for  
1671 example Fig. 6.7) is chosen to span the lower efficiencies achieved in the  $Z'$  sample  
1672 at high- $p_T$ .

1673 For jets in the  $t\bar{t}$  sample with  $20 < p_T < 250 \text{ GeV}$ , GN1 demonstrates considerably  
1674 better  $c$ - and light-jet rejection when compared with DL1r across the full range of  
1675  $b$ -jet tagging efficiencies studied. The relative improvement is strongly dependent  
1676 on the  $b$ -jet tagging efficiency under study. The largest improvements are found at  
1677 lower  $b$ -jet tagging efficiencies. At a  $b$ -jet tagging efficiency of 70%, the  $c$ -jet rejection  
1678 improves by a factor of  $\sim 2.1$  while the light-jet rejection improves by a factor of  $\sim 1.8$   
1679 with respect to DL1r. For high- $p_T$  jets in the  $Z'$  sample with  $250 < p_T < 5000 \text{ GeV}$ ,  
1680 GN1 also brings a significant performance improvement with respect to DL1r across  
1681 the range of  $b$ -jet tagging efficiencies studied. Again, the largest relative improvement  
1682 in performance comes at the lower  $b$ -jet tagging efficiencies. At a  $b$ -jet efficiency of  
1683 30%, GN1 improves the  $c$ -jet rejection with respect to DL1r by a factor of  $\sim 2.8$  and  
1684 the light-jet rejection by a factor of  $\sim 6$ . The performance comparison at lower  $b$ -jet  
1685 tagging efficiencies is made more difficult due to the increased statistical uncertainties  
1686 which result from the high rejection of background.

1687 The GN1Lep variant of GN1 demonstrates further improved performance with respect  
1688 to the baseline model. This demonstrates the additional jet flavour discrimination  
1689 power provided by the leptonID track input. For jets in the  $t\bar{t}$  sample, the relative  $c$ -  
1690 jet rejection improvement with respect to GN1 at the 70%  $b$ -jet WP is approximately  
1691 25%. The improvement in light-jet rejection also increases by 40% at the same WP.  
1692 For jets in the  $Z'$  sample, the relative  $c$ -jet rejection (light-jet rejection) performance

1693 with respect to GN1 improves by approximately 10% (25%) at a  $b$ -jet tagging  
1694 efficiency of 30%.

1695 In general, the performance of all the taggers is strongly dependent on jet  $p_T$ , due  
1696 to the increased multiplicity and collimation of tracks, and the displaced decays  
1697 that result from within the heavy flavour jets (see Chapter 4). Together, they  
1698 contribute to a reduced reconstruction efficiency for heavy flavour tracks, and a  
1699 general degradation in quality of tracks inside the core of a jet, which in turn reduces  
1700 the jet tagging performance. In order to study how the tagging performance changes  
1701 as a function of the jet  $p_T$ , the  $b$ -jet tagging efficiency as a function of  $p_T$  for a fixed  
1702 light-jet rejection of 100 in each bin is shown in Fig. 6.8. For jets in the  $t\bar{t}$  sample,  
1703 at a fixed light-jet rejection of 100, GN1 improves the  $b$ -jet tagging efficiency by  
1704 approximately 4% across all the jet  $p_T$  bins. Meanwhile, GN1Lep again demonstrates  
1705 improved performance with respect to GN1, in particular at lower  $p_T$ . The relative  
1706 increase in the  $b$ -jet tagging efficiency increases from 4% to 8% with respect to DL1r.  
1707 For jets in the  $Z'$  sample, GN1 again outperforms DL1r across the entire jet  $p_T$  range  
1708 studied. The largest relative improvement in performance is found at the highest  
1709 transverse momenta of jet  $p_T > 2 \text{ TeV}$ , and corresponds to an approximate factor of  
1710 2 improvement in efficiency with respect to DL1r.

1711 The performance of the model was also evaluated as a function of the average  
1712 number of pile-up interactions in the event. No significant dependence of the tagging  
1713 performance was observed.

### 1714 6.5.2 $c$ -tagging Performance

1715 As discussed previously, GN1 does not rely on any inputs from manually optimised  
1716 low-level tagging algorithms. Since these algorithms were originally designed and  
1717 tuned with the aim of  $b$ -tagging, and not  $c$ -tagging, the low level tagging algorithms  
1718 may perform suboptimally for  $c$ -tagging purposes. The tagging of  $c$ -jets therefore  
1719 presents a compelling use case for GN1. As each of the models is trained with three  
1720 output classes, using it as a  $c$ -tagging algorithm is trivially analogous to the approach  
1721 used for  $b$ -tagging. The model output probabilities are combined into a single score  
1722  $D_c$ , which is defined similarly to Eq. (6.8) as

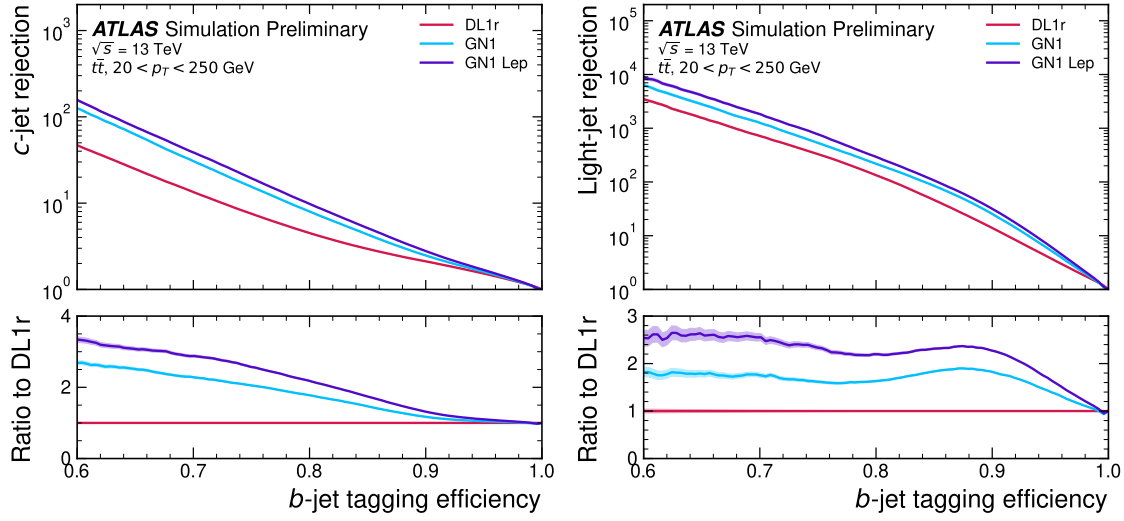


**Figure 6.6:** The  $c$ -jet (left) and light-jet (right) rejections as a function of the  $b$ -jet tagging efficiency for jets in the  $t\bar{t}$  sample with  $20 < p_T < 250 \text{ GeV}$ . The ratio with respect to the performance of the DL1r algorithm is shown in the bottom panels. A value of  $f_c = 0.018$  is used in the calculation of  $D_b$  for DL1r and  $f_c = 0.05$  is used for GN1 and GN1Lep. Binomial error bands are denoted by the shaded regions. The  $x$ -axis range is chosen to display the  $b$ -jet tagging efficiencies usually probed in these regions of phase space [3].

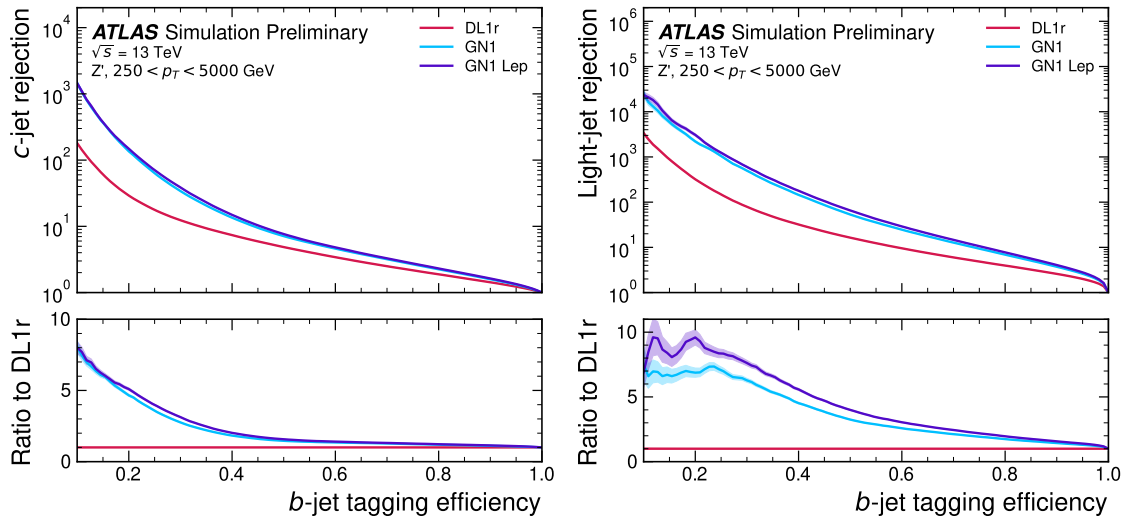


**Figure 6.7:** The  $c$ -jet (left) and light-jet (right) rejections as a function of the  $b$ -jet tagging efficiency for jets in the  $Z'$  sample with  $250 < p_T < 5000 \text{ GeV}$ . The ratio with respect to the performance of the DL1r algorithm is shown in the bottom panels. A value of  $f_c = 0.018$  is used in the calculation of  $D_b$  for DL1r and  $f_c = 0.05$  is used for GN1 and GN1Lep. Binomial error bands are denoted by the shaded regions. The  $x$ -axis range is chosen to display the  $b$ -jet tagging efficiencies usually probed in these regions of phase space [3].

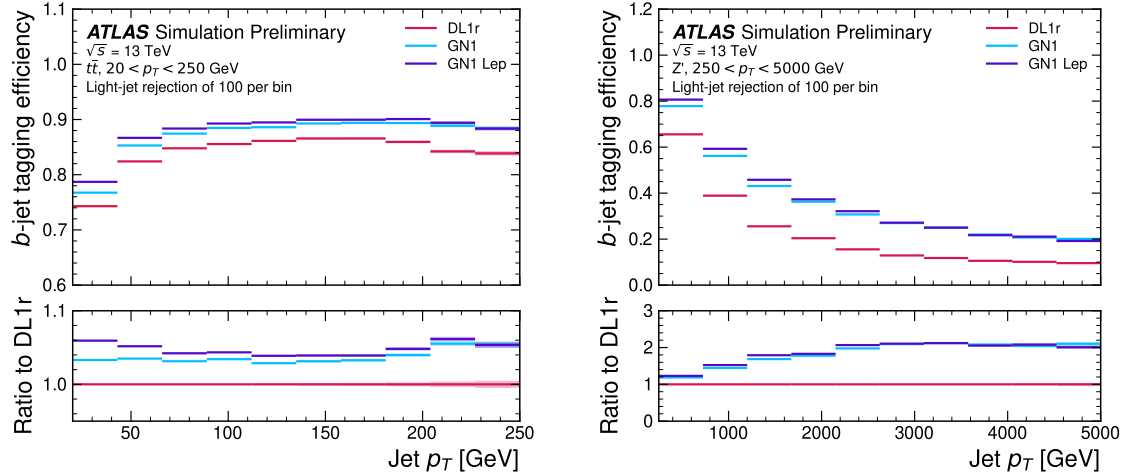


**Figure 6.8:** The  $b$ -jet tagging efficiency for jets in the  $t\bar{t}$  sample (left) and jets in the  $Z'$  sample (right) as a function of jet  $p_T$  with a fixed light-jet rejection of 100 in each bin. A value of  $f_c = 0.018$  is used in the calculation of  $D_b$  for DL1r and  $f_c = 0.05$  is used for GN1 and GN1Lep. GN1 demonstrates improved performance with respect to DL1r across the  $p_T$  range shown. Binomial error bands are denoted by the shaded regions [3].

$$D_c = \log \frac{p_c}{(1 - f_b)p_l + f_b p_b}. \quad (6.9)$$

A value of  $f_b = 0.2$  is used for all models, based on the same optimisation procedure that was used for the  $b$ -tagging use case. Similar to Section 6.5.1, the different taggers are compared to one another by scanning through a range of  $c$ -jet tagging efficiencies and plotting the corresponding  $b$ - and light-jet rejection rates, and the WPs are defined using jets in the  $t\bar{t}$  sample. Standard  $c$ -jet tagging efficiency WPs used by physics analyses are significantly lower than the  $b$ -tagging WPs in order to maintain reasonable  $b$ - and light-jet rejection rates. This is reflected in the range of  $c$ -jet tagging efficiencies used in  $c$ -tagging plots such as Figs. 6.9 and 6.10. Fig. 6.9 displays the  $c$ -tagging performance of the models on the jets in the  $t\bar{t}$  sample. GN1 is shown to perform significantly better than DL1r. Similar to the  $b$ -tagging case, the  $b$ - and light-jet rejection improve most at lower  $c$ -jet tagging efficiencies, with the  $c$ -jet rejection (light-jet rejection) improving by a factor 2 (1.6) with respect to DL1r at a  $c$ -jet tagging efficiency of 25%. GN1Lep again outperforms GN1, though the improvements are more modest than observed for the  $b$ -tagging use case,

1737 with both the  $b$ -jet rejection (light-jet rejection) improving with respect to GN1  
1738 by approximately 10% (20%) at the 25%  $c$ -jet WP. Fig. 6.10 shows the  $c$ -tagging  
1739 performance on the jets in the  $Z'$  sample with  $250 < p_T < 5000$  GeV. Both GN1 and  
1740 GN1Lep perform similarly, improving the  $b$ -jet rejection by 60% and the light-jet  
1741 rejection by a factor of 2 at the 25%  $c$ -jet WP.

### 1742 6.5.3 Ablations

1743 Ablation studies (the removal of certain components of a model in order to study  
1744 the impact of that component) are carried out to determine the importance of the  
1745 auxiliary training objectives of GN1 to the overall performance. The “GN1 No  
1746 Aux” variant retains the primary jet classification objective, but removes both track  
1747 classification and vertexing auxiliary objectives and correspondingly only minimises  
1748 the jet classification loss. The “GN1 TC” variant includes the track classification  
1749 objective but not the vertexing objective. Finally, the “GN1 Vert” includes the  
1750 vertexing objective, but not the track classification objective.

1751 For jets in both the  $t\bar{t}$  and  $Z'$  samples, a general trend is observed that the models  
1752 trained without one or both of the auxiliary objectives results in significantly reduced  
1753  $c$ - and light-jet rejection when compared with the baseline GN1 model, as shown  
1754 in Figs. 6.11 and 6.12. For jets in the  $t\bar{t}$  sample, the performance of GN1 No Aux  
1755 is similar to DL1r, while GN1 TC and GN1 Vert perform similarly to each other.  
1756 For jets in the  $Z'$  sample, the GN1 No Aux model shows a clear improvement in  $c$ -  
1757 and light-jet rejection when compared with DL1r at lower  $b$ -jet tagging efficiencies.  
1758 Similar to jets in the  $t\bar{t}$  sample, GN1 TC and GN1 Vert perform similarly, and bring  
1759 large gains in background rejection when compared with GN1 No Aux, but the  
1760 combination of both auxiliary objectives yields the best performance.

1761 It is notable that the GN1 No Aux model matches or exceeds the performance of  
1762 DL1r without the need for inputs from the low-level algorithms. This indicates that  
1763 the performance improvements enabled by the improved neural network architecture  
1764 used in GN1 appear to be able to compensate for the removal of the low-level  
1765 algorithm inputs. The GN1 TC and GN1 Vert variants each similarly outperform  
1766 DL1r, demonstrating that both contribute to the overall high performance of the  
1767 baseline model. The overall best performing model is the full version of GN1 trained

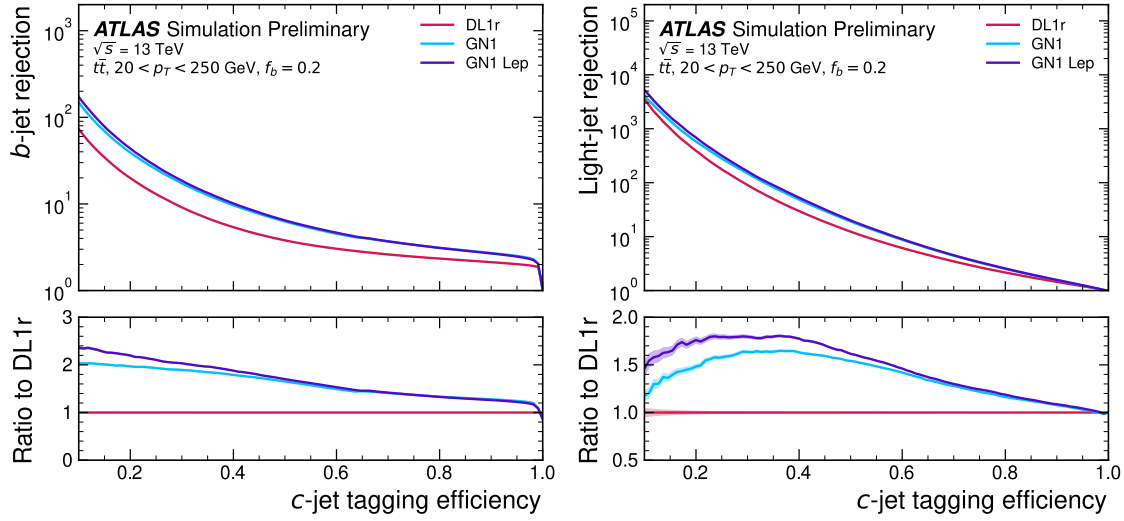


**Figure 6.9:** The  $b$ -jet (left) and light-jet (right) rejections as a function of the  $c$ -jet tagging efficiency for  $t\bar{t}$  jets with  $20 < p_T < 250$  GeV. The ratio to the performance of the DL1r algorithm is shown in the bottom panels. Binomial error bands are denoted by the shaded regions. The  $x$ -axis range is chosen to display the  $c$ -jet tagging efficiencies usually probed in these regions of phase space [3].

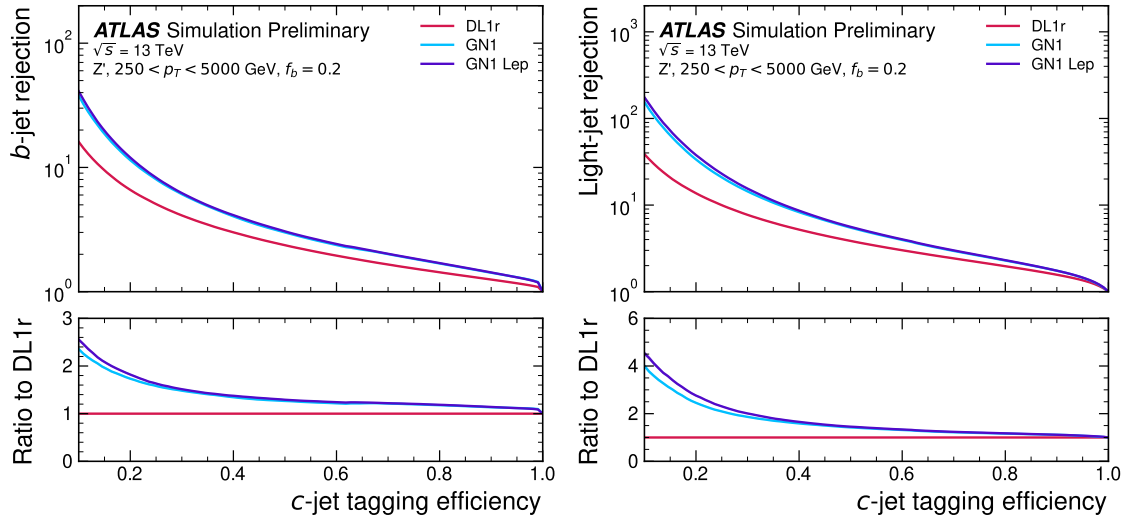


**Figure 6.10:** The  $b$ -jet (left) and light-jet (right) rejections as a function of the  $c$ -jet tagging efficiency for  $Z'$  jets with  $250 < p_T < 5000$  GeV. The ratio to the performance of the DL1r algorithm is shown in the bottom panels. Binomial error bands are denoted by the shaded regions. The  $x$ -axis range is chosen to display the  $c$ -jet tagging efficiencies usually probed in these regions of phase space [3].

1768 with both auxiliary objective, demonstrating that the two auxiliary objectives are  
1769 complementary.

1770 **6.5.4 Inclusion of Low-Level Vertexing Algorithms**

1771 As already mentioned, GN1 does not include any inputs from the low-level tagging  
1772 algorithms, including the vertexing algorithms SV1 and JetFitter [61]. Since these  
1773 algorithms are known to play a key role in contributing to the performance of DL1r,  
1774 it was studied whether their inclusion in GN1 could result in further performance  
1775 improvements. In a dedicated training of GN1, the SV1 and JetFitter tagger outputs  
1776 were added to the GN1 jet classification network as an input, similar to how they  
1777 are used in DL1r. These outputs include information on the reconstructed vertices,  
1778 including the number of vertices, and the properties of the reconstructed vertices.  
1779 In addition, if track was used in the reconstruction of a vertex, a corresponding  
1780 index to the vertex was included as a track-level inputs to GN1. These indices were  
1781 also used to construct an input feature for the edge classification network used to  
1782 identify vertices, which was given a value of one if the track-pair were from a common  
1783 reconstructed SV1 or JetFitter vertex, and zero otherwise. The jet classification  
1784 performance of this GN1 model was not significantly different to the baseline model,  
1785 and in some cases the performance was slightly reduced. It was therefore concluded  
1786 that GN1 does not benefit from the inclusion of information from SV1 and JetFitter,  
1787 indicating that the model is able to reconstruct the relevant information provided  
1788 by these low-level algorithms. The study also demonstrates that the model can  
1789 function as a highly performant standalone tagger that does not require (beyond  
1790 retraining) any manual optimisation to achieve good performance in a wide range  
1791 of phase spaces. A dedicated look at the vertexing performance of GN1 with some  
1792 comparisons to SV1 and JetFitter is found in Section 6.5.6

1793 **6.5.5 Jet Display Diagrams**

1794 The auxiliary training objectives of GN1 allow for improved model interpretability,  
1795 which is especially important for a monolithic approach as the low level taggers,  
1796 which provide useful physical insight, are no longer present. Figs. 6.13 and 6.14  
1797 provide example comparisons of the true origin and vertexing information compared

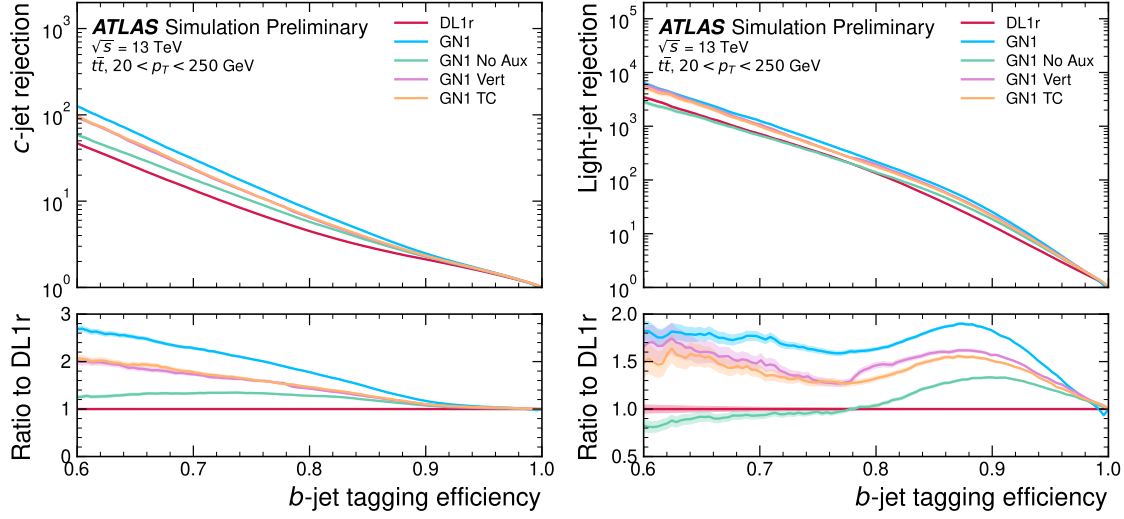


**Figure 6.11:** The  $c$ -jet (left) and light-jet (right) rejections as a function of the  $b$ -jet tagging efficiency for  $t\bar{t}$  jets with  $20 < p_T < 250$  GeV, for the nominal GN1, in addition to configurations where no (GN1 No Aux), only the track classification (GN1 TC) or only the vertexing (GN1 Vert) auxiliary objectives are deployed. The ratio to the performance of the DL1r algorithm is shown in the bottom panels. A value of  $f_c = 0.018$  is used in the calculation of  $D_b$  for DL1r and  $f_c = 0.05$  is used for GN1 [3].

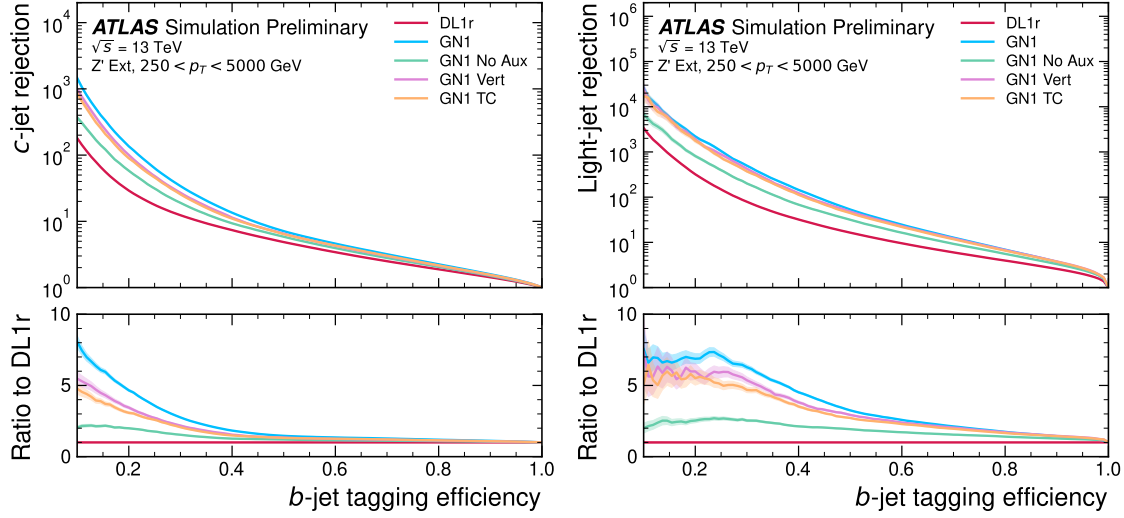


**Figure 6.12:** The  $c$ -jet (left) and light-jet (right) rejections as a function of the  $b$ -jet tagging efficiency for  $Z'$  jets with  $250 < p_T < 5000$  GeV, for the nominal GN1, in addition to configurations where no (GN1 No Aux), only the track classification (GN1 TC) or only the vertexing (GN1 Vert) auxiliary objectives are deployed. The ratio to the performance of the DL1r algorithm is shown in the bottom panels. A value of  $f_c = 0.018$  is used in the calculation of  $D_b$  for DL1r and  $f_c = 0.05$  is used for GN1 [3].

1798 with the predicted values from GN1, SV1 and JetFitter. Such comparisons can be  
 1799 used to provide an indication that GN1 reconstructs the correct representation of the  
 1800 jet structure, and may also help to identify limitations of the model. In the figures,  
 1801 the tracks in the jet are indexed twice on each of the  $x$ - and  $y$ -axes, and tracks are  
 1802 grouped into vertices along with other tracks as indicated by common markings in  
 1803 the relevant rows and columns.

1804 In Fig. 6.13, GN1 correctly groups the three primary tracks as having come from the  
 1805 primary vertex. The  $b$ -hadron and  $b \rightarrow c$ -hadron decay vertices are also correctly  
 1806 predicted, and the origin of the tracks in each is correct. There is a single OtherSec-  
 1807 ondary track which GN1 incorrectly predicts as having come from pile-up. Meanwhile  
 1808 SV1 (by design) merges the two heavy flavour decay vertices, but incorrectly includes  
 1809 a track from the primary vertex. JetFitter reconstructs two vertices, one which is a  
 1810 combination of two tracks from different truth vertices and two other single track  
 1811 vertices in each of the heavy flavour vertices. GN1 also predicts the flavour of the jet  
 1812 with a high degree of certainty.

1813 Similarly Fig. 6.13 shows that GN1 is also able to relatively accurately predict the  
 1814 origin and vertex information of tracks inside a jet. The pile-up tracks and primary  
 1815 vertex tracks are correctly identified, and the heavy flavour decay tracks are also  
 1816 correctly identified with the exception of one of the  $b$ -hadron decay tracks. Again,  
 1817 SV1 merges the two heavy flavour decay vertices along with a track from pile-up,  
 1818 while JetFitter shows signs of being under-constrained by reconstructing two single  
 1819 track vertices, one with a pile-up track and one with a track from a  $b \rightarrow c$ -hadron  
 1820 decay. While these examples do not give a complete picture of the performance of  
 1821 GN1, they do show provide a powerful way to visualise and diagnose the behaviour  
 1822 of GN1.

### 1823 6.5.6 Vertexing Performance

1824 From the track-pair vertex prediction, tracks can be partitioned into compatible  
 1825 groups representing vertices through the use of a deterministic clustering algorithm  
 1826 (see Ref. [115]). As such, GN1 can perform vertex “finding”, but not vertex “fitting”,  
 1827 i.e. the reconstruction of a vertex’s properties, which currently still requires the  
 1828 use of a dedicated vertex fitter. In order to study the performance of the different  
 1829 vertexing tools, the truth vertex label of the tracks are used.

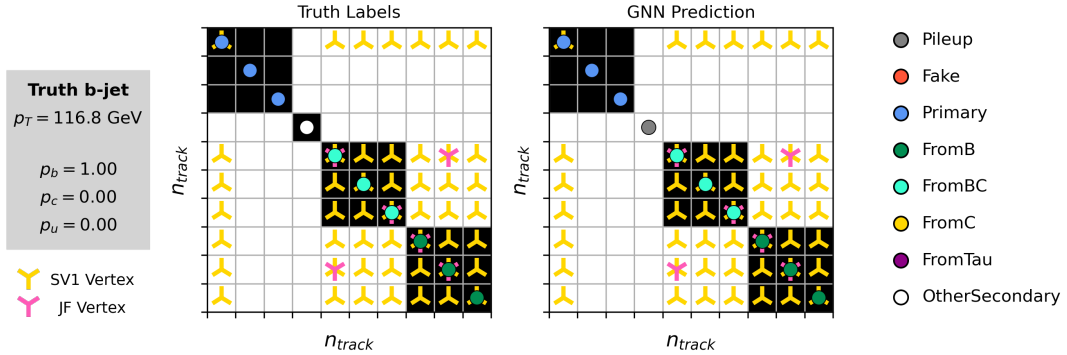


**Figure 6.13:** A schematic showing the truth track origin and vertex information (left) compared with the predictions from GN1 (right). The diagrams show the truth (left) and predicted (right) structure of a  $b$ -jet. The true and predicted origins of the tracks is shown by the coloured circles along the diagonal. The shaded black boxes show the groupings of tracks into different vertices. Vertices reconstructed by SV1 and JetFitter are also marked. Class probabilities  $p_b$ ,  $p_c$  and  $p_u$  are rounded to three significant figures. GN1 improves over SV1 and JetFitter by successfully determining the origins and vertex compatibility of all the tracks in the jet with the exception of the truth OtherSecondary track, which is misidentified as pile-up.

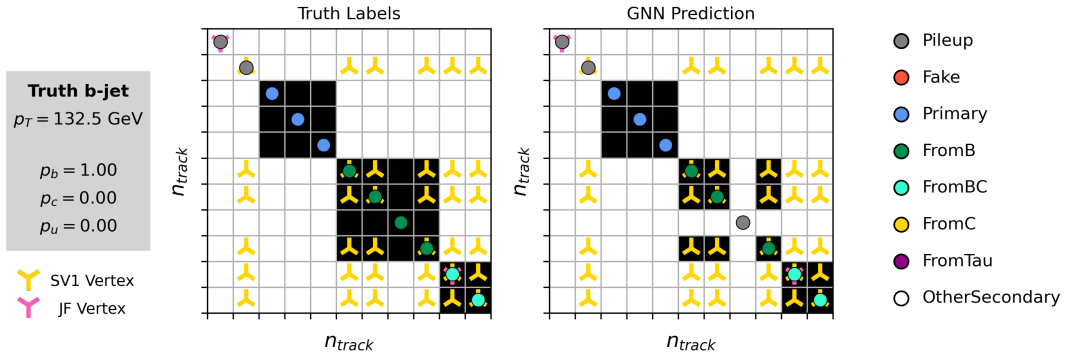


**Figure 6.14:** A schematic showing the truth track origin and vertex information (left) compared with the predictions from GN1 (right). The diagrams show the truth (left) and predicted (right) structure of a  $b$ -jet. The true and predicted origins of the tracks is shown by the coloured circles along the diagonal. The shaded black boxes show the groupings of tracks into different vertices. Vertices reconstructed by SV1 and JetFitter are also marked. Class probabilities  $p_b$ ,  $p_c$  and  $p_u$  are rounded to three significant figures. GN1 improves over SV1 and JetFitter by successfully determining the origins and vertex compatibility of all but one tracks in the jet.

1830 There are several caveats to a comparison of the vertexing tools which are a result  
1831 of the different approaches they take to vertexing. SV1 and JetFitter are designed  
1832 to only find secondary vertices in the jet, whereas GN1 is also trained to determine  
1833 which tracks in the jet belong to the primary vertex. To account for this the GN1  
1834 vertex with the largest number of predicted primary tracks is excluded from the  
1835 vertex finding efficiency calculation. While JetFitter and GN1 aim to resolve each  
1836 displaced vertex inside the jet, such that secondary vertices from  $b$ -hadron decays  
1837 are found separately to tertiary vertices from  $b \rightarrow c$  decay chains, SV1 by design  
1838 attempts to find a single inclusive vertex per jet. This inclusive vertex groups tracks  
1839 from the  $b$ -hadron decay itself (FromB) and tracks from  $b \rightarrow c$  decays (FromBC). In  
1840 order to fairly compare the performance of the different tools, both the exclusive and  
1841 inclusive vertex finding efficiencies are studied. For the exclusive vertex finding case  
1842 JetFitter and GN1 can be directly compared, while a comparison with SV1 is not  
1843 possible due to the aforementioned design constraints. The inclusive vertex finding  
1844 performance of all three tools can be compared using the procedure outlined below.

1845 The starting point for the secondary vertex finding efficiency in both the exclusive and  
1846 inclusive cases is to select truth HF secondary vertices, defined as those containing  
1847 only inclusive  $b$ -hadron decays. For exclusive HF vertex finding, these truth secondary  
1848 HF vertices can be used directly as the denominator for the efficiency calculation.  
1849 Meanwhile for the inclusive efficiency all such truth HF secondary vertices in the jet  
1850 are merged into a single inclusive target vertex. Correspondingly, for the inclusive  
1851 HF vertex finding case, the vertices found by JetFitter are merged into a single  
1852 vertex, and the vertices found by GN1 which contain at least one predicted  $b$ -hadron  
1853 decay track, are also merged. SV1 does not require any vertex merging. Only jets  
1854 containing a single  $b$ -hadron at truth level are considered.

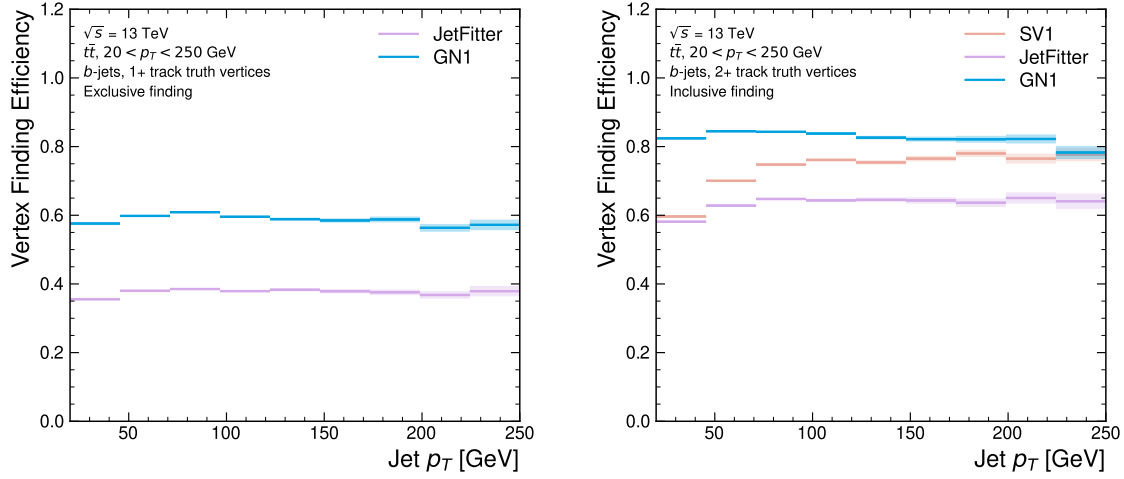
1855 Next, vertices in the jet found by the different vertexing tools are compared with  
1856 the target truth vertices. The number of correctly and incorrectly assigned tracks is  
1857 computed. In order to call a vertex efficient, it is required to contain at least 65% of  
1858 the tracks in the corresponding truth vertex, and to have a purity of at least 50%.  
1859 Single track vertices are required to have a purity of 100%. Additionally, for GN1  
1860 only, at least one track in the vertex is required to have a predicted heavy flavour  
1861 origin.

1862 Vertex finding efficiencies for  $b$ -jets in the  $t\bar{t}$  sample are displayed as a function of  
1863  $p_T$  separately for the inclusive and exclusive approaches in Fig. 6.15. For  $b$ -jets in

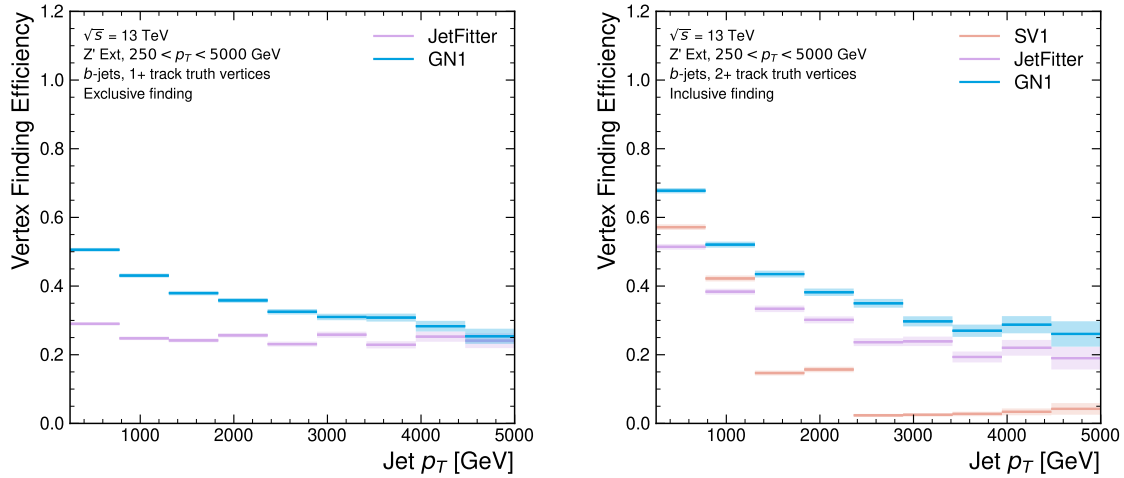
the  $t\bar{t}$  sample with  $20 < p_T < 250$  GeV, the exclusive vertex finding efficiency of JetFitter and GN1 is relatively flat as a function of  $p_T$ . For the truth secondary vertices in this  $p_T$  region, JetFitter efficiently finds approximately 40% and GN1 finds approximately 55%. When finding vertices inclusively the vertex finding efficiency is generally higher. An increased dependence on  $p_T$  is also visible for JetFitter and SV1. As the jet  $p_T$  increases from 20 GeV to 100 GeV, the efficiency of JetFitter increases from 60% to 65%. In the same range, the efficiency of SV1 increases from 60% to 75%. GN1 displays less dependence on  $p_T$  than JetFitter and SV1, finding upwards of 80% of vertices in  $b$ -jets in this  $p_T$  region. For  $b$ -jets with  $p_T > 100$  GeV, JetFitter finds approximately 65% of vertices, SV1 finds approximately 75% of vertices, and GN1 finds approximately 80% of vertices.

Fig. 6.16 compares the exclusive and inclusive HF vertex finding efficiencies for  $b$ -jets in the  $Z'$  sample. The inclusive vertex finding efficiency drops steeply with increasing  $p_T$  up until  $p_T = 3$  TeV. GN1 outperforms SV1 and JetFitter across the  $p_T$  spectrum. In the first bin, the efficiency of GN1 is 65%, while the efficiencies of SV1 and JetFitter are around 55%. The efficiency of SV1 drops rapidly to almost zero above 3 TeV, while JetFitter and GN1 retain approximately 20% and 30% efficiency respectively. For the exclusive HF vertex finding efficiency, JetFitter finds 35% of vertices in the first bin, dropping to 20% of vertices above 2 TeV. GN1 finds 55% of vertices in the first bin, dropping to 30% above 2 TeV.

While Figs. 6.15 and 6.16 indicate that GN1 is able to successfully find displaced heavy flavour vertices in  $b$ -jets, it is also important to consider the vertexing performance inside light-jets. Light-jets may also contain real displaced vertices due to long lived secondary particles and material interactions. These tracks have a truth origin of OtherSecondary in the truth labelling scheme enumerated in see Table 5.1. The efficiency to reconstruct vertices comprised of OtherSecondary tracks can be computed in an analogous way to the heavy flavour vertexing efficiency, which is described above. Figs. 6.17 and 6.18 show the efficiency to reconstruct displaced OtherSecondary vertices in light-jets as a function of  $p_T$  for jets in the  $t\bar{t}$  sample and jets in the  $Z'$  sample respectively. The figures demonstrate that GN1 is able to more effectively find such vertices in light-jets as compared with SV1 and JetFitter. Since the properties of the displaced vertices in light-jets are likely to be significantly different to heavy flavour vertices found in heavy flavour jets, the improved reconstruction of such vertices may help to differentiate between different flavour of jet.



**Figure 6.15:** Heavy flavour vertex finding efficiency as a function of jet  $p_T$  for  $b$ -jets in the  $t\bar{t}$  sample using the exclusive (left) and inclusive (right) vertex finding approaches. The exclusive vertexing approach includes single track vertices while the inclusive approach requires vertices to contain at least two tracks. Efficient vertex finding requires the recall of at least 65% of the tracks in the truth vertex, and allows no more than 50% of the tracks to be included incorrectly. Binomial error bands are denoted by the shaded regions.



**Figure 6.16:** Heavy flavour vertex finding efficiency as a function of jet  $p_T$  for  $b$ -jets in the  $Z'$  sample using the exclusive (left) and inclusive (right) vertex finding approaches. The exclusive vertexing approach includes single track vertices while the inclusive approach requires vertices to contain at least two tracks. Efficient vertex finding requires the recall of at least 65% of the tracks in the truth vertex, and allows no more than 50% of the tracks to be included incorrectly. Binomial error bands are denoted by the shaded regions.

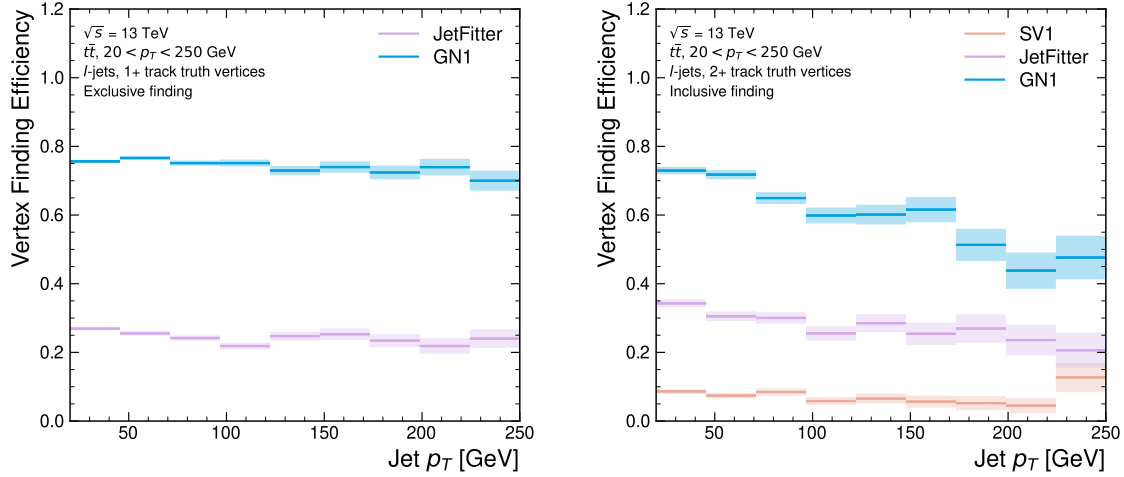


**Figure 6.17:** Vertex finding efficiency for other secondary decays as a function of jet  $p_T$  for light-jets in the  $t\bar{t}$  sample using the exclusive (left) and inclusive (right) vertex finding approaches. The exclusive vertexing approach includes single track vertices while the inclusive approach requires vertices to contain at least two tracks. Efficient vertex finding requires the recall of at least 65% of the tracks in the truth vertex, and allows no more than 50% of the tracks to be included incorrectly. Binomial error bands are denoted by the shaded regions.

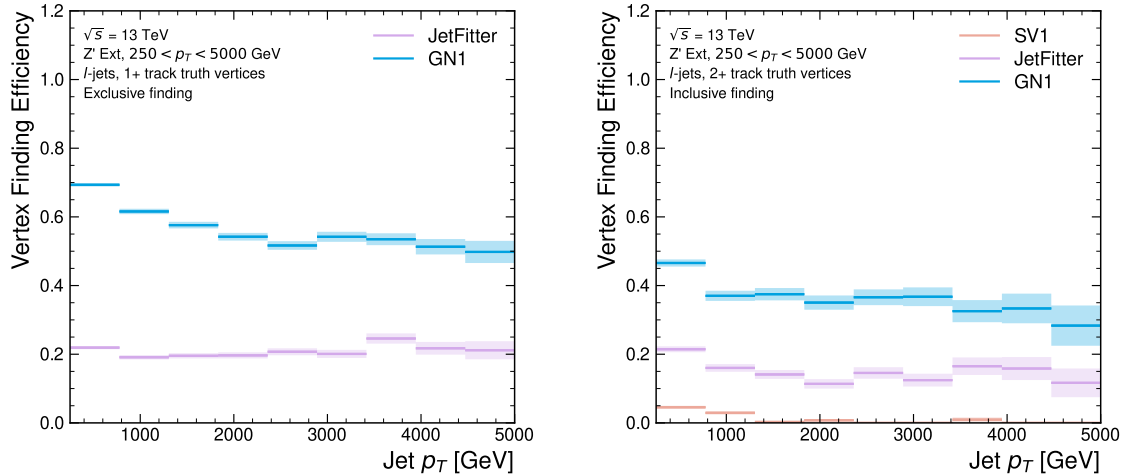


**Figure 6.18:** Vertex finding efficiency as a function of jet  $p_T$  for light-jets in the  $Z'$  sample using the exclusive (left) and inclusive (right) vertex finding approaches. The exclusive vertexing approach includes single track vertices while the inclusive approach requires vertices to contain at least two tracks. Efficient vertex finding requires the recall of at least 65% of the tracks in the truth vertex, and allows no more than 50% of the tracks to be included incorrectly. Binomial error bands are denoted by the shaded regions.

1898 Collectively, the results in this section demonstrate that GN1 is able to accurately  
1899 group tracks by their spatial origin in both  $b$ -jets and light-jets. The purity of the  
1900 found vertices was also investigated and was found to be comparable or better than  
1901 that of SV1 and JetFitter.

### 1902 6.5.7 Track Classification Performance

1903 One of the two auxiliary training objectives used by GN1 is to predict the truth origin  
1904 of each track associated to the jet. Since the equivalent information is not provided  
1905 by any of the existing flavour tagging tools, a benchmark model used to predict the  
1906 truth origin of each track is trained based on a standard multi-class feed-forward  
1907 classification network. The benchmark model is trained on the same tracks used for  
1908 the baseline GN1 training. The model uses precisely the same concatenated track-  
1909 and-jet inputs as used by GN1, but processes only a single track at a time, meaning  
1910 it cannot take into account the correlations between tracks when determining the  
1911 track origin. The model is made up of five densely connected linear layers with 200  
1912 neurons in each layer. The performance of the model was found to be insensitive to  
1913 changes in the network structure.

1914 To measure the track classification performance, the area under the curve (AUC) of  
1915 the receiver operating characteristic (ROC) curve is computed for each origin class,  
1916 using a one-versus-all classification approach<sup>2</sup>. The AUCs for the different truth  
1917 origins are averaged using both an unweighted and a weighted mean. The unweighted  
1918 mean treats the performance of each class equally, while the weighted mean uses  
1919 as a weight the relative abundance of tracks of each class. The same approach is  
1920 used to compute the precision, recall and F1 scores<sup>3</sup>. Table 6.3 demonstrates clearly  
1921 that GN1 outperforms the MLP both at  $20 < p_T < 250$  GeV for jets in the  $t\bar{t}$  sample  
1922 and at  $250 < p_T < 5000$  GeV for jets in the  $Z'$  sample. For example, GN1 can reject  
1923 65% of fake tracks in jets in the  $t\bar{t}$  sample, while retaining more than 99% of good  
1924 tracks (i.e. those tracks which are not fake). The GN1 model has two advantages  
1925 over the MLP which can explain the performance improvement. Firstly, the graph

---

<sup>2</sup>One class is taken to be signal and the rest are taken as background, subsequently a binary classification approach is used.

<sup>3</sup>The precision is the fraction of selected tracks from the signal class. The recall, similar to the efficiency, is the fraction of tracks from the signal class which are selected. The F1 score is the harmonic mean of the precision and recall.

1926 neural network architecture enables the sharing of information between tracks. This  
1927 is likely to be beneficial since the origins of different tracks within a jet are correlated.  
1928 Secondly, the jet classification and vertexing objectives may be complementary to the  
1929 track classification objective, and so the track classification performance is improved  
1930 by the combined training of complementary objectives.

		AUC		Precision		Recall		F1	
		Mean		Weighted		Mean		Weighted	
		MLP	GN1	MLP	GN1	MLP	GN1	MLP	GN1
$t\bar{t}$	MLP	0.87	<b>0.92</b>	0.39	<b>0.51</b>	0.51	<b>0.64</b>	0.36	0.62
	GN1	<b>0.95</b>	<b>0.95</b>	<b>0.71</b>	<b>0.82</b>	<b>0.56</b>	<b>0.70</b>	<b>0.51</b>	<b>0.74</b>
$Z'$	MLP	0.90	0.94	0.36	0.84	0.47	0.72	0.31	0.76
	GN1	<b>0.94</b>	<b>0.96</b>	<b>0.48</b>	<b>0.88</b>	<b>0.60</b>	<b>0.79</b>	<b>0.48</b>	<b>0.82</b>

**Table 6.3:** The area under the ROC curves (AUC) for the track classification from GN1, compared to a standard multilayer perceptron (MLP) trained on a per-track basis. The unweighted mean AUC over the origin classes and weighted mean AUC (using as a weight the fraction of tracks from the given origin) is provided. GN1, which uses an architecture that allows track origins to be classified in a conditional manner as discussed in Section 6.4.3, outperforms the MLP model for both  $t\bar{t}$  and  $Z'$  jets.

1931 Fig. 6.19 shows the track origin classification ROC curves for the different track  
1932 origins for jets in both the  $t\bar{t}$  and  $Z'$  samples. In order to improve visual readability  
1933 of the plot, the curves for the heavy flavour truth origins (FromB, FromBC and  
1934 FromC) have been combined (weighted by their relative abundance), as have the  
1935 Primary and OtherSecondary origins. In jets in both the  $t\bar{t}$  and  $Z'$  samples, the AUC  
1936 of all the different origin groups exceeds 0.9, representing strong overall classification  
1937 performance. In both samples fake tracks are the easiest to classify, followed by  
1938 pile-up tracks. The FromC tracks which are  $c$ -hadron decay products, are the hardest  
1939 to classify, possibly due to their similarity to both fragmentation tracks and  $b$ -hadron  
1940 decay tracks, depending on the  $c$ -hadron species in question.

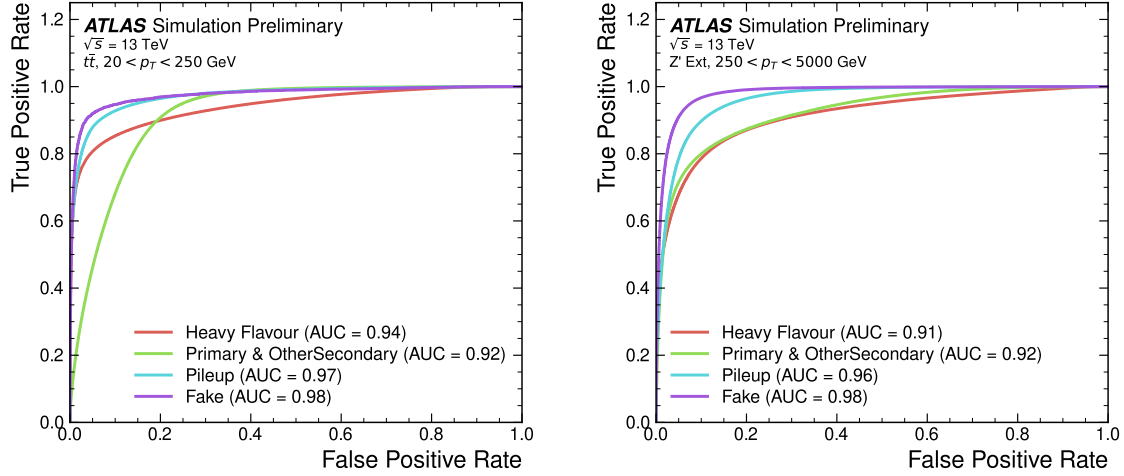


**Figure 6.19:** ROC curves for the different groups of truth origin labels defined in Table 5.1 for jets in the  $t\bar{t}$  sample (left) and jets in the  $Z'$  sample (right). The FromB, FromBC and FromC labels have been combined, weighted by their relative abundance, into the Heavy Flavour category, and the Primary and OtherSecondary labels have similarly been combined into a single category. The mean weighted area under the ROC curves (AUC) is similar for both samples [3].

## 1941 6.6 Further Studies

### 1942 6.6.1 Looser Track Selection

1943 The track selections used to produce the main results are listed in Table 3.2. This  
 1944 includes a selection on the number of shared silicon modules used to reconstruct the  
 1945 track  $N_{\text{shared}}^{\text{Si}}$ . This value is calculated as

$$N_{\text{shared}}^{\text{Si}} = N_{\text{shared}}^{\text{Pix}} + N_{\text{shared}}^{\text{SCT}}/2 \quad (6.10)$$

1946 where  $N_{\text{shared}}^{\text{Pix}}$  is the number of shared pixel hits and  $N_{\text{shared}}^{\text{SCT}}$  is the number of shared  
 1947 SCT modules on a track. The nominal selection used elsewhere in this thesis is  
 1948  $N_{\text{shared}}^{\text{Si}} < 2$ . As the rate of shared hits is significantly higher for  $b$ -hadron decay  
 1949 tracks than for other tracks, especially at high- $p_T$ , this selection rejects a significant  
 1950 proportion of these tracks.

1951 Figs. 6.20 and 6.21 show the result of training the GN1 tagger with the full relaxation  
 1952 of this selection, i.e. allowing tracks with any number of shared hits. The shared hit

requirements applied by the ambiguity solver as part of track reconstruction (see Section 3.4.1) are still applied. In addition, the maximum allowed value of  $d_0$  is increased from 3.5 mm to 5.0 mm. The results show that optimisation of the input track selection can lead to significant improvements in performance over the default selection. For the jets in the  $t\bar{t}$  sample shown in Fig. 6.20, the effect of loosening the track selection is limited. This is expected due to the lower prevalence of shared hits at lower transverse momenta. However for jets in the  $Z'$  sample as shown in Fig. 6.21, the  $c$ -jet rejection improves with respect to the baseline GN1 model by 35%, while the light-jet rejection improves by 40% at the 20%  $b$ -jet WP. Relative improvements of a similar magnitude are also observed for GN1Lep.

### 6.6.2 High Level Trigger

The implementation of GN1 described in this chapter has been re-used in several other contexts, demonstrating its flexibility to easily provide good jet flavour tagging performance with minimal overhead. The model has been implemented as a  $b$ -jet tagger in the High Level Trigger (HLT) (see Section 3.3.4). The inputs to the model are the running on precision tracks<sup>4</sup> and jet level quantities reconstructed after primary vertex reconstruction has been performed. Fig. 6.22 shows the performance of GN1 versus a comparable DL1d model [86], and two versions of DIPS [83], with EMTopo and PFlow jets (see Section 3.4.3) based on a low-precision region-of-interest based tracking pass, which is optimised for speed. The trigger implementation of GN1 improves upon the light-jet rejection of DL1d by 50% at the 60%  $b$ -jet WP for jets in the  $t\bar{t}$  sample with  $20 < p_T < 250$  GeV.

### 6.6.3 High Luminosity LHC

The model also demonstrates strong performance for the High Luminosity LHC (HL-LHC) using the proposed ITk inner tracking detector, as documented in Ref. [126]. Figs. 6.23 and 6.24 are reproduced from Ref. [126]. The results show that GN1 outperforms other existing flavour tagging algorithms when trained on an entirely different detector geometry, the ITk (see Section 3.3.1). When compared with

---

<sup>4</sup>Precision tracking refers to tracks reconstructed in the trigger using the same reconstruction algorithms as for the offline event reconstruction.

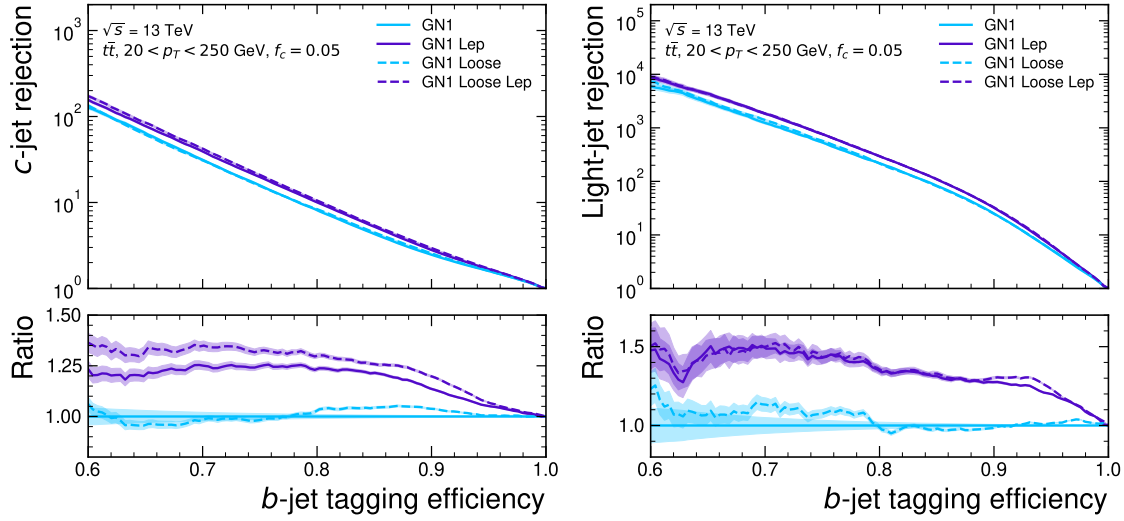


**Figure 6.20:** The  $c$ -jet (left) and light-jet (right) rejections as a function of the  $b$ -jet tagging efficiency for  $t\bar{t}$  jets with  $20 < p_T < 250$  GeV, for the looser track selection trainings of GN1. The ratio to the performance of the baseline GN1 model is shown in the bottom panels. A value of  $f_c = 0.05$  is used for all models. Binomial error bands are denoted by the shaded regions.

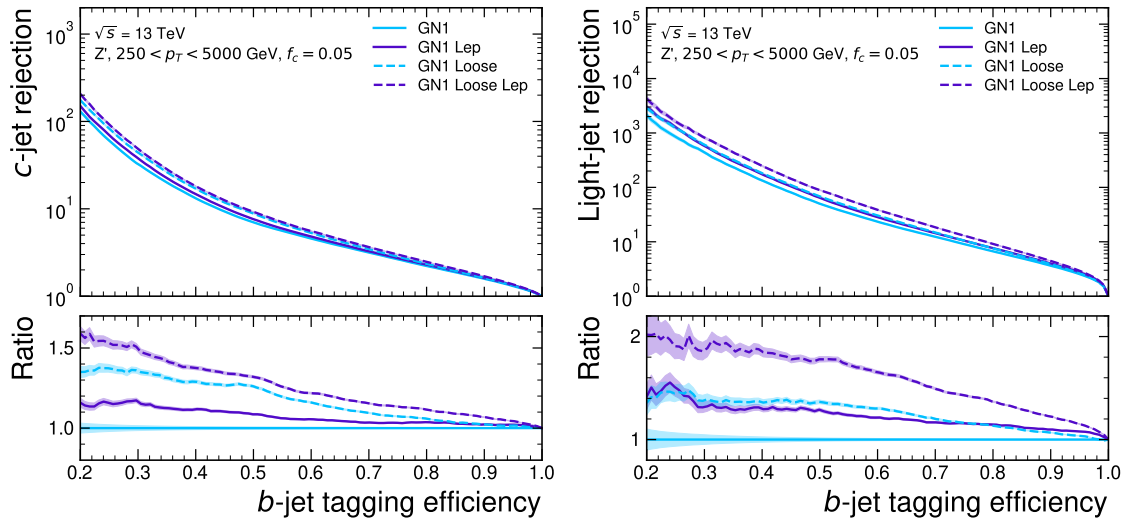


**Figure 6.21:** The  $c$ -jet (left) and light-jet (right) rejections as a function of the  $b$ -jet tagging efficiency for  $Z'$  jets with  $250 < p_T < 5000$  GeV, for the looser track selection trainings of GN1. The ratio to the performance of the baseline GN1 model is shown in the bottom panels. A value of  $f_c = 0.05$  is used for all models. Binomial error bands are denoted by the shaded regions.

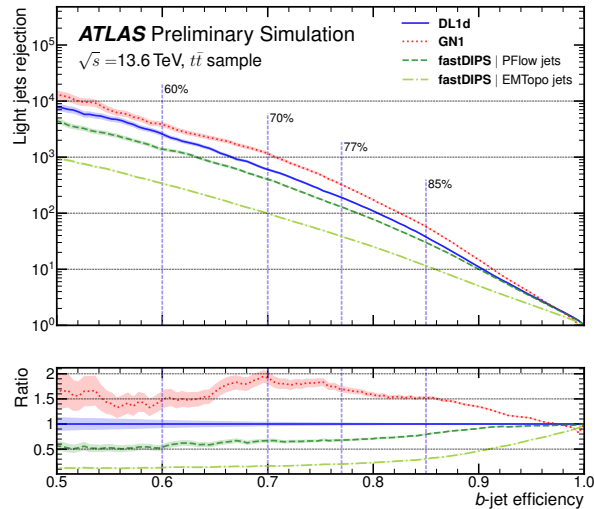


**Figure 6.22:** The HLT light-jet rejection as a function of the  $b$ -jet efficiency jets in the  $t\bar{t}$  sample with  $20 < p_T < 250 \text{ GeV}$  for events with a centre of mass energy  $\sqrt{s} = 13.6 \text{ TeV}$  [125]. The ratio to the performance of the DL1d algorithm [86] is shown in the bottom panels. Binomial error bands are denoted by the shaded regions. The purple vertical dashed lines represent the most common working points used for  $b$ -tagging.

1981 DL1d [86], GN1 improves on the  $c$ -jet rejection (light-jet rejection) by a factor of  $\sim 2$   
1982 ( $\sim 2.5$ ) for jets in the  $t\bar{t}$  sample at the 60%  $b$ -jet WP. Significant improvements in  
1983 rejections are also observed for jets in the  $Z'$  sample.

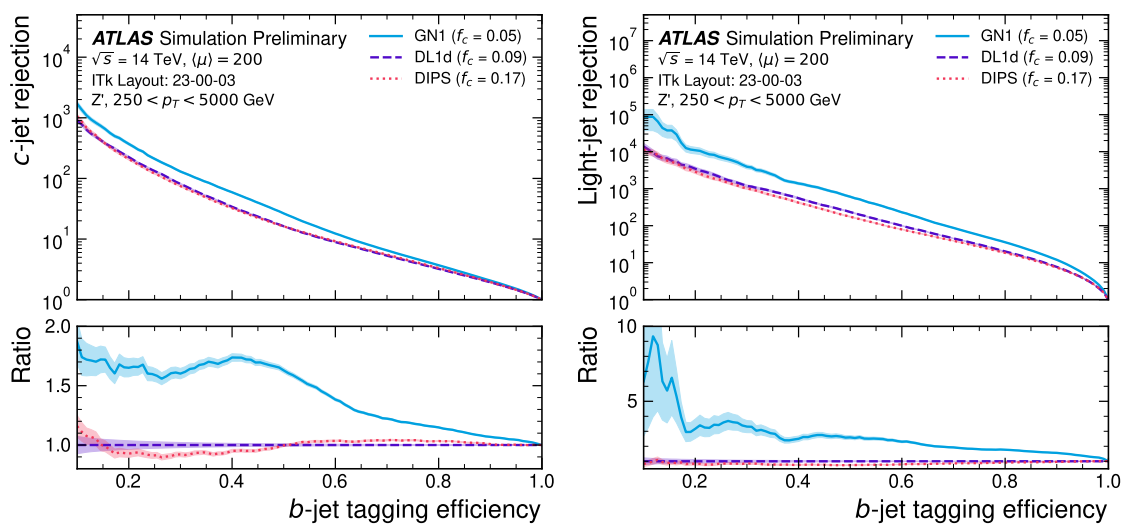
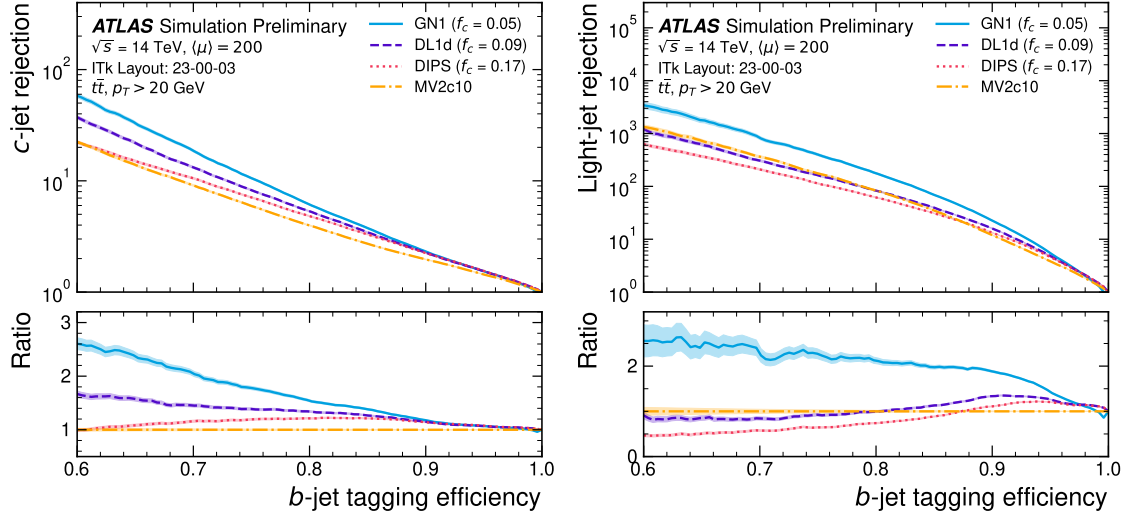
## 1984 6.7 Conclusion

1985 In this chapter a novel jet tagger, GN1, is presented. The model has a graph neural  
1986 network architecture and is trained with auxiliary training objectives, which are  
1987 shown to improve the performance of the basic model. GN1 significantly improves  
1988 flavour tagging performance with respect to DL1r, the current default ATLAS flavour  
1989 tagging algorithm, when compared in simulated collisions. GN1 improves  $c$ - and  
1990 light-jet rejection for jets in the  $t\bar{t}$  sample with  $20 < p_T < 250$  GeV by factors of  
1991  $\sim 2.1$  and  $\sim 1.8$  respectively at a  $b$ -jet tagging efficiency of 70% when compared with  
1992 DL1r. For jets in the  $Z'$  sample with  $250 < p_T < 5000$  GeV, GN1 improves the  
1993  $c$ -jet rejection by a factor of  $\sim 2.8$  and light-jet rejection by a factor of  $\sim 6$  for a  
1994 comparative  $b$ -jet efficiency of 30%.

1995 Previous multivariate flavour tagging algorithms relied on inputs from low-level  
1996 tagging algorithms, whereas GN1 needs no such inputs, making it more flexible.  
1997 It can be easily fully optimised via a retraining for specific flavour tagging use  
1998 cases, as demonstrated with  $c$ -tagging and high- $p_T$   $b$ -tagging, without the need for  
1999 time-consuming retuning of the low-level tagging algorithms. The model is also  
2000 simpler to maintain and study due to the reduction in the number of constituent  
2001 components.

2002 GN1 demonstrates improved track classification performance when compared with a  
2003 simple per-track MLP. The model is also able to perform vertex finding, and prelimi-  
2004 nary studies suggest it outperforms previous manually optimised approaches. The  
2005 auxiliary track classification and vertex finding objectives are shown to significantly  
2006 contribute to the performance in the jet classification objective, and, along with the  
2007 more advanced graph neural network architecture, are directly responsible for the  
2008 improvement over DL1r.

2009 GN1 has also been shown to perform well for  $b$ -tagging in the High Level Trigger,  
2010 and in the projected environment for the upgraded High Luminosity LHC. The



2011 performance of the model at high- $p_T$  can be improved by loosening the input track  
2012 selection, which increases the number of  $b$ -hadron decay tracks that are inputted to  
2013 the model.

2014 Preliminary validation of the model demonstrates that the level of discrepancy  
2015 between different Monte Carlo event generators is similar to that seen for previous  
2016 ATLAS ML based taggers such as DL1r, suggesting that the model has not learnt  
2017 additional information that is specific to a single event generator. Initial comparisons  
2018 between simulated events and data also show similar levels of agreement as for  
2019 previous taggers [127].

2020 **Future Work**

2021 Further improvements in the  $b$ - and  $c$ -tagging performance are likely possible with  
2022 a more thorough optimisation of the model architecture, and the integration of  
2023 additional information from other parts of the ATLAS detector. The addition of  
2024 other auxiliary training objectives, such as the prediction of the truth  $b$ -hadron decay  
2025 radius and transverse momentum and the truth type of input tracks may also yield  
2026 additional performance gains.

2027 Although the results demonstrate a significant performance improvement at high- $p_T$ ,  
2028 it is also possible that additional studies on further loosening the selection could yield  
2029 further improved results. For example the selections on the number of number of  
2030 holes and the longitudinal impact parameter could be further relaxed. The maximum  
2031 number of tracks provided as input to the model could also be increased from the  
2032 default value of 40. In order to validate the change from the default tracking setup,  
2033 studies investigating the modelling uncertainties of the additional tracks need to be  
2034 carried out.

2035 Given that GN1 exploits the input information in a more sophisticated way than  
2036 DL1r, further studies are needed to confirm that the performance gain observed in  
2037 these simulated samples is also observed in experimental data. Additional future  
2038 work includes the full calibration of the model so it can be used by physics analyses.

2039 The flexible nature of the model means it can also be readily applied to other related  
2040 problems outside of standard  $b$ - and  $c$ -tagging applications, as demonstrated in  
2041 Section 6.6. Additional applications for the architecture include  $X \rightarrow bb$  and  $X \rightarrow cc$

2042 tagging. The model could also be repurposed as a pile-up jet or  $\tau$  tagger, or general  
2043 primary and secondary vertexing tool. Using a vertex fitting algorithm to compare  
2044 the reconstructed vertex quantities with those from SV1 and JetFitter is left for  
2045 future work.

2046 Chapter 7

2047 Boosted VHbb Analysis

2048 The Higgs boson, first observed by ATLAS and CMS at the LHC in 2012 [14, 15],  
2049 is predicted by the Standard Model to decay primarily to a pair of  $b$ -quarks, with  
2050 a branching fraction of  $0.582 \pm 0.007$  for  $m_H = 125$  GeV [26]. Observation of this  
2051 decay mode was reported by ATLAS [79] and CMS [28] in 2018, establishing the  
2052 first direct evidence for the Yukawa coupling of the Higgs boson to down-type quarks  
2053 (see Section 2.2.2). The  $H \rightarrow b\bar{b}$  process is also important for constraining the total  
2054 decay width of the Higgs [128].

2055 Whilst the dominant Higgs production mechanism at the LHC is gluon-gluon fusion  
2056 as outlined in Section 2.2.3, this mechanism has an overwhelming QCD multijet  
2057 background and so overall sensitivity to the Higgs is low. The QCD multijet  
2058 background refers to events containing one or more strongly produced jets which  
2059 are not the decay product of heavy resonances, for example  $g \rightarrow q\bar{q}$ . In the  $H \rightarrow b\bar{b}$   
2060 gluon-gluon fusion channel the vast majority of events will contain only jets in the  
2061 final state, and therefore it is extremely difficult to distinguish signal events from the  
2062 overwhelming multijet background. The  $H \rightarrow b\bar{b}$  observation therefore searched for  
2063 Higgs bosons produced in association with a vector boson  $V$  (where  $V$  can be a  $W$   
2064 or  $Z$  boson) which subsequently decays leptonically. The leptonic final states allow  
2065 for leptonic triggering whilst at the same time significantly reducing the multijet  
2066 background.

2067 Two full Run 2 dataset analyses were carried out as a follow-up to the  $H \rightarrow b\bar{b}$   
2068 observation [79]. Similar to the observation, both measured the associated production  
2069 of a Higgs with a vector boson, with the Higgs boson decaying to a pair of  $b$ -quarks.  
2070 The first analysis [129] was focussed on the resolved phase-space, where the Higgs

2071 candidate is reconstructed as two distinct jets with radius parameter  $R = 0.4$ .  
2072 The second analysis [130] was focussed on the boosted phase-space, where the  
2073 Higgs candidate had a sufficiently large transverse momenta such that it can be  
2074 reconstructed as a single jet with a radius parameter of  $R = 1.0$ . This chapter  
2075 will focus on the latter analysis, which is referred to as the boosted  $VH$ ,  $H \rightarrow b\bar{b}$   
2076 analysis.

2077 In this chapter, the boosted  $VH$ ,  $H \rightarrow b\bar{b}$  analysis is outlined in Section 7.1. An  
2078 introduction to the systematic uncertainties used in the analysis is provided in  
2079 Section 7.1.6. Detailed information about the modelling studies performed for  
2080 the analysis are described in Section 7.3. The statistical treatment is detailed in  
2081 Section 7.4, and the results of the analysis are presented in Section 7.5. This analysis  
2082 has been published in Ref. [130]. Figures and tables from the published work are  
2083 reproduced here.

## 2084 7.1 Analysis Overview

2085 The boosted  $VH$ ,  $H \rightarrow b\bar{b}$  analysis is focused on the high transverse momentum  
2086 regime, which has the benefit of being more sensitive to physics beyond the Standard  
2087 Model [131], but the disadvantage of being more challenging due to the increased  
2088 difficulty in the accurate reconstruction of high transverse momentum physics objects  
2089 (discussed in Chapter 4). In order to focus on the high- $p_T$  regime, the reconstructed  
2090 vector boson  $p_T^V$  is required to be  $p_T^V > 250$  GeV (see Section 7.1.1). Events are  
2091 also split into two  $p_T$  bins with the first bin covering  $250 \text{ GeV} < p_T^V < 400 \text{ GeV}$  and  
2092 the second covering  $p_T^V > 400$  GeV, which allows the analysis to benefit from the  
2093 improved signal-to-background in the high- $p_T$  regime.

2094 The previous ATLAS analysis in Ref. [79] was primarily sensitive to vector bosons  
2095 with a more modest  $p_T^V$  boost in the region of 150–300 GeV (for the 0- and 1-lepton  
2096 channels) and 75–300 GeV (for the 2-lepton channel). In this regime, the Higgs  
2097 candidate was reconstructed using a pair of jets with radius parameter of  $R = 0.4$ ,  
2098 called small- $R$  jets. However in the high- $p_T$  regime, the decay products of the Higgs  
2099 boson become increasingly collimated and the small- $R$  jets may not be individually  
2100 resolved. In order to enhance the reconstruction of the Higgs boson candidate, this  
2101 analysis uses a large- $R$  jet with radius parameter  $R = 1.0$  to reconstruct the Higgs

2102 boson candidate. The Higgs candidate is required to have exactly two ghost-associated  
2103 and  $b$ -tagged variable-radius track-jets ( $b$ -track-jets). The candidate large- $R$  jet is  
2104 reconstructed using jet substructure techniques, in particular it is trimmed by  
2105 removing soft and wide-angle components, which helps to remove particles from the  
2106 underlying event and pile-up collisions [132]. Refer to Section 3.4.3 for more details  
2107 on jet reconstruction.

2108 On top of the binning in  $p_T^V$ , selected events are further categorised into the 0-, 1-  
2109 and 2-lepton channels depending on the number of charged leptons (electrons and  
2110 muons) present in the reconstructed final state (also referred to as the 0L, 1L, and 2L  
2111 channels respectively). The 0-lepton channel targets the  $ZH \rightarrow \nu\nu b\bar{b}$  process, the  
2112 1-lepton channel targets  $WH \rightarrow \ell\nu b\bar{b}$ , and the 2-lepton channel targets  $ZH \rightarrow \ell\ell b\bar{b}$ ,  
2113 where  $\ell$  is an electron or muon and  $\nu$  is a neutrino. Each channel has a dedicated  
2114 set of selections which are listed in more detail in Section 7.1.2. Events in the 0- and  
2115 1-lepton channels are further split depending on the number of additional small- $R$   
2116 jets not matched to the Higgs candidate. The high-purity signal region (HP SR)  
2117 has zero such jets, while the low-purity signal region (LP SR) has one or more, and  
2118 therefore absorbs a larger number of background  $t\bar{t}$  events. Maintaining a high purity  
2119 signal region is important for the extraction of the signal yield. The 0- and 1-lepton  
2120 channels also make use of a dedicated  $t\bar{t}$  control region for jets with one or more  
2121 additional  $b$ -tagged small- $R$  jets, described in Section 7.1.3. A complete overview of  
2122 the different analysis regions is given in Table 7.1.

2123 The large- $R$  jet mass is used as the main discriminant in the analysis. The signal  
2124  $VH$ ,  $H \rightarrow b\bar{b}$  yields is extracted from a profile likelihood fit to the large- $R$  jet mass  
2125 over several signal and control analysis regions, which are described in Sections 7.1.2  
2126 and 7.1.3. The diboson background  $VZ$ ,  $Z \rightarrow b\bar{b}$  yield is simultaneously extracted  
2127 from the fit, and provides a cross check on the signal extraction. The fit model  
2128 (described henceforth only as “the fit”) is described in more detail in described in  
2129 Section 7.4.

### 2130 7.1.1 Object Reconstruction

2131 The presence of neutrinos in the  $WH \rightarrow \ell\nu b\bar{b}$  and  $ZH \rightarrow \ell\ell b\bar{b}$  signatures can be  
2132 inferred from a momentum imbalance in the transverse plane (see Section 3.4.5). The

		Analysis Regions					
		250 < $p_T^V$ < 400 GeV			$p_T^V \geq 400$ GeV		
Channel	0 add. $b$ -track-jets		$\geq 1$ add. $b$ -track-jets	0 add. $b$ -track-jets		$\geq 1$ add. $b$ -track-jets	
	0 add. small- $R$ jets	$\geq 1$ add. small- $R$ jets		0 add. small- $R$ jets	$\geq 1$ add. small- $R$ jets		
0-lepton	HP SR	LP SR	CR	HP SR	LP SR	CR	
1-lepton	HP SR	LP SR	CR	HP SR	LP SR	CR	
2-lepton	SR			SR			

**Table 7.1:** Summary of the definitions of the different analysis regions . Signal enriched regions are marked with the label SR. There are regions with relatively large signal purity (HP SR) and with low purity (LP SR). Background enriched control regions are marked with the label CR. The shorthand “add” stands for additional small- $R$  jets, i.e. number of small- $R$  jets not matched to the Higgs-jet candidate. The medium and high  $p_T^V$  regions are referred to as  $Mp_T^V$  and  $Hp_T^V$ , respectively [130].

2133 vector boson transverse momentum  $p_T^V$  is reconstructed as the missing transverse  
 2134 energy  $E_T^{\text{miss}}$  in the 0-lepton channel, as the magnitude of the summed  $\mathbf{E}_T^{\text{miss}}$  and  
 2135 charged-lepton momentum in the 1-lepton channel, and as the transverse momentum  
 2136 of the 2-lepton system in the 2-lepton channel.

2137 Electrons and muons are reconstructed and identified as outlined in Section 3.4.4,  
 2138 and following the approach described in Ref. [79]. Leptons are required to satisfy  
 2139 the selections listed in Table 7.2. *Baseline* electrons are required to pass the looser  
 2140 likelihood-based identification selection described in Section 3.4.4, whilst *Signal*  
 2141 electrons are required to satisfy a tighter likelihood identification selection. *Baseline*  
 2142 muons are required to pass the ‘loose’ identification described in Ref. [51], while  
 2143 *signal* muons are required to pass the ‘medium’ identification working point. All  
 2144 signal leptons are required to additionally satisfy a  $p_T > 27$  GeV selection criteria,  
 2145 except for muons in the 1-lepton channel where a cut of 25 GeV is used. The number  
 2146 of baseline leptons is used to categorise the event into the 0-, 1- or 2-lepton channels.  
 2147 The 1- and 2-lepton channels additionally require one signal lepton to be present.

2148 The analysis makes use of large- $R$  and variable-radius small- $R$  track-jets, which are  
 2149 described in Section 3.4.3. The large- $R$  jets are required to satisfy  $p_T > 250$  GeV and  
 2150  $|\eta| < 2.0$ , and are used to reconstruct the Higgs boson candidate, while small- $R$  jets  
 2151 are used for  $b$ -tagging and for selection of the analysis region. These track-jets are

Variable	Electrons	Muons
$p_T$	$> 7 \text{ GeV}$	
$ \eta $	$< 2.47$	$< 2.7$
$s(d_0)$	$< 5$	$< 3$
$ z_0 \sin(\theta) $	$< 0.5 \text{ mm}$	

**Table 7.2:** Selections applied to baseline and signal electrons and muons. Signal leptons are additionally required to satisfy a  $p_T > 27 \text{ GeV}$  ( $25 \text{ GeV}$  in the 1-lepton channel).

required to have at least two constituent tracks with  $p_T > 500 \text{ MeV}$  and  $|\eta| < 2.5$ , and must themselves satisfy  $p_T > 10 \text{ GeV}$  and  $|\eta| < 2.5$ . The track-jets matched to the Higgs candidate are  $b$ -tagged using the MV2c10  $b$ -tagging algorithm (see Chapter 4). The efficiency of the tagging algorithm is calibrated to events in data [133–135]. The jet tagging strategy relies on extensive studies into track-jet  $b$ -tagging in boosted topologies [136, 137].

### 7.1.2 Event Selection

An extensive list of selection cuts are applied to each event in order to reject background events whilst retaining as many signal events as possible. A full list of selection cuts applied to the different analysis regions is given in Table 7.3, while some key selections are listed below.

All channels require events with at least one large- $R$  jet. The vector boson transverse momentum is also required to satisfy  $p_T^V > 250 \text{ GeV}$ . The Higgs candidate is chosen as the highest  $p_T$  large- $R$  jet satisfying these requirements. As mentioned, the candidate large- $R$  jet is required to have two ghost-associated and  $b$ -tagged variable-radius track-jets.

In the 0-lepton channel, trigger selections are applied using an  $E_T^{\text{miss}}$  trigger with a luminosity-dependent threshold that varied between 70–110 GeV depending on the data taking period. In the 1-lepton electron sub-channel a combination of single electron triggers is used with minimum  $p_T$  thresholds between 24–26 GeV. In the muon sub-channel the same  $E_T^{\text{miss}}$  trigger as the 0-lepton channel is used. Since muons are not used for the  $E_T^{\text{miss}}$  trigger calculations, this is in effect a  $p_T$  requirement on

2174 the muon-neutrino system, which in the analysis phase space is more efficient than a  
2175 single-muon trigger. The 2-lepton channel uses the same triggering strategy as the  
2176 1-lepton channel. In all channels, the trigger selections applied are fully efficient for  
2177 events selected using the full requirements in Table 7.3.

2178 The combined selections in Table 7.3 result in a signal efficiency ranging from 6–16%  
2179 for the  $WH$  and  $ZH$  processes depending on the channel and  $p_T^V$  bin.

### 2180 7.1.3 Control Regions

2181 The  $t\bar{t}$  process presents a major background in the 0- and 1-lepton channels. In these  
2182 events, the Higgs candidate is often reconstructed from a correctly tagged  $b$ -jet from  
2183 the top decay  $t \rightarrow Wb$ , and an incorrectly tagged  $c$ - or light-jet from the subsequent  
2184 decay of the  $W$ , as shown in Fig. 7.1.

2185 The top quark decays to a  $W$  and a  $b$ -quark the vast majority of the time. Hence,  
2186 the second top quark from the  $t\bar{t}$  pair is also likely to result in a second tagged  
2187  $b$ -tagged track-jet outside of the large- $R$  Higgs candidate. To ensure sufficient  $t\bar{t}$   
2188 rejection, 0- and 1-lepton channel signal regions are defined using a veto on events  
2189 with  $b$ -tagged track-jets outside the Higgs candidate. These events are used to  
2190 construct a control region (CR) which is enriched in  $t\bar{t}$  events. The CR is used to  
2191 constrain the normalisation of the  $t\bar{t}$  background in the fit.

### 2192 7.1.4 Background Composition

2193 After the selections described in Section 7.1.2 the number of background events  
2194 mimicking the  $VH$ ,  $H \rightarrow b\bar{b}$  signal is greatly reduced. However, the number of  
2195 background events still greatly outnumbers that of signal events. The background  
2196 processes are channel dependent. In the 0-lepton channel the dominant sources of  
2197 backgrounds are  $Z$ +jets ( $Z \rightarrow \nu\nu$ ) and  $t\bar{t}$ , with  $W$ +jets and diboson events being  
2198 subdominant.  $W$ +jets contribute in the event of  $W \rightarrow \tau\nu$ , and subsequent hadronic  
2199 decay of the  $\tau$  or lack of successful reconstruction/selection of the leptonic decay  
2200 products.  $t\bar{t}$  and  $W$ +jets (with a leptonic decay of the  $W$  as in  $W \rightarrow \ell\nu$ ) are  
2201 dominant in the 1-lepton channel, while single-top is subdominant. In the 2-lepton  
2202 channel,  $Z$ +jets ( $Z \rightarrow \ell\ell$ ) is again dominant followed by  $ZZ$  diboson events.

Selection	0 lepton channel	1 lepton channel	2 leptons channel
Trigger	$E_T^{\text{miss}}$	$e$ sub-channel $\mu$ sub-channel	$e$ sub-channel $\mu$ sub-channel
Leptons	0 <i>baseline</i> leptons	Single electron 1 <i>signal</i> lepton $p_T > 27 \text{ GeV}$	Single electron 2 <i>baseline</i> leptons among which $p_T > 25 \text{ GeV}$ no second <i>baseline</i> lepton $\geq 1$ <i>signal</i> lepton, $p_T > 27 \text{ GeV}$ both leptons of the same flavour -
$E_T^{\text{miss}}$	$> 250 \text{ GeV}$	$> 50 \text{ GeV}$	-
$p_T^V$		$p_T^V > 250 \text{ GeV}$	-
Large- $R$ jets		at least one large- $R$ jet, $p_T > 250 \text{ GeV},  \eta  < 2.0$	
Track-jets		at least two track-jets, $p_T > 10 \text{ GeV},  \eta  < 2.5$ , matched to the leading large- $R$ jet	
<i>b</i> -tagged jets		leading two track-jets matched to the leading large- $R$ must be <i>b</i> -tagged (MV2c10, 70%)	
$m_J$			$> 50 \text{ GeV}$
$\min[\Delta\phi(\mathbf{E}_T^{\text{miss}}, \text{small-}R \text{ jets})]$	$> 30^\circ$		-
$\Delta\phi(\mathbf{E}_T^{\text{miss}}, H_{\text{cand}})$	$> 120^\circ$		-
$\Delta\phi(\mathbf{E}_T^{\text{miss}}, \mathbf{E}_{T,\text{trk}}^{\text{miss}})$	$< 90^\circ$		-
$\Delta y(V, H_{\text{cand}})$	-		$ \Delta y(V, H_{\text{cand}})  < 1.4$
$m_{\ell\ell}$			$66 \text{ GeV} < m_{\ell\ell} < 116 \text{ GeV}$
Lepton $p_T$ imbalance			$(p_T^{\ell_1} - p_T^{\ell_2})/p_T^Z < 0.8$

**Table 7.3:** Event selection requirements for the boosted  $VH$ ,  $H \rightarrow b\bar{b}$  analysis channels and sub-channels [130]. Various channel dependent selections are used to maximise the signal efficiency and reduce the number of background events in each analysis region. The  $\min[\Delta\phi(\mathbf{E}_T^{\text{miss}}, \text{small-}R \text{ jets})]$  selection is used to remove jets when the missing transverse momentum  $\mathbf{E}_T^{\text{miss}}$  is pointing in the direction of the Higgs candidate, and the  $\Delta\phi(\mathbf{E}_T^{\text{miss}}, \mathbf{E}_{T,\text{trk}}^{\text{miss}})$  is used to reject events where the calorimeter missing transverse momentum  $\mathbf{E}_T^{\text{miss}}$  is not pointing in the direction of the track-based missing transverse momentum  $\mathbf{E}_{T,\text{trk}}^{\text{miss}}$ . The  $\Delta y(V, H_{\text{cand}})$  quantifies the rapidity difference between the reconstructed vector boson and Higgs candidate ( $H_{\text{cand}}$ ).  $m_{\ell\ell}$  refers to the invariant mass of the two leptons, while  $p_T^{\ell_1}$  and  $p_T^{\ell_2}$  refer to the  $p_T$  of the first and second leptons, respectively.

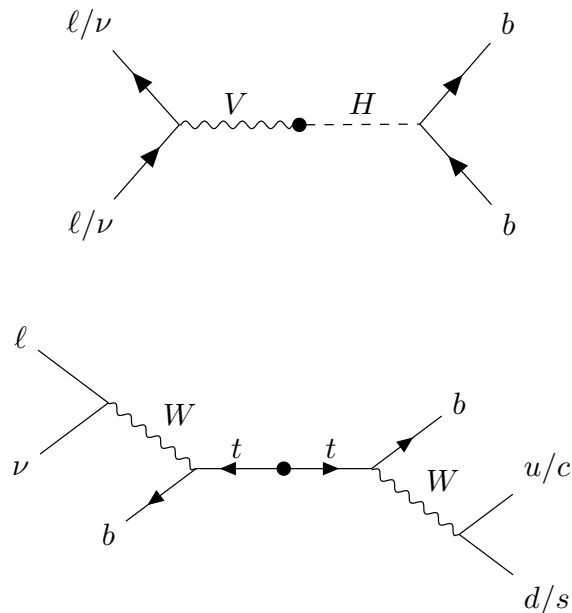


**Figure 7.1:** Diagrams of the signal process (top) and  $t\bar{t}$  background (bottom). The object to the right of centre are reconstructed within the large- $R$  jet. For the  $t\bar{t}$  background, the large- $R$  jet contains a mistagged  $c$ -jet or (less often) a mistagged light-jet. The contribution in the 0-lepton channel results from hadronically decaying  $\tau$  lepton, or a electron or muon which is out of the analysis acceptance. For the  $t\bar{t}$  background process to be in the signal region, the  $b$ -jet on the left hand side must either be not within acceptance, not reconstructed, or not tagged.

- 2203 The diboson background  $VV$  consists primarily of  $WZ$  and  $ZZ$  events in which the  
2204  $Z$  decays to a pair of  $b$ -quarks. This process very closely matches the signal, with a  
2205 resonant peak occurring at  $m_Z = 91 \text{ GeV}$ . As it is a well understood process, the  
2206 diboson background can be used as a cross-check on the Higgs results.
- 2207 The  $t\bar{t}V$ ,  $t\bar{t}H$  and multijet backgrounds are negligible in the analysis phase space  
2208 after the selections have been applied, with the exception of the 1-lepton electron  
2209 sub-channel, in which multijet background is not negligible. The multijet background  
2210 in this region is generally made up of events where the isolated leptonic signature  
2211 has been mimicked by either a jet or electron from a semi-leptonic heavy flavour  
2212 decay, where the electron has escaped the jet.
- 2213 The contributions from the different backgrounds are modelled using Monte Carlo  
2214 event generators and the uncertainties associated with these samples are studied in  
2215 Section 7.3. The multijet background is modelled using a data-driven technique.

### 2216 7.1.5 Data & Simulated Samples

- 2217 Data from centre-of-mass energy  $\sqrt{s} = 13 \text{ TeV}$  proton-proton collisions at the LHC  
2218 recorded over the course of Run 2 (between 2015 and 2018) were used for the analysis.  
2219 The resulting dataset corresponds to a total integrated luminosity of  $139 \text{ fb}^{-1}$ .
- 2220 An overview of the MC simulated samples used in the analysis is given in Table 7.4.  
2221 These samples are used to model the signal and background processes relevant to the  
2222 analysis, with the exception of the multijet background which is modelled using a  
2223 data-driven technique. Data and simulated events are reconstructed using the same  
2224 algorithms, and a reweighting is applied to the simulated events in order to match  
2225 the pile-up distribution observed in the data.

### 2226 7.1.6 Overview of Systematic Uncertainties

- 2227 Systemic uncertainties are extensively employed to reflect assumptions and inaccura-  
2228 cies in the various inputs used by the fit. Two main types of systematic uncertainty  
2229 are considered: experimental and modelling. Experimental uncertainties arise due  
2230 to the imperfect modelling of the reconstruction algorithms (in particular the jet  
2231 reconstruction and  $b$ -tagging algorithms), and due to the imperfect modelling of

Process	ME generator	ME PDF	PS and Hadronisation	UE model tune	Cross-section order
Signal ( $m_H = 125$ GeV and $b\bar{b}$ branching fraction set to 58%)					
$qg \rightarrow W H \rightarrow \ell\nu b\bar{b}$	POWHEG-Box v2 [138] + GoSam [140] + MiNLO [141, 142]	NNPDF3.0NLO <sup>(*)</sup> [91]	PyTHIA 8.212 [93]	AZNLO	NNLO(QCD) + NLO(EW) [143–149]
$qq \rightarrow ZH \rightarrow \nu\nu b\bar{b}/\ell\ell b\bar{b}$	POWHEG-Box v2 + GoSAM + MiNLO	NNPDF3.0NLO <sup>(*)</sup>	PyTHIA 8.212	AZNLO	NNLO(QCD) <sup>(†)</sup> + NLO(EW)
$gg \rightarrow ZH \rightarrow \nu\nu b\bar{b}/\ell\ell b\bar{b}$	POWHEG-Box v2	NNPDF3.0NLO <sup>(*)</sup>	PyTHIA 8.212	AZNLO	NLO+ NLL [150–154]
Top quark ( $m_t = 172.5$ GeV)					
$t\bar{t}$	POWHEG-Box v2 [138, 155]	NNPDF3.0NLO	PyTHIA 8.230	A14 [94]	NNLO+NNLL [156]
$s$ -channel	POWHEG-Box v2 [138, 157]	NNPDF3.0NLO	PyTHIA 8.230	A14	NLO [158]
$t$ -channel	POWHEG-Box v2 [138, 157]	NNPDF3.0NLO	PyTHIA 8.230	A14	NLO [159]
$Wt$	POWHEG-Box v2 [138, 160]	NNPDF3.0NLO	PyTHIA 8.230	A14	Approximate NNLO [161]
Vector boson + jets					
$W \rightarrow \ell\nu$	SHERPA 2.2.1 [162–165]	NNPDF3.0NNLO	SHERPA 2.2.1 [166, 167]	Default	NNLO [168]
$Z/\gamma^* \rightarrow \ell\ell$	SHERPA 2.2.1	NNPDF3.0NNLO	SHERPA 2.2.1	Default	NNLO
$Z \rightarrow \nu\nu$	SHERPA 2.2.1	NNPDF3.0NNLO	SHERPA 2.2.1	Default	NNLO
Diboson					
$qq \rightarrow WW$	SHERPA 2.2.1	NNPDF3.0NNLO	SHERPA 2.2.1	Default	NLO
$qq \rightarrow WZ$	SHERPA 2.2.1	NNPDF3.0NNLO	SHERPA 2.2.1	Default	NLO
$qq \rightarrow ZZ$	SHERPA 2.2.1	NNPDF3.0NNLO	SHERPA 2.2.1	Default	NLO
$gg \rightarrow VV$	SHERPA 2.2.2	NNPDF3.0NNLO	SHERPA 2.2.2	Default	NLO

**Table 7.4:** Signal and background processes with the corresponding generators used for the nominal samples [130]. If not specified, the order of the cross-section calculation refers to the expansion in the strong coupling constant ( $\alpha_s$ ). <sup>(\*)</sup> The events were generated using the first PDF in the NNPDF3.0NLO set and subsequently reweighted to the PDF4LHC15NLO set [169] using the internal algorithm in POWHEG-BOX v2. <sup>(†)</sup> The NNLO(QCD)+NLO(EW) cross-section calculation for the  $pp \rightarrow ZH$  process already includes the  $gg \rightarrow ZH$  contribution. The  $qg \rightarrow ZH$  process is normalised using the cross-section for the  $pp \rightarrow ZH$  process, after subtracting the  $gg \rightarrow ZH$  contribution. An additional scale factor is applied to the  $qg \rightarrow VH$  processes as a function of the transverse momentum of the vector boson, to account for electroweak (EW) corrections at NLO. This makes use of the  $VH$  differential cross-section computed with HAWK [170, 171].

pile-up and other effects, as described in Section 7.2. Modelling uncertainties arise due to the imperfections in the Monte-Carlo generators used to model the signal and background events. In order to observe a certain process, for example  $VH$ ,  $H \rightarrow b\bar{b}$ , an increase in the number of observed events with respect to the background-only hypothesis is looked for. The excess is often relatively small against the total number of background events, and hence accurate modelling of the expected number of background and signal events is crucial for successfully performing the analysis.

## 7.2 Experimental Uncertainties

The main experimental uncertainties in the analysis are due to the modelling of following sources:

- The small- $R$  jet energy scale and resolution, which are informed by in situ calibration studies [69].
- The large- $R$  jet energy and mass scales and resolutions. The scales are calibrated as described in Ref. [73], and an uncertainty of 2% and 20% is applied for the jet energy and mass resolutions, respectively.
- $b$ -tagging uncertainties, which are computed separately for  $b$ -,  $c$ - and light-flavour jets as described in the data-based calibration studies in Refs. [133–135]. An additional extrapolation uncertainty is added to account for jets with transverse momenta above that which is accessible in the calibration analyses.
- Uncertainties associated with the lepton energy and momentum scales, and reconstruction and identification efficiencies.
- Uncertainty on the pile-up models which are used in the simulated samples, described in Ref. [172].
- Uncertainties associated with the reconstruction of the missing transverse energy  $E_T^{\text{miss}}$ , as described in Ref. [78].
- Uncertainty on the total recorded integrated luminosity, as described in Ref. [40].

The impact of these uncertainties on the analysis can be found in Table 7.18.

## 2259 7.3 Background Modelling Uncertainties

2260 Particular care is paid to the uncertainties on the modelling predictions as discussed  
2261 in the following sections. The *Nominal* MC samples are used as a reference to  
2262 which different variations can be compared. The nominal samples are chosen as the  
2263 best possible representation of the underlying physical process. *Alternative* samples  
2264 are used to understand inaccuracies that may be present in the nominal samples.  
2265 Some aspect of the nominal model is varied, and the discrepancy with respect to  
2266 the nominal model is quantified. The discrepancy is used to estimate a systematic  
2267 uncertainty associated with the model parameter which was varied. The alternate  
2268 samples are sometimes obtained via internal weight variations or parameterisation  
2269 methods, rather than by re-running the simulation. This is discussed in more detail  
2270 in Section 7.3.3.

2271 Modelling systematics can have several impacts, including affecting the overall  
2272 normalisation for different processes, the relative acceptances between different  
2273 analysis regions (i.e. migrations between HP and LP SRs, between the SR and  
2274 CR, and between  $p_T^V$  bins), and the shapes of the  $m_J$  distributions. For each  
2275 source of uncertainty, acceptance and shape uncertainties are therefore derived.  
2276 Acceptance uncertainties account for the uncertainty in the overall number of events  
2277 in each channel, and for the relative numbers of events in the various analysis  
2278 regions. Meanwhile, shape uncertainties account for the uncertainty on the kinematic  
2279 distributions of the events, but not overall normalisations. They are measured for  
2280 the shape of the large- $R$  jet mass distribution, since this is the variable used in the  
2281 fit to data.

2282 In this section, truth tagging, the method used to ensure sufficient numbers of jets  
2283 are available to calculate uncertainties, is described in Section 7.3.1. The different  
2284 sources of background modelling uncertainty which have been assessed are described  
2285 in Section 7.3.2, and details of their implementations are found in Section 7.3.3.  
2286 Full descriptions of the modelling uncertainties applied for the  $V+jets$  and diboson  
2287 backgrounds are given in Section 7.3.4 and Section 7.3.5, respectively.

### 2288 7.3.1 Truth Tagging

2289 Modelling studies involving  $c$ - and light-jets is hampered by the low number of events  
2290 available after the analysis selection is applied, due to the high rejection rates of the  
2291  $b$ -tagging algorithm MV2c10. For modelling studies, truth tagging (TT) is therefore  
2292 employed to ensure sufficient numbers of jets are available to calculate uncertainties.  
2293 TT works by computing a 2-dimensional efficiency map using the jet  $p_T$  and  $\eta$ . The  
2294 two leading track-jets associated to the large- $R$  jet are weighted based on their  
2295 probability to pass the  $b$ -tagging selection, rather than being required to explicitly  
2296 pass the  $b$ -tagging requirement. The probability to pass the  $b$ -tagging selection is  
2297 parameterised by the jet  $p_T$  and  $\eta$ , and is extracted using a pre-calculated efficiency  
2298 map.

### 2299 7.3.2 Sources of Systematic Modelling Uncertainties

2300 This section briefly describes the different sources of uncertainty in the analysis, and  
2301 how each is implemented.

#### 2302 QCD Scales

2303 The  $V+jets$  matrix element calculations contains infrared and ultraviolet divergences.  
2304 These are handled by introducing arbitrary parameters corresponding to the renormalisation scale ( $\mu_R$ ) and factorisation scale ( $\mu_F$ ). Physical observables are not  
2305 dependent on these parameters when using the infinite perturbation series expansion,  
2306 however at some fixed order in QCD a limited is present. To assess the impact of  
2307 this, both  $\mu_R$  and  $\mu_F$  are independently varied from their nominal values by factors  
2308 of 0.5 and 2 to account for higher order corrections to the calculation of the matrix  
2309 element used to simulate the process.

#### 2311 PDF Sets

2312 Parton distribution functions (PDFs) specify the probability of finding a parton with  
2313 a given momentum inside a hadron (in this case, colliding protons). PDFs have  
2314 to be derived from data and are a significant source of uncertainty in analyses of

hadronic collision data. There are three sources of PDF uncertainties: the statistical and systematic errors on the underlying data used to derive the PDFs, the theory which is used to describe them (which is based on some fixed order perturbative QCD expansion), and finally the procedure which is used to extract the PDFs from the data. PDF-related uncertainties were derived following Ref. [169]. This involves considering 100 PDF replicas which, when combined, form a central value and associated uncertainty, and also in parallel direct changes to the central values of PDFs using the MMHT2014 [173] and CT14NLO [174] PDF sets.

### Event Generator

The choice of parton shower (PS) and underlying event (UE) generators can affect the analysis outcome. Changing these models modifies several aspects of the event generation at the same time, such as the accuracy of matrix element predictions and different approaches to parton showering. This change tends to lead to the largest discrepancy with respect to the nominal samples.

### Resummation and Merging Scales

Resummation is a technique used in QCD to help cope with calculations involving disparate energy scales, and involves the introduction of an associated resummation scale, the choice of which introduces some systematic uncertainty into the model. Parton showering models are accurate when simulating low- $p_T$  radiation, however inaccuracies start to arrive when simulating hard emissions. To combat this, parton showering models utilise more precise matrix element calculations above some momentum threshold. The choice of threshold, or *merging scale* introduces some uncertainty into the final result. Resummation (QSF) and merging (CKKW) scale variations are available for a subset of the SHERPA samples. The number of available events is significantly lower than the number of events in the nominal sample, and no statistically significant discrepancy with respect to the nominal samples is observed. The corresponding uncertainties and therefore neglected.

### 7.3.3 Implementation of Variations

Modelling variations are implemented in various ways, depending on the associated uncertainty. Table 7.5 lists the different sources of uncertainty described in Section 7.3.2 and for each lists the implementation.

Source of Uncertainty	Implementation
Renormalisation scale ( $\mu_R$ )	Internal weights
Factorisation scale ( $\mu_F$ )	Internal weights
PDF set	Internal weights
Parton Shower (PS) models	Alternative samples
Underlying Event (UE) models	Alternative samples
Resummation scale (QSF)	Parameterisation
Merging scale (CKKW)	Parameterisation

**Table 7.5:** Different sources of uncertainty (i.e. variations in the model) considered for the  $V+jets$  background, and the corresponding implementation. For each uncertainty, acceptance and shape uncertainties are derived.

As production of large numbers of MC events is computationally expensive, a technique in state of the art simulation packages is to store some sources of variation as internal weights, which can be generated alongside the nominal samples, saving computation time. The nominal sample then effectively contains information about an ensemble of different samples, corresponding to different model parameters, which are accessible via reweightings.

While the inclusion of internal weight variation in some MC event generators has decreased simulation times and increased available statistics, there are currently some sources of systematic uncertainty that are unable to be stored as internal weight variations due to technical limitations in some of these generators. Two examples are the choice of resummation and merging scales. A method to parameterise the systematic variation using one sample, and to then apply this parameterisation to another sample, has been developed by ATLAS [175]. This method was used to derive resummation and merging uncertainties for the nominal SHERPA 2.2.1 sample, using a previous SHERPA 2.1 alternate sample. The resulting uncertainties were studied and found to be negligible in comparison with systematics from other sources.

### 7.3.4 Vector Boson + Jets Modelling

- After event selection, the  $V+jets$  background is a dominant background in all three analysis channels as described in Section 7.1.4. The  $V+jets$  samples are split into categories depending on the truth flavour of the track-jets which are ghost-associated to the large- $R$  jet Higgs candidate. The categories are  $V+bb$ ,  $V+bc$ ,  $V+bl$ ,  $V+cc$ ,  $V+cl$ ,  $V+ll$ , and  $V+hf$  refers collectively to the  $bb$ ,  $bc$ ,  $bl$ , and  $cc$  categories.  $V+bb$  is dominant generally accounting for 80% of the events, while  $V+hf$  accounts for around 90% of the events. The full flavour composition breakdown for each channel and analysis region are given in Tables 7.6, 7.8 and 7.9.
- The nominal MC event generator used for  $V+jets$  events is SHERPA 2.2.1, while MADGRAPH5\_AMC@NLO+PYTHIA8 (which uses a different parton showering model) is used as an alternative generator.

Sample	$Mp_T^V$ HP SR	$Hp_T^V$ HP SR	$Mp_T^V$ LP SR	$Hp_T^V$ LP SR	$Mp_T^V$ CR	$Hp_T^V$ CR
<b>Wbb</b>	$79.3\% \pm 4.4\%$	$75.0\% \pm 8.6\%$	$77.4\% \pm 2.5\%$	$71.7\% \pm 4.5\%$	$68.0\% \pm 7.6\%$	$63.5\% \pm 14.0\%$
<b>Wbc</b>	$6.6\% \pm 0.9\%$	$3.4\% \pm 1.7\%$	$6.2\% \pm 0.5\%$	$5.3\% \pm 0.9\%$	$14.5\% \pm 3.2\%$	$3.4\% \pm 3.2\%$
<b>Wbl</b>	$3.9\% \pm 0.9\%$	$11.4\% \pm 3.5\%$	$4.5\% \pm 0.5\%$	$8.7\% \pm 1.4\%$	$9.8\% \pm 2.2\%$	$9.1\% \pm 3.8\%$
<b>Wcc</b>	$5.1\% \pm 1.7\%$	$6.8\% \pm 2.4\%$	$7.1\% \pm 1.0\%$	$6.3\% \pm 1.4\%$	$4.2\% \pm 2.4\%$	$12.3\% \pm 7.0\%$
<b>Wcl</b>	$2.3\% \pm 1.4\%$	$2.4\% \pm 2.1\%$	$3.4\% \pm 0.7\%$	$5.2\% \pm 1.5\%$	$2.6\% \pm 1.5\%$	$3.4\% \pm 2.1\%$
<b>Wl</b>	$2.9\% \pm 1.0\%$	$0.9\% \pm 1.6\%$	$1.3\% \pm 0.7\%$	$2.8\% \pm 0.7\%$	$0.9\% \pm 0.6\%$	$8.4\% \pm 5.1\%$
Events	<b><math>187.5 \pm 7.7</math></b>	<b><math>38.2 \pm 3.1</math></b>	<b><math>429.5 \pm 10.0</math></b>	<b><math>97.8 \pm 4.2</math></b>	<b><math>33.8 \pm 2.5</math></b>	<b><math>8.3 \pm 1.2</math></b>

**Table 7.6:** 0-lepton  $W+jets$  nominal sample flavour composition and total event yield [176].  $Mp_T^V$  refers to the medium  $p_T^V$  region, and  $Hp_T^V$  refers to the high  $p_T^V$  region (see Table 7.1).

Sample	$Mp_T^V$ HP SR	$Hp_T^V$ HP SR	$Mp_T^V$ LP SR	$Hp_T^V$ LP SR	$Mp_T^V$ CR	$Hp_T^V$ CR
<b>Wbb</b>	$77.2\% \pm 2.6\%$	$72.4\% \pm 4.3\%$	$77.8\% \pm 1.8\%$	$69.3\% \pm 2.5\%$	$64.6\% \pm 4.9\%$	$53.5\% \pm 6.3\%$
<b>Wbc</b>	$7.4\% \pm 0.7\%$	$7.3\% \pm 1.1\%$	$6.6\% \pm 0.4\%$	$6.3\% \pm 0.6\%$	$13.7\% \pm 1.9\%$	$16.4\% \pm 3.7\%$
<b>Wbl</b>	$4.0\% \pm 0.5\%$	$6.7\% \pm 1.1\%$	$5.1\% \pm 0.3\%$	$8.7\% \pm 0.8\%$	$10.3\% \pm 1.7\%$	$14.6\% \pm 3.0\%$
<b>Wcc</b>	$6.2\% \pm 1.1\%$	$5.5\% \pm 1.7\%$	$6.6\% \pm 0.6\%$	$6.4\% \pm 0.7\%$	$4.5\% \pm 1.7\%$	$9.5\% \pm 3.0\%$
<b>Wcl</b>	$3.6\% \pm 0.8\%$	$4.2\% \pm 1.8\%$	$2.8\% \pm 0.5\%$	$6.2\% \pm 0.8\%$	$4.6\% \pm 1.2\%$	$4.4\% \pm 1.5\%$
<b>Wl</b>	$1.5\% \pm 0.5\%$	$3.9\% \pm 1.3\%$	$1.1\% \pm 0.2\%$	$3.1\% \pm 0.5\%$	$2.3\% \pm 1.2\%$	$1.6\% \pm 0.6\%$
Events	<b><math>477.1 \pm 11.7</math></b>	<b><math>147.5 \pm 6.4</math></b>	<b><math>784.7 \pm 12.3</math></b>	<b><math>301.8 \pm 7.2</math></b>	<b><math>68.7 \pm 3.5</math></b>	<b><math>26.9 \pm 2.0</math></b>

**Table 7.7:** 1-lepton  $W+jets$  nominal sample flavour composition and total event yield [176].  $Mp_T^V$  refers to the medium  $p_T^V$  region, and  $Hp_T^V$  refers to the high  $p_T^V$  region (see Table 7.1).

Channel	$Mp_T^V$ HP SR	$Hp_T^V$ HP SR	$Mp_T^V$ LP SR	$Hp_T^V$ LP SR	$Mp_T^V$ CR	$Hp_T^V$ CR
<b>Zbb</b>	84.56%	81.84%	82.37%	76.06%	66.12%	63.18%
<b>Zbc</b>	6.03%	6.98%	5.80%	7.46%	15.04%	14.30%
<b>Zbl</b>	4.06%	6.55%	3.83%	6.59%	12.66%	12.81%
<b>Zcc</b>	3.68%	3.40%	5.82%	3.75%	3.36%	3.38%
<b>Zcl</b>	1.23%	0.44%	1.47%	3.97%	1.82%	4.95%
<b>Zl</b>	0.44%	0.78%	0.70%	2.16%	1.00%	1.38%
Events	$259.91 \pm 4.86$	$66.12 \pm 2.04$	$420.45 \pm 5.73$	$141.97 \pm 2.50$	$43.49 \pm 1.73$	$16.07 \pm 0.83$

**Table 7.8:** 0-lepton  $Z+jets$  nominal sample flavour composition and total event yield [176].  $Mp_T^V$  refers to the medium  $p_T^V$  region, and  $Hp_T^V$  refers to the high  $p_T^V$  region (see Table 7.1).

Channel	$Mp_T^V$	$Hp_T^V$	$p_T^V$ inclusive
<b>Zbb</b>	80.80%	76.95%	79.76%
<b>Zbc</b>	8.10%	6.26%	7.60%
<b>Zbl</b>	4.95%	7.06%	5.52%
<b>Zcc</b>	3.97%	4.46%	4.10%
<b>Zcl</b>	1.61%	3.60%	2.14%
<b>Zll</b>	0.57%	1.68%	0.87%
Events	$115.49 \pm 2.42$	$42.42 \pm 1.27$	$157.92 \pm 2.73$

**Table 7.9:** 2-lepton  $Z+jets$  nominal sample flavour composition and total event yield [176].  $Mp_T^V$  refers to the medium  $p_T^V$  region, and  $Hp_T^V$  refers to the high  $p_T^V$  region (see Table 7.1).

## <sup>2374</sup> $V+jets$ Acceptance Uncertainties

<sup>2375</sup> Several different types of acceptance uncertainties have been calculated and im-  
<sup>2376</sup> plemented as nuisance parameters in the fit. These account for the uncertainty  
<sup>2377</sup> in the overall number of events in each channel, and for the migration of events  
<sup>2378</sup> between different analysis regions. The acceptance uncertainties relevant to the  
<sup>2379</sup>  $V+jets$  processes are summarised below.

- <sup>2380</sup> • **Overall normalisation:** only relevant where normalisation cannot be left  
<sup>2381</sup> unconstrained (or “floating”, i.e. determined as part of the fit). The  $V+hf$   
<sup>2382</sup> component is left floating in the fit, with independent normalisations used for  
<sup>2383</sup>  $W+hf$  and  $Z+hf$ . The normalisations are mainly determined by the 1-lepton  
<sup>2384</sup> (for  $W+hf$ ) and 2-lepton (for  $Z+hf$ ) regions respectively and then extrapolated  
<sup>2385</sup> to the 0-lepton channel. The negligible  $V+jets$  backgrounds were constrained to  
<sup>2386</sup> their cross-sections in the fit.
- <sup>2387</sup> • **SR-to-CR relative acceptance:** the uncertainty on the relative number of  
<sup>2388</sup>  $V+jets$  events in the signal and control regions.
- <sup>2389</sup> • **HP-to-LP relative acceptance:** the uncertainty on the relative number of  
<sup>2390</sup>  $V+jets$  events in the HP and LP SRs.
- <sup>2391</sup> • **Medium-to-high  $p_T^V$  relative acceptance:** the uncertainty on the relative  
<sup>2392</sup> number of  $V+jets$  events in the medium and high  $p_T^V$  bins.
- <sup>2393</sup> • **Flavour relative acceptance:** for each flavour  $V+xx$ , where  $xx \in \{bc, bl, cc\}$   
<sup>2394</sup> the ratio of  $V+xx/V+bb$  events is calculated. This corresponds to the uncer-  
<sup>2395</sup> tainty on the heavy flavour composition of the  $V+hf$  background.
- <sup>2396</sup> • **Channel relative acceptance:** the uncertainty on the relative number of  
<sup>2397</sup>  $V+jets$  events between the channels.

<sup>2398</sup> The uncertainties arising from the different sources described in Section 7.3.2 are  
<sup>2399</sup> summed in quadrature to give a total uncertainty on each region. A summary of  
<sup>2400</sup> the different acceptance uncertainties that were derived and subsequently applied  
<sup>2401</sup> in the fit are given in Table 7.10. An effort has been made, wherever possible, to  
<sup>2402</sup> harmonise similar uncertainties across different analysis regions and channels.

V+jets Acceptance Uncertainties				
Boson	W		Z	
Channel	0L	1L	0L	2L
SR-to-CR	90% <sup>†</sup>	40% <sup>†</sup>	40%	-
HP-to-LP SR	18%		18%	-
Medium-to-high $p_T^V$	30%	10%*	10%	
Channel relative acceptance	20%	-	16%	-
Vbc/Vbb	30%			
Vbl/Vbb	30%			
Vcc/Vbb	20%			
Vcl Norm.	30%			
VI Norm.	30%			

**Table 7.10:**  $V$ +jets acceptance uncertainties.  $W$ +jets SR and CR uncertainties marked with a superscript  $\dagger$  are correlated. The 1L  $W$ +jets medium-to-high  $p_T^V$  uncertainty marked by \* is applied as independent and uncorrelated NPs in both HP and LP signal regions [176].

### 2403 $V$ +jets Shape Uncertainties

2404 In order to derive shape uncertainties for a given background or signal process,  
 2405 normalised distributions of the reconstructed large- $R$  Higgs candidate jet mass  $m_J$   
 2406 are compared for the nominal sample and variations. For each variation, the ratio of  
 2407 the variation to nominal is calculated, the up and down variations are symmetrised,  
 2408 and an analytic function is used to parameterise the ratio. If different analysis regions  
 2409 or channels show the same pattern of variation, a common uncertainty is assigned.

2410 An example of a significant source of uncertainty, arising from the choice of factorisa-  
 2411 tion scale  $\mu_R$  is shown in Fig. 7.2. The HP SRs in the medium and high  $p_T^V$  bins are  
 2412 shown for the 0-lepton channel for the  $W$ +hf and  $Z$ +hf jet backgrounds. The 0- and  
 2413 1-lepton channels for the  $W$ +hf contribution and the 0- and 2-lepton channels for  
 2414 the  $Z$ +jets contribution were found to have compatible shapes in  $m_J$ , and so were  
 2415 jointly measured. An exponential function  $e^{p_0 + p_1 x} + p_2$  has been fitted to the ratio of  
 2416 the normalised distributions. The magnitude of the variation is  $p_T^V$  dependent, and  
 2417 so separate uncertainties are implemented in the fit for each  $p_T^V$  region.

2418 The shape uncertainties for  $\mu_R$  were derived on the SRs but are also applied to the  
 2419 CRs, as the low statistics in the CRs make it difficult to derive dedicated shape  
 2420 uncertainties. All the shape uncertainties are fully correlated across regions.

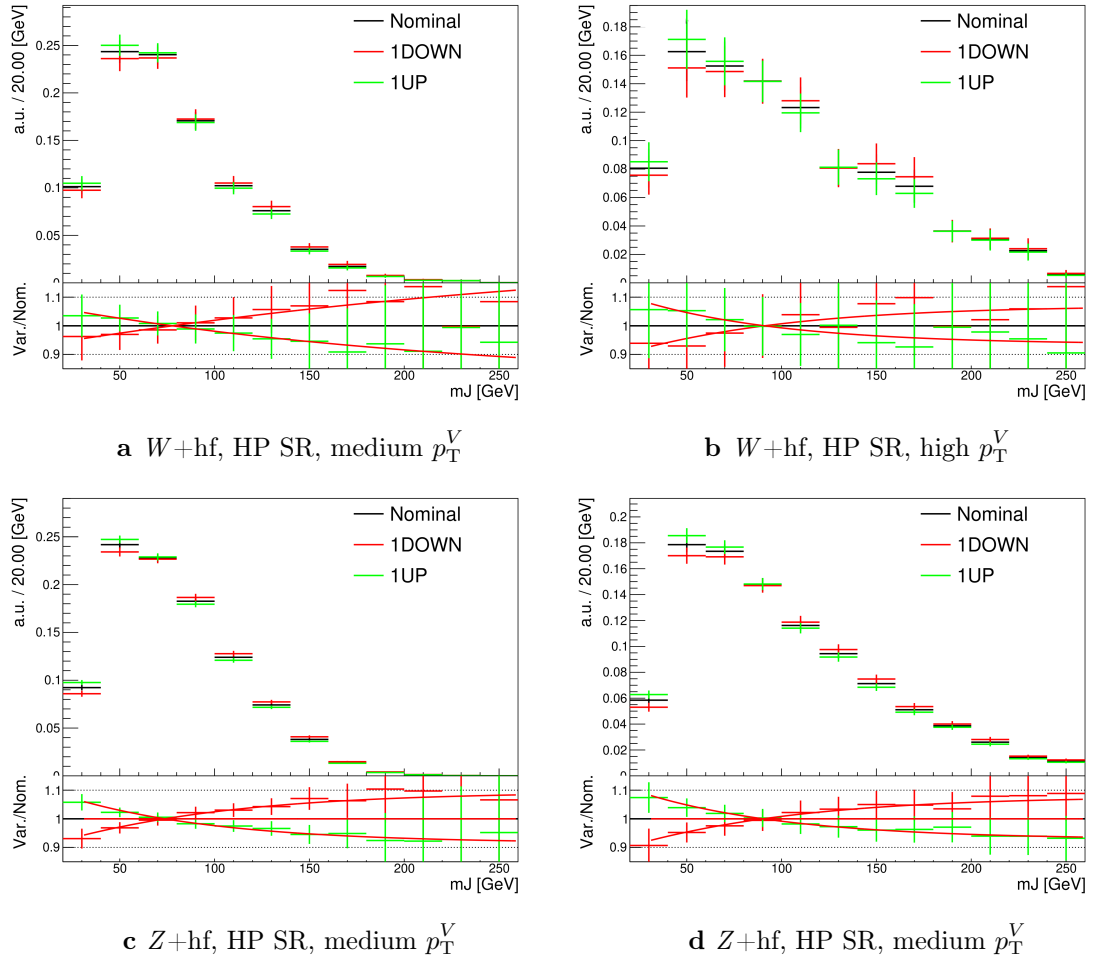


**Figure 7.2:** Leading large- $R$  jet mass for the  $Z$  and  $W+\text{hf}$  processes in the HP SR of the 0-lepton channel [176]. The renormalisation scale  $\mu_r$  has been varied by a factor of 0.5 (1DOWN) and 2 (1UP). An exponential function is fitted to the ratio between the nominal and alternate samples.

As an example where no significant deviation is seen, a comparison of the  $m_J$  shapes between SHERPA and MADGRAPH is shown in Fig. 7.3. The plots are split by process and channel, but merged in SR and  $p_T^V$  bins reflecting similarities between the  $m_J$  shapes and variations. Due to the lack of statistically significant variation between the samples, no additional shape uncertainty was added to the fit in this case.

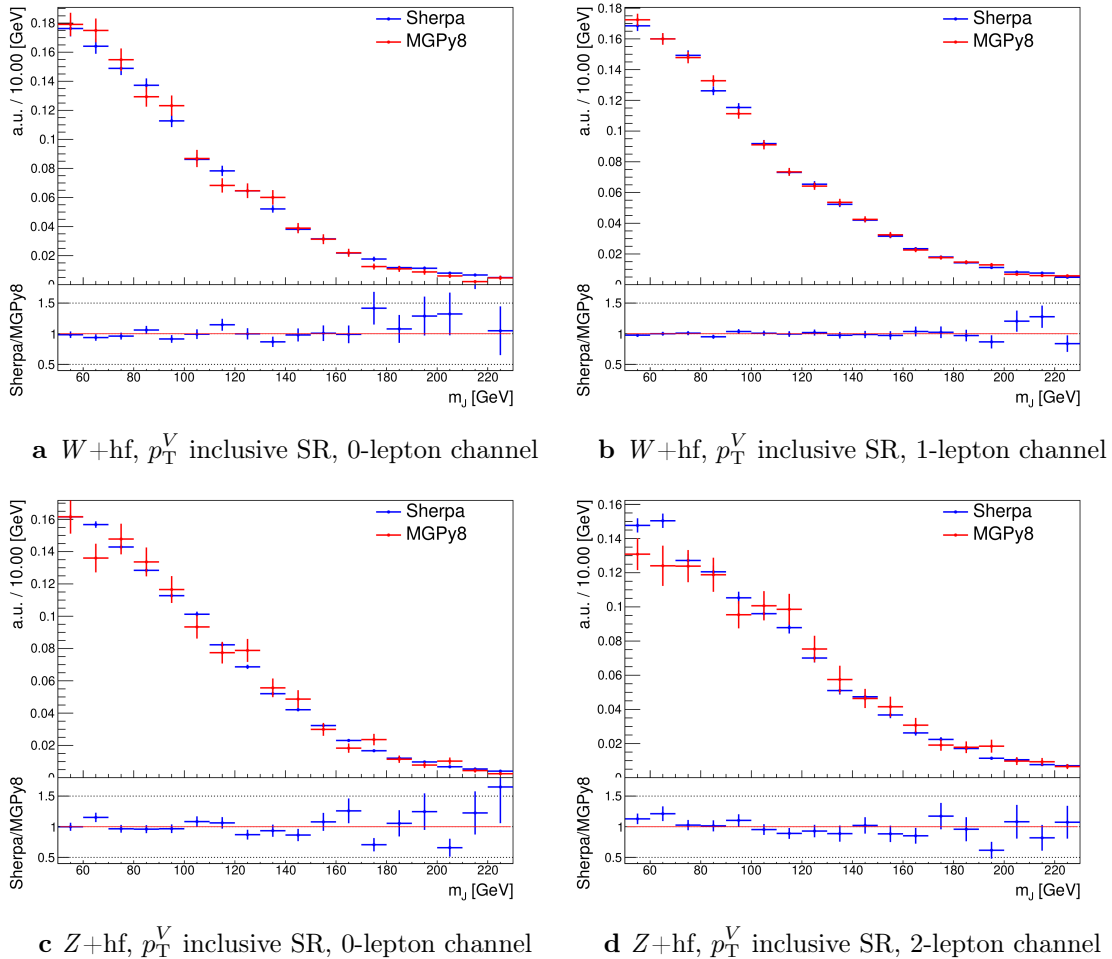


**Figure 7.3:** Leading large- $R$  jet  $m_J$  inclusive in  $p_T^V$  for the  $V+hf$  process modelled using both the SHERPA +PYTHIA8 (blue) and MADGRAPH +PYTHIA8 (red) samples [176].

The impacts of variations in the factorisation scale  $\mu_F$  and the choice of PDF set on  $m_J$  shape were also found to be negligible in comparison with  $\mu_R$  and are hence no additional uncertainty was added to the fit.

### **2429 7.3.5 Diboson Modelling**

**2430** The procedure to derive the uncertainties for the diboson background generally  
**2431** follows that of  $V+jets$ .

**2432** The nominal diboson samples are generated using SHERPA 2.2.1 (except for  $gg \rightarrow VV$   
**2433** which uses SHERPA 2.2.2) with the NNPDF3.0NNLO tune. alternate samples were  
**2434** generated using POWHEG interfaced with PYTHIA8, using the AZNLO shower tune  
**2435** with the CTEQ6L1 PDFs [177]. Unlike SHERPA, POWHEG models the off-shell  $Z$   
**2436** contribution at NLO.

**2437** Acceptance and shape uncertainties are derived in an analogous fashion to  $V+jets$   
**2438** as described below.

### **2439 Diboson Acceptance Uncertainties**

**2440** Diboson acceptance uncertainties are summarised in Table 7.11. Variations from  
**2441**  $\mu_R$ ,  $\mu_F$ , PDF choice and an alternative generator are considered and are combined  
**2442** via a sum in quadrature as described in Section 7.3.4. The largest modification to  
**2443** the nominal acceptance is from the POWHEG+PYTHIA8 alternate sample. Since  
**2444** the diboson contribution to the  $t\bar{t}$  control region is negligible, no SR-to-CR relative  
**2445** acceptance uncertainty is necessary.

**2446** For the  $WZ$  contribution, uncertainties are derived using the 1-lepton channel  
**2447** and applied to all three channels. The 1-lepton channel was used as it has the  
**2448** largest amount of available statistics, with the compatibility checked between the  
**2449** derived uncertainties and the other channels. An additional 8% channel migration  
**2450** uncertainty is applied on the  $WZ$  0-lepton channel. For the  $ZZ$  contribution, the  
**2451** normalisation uncertainty is calculated using the 2-lepton channel and applied to all  
**2452** three channels. The 0- and 1-lepton channels were found to have a similar HP-to-LP  
**2453** relative acceptance uncertainty of 18%. The 1-lepton medium-to-high  $p_T^V$  relative  
**2454** acceptance is estimated using the 2-lepton channel, since the 1-lepton channel had  
**2455** an insufficient number of events to estimate the uncertainty directly. 30% and  
**2456** 18% channel migration uncertainties are applied in the 0- and 1-lepton channels  
**2457** respectively.

2458 Since the contribution from  $WW$  is negligible, dedicated studies are not performed,  
2459 but a 25% normalisation uncertainty is applied in all the three channels which is  
2460 based on the modelling studies performed for the previous analysis [79].

Diboson Acceptance Uncertainties							
Bosons	WZ			ZZ			
Channel	0L	1L	2L	0L	1L	2L	
Normalisation	16%			10%			
HP-to-LP SR	18%		18%		-		
Medium-to-high $p_T^V$	10%		6%	18%		-	
Channel Relative acceptance	8%	-	30%	18%	-	-	

**Table 7.11:** Diboson acceptance uncertainties. All uncertainties except channel extrapolation uncertainties are fully correlated between the  $ZZ$  and  $WZ$  processes and channels [176].

### 2461 Diboson Shape Uncertainties

2462 Diboson shape uncertainties are derived in a similar fashion to  $V+jets$ . Only the  
2463 uncertainties associated with the systematic variations of  $\mu_R$  and the alternate event  
2464 generator have a non-negligible impact on the  $m_J$  shape. Variation of  $\mu_R$  produces  
2465 consistent  $m_J$  shape changes across all regions and channels, and hence only a single  
2466 associated uncertainty is derived, shown in Fig. 7.4. A hyperbolic tangent is fitted  
2467 to the symmetrised ratio.

2468 In the 2-lepton channel, no significant shape differences between the nominal and  
2469 alternate was observed. The comparison between the nominal SHERPA and alternate  
2470 POWHEG+PYTHIA8 samples is shown in Fig. 7.5 for the 0- and 1-lepton channels  
2471 for both the  $WZ$  and  $ZZ$  processes. For these channels, the shape of  $m_J$  varies in  
2472 opposite directions in the LP and HP signal regions. Shapes are similar between  
2473  $p_T^V$  bins, the 0- and 1-lepton channels and for  $WZ$  and  $ZZ$ . In order to reduce the  
2474 effects of statistical fluctuations on the fitted shape, these regions are merged before  
2475 deriving the shape uncertainty. A third order polynomial is fitted to the ratio, and  
2476 this function transitions to a constant piecewise function in the high mass region  
2477 to accurately represent the shape. Dependence on the event generator was found  
2478 to be negligible within statistical uncertainty in the 2-lepton channel, and so no

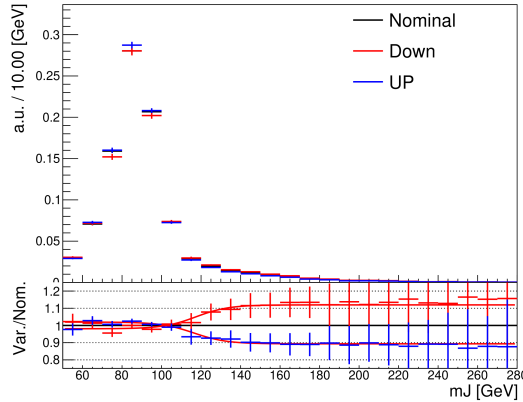


**Figure 7.4:** Leading large- $R$  jet mass distribution for the combined  $WZ$  and  $ZZ$  processes, inclusive across all signal regions and lepton channels [176]. The renormalisation scale  $\mu_R$  has been varied by a factor of 2 (UP) and 0.5 (DOWN). The red and blue curves show the fitted results of the hyperbolic tangent function.

2479 uncertainty was applied. All diboson shape uncertainties are fully correlated in the  
2480 fit.

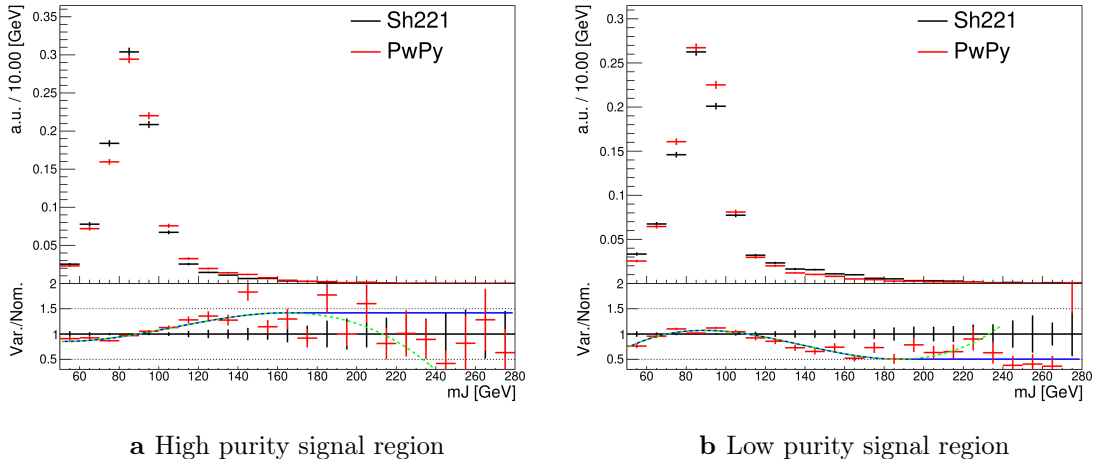


**Figure 7.5:** Comparison of the shapes of the large- $R$  jet mass  $m_J$  between SHERPA (Sh221) (black) and POWHEG+PYTHIA8 (PwPy) (red) samples from the  $WZ$  and  $ZZ$  processes in high and low purity signal regions, integrated over  $p_T^V$  regions and the 0- and 1-lepton channels [176]. The dashed green line shows the fitted third order polynomial function and the blue lines show the function after protection is added in the high mass region.

### 7.3.6 $t\bar{t}$ and single-top Modelling

The main features of the systematic uncertainties on the remaining two modelled backgrounds,  $t\bar{t}$  and single-top, are described below.

The modelling of the  $t\bar{t}$  background uses a POWHEG+PYTHIA8 nominal sample. Two alternate samples were considered: POWHEG+HERWIG7 (providing an alternate parton shower model) and MADGRAPH5+PYTHIA8.2 (providing an alternate hard scatter model). Effects of initial and final state radiation (ISR and FSR, respectively) were assessed using internal weight variations in the nominal sample. Acceptance and shape uncertainties were derived for each of the variations. The largest contribution for the acceptance uncertainties is due to the matrix element calculation, with the parton showering model being second. The ISR and FSR acceptance uncertainties were found to be subdominant. Acceptance uncertainties for the single-top background are enumerated in Table 7.12. For the shape uncertainties, only the ISR and parton showering variations have non-negligible impacts on the  $m_J$  shape.

$t\bar{t}$ Acceptance Uncertainties	
HP-to-LP SR	18%
Medium-to-high $p_T^V$	20%
SR-to-CR	6%

**Table 7.12:** Acceptance uncertainties for the  $t\bar{t}$  background. The uncertainties on the 0- and 1-lepton channels are found to be similar, but are conservatively taken to be uncorrelated. The HP-to-LP SR uncertainty is applied in the HP SR. The Medium-to-high  $p_T^V$  uncertainty is applied in the high  $p_T^V$  bin, and is larger than the computed uncertainty in order to account for the known mismodelling of the  $t\bar{t}$   $p_T$  spectrum. [176].

The dominant process contributing to the single-top background is  $Wt$  production for the 0- and 1-lepton channels. The same nominal and alternate generators are used as for the  $t\bar{t}$  background. Again, ISR and FSR variations are obtained from internal weight variations in the nominal sample. At higher orders in QCD, diagrams contributing to the  $Wt$  production process can also be found in leading-order  $t\bar{t}$  production processes. To account for the arising interference effects, the diagram removal (DR) scheme in Ref. [178] was employed for the nominal sample. The uncertainty on the DR scheme was assessed using an alternate sample using a diagram subtraction (DS) method which removes interference at the generator level.

2504 The largest sources of acceptance and shape uncertainties were due to this DS-DR  
2505 variation. Acceptance uncertainties for the single-top background are enumerated in  
2506 Table 7.13.

Single-Top Acceptance Uncertainties	
Normalisation	20%
HP-to-LP SR	25%
Medium-to-high $p_T^V$	20%
SR-to-CR	30%
Channel Relative acceptance	20%

**Table 7.13:** Single-top acceptance uncertainties. Uncertainties are derived in the 1-lepton channel but applied in a correlated fashion to both the 0- and 1-lepton channels. The HP-to-LP SR uncertainty is applied in the HP SR. The Medium-to-high  $p_T^V$  uncertainty is applied in the high  $p_T^V$  bin. The channel relative acceptance uncertainty is applied in the 0-lepton channel. [176].

### 2507 7.3.7 Signal Modelling

2508 The modelling of the systematic uncertainties affecting the signal processes follows  
2509 the procedure described in Refs. [26, 179, 180]. The  $qq \rightarrow VH$  signal samples are  
2510 generated with POWHEG BOX v2 +GoSAM at next-to-leading order (NLO) accuracy  
2511 in QCD. An additional  $gg \rightarrow ZH$  sample is generated using POWHEG BOX v2 at  
2512 leading order (LO) in QCD. In both cases, the generated events are interfaced with  
2513 PYTHIA 8 for the parton showering modelling. An alternate HERWIG7 sample is used  
2514 to assess the uncertainty on the parton showering model. Recommended systematic  
2515 uncertainties on the signal production cross-sections and  $H \rightarrow b\bar{b}$  branching ratio  
2516 from the LHC Higgs Cross Section Working Group are applied [181, 182]. This  
2517 includes acceptance and shape uncertainties arising from missing higher-order QCD  
2518 and electroweak corrections, PDF uncertainties, renormalisation and factorisation  
2519 scales, and an alternate parton showering model.

## 2520 7.4 Statistical Treatment

2521 A binned global maximum-profile-likelihood fit of the  $m_J$  distribution is performed  
 2522 to extract information on the signal, combining all the analysis regions defined  
 2523 in Table 7.1. The signal strength  $\mu = \sigma/\sigma_{\text{SM}}$  is defined as the ratio between the  
 2524 observed and predicted cross-sections, where  $\mu = 0$  corresponds to the background-  
 2525 only hypothesis and  $\mu = 1$  corresponds to the SM prediction. This is a parameter of  
 2526 interest (POI) which acts to scale the total number of signal events, and is determined  
 2527 during the fit procedure.

2528 The present analysis makes use of two POIs. The first,  $\mu_{VH}^{bb}$ , is the signal strength  
 2529 for the  $VH$ ,  $H \rightarrow b\bar{b}$  process, the primary process under investigation. The diboson  
 2530 production strength  $\mu_{VZ}^{bb}$  for the  $VZ$ ,  $Z \rightarrow b\bar{b}$  process is measured simultaneously and  
 2531 provides a validation of the analysis apparatus used for the primary  $H \rightarrow b\bar{b}$  measure-  
 2532 ment. Alongside the two POIs, the predictive model depends on several parameters  
 2533 which are not the primary target of measurement, and represent the systematic  
 2534 uncertainties discussed previously. These parameters are called nuisance parameters  
 2535 (NPs), collectively referred to as  $\theta$ . Freely floating background normalisations are  
 2536 implemented as NPs and are also extracted during the fitting processes.

### 2537 7.4.1 The Likelihood Function

2538 The statistical setup treats each bin as a Poisson counting experiment and is based on  
 2539 the ROOSTATS framework [183]. The combined likelihood over  $N$  bins is constructed  
 2540 as the product of Poisson probabilities in each bin. Considering the simplified case  
 2541 of a single signal strength parameter  $\mu$ , and neglecting sources of systematic or  
 2542 statistical uncertainty, this is given by

$$\mathcal{L}(\mu) = \prod_{i=1}^N \frac{(\mu s_i + b_i)^{n_i}}{n_i!} \exp [-(\mu s_i + b_i)], \quad (7.1)$$

2543 where  $s_i$  ( $b_i$ ) is the expected number of signal (background) events in bin  $i$ , and  $n_i$  is  
 2544 the number of observed data events in bin  $i$ .

2545 **Treatment of Uncertainties**

2546 Systematic uncertainties can modify the predicted signal and background yields  $s_i$   
2547 and  $b_i$ . Each source of systematic uncertainty is taken into account by adding an  
2548 additional NP  $\theta_j$  to the likelihood in the form of a Gaussian cost function. The  
2549 combined effect of the NPs is then

$$\mathcal{L}(\theta) = \prod_{j=1}^{N_\theta} \frac{1}{\sqrt{2\pi\sigma_j}} \exp \left[ \frac{-(\theta_j - \hat{\theta}_j)^2}{2\sigma_j^2} \right], \quad (7.2)$$

2550 where  $N_\theta$  is the number of NPs,  $\theta_j$  is the nominal value of the  $j$ th NP,  $\hat{\theta}_j$  is the fitted  
2551 value, and  $\sigma_j$  is the corresponding associated prior uncertainty on the NP. As the  
2552 fitted value  $\hat{\theta}_j$  deviates from its nominal value, a cost is introduced. The presence of  
2553 NPs modifies the likelihood as

$$\mathcal{L}(\mu) \rightarrow \mathcal{L}(\mu, \theta) = \mathcal{L}(\mu)\mathcal{L}(\theta). \quad (7.3)$$

2554 The predicted signal and background yields are also modified by the presence of the  
2555 NPs with

$$s_i \rightarrow s_i(\theta), \quad b_i \rightarrow b_i(\theta). \quad (7.4)$$

2556 For NPs which are left freely floating in the fit, no corresponding Gaussian constraints  
2557 are added to the likelihood.

2558 The pull of a NP is defined as the difference between the fitted value  $\hat{\theta}_j$  and the  
2559 nominal value  $\theta_j$ , divided by the uncertainty on the NP  $\sigma_j$ . To obtain the uncertainty  
2560 on the pull of a NP, the following procedure is used. The Hessian matrix  $\mathbf{H}$  is  
2561 calculated as

$$\mathbf{H} = \begin{bmatrix} \frac{\partial^2 \mathcal{L}}{\partial \theta_1^2} & \frac{\partial^2 \mathcal{L}}{\partial \theta_1 \partial \theta_2} & \dots & \frac{\partial^2 \mathcal{L}}{\partial \theta_1 \partial \theta_n} \\ \frac{\partial^2 \mathcal{L}}{\partial \theta_2 \partial \theta_1} & \frac{\partial^2 \mathcal{L}}{\partial \theta_2^2} & \dots & \frac{\partial^2 \mathcal{L}}{\partial \theta_2 \partial \theta_n} \\ \vdots & \vdots & \ddots & \vdots \\ \frac{\partial^2 \mathcal{L}}{\partial \theta_n \partial \theta_1} & \frac{\partial^2 \mathcal{L}}{\partial \theta_n \partial \theta_2} & \dots & \frac{\partial^2 \mathcal{L}}{\partial \theta_n^2} \end{bmatrix}. \quad (7.5)$$

2562 Taking the inverse of the Hessian matrix  $\mathbf{H}^{-1}$  yields the covariance matrix, from  
2563 which the post-fit uncertainties on the different NPs can be extracted. If the post-fit  
2564 uncertainty is smaller than the nominal uncertainty, additional information about  
2565 the NP has been extracted by the fit, and NP is said to be *constrained*.

2566 Following Ref. [184], the statistical uncertainty on the simulated events is implemented  
2567 using a dedicated NP for each bin which can scale the background yield in that bin.  
2568 Statistical NPs are also implemented using a Gaussian constraint.

### 2569 Smoothing and Pruning

2570 To simplify the fit to reduce and improve its robustness, systematic uncertainties  
2571 are smoothed and pruned. Smoothing accounts for the large statistical uncertainty  
2572 present in some samples that can lead to unphysical fluctuations in the shape  
2573 systematics. The smoothing procedure relies on the assumption that the impact of  
2574 systematics should be approximately monotonic and correlated between neighbouring  
2575 bins.

2576 In addition to smoothing, pruning is the process of removing from the fit those  
2577 systematics which only have a very small effect. This improves the stability of the  
2578 fit by reducing the number of degrees of freedom. Acceptance uncertainties are  
2579 pruned in a given region if they have a variation of less than 0.5%, or if the up and  
2580 down variations have the same sign in that region. Shape uncertainties are pruned  
2581 in a given region if the deviation in each bin is less than 0.5% in that region. In  
2582 addition, acceptance and shape uncertainties are neglected in a given region for any  
2583 background which makes up less than 2% of the total background in that region.

## 2584 Fit Procedure and Statistical Tests

2585 The best-fit value of  $\mu$ , denoted  $\hat{\mu}$ , is obtained via an unconditional maximisation of  
 2586 the likelihood. The likelihood is also used to construct a statistical test which can  
 2587 confirm or reject the background-only hypothesis. The test statistic  $q_\mu$  is constructed  
 2588 from the profile likelihood ratio,

$$q_\mu = -2 \ln \frac{\mathcal{L}(\mu, \hat{\theta}_\mu)}{\mathcal{L}(\hat{\mu}, \hat{\theta})} \quad (7.6)$$

2589 where  $\hat{\mu}$  and  $\hat{\theta}$  are chosen to maximise the likelihood  $\mathcal{L}$ , and the profile value  $\hat{\theta}_\mu$  is  
 2590 obtained from a conditional maximisation of the likelihood for a specific choice of  
 2591  $\mu = 0$  corresponding to the background-only hypothesis.

2592 The test statistic is used to construct a  $p$ -value which is used to probe the background-  
 2593 only hypothesis. The  $p$ -value is typically reported in terms of the significance  $Z$ ,  
 2594 defined as the number of standard deviations for a Gaussian Normal distribution  
 2595 which will produce a one-sided tail integral equal to the  $p$ -value, as in

$$p = \int_Z^\infty \frac{1}{\sqrt{2\pi}} e^{-x^2/2} dx = 1 - \Phi(Z). \quad (7.7)$$

2596 Typically a value of  $Z = 3$  constitutes *evidence* of a processes, while  $Z = 5$  is  
 2597 required for a *discovery*, or *observation*. Alongside the  $p$ -value, the best-fit value of  
 2598 the signal strength  $\hat{\mu}$  and its corresponding uncertainty are quoted, and compared to  
 2599 their expected values. More detail on the statistical methodology can be found in  
 2600 Ref. [185].

### 2601 7.4.2 Background Normalisations

2602 The backgrounds which can be constrained by the fit are left freely floating and  
 2603 the corresponding normalisation factors are extracted. Normalisation factors (NF),  
 2604 represent the value by which the predicted normalisations are scaled, and are im-  
 2605 plemented for the dominant backgrounds ( $t\bar{t}$ ,  $Z+hf$ ,  $W+hf$ ). The NFs are also  
 2606 subdivided into different regions of phase-space for  $t\bar{t}$ , given it is possible to obtain

2607 a strong constraint in the individual channels. This also removes the need for an  
2608 extrapolation uncertainty.

2609 The normalisations and shapes of all other backgrounds, with the exception of the  
2610 multijet background which is estimated using a data driven technique, are initialised  
2611 using the nominal samples and the state-of-the art process normalisations, as outlined  
2612 in Table 7.4.

### 2613 7.4.3 Asimov Dataset & Expected Results

2614 The Asimov dataset is constructed by replacing the data with the sum of the signal  
2615 and background predictions  $n_i = s_i + b_i$ . A fit to this dataset using the nominal  
2616 values of the NPs from the simulation will recover the input values and is useful for  
2617 studying the expected result, in addition to constraints on and correlations between  
2618 the NPs.

2619 Alternatively, a conditional fit to the Asimov dataset can be performed using values  
2620 of the background NPs which are determined from an unconditional fit to data. The  
2621 signal NPs and POIs are fixed at their nominal values from the SM simulation. The  
2622 result of this fit can be used to calculate expected (median) significances given a  
2623 more realistic background model, which can be compared to their observed values,  
2624 as is done in Section 7.5.2.

## 2625 7.5 Results

2626 In the present analysis, the two signal strength parameters  $\mu_{VH}^{bb}$  and  $\mu_{VZ}^{bb}$  are extracted  
2627 from a simultaneous maximisation of the likelihood described in Section 7.4. The  
2628 results of the analysis are summarised in this section. Post-fit  $m_J$  distributions are  
2629 shown in Section 7.5.1. The observed signal strengths are given in Section 7.5.2,  
2630 along with observed and expected significances. Finally in Section 7.5.3 the impact  
2631 of systematic uncertainties on the results is examined.

### 2632 7.5.1 Post-fit Results

2633 In addition to the observed significance and signal strength, it is also necessary to  
 2634 study the post-fit  $m_J$  yields and distributions to compare the level of the agreement  
 2635 between the simulation (using the best-fit values of the signal strength  $\hat{\mu}$  and the  
 2636 NP  $\hat{\theta}$ ) and the data. The best-fit values  $\hat{\mu}$  and  $\hat{\theta}$  are obtained from an unconditional  
 2637 fit to data over all analysis regions. The post-fit background normalisation factors  
 2638 extracted from the unconditional fit to data fit are shown in Table 7.14, and the  
 2639 post-fit yields are presented in Table 7.15, Table 7.16, and Table 7.17 for the 0-, 1-  
 2640 and 2-lepton channels, respectively.

Process	Normalisation factor
$t\bar{t}$ 0-lepton	$0.88 \pm 0.10$
$t\bar{t}$ 1-lepton	$0.83 \pm 0.09$
$W+hf$	$1.12 \pm 0.14$
$Z+hf$	$1.32 \pm 0.16$

**Table 7.14:** Factors applied to the nominal normalisations of the  $t\bar{t}$ ,  $W+hf$ , and  $Z+hf$  backgrounds, as obtained from the likelihood fit [130]. The errors represent the combined statistical and systematic uncertainties.

Processes	$250 \text{ GeV} < p_T^V \leq 400 \text{ GeV}$			$p_T^V > 400 \text{ GeV}$		
	HP	LP	CR	HP	LP	CR
Signal	$21.93 \pm 11.17$	$18.99 \pm 9.76$	$1.05 \pm 0.54$	$5.69 \pm 2.88$	$5.85 \pm 3.01$	$0.33 \pm 0.17$
$W+t$	$14.70 \pm 5.37$	$45.55 \pm 19.44$	$17.18 \pm 8.09$	$2.03 \pm 0.98$	$8.93 \pm 6.33$	$3.76 \pm 2.49$
other $t+X$	$0.79 \pm 0.03$	$3.18 \pm 0.66$	$4.51 \pm 1.28$	-	$0.66 \pm 0.03$	$0.11 \pm 0.00$
$t\bar{t}$	$75.19 \pm 13.60$	$423.85 \pm 36.12$	$539.21 \pm 31.39$	$7.54 \pm 1.77$	$38.20 \pm 6.75$	$44.07 \pm 7.43$
$VZ$	$77.01 \pm 17.09$	$87.70 \pm 19.36$	$6.16 \pm 1.56$	$17.30 \pm 4.10$	$28.77 \pm 6.55$	$2.79 \pm 0.72$
$WW$	-	$2.15 \pm 0.05$	$0.24 \pm 0.01$	$0.33 \pm 0.02$	$1.80 \pm 0.06$	-
$Whf$	$100.78 \pm 20.01$	$331.31 \pm 59.54$	$29.97 \pm 21.85$	$20.19 \pm 6.24$	$59.82 \pm 17.91$	$6.61 \pm 5.09$
$Wcl$	$5.13 \pm 2.31$	$8.44 \pm 3.24$	$0.46 \pm 0.01$	$0.99 \pm 0.69$	$2.77 \pm 1.14$	$0.19 \pm 0.07$
$Wl$	$5.61 \pm 3.93$	$4.61 \pm 2.45$	$0.16 \pm 0.00$	$1.41 \pm 2.06$	$2.67 \pm 1.67$	$0.57 \pm 0.36$
$Zhf$	$318.76 \pm 35.27$	$548.71 \pm 61.84$	$76.97 \pm 21.47$	$86.79 \pm 10.63$	$184.99 \pm 21.43$	$25.76 \pm 7.43$
$Zcl$	$3.97 \pm 1.63$	$6.74 \pm 2.68$	$0.83 \pm 0.02$	-	$6.36 \pm 2.73$	$0.93 \pm 0.41$
$Zl$	$1.34 \pm 0.67$	$3.61 \pm 2.14$	$0.42 \pm 0.01$	$1.05 \pm 0.63$	$3.68 \pm 2.47$	$0.29 \pm 0.16$
Data	623	1493	683	146	330	85
Background	$603 \pm 25$	$1466 \pm 36$	$676 \pm 25$	$138 \pm 9$	$339 \pm 15$	$85 \pm 7$

**Table 7.15:** Post-fit yields in the 0-lepton channel. Combined statistical and systematic uncertainties are shown [176].

Processes	$250 \text{ GeV} < p_T^V \leq 400 \text{ GeV}$			$p_T^V > 400 \text{ GeV}$		
	HP	LP	CR	HP	LP	CR
Signal	$24.23 \pm 12.34$	$18.02 \pm 9.29$	$0.88 \pm 0.45$	$7.84 \pm 3.96$	$7.50 \pm 3.87$	$0.39 \pm 0.20$
W+t	$64.35 \pm 21.12$	$159.95 \pm 75.14$	$73.44 \pm 29.96$	$16.40 \pm 7.31$	$53.28 \pm 41.74$	$21.16 \pm 15.36$
other t+X	$1.92 \pm 0.48$	$16.33 \pm 0.31$	$21.89 \pm 6.18$	$0.13 \pm 0.01$	$1.70 \pm 0.06$	$3.95 \pm 1.40$
$t\bar{t}$	$234.76 \pm 30.21$	$1189.51 \pm 75.91$	$1758.08 \pm 57.99$	$50.87 \pm 7.34$	$226.85 \pm 23.98$	$340.61 \pm 25.32$
VZ	$35.94 \pm 8.87$	$56.30 \pm 13.98$	$4.93 \pm 1.38$	$8.63 \pm 2.30$	$20.02 \pm 5.29$	$2.61 \pm 0.84$
WW	-	$6.48 \pm 1.63$	-	-	$4.35 \pm 1.32$	$0.93 \pm 0.03$
Whf	$265.13 \pm 27.68$	$617.81 \pm 63.56$	$59.91 \pm 21.90$	$91.42 \pm 11.51$	$238.81 \pm 29.53$	$26.55 \pm 9.84$
Wcl	$7.33 \pm 2.95$	$13.81 \pm 5.65$	$2.10 \pm 0.04$	$6.23 \pm 2.49$	$10.17 \pm 4.09$	$0.63 \pm 0.02$
Wl	$2.99 \pm 1.47$	$5.66 \pm 3.39$	$0.65 \pm 0.01$	$2.21 \pm 1.35$	$7.67 \pm 4.98$	$0.31 \pm 0.01$
Zhf	$10.16 \pm 1.24$	$24.61 \pm 2.46$	$3.45 \pm 0.41$	$2.12 \pm 0.30$	$6.56 \pm 0.79$	$0.98 \pm 0.12$
Zcl	$0.02 \pm 0.00$	$0.75 \pm 0.02$	-	-	$0.33 \pm 0.01$	$0.02 \pm 0.00$
Zl	-	$0.49 \pm 0.01$	$0.03 \pm 0.00$	$0.30 \pm 0.19$	$0.23 \pm 0.01$	$0.02 \pm 0.00$
ggWW	-	$0.35 \pm 0.01$	$0.27 \pm 0.01$	$0.15 \pm 0.02$	$0.33 \pm 0.01$	-
MultiJet	$17.04 \pm 8.87$	$44.29 \pm 22.82$	$21.78 \pm 11.22$	$7.81 \pm 4.50$	$21.85 \pm 12.73$	$7.86 \pm 4.01$
Data	668	2161	1946	185	597	410
Background	$640 \pm 26$	$2136 \pm 44$	$1947 \pm 43$	$186 \pm 11$	$592 \pm 21$	$406 \pm 18$

**Table 7.16:** Post-fit yields in the 1-lepton channel. Combined statistical and systematic uncertainties are shown [176].

Processes	$250 \text{ GeV} < p_T^V \leq 400 \text{ GeV}$	$p_T^V > 400 \text{ GeV}$
	SR	SR
Signal	$7.62 \pm 3.88$	$2.79 \pm 1.41$
W+t	$1.28 \pm 0.39$	-
$t\bar{t}$	$1.64 \pm 0.35$	$0.45 \pm 0.10$
VZ	$19.90 \pm 4.86$	$7.49 \pm 2.05$
Whf	$0.41 \pm 0.07$	$0.07 \pm 0.01$
Zhf	$150.94 \pm 12.72$	$57.15 \pm 5.81$
Zcl	$2.20 \pm 0.91$	$1.80 \pm 0.76$
Zl	$0.94 \pm 0.67$	$1.01 \pm 0.67$
Data	179	73
Background	$177 \pm 12$	$68 \pm 6$

**Table 7.17:** Post-fit yields in the 2-lepton channel. Combined statistical and systematic uncertainties are shown [176].

Post-fit  $m_J$  distributions are given for the signal regions in the 0-, 1- and 2-lepton channels in Fig. 7.6. The LP and HP regions are merged for the 0- and 1-lepton channels for the sake of simplicity. In general there is a good level of agreement between the simulation and data, indicating the fit model is performing as expected. Fig. 7.7 shows the post-fit plots for the  $t\bar{t}$  control regions. Again, a good level of agreement is observed given the statistical uncertainties on the distributions.

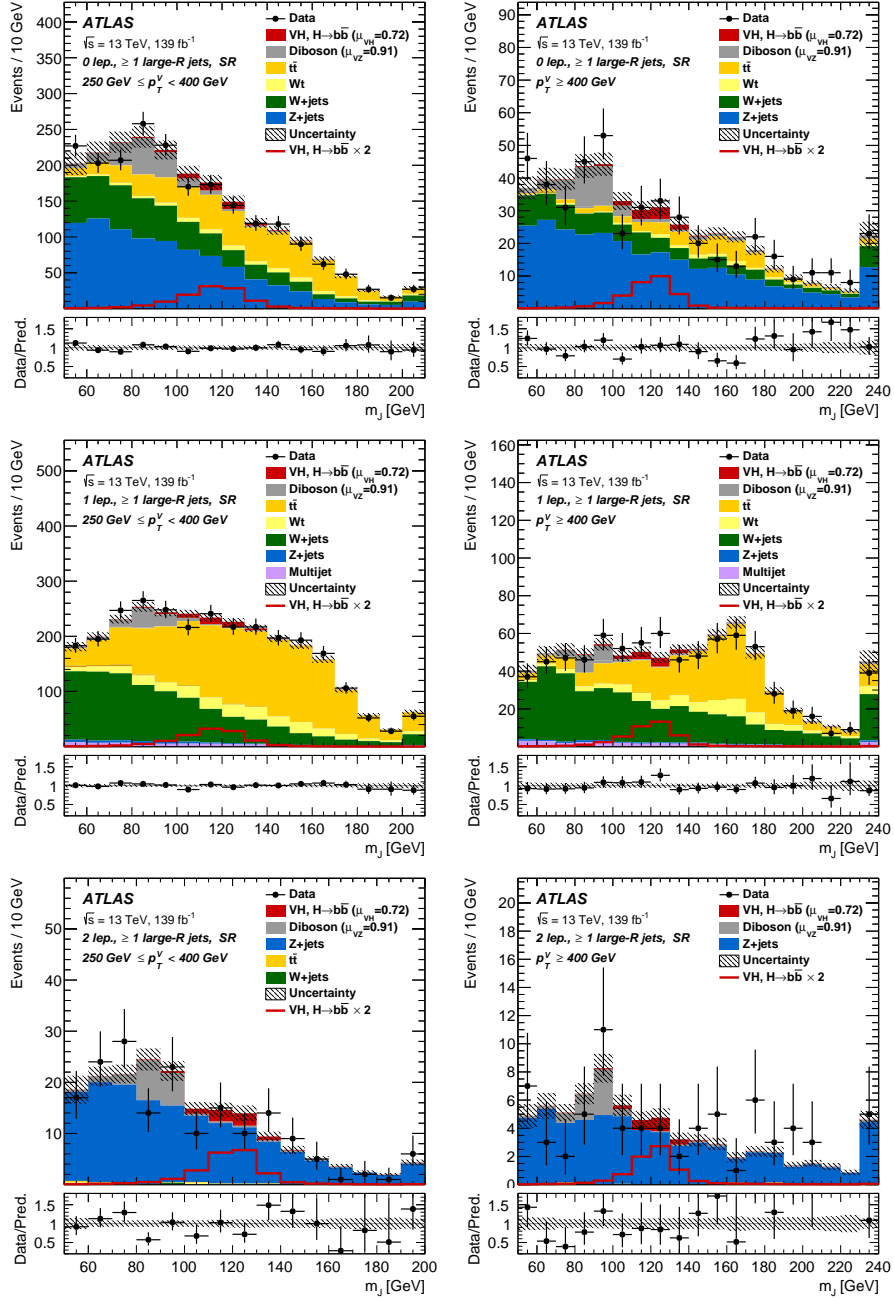


**Figure 7.6:** The  $m_J$  post-fit distributions in (top) the 0-, (middle) 1- and (bottom) 2-lepton SRs for (left)  $250 \text{ GeV} < p_T^V < 400 \text{ GeV}$  and (right)  $p_T^V \geq 400 \text{ GeV}$ . The LP and HP regions are merged for the 0-lepton and 1-lepton channels. The fitted background contributions are shown as filled histograms. The Higgs boson signal ( $m_H = 125 \text{ GeV}$ ) is shown as a filled histogram and is normalised to the signal yield extracted from data ( $\mu_{VH}^{bb} = 0.72$ ), and as an unstacked unfilled histogram, scaled by the SM prediction times a factor of two. The size of the combined on the sum of the fitted signal and background is shown in the hatched band. The highest bin contains the overflow [130].

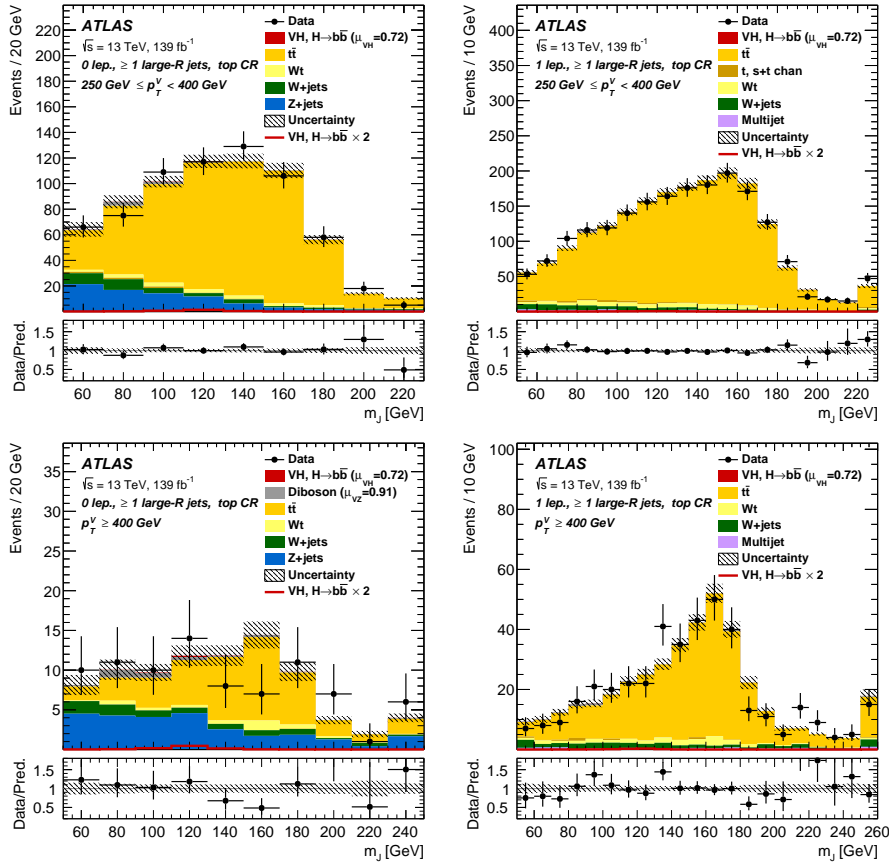


**Figure 7.7:** The  $m_J$  post-fit distributions in the  $t\bar{t}$  control region for (top) the 0-lepton channel and the 1-lepton channel for  $250 \text{ GeV} < p_T^V < 400 \text{ GeV}$  and (bottom) the 0-lepton channel and the 1-lepton channel for  $p_T^V > 400 \text{ GeV}$ . The background contributions after the likelihood fit are shown as filled histograms. The Higgs boson signal ( $m_h = 125 \text{ GeV}$ ) is shown as a filled histogram on top of the fitted backgrounds normalised to the signal yield extracted from data ( $\mu_{VH}^{bb} = 0.72$ ), and unstacked as an unfilled histogram, scaled by the SM prediction times a factor of 2. The size of the combined statistical and systematic uncertainty for the sum of the fitted signal and background is indicated by the hatched band. The highest bin in the distributions contains the overflow [130].

### 2647 7.5.2 Observed Signal Strength & Significance

2648 The measured signal strength is computed as the ratio between the measured signal  
 2649 yield to the prediction from the SM. The combed result for all three lepton channels  
 2650 and all analysis regions is given for  $\mu_{VH}^{bb}$  in Eq. (7.8), and for  $\mu_{VZ}^{bb}$  in Eq. (7.9). Both  
 2651 results include a full breakdown of the systematic and statistical uncertainties.

$$\mu_{VH}^{bb} = 0.72_{-0.36}^{+0.39} = 0.72_{-0.28}^{+0.29}(\text{stat.})_{-0.22}^{+0.26}(\text{syst.}) \quad (7.8)$$

2652

$$\mu_{VZ}^{bb} = 0.91_{-0.23}^{+0.29} = 0.91 \pm 0.15(\text{stat.})_{-0.17}^{+0.24}(\text{syst.}) \quad (7.9)$$

2653 The results for  $\mu_{VH}^{bb}$  and  $\mu_{VZ}^{bb}$  are consistent with the expectation from the SM. The  
 2654  $\mu_{VH}^{bb}$  measurement is dominated by statistical uncertainty, while the  $\mu_{VZ}^{bb}$  measurement  
 2655 is dominated by systematic sources of uncertainty. The measured signal strength  
 2656 for  $\mu_{VZ}^{bb}$  corresponds to an observed significance of 2.1 standard deviations, with an  
 2657 expected (median) significance given the SM prediction of 2.7 standard deviations.  
 2658 The diboson observed (expected) signal strength significance is 5.4 (5.7). These results  
 2659 are summarised in Fig. 7.8, which shows the weighted and background-subtracted  $m_J$   
 2660 distribution. A clear signal excess is visible around the Higgs mass of  $m_H = 125$  GeV.

### 2661 Compatibility Studies

2662 Alongside the standard 2-POI fit, a (3+1)-POI fit can be performed by splitting  $\mu_{VH}^{bb}$   
 2663 into three separate POIs, one for each channel. A simultaneous fit to the channel  
 2664 specific signal strengths can then be performed, which allows a comparison of the  
 2665 contributions from each channel. Fig. 7.9 compares the best-fit signal strengths.  
 2666 The 0- and 1-lepton channels show a signal strength which is consistent with the  
 2667 SM prediction, while the 2-lepton channel shows a small deviation within the  $1\sigma$   
 2668 uncertainty. Overall, good compatibility is observed via a  $\chi^2$  test with a corresponding  
 2669  $p$ -value of 49%.

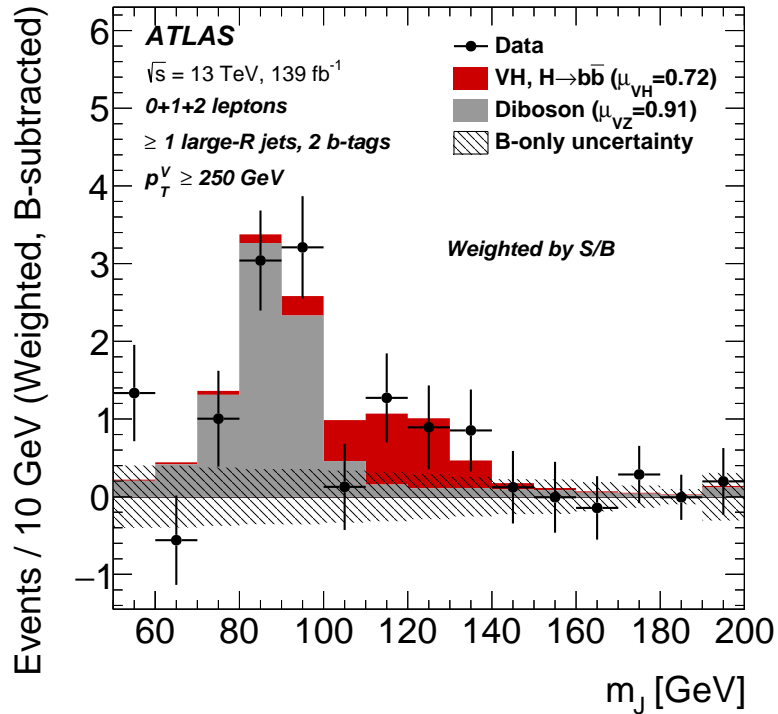


**Figure 7.8:**  $m_J$  distribution in data after subtraction of all backgrounds except for the  $WZ$  and  $ZZ$  diboson processes. The contributions from all lepton channels and signal regions are summed and weighted by their respective values of the ratio of fitted Higgs boson signal and background yields. The expected contribution of the associated  $WH$  and  $ZH$  production of a SM Higgs boson with  $m_H = 125 \text{ GeV}$  is shown scaled by the measured combined signal strength ( $\mu_{VH}^{bb} = 0.72$ ). The diboson contribution is normalised to its best-fit value of  $\mu_{VZ}^{bb} = 0.91$ . The size of the combined statistical and systematic uncertainty is indicated by the hatched band. This error band is computed from a full signal-plus-background fit including all the systematic uncertainties defined in Section 7.3, except for the  $VH/VZ$  experimental and theory uncertainties [130].

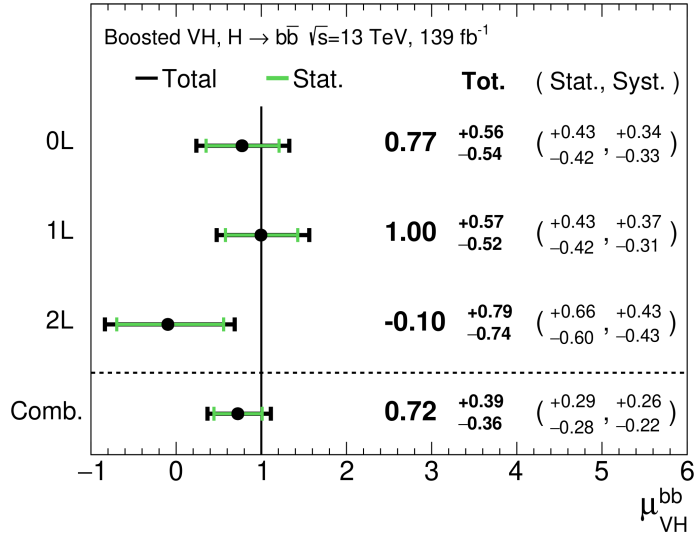


**Figure 7.9:** Signal strength compatibility test between the (3+1)-POI fit (with the three lepton channels fit separately) and the default (1+1)-POI fit. The compatibility of the three channels is evaluated via a  $\chi^2$  difference test and results in a p-value of 49% [130].

### 2670 7.5.3 Impact of Systematics

2671 The impact of systematic uncertainties on the final fitted value  $\hat{\mu}^{bb}$  can be studied  
 2672 using the NP rankings, and the uncertainty breakdown.

2673 Fig. 7.10 shows the NP ranking, which is used to visualise which NPs have the largest  
 2674 impact on the sensitivity to the fitted POI. To obtain the ranking, a likelihood scan  
 2675 is performed for each NP  $\theta_j$ . First, an unconditional fit is used to determine  $\hat{\theta}_j$ .  
 2676 The NP is then fixed to its post-fit value varied by  $\pm 1\sigma$ , the fit is repeated and the  
 2677 difference between the best-fit value of the POI,  $\Delta\hat{\mu}_{VH}^{bb}$ , is calculated, and used to  
 2678 rank the NPs. In addition, the pulls and constraints for the highest ranked NPs are  
 2679 also shown.

2680 The experimental uncertainty on the signal large- $R$  jet mass resolution (JMR) has  
 2681 the largest impact. JMR and jet energy scale (JES) uncertainties also have large  
 2682 impacts for the  $V+jets$  and for the diboson backgrounds. The freely-floating  $Z+hf$   
 2683 normalisation is the second highest ranked NP, and is heavily constrained by the  
 2684 fit. The  $VZ$  POI  $\mu_{VZ}^{bb}$  is also a significant NP when considering the primary  $\mu_{VH}^{bb}$   
 2685 measurement.

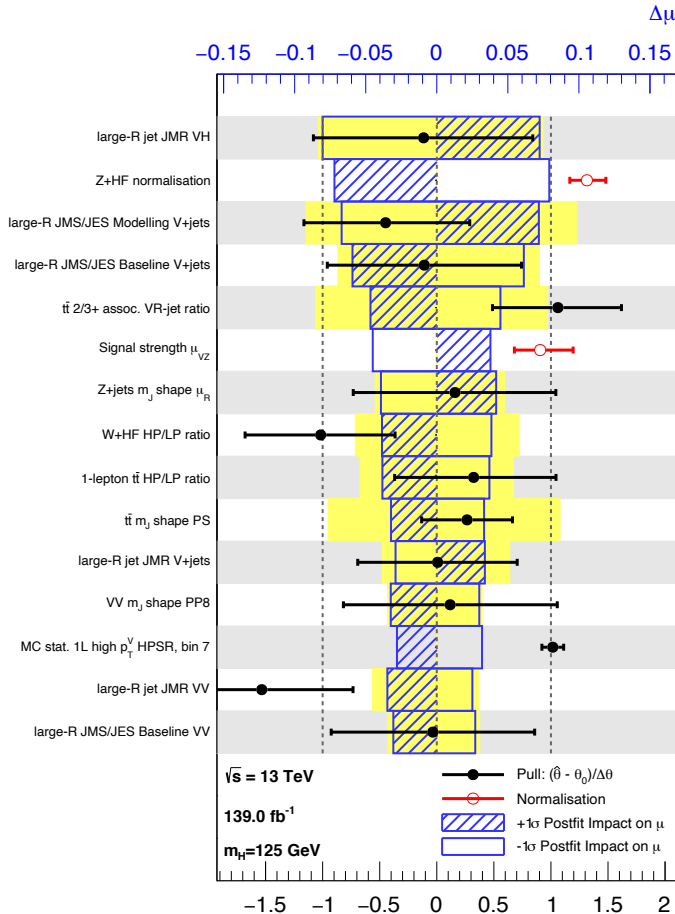


**Figure 7.10:** Impact of systematic uncertainties on the fitted  $VH$  signal-strength parameter  $\hat{\mu}_{VH}^{\text{bb}}$  sorted in decreasing order. The boxes show the variations of  $\hat{\mu}$ , referring to the top  $x$ -axis, when fixing the corresponding individual nuisance parameter to its post-fit value modified upwards or downwards by its post-fit uncertainty, i.e.  $\hat{\theta} \pm \sigma_{\hat{\theta}}$ , and repeating the fit. The impact of up- and down-variations can be distinguished via the dashed and plane box fillings. The yellow boxes show the pre-fit impact (top  $x$ -axis) by varying each nuisance parameter by  $\pm 1$ . The filled circles show the deviation of the fitted value for each nuisance parameter,  $\hat{\theta}$ , from their nominal input value  $\theta_0$  expressed in standard deviations with respect to their nominal uncertainties  $\Delta\theta$  (bottom  $x$ -axis). The error bars show the post-fit uncertainties on  $\hat{\theta}$  with respect to their nominal uncertainties. The open circles show the fitted values and uncertainties of the normalization parameters that are freely floating in the fit. Pre-fit, these parameters have a value of one [176].

2686 The NP ranking highlights individual NPs which have a large impact on the POI  
 2687 measurement sensitivity. Complementary information is provided at a higher level  
 2688 by considering the overall impact of different groups of systematics. The groups  
 2689 are constructed from NPs which have similar physical origins. The impact of each  
 2690 group is calculated by running a fit with all the NPs in the given group fixed to their  
 2691 nominal values. The uncertainty on the POI extracted from this fit is subtracted in  
 2692 quadrature from the uncertainty on the POI from the nominal fit, and the resulting  
 2693 values are provided as the impact for each group. The total systematic impact  
 2694 is the difference in quadrature between the nominal uncertainty on  $\mu_{VH}^{bb}$  and the  
 2695 estimated impact for the combined statistical uncertainties. The “data stat only”  
 2696 group fixes all NPs at their nominal value, while the total statistical impact fixes all  
 2697 NPs except floating normalisations. The floating normalisations group fixes only the  
 2698 NPs associated with normalisation which are left floating in the fit.

2699 The full breakdown for the observed impact of uncertainties on the  $\mu_{VH}^{bb}$  signal  
 2700 strength is provided in Table 7.18. The uncertainty on  $\mu_{VH}^{bb}$  is dominated by com-  
 2701 bined statistical effects (0.28), although the combined impact of systematics (0.24) is  
 2702 of a comparable size. The signal largest group is the data stat uncertainty (0.25),  
 2703 demonstrating that the analysis would benefit from an increased integrated lumi-  
 2704 nosity or improved efficiency to select signal events (recall from Section 7.1.2 the  
 2705 signal efficiency is in the range of 10%). Of the experimental systematic sources of  
 2706 uncertainty, the dominant impact is from the experimental uncertainties associated  
 2707 with the simulation of large- $R$  jets (0.13). Other experimental sources of uncertainty  
 2708 are small in comparison. Modelling uncertainties also have a large contribution to the  
 2709 overall systematic uncertainty. The biggest contribution to the overall uncertainty  
 2710 is the combined statistical uncertainty on the simulated samples (0.09). Out of the  
 2711 backgrounds, the  $W+jets$  and  $Z+jets$  have the highest (0.06) and second-highest  
 2712 (0.05) impact respectively.

#### 2713 7.5.4 STXS Interpretation

2714 The Simplified Template Cross Sections (STXS) framework provides a common  
 2715 categorisation of candidate Higgs boson events according to certain truth-level  
 2716 properties of the production mode under study [26, 186]. The STXS framework is

Source of uncertainty	Signed impact	Avg. impact
Total	+0.388 / -0.356	0.372
Statistical	+0.286 / -0.280	0.283
↔ Data stat only	+0.251 / -0.245	0.248
↔ Floating normalisations	+0.096 / -0.092	0.094
Systematic	+0.261 / -0.219	0.240
<hr/>		
Experimental uncertainties		
Small- $R$ jets	+0.041 / -0.034	0.038
Large- $R$ jets	+0.161 / -0.105	0.133
$E_T^{\text{miss}}$	+0.008 / -0.007	0.007
Leptons	+0.013 / -0.007	0.010
$b$ -tagging	$b$ -jets	+0.028 / -0.004
	$c$ -jets	+0.012 / -0.011
	light-flavour jets	+0.009 / -0.007
	extrapolation	+0.004 / -0.005
Pile-up	+0.001 / -0.002	0.001
Luminosity	+0.019 / -0.007	0.013
<hr/>		
Theoretical and modelling uncertainties		
Signal	+0.073 / -0.026	0.050
Backgrounds	+0.106 / -0.095	0.100
↔ $Z + \text{jets}$	+0.049 / -0.047	0.048
↔ $W + \text{jets}$	+0.059 / -0.056	0.058
↔ $t\bar{t}$	+0.037 / -0.032	0.035
↔ Single top quark	+0.031 / -0.023	0.027
↔ Diboson	+0.034 / -0.029	0.032
↔ Multijet	+0.009 / -0.009	0.009
↔ MC statistical	+0.091 / -0.092	0.092

**Table 7.18:** Breakdown of the absolute contributions to the uncertainty on the signal strength  $\mu_{VH}^{bb}$  obtained from the (1+1)-POI fit. The average impact represents the average between the positive and negative uncertainties on  $\mu_{VH}^{bb}$ . The sum in quadrature of the systematic uncertainties attached to the categories differs from the total systematic uncertainty due to correlations [176].

2717 designed to be independent of the decay mode of the Higgs boson, and is therefore  
2718 well suited to the combination of measurements between different decay channels  
2719 and experiments.

2720 The STXS cross sections are independently measured for the  $ZH$  and  $WH$  production  
2721 modes following the approach described in [179]. For each production mode, two  
2722 bins in the truth vector boson transverse momentum  $p_T^{V,t}$  are considered,  $250 \text{ GeV} < p_T^{V,t} < 400 \text{ GeV}$  and  $p_T^{V,t} \geq 400 \text{ GeV}$ , leading to four independent analysis regions.  
2724 Events from the simulated signal samples are categorised into the regions and used  
2725 to estimate the expected cross section times branching ratio  $\sigma \times B$  in each region,  
2726 where

$$B = B(H \rightarrow b\bar{b}) \times B(V \rightarrow \text{leptons}), \quad (7.10)$$

2727 A simultaneous fit of the four cross section times branching ratios is performed.  
2728 The uncertainties described in Section 7.3 are reused for the STXS fit, with the  
2729 exception of the theoretical uncertainties on the signal cross section and branching  
2730 ratios. The result from the fit is shown in Section 7.5.4 and compared with the  
2731 expected prediction from the SM. The expected and observed results agree within  
2732 the given uncertainties.

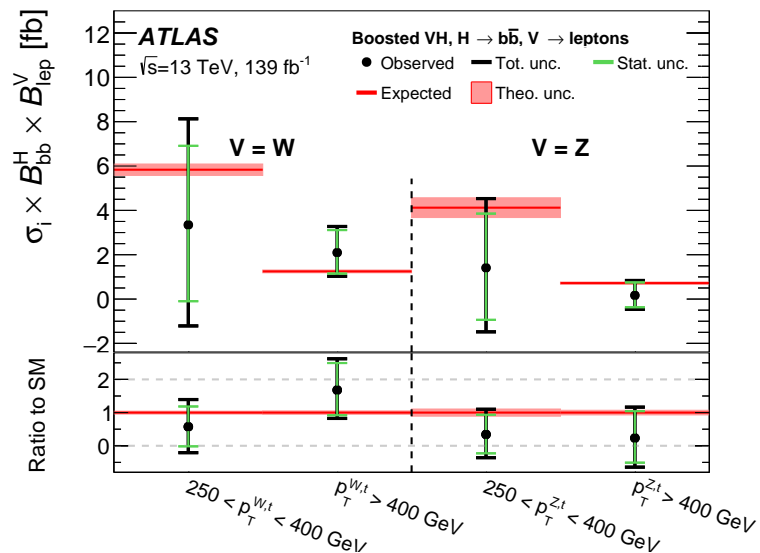


**Figure 7.11:** Measured  $VH$  simplified template cross sections times the  $H \rightarrow b\bar{b}$  and  $V \rightarrow \text{leptons}$  branching fractions in the medium and high  $p_T^{V,t}$  bins [130].

## 2733 7.6 Conclusion

2734 The analysis of the associated production of vector bosons with boosted Higgs bosons  
2735 decaying to a pair of  $b$ -quarks using large- $R$  jets is presented. The Higgs candidate is  
2736 reconstructed as a large- $R$  jet in order to improve sensitivity in the boosted regime  
2737 in which the Higgs decay products are significantly collimated. The analysis is  
2738 performed using  $139\text{ fb}^{-1}$  of proton–proton collision data at  $\sqrt{s} = 13\text{ TeV}$  collected  
2739 throughout the duration of Run 2 of the LHC.

2740 In comparison with the null hypothesis, the Standard Model (SM)  $VH$ ,  $H \rightarrow b\bar{b}$   
2741 process is found to have an observed significance of 2.1 standard deviations, whereas  
2742 the corresponding expected significance is 2.7 standard deviations. The  $VH$ ,  $H \rightarrow b\bar{b}$   
2743 process is measured simultaneously with the diboson  $VZ$ ,  $Z \rightarrow b\bar{b}$  process, which  
2744 provide a cross-check for the main analysis. The observed (expected) significance for  
2745 the diboson process is 5.4 (5.7).

2746 The results are interpreted in the context of the STXS framework. The cross sections  
2747 for the  $WH$  and  $ZH$  processes are measured in two  $p_T^V$  bins, and are found to agree  
2748 with the SM prediction within the given uncertainties. At the time of publication,  
2749 the results are the most precise measurements of the  $WH$  and  $ZH$ ,  $H \rightarrow b\bar{b}$  cross  
2750 sections in the high  $p_T^V$  regime.

2751 The statistical and systematic sources of uncertainty contribute a similar amount  
2752 to the overall uncertainty on the result. This analysis would therefore likely benefit  
2753 greatly from the improved  $b$ -tagging efficiency at high- $p_T$  enabled by GN1 as discussed  
2754 in Chapter 6, due to the associated reduction in statistical uncertainty provided by  
2755 the increased number of events used in the analysis.

2756 The large- $R$  jet mass resolution is found to be the dominant source of systematic  
2757 uncertainty on the  $\mu_{VH}^{bb}$  measurement. An improved method of reconstructing the  
2758 large- $R$  jet mass, for example by using a machine learning based regression approach,  
2759 possibly as an additional auxiliary task to GN1 (see Chapter 6), could reduce the  
2760 systematic uncertainty on the  $\mu_{VH}^{bb}$  measurement. Statistical uncertainty could be  
2761 reduced by increasing the integrated luminosity used to perform the analysis by  
2762 combining with Run 3 data.

2763 **Chapter 8**

2764 **Conclusion**

2765 **8.1 Summary**

2766 The current understanding of particle physics contains many unanswered questions,  
2767 and improving our understanding of the Standard Model is a promising way to  
2768 attempt to answer some of them. One of the key particles which may enhance this  
2769 understanding is the Higgs boson, which was first observed only a decade ago and  
2770 remains under intense scrutiny at the LHC. Given it's propensity to decay to heavy  
2771 flavour  $b$ -quarks, reconstructing and identifying  $b$ -jets is of crucial importance to  
2772 improving our understanding in this area. As discussed in Chapter 4, this task  
2773 becomes increasingly difficult at high transverse momenta.

2774 One of the effects that hampered tracking and  $b$ -tagging performance at high- $p_T$  was  
2775 identified to be the increased rate of fake tracks. To address this issue, an algorithm  
2776 was developed which is able to successfully identify fake tracks within jets 45% of  
2777 the time, with a minimal loss of signal tracks of 1.2%. Removal of such tracks was  
2778 found to improve the light-jet mistagging rate of the SV1 and JetFitter algorithms  
2779 by up to 20% at high transverse momentum.

2780 A novel approach to  $b$ -tagging, GN1 was also developed using a Graph Neural Network  
2781 (GNN) architecture. The model is encouraged to learn the topology of the jet through  
2782 vertexing and track classification auxiliary tasks. As a single end-to-end trained  
2783 model, GN1 simplifies the complexity of the flavour tagging pipeline and is able to  
2784 achieve superior performance to the current state-of-the-art algorithms, which rely  
2785 on a two-tiered approach. Compared with DL1r, GN1 improves the light-jet rejection

2786 by a factor of  $\sim 1.8$  for jets in the  $t\bar{t}$  sample with  $20 < p_T < 250 \text{ GeV}$  at the 70%  
2787  $b$ -jet WP and by a factor of  $\sim 6$  for jets in the  $Z'$  sample with  $250 < p_T < 5000 \text{ GeV}$   
2788 for a corresponding  $b$ -jet efficiency of 30%. GN1 also demonstrates a significant  
2789 improvement in the discrimination between  $b$ - and  $c$ -jets, which also contributes to  
2790 improved  $c$ -tagging performance. In the high- $p_T$  regime, GN1 improves the  $b$ -jet  
2791 tagging efficiency by 100% for a fixed light-jet rejection of 100. Initial validation of  
2792 the model in data has been performed. The level of agreement between the simulation  
2793 and data that is observed is similar to previous flavour tagging algorithms. GN1 has  
2794 been successfully deployed in the ATLAS High Level Trigger, and shows promising  
2795 performance when trained on high pile-up samples corresponding to the HL-LHC  
2796 conditions. Ultimately the improved jet tagging performance enabled by the new  
2797 algorithm will have a large impact across a broad spectrum of the ATLAS physics  
2798 programme.

2799 This thesis demonstrates that even with suboptimal track reconstruction in this  
2800 regime, it is possible to make algorithmic advancements to the flavour tagging pipeline  
2801 to improve the identification of  $b$ -jets. This work has impacts for any analysis which  
2802 relies on the identification of  $b$ -jets, including those which are sensitive to the Higgs  
2803 boson.

2804 Analysis of  $VH$ ,  $H \rightarrow b\bar{b}$  events was also carried out with  $139 \text{ fb}^{-1}$  of Run 2  
2805 ATLAS at  $\sqrt{s} = 13 \text{ TeV}$ . Various background modelling uncertainties were derived  
2806 and investigations into the fit model were carried out. The analysis observed a  
2807 signal strength of  $\mu_{VH}^{bb} = 0.72^{+0.39}_{-0.36} = 0.72^{+0.29}_{-0.28}(\text{stat.})^{+0.26}_{-0.22}(\text{syst.})$  corresponding to an  
2808 observed (expected) significance of  $2.1\sigma$  ( $2.7\sigma$ ). The result was validated using a  
2809 simultaneous fit to the  $VZ$ ,  $Z \rightarrow b\bar{b}$  process, which acts as a cross check to validate  
2810 the primary analysis. The results of the analysis are the most precise measurements  
2811 available in the high- $p_T$  for the  $VH$ ,  $H \rightarrow b\bar{b}$  process. The high- $p_T$  region is of  
2812 particular interest as it is a region of phase space with good sensitivity to new physics.

## 2813 8.2 Future Work

2814 Additional algorithmic improvements are likely to yield further improved flavour  
2815 tagging performance. Aside from these, large improvements to the flavour tagging  
2816 performance at high- $p_T$  will be possible if the  $b$ -hadron decay track reconstruction

efficiency and accuracy is improved. Investigations into such improvements, for example loosening the track reconstruction requirements in high- $p_T$  environments, are currently ongoing.

At the moment only the tracks from the Inner Detector and kinematic information about the jet are provided as inputs to the tagging algorithms. In Chapter 6 it was shown that the addition of a simple track-level variable corresponding to the ID of the reconstruction lepton to the model improved tagging performance. However there is still untapped potential in the form of additional information from the full parameters of the reconstructed leptons (making full use of the Calorimeters and Muon Spectrometer), the calorimeter clusters, and even the individual clusters which are used to reconstruct tracks. Providing such additional inputs to the model is likely to complement the information provided by the tracks and further improve performance.

Additional auxiliary training objectives may yield improved performance and also help to add to the explainability of the model. Regression of jet-level quantities such as the transverse momentum and mass, in addition to the truth  $b$ -hadron decay length are promising targets.

The GN1 architecture can be easily optimised for new use cases and topologies, as demonstrated by the studies described in Section 6.6. Other opportunities include a model with only cluster-based inputs, which could be used for a fast trigger preselection on jets without the need to run the computationally expensive tracking algorithms, or improved primary vertexing and pile-up jet tagging algorithms.

For an improved analysis of the  $VH$ ,  $H \rightarrow b\bar{b}$  process, the following considerations could be taken into account. Firstly, the addition of Run 3 data will provide a significant increase in statistics and a corresponding reduction in statistical uncertainties. Improved  $b$ -tagging, enabled by the GN1 model, will also improve the sensitivity of the analysis through improvements in the signal-to-background ratio. A dedicated  $X \rightarrow bb$  version of GN1 which is trained to identify the flavour of large- $R$  jets directly would also be of benefit. Improvements in signal-to-background ratio could also be further improved through the use of a dedicated MVA to select signal events, rather than relying on a series of selection cuts. Finally, the dominant systematic uncertainties relating to the modelling of large- $R$  jets could be reduced via improved reconstruction and calibration techniques.

2850    **Bibliography**

- 2851 [1] A. Buckley, *A class for typesetting academic theses*, (2010). [http://ctan.tug.org/  
2852 tex-archive/macros/latex/contrib/heptesis/heptesis.pdf](http://ctan.tug.org/tex-archive/macros/latex/contrib/heptesis/heptesis.pdf).
- 2853 [2] J. Shlomi, S. Ganguly, E. Gross, K. Cranmer, Y. Lipman, H. Serviansky et al.,  
2854 *Secondary vertex finding in jets with neural networks*, *The European Physical Journal C* 81 (2021) .  
2855
- 2856 [3] ATLAS Collaboration, *Graph Neural Network Jet Flavour Tagging with the ATLAS  
2857 Detector*, ATL-PHYS-PUB-2022-027 (2022).
- 2858 [4] L. Morel, Z. Yao, P. Cladé and S. Guellati-Khélifa, *Determination of the  
2859 fine-structure constant with an accuracy of 81 parts per trillion*, *Nature* 588 (2020)  
2860 pp. 61–65.
- 2861 [5] T. Sailer, V. Debierre, Z. Harman, F. Heiße, C. König, J. Morgner et al.,  
2862 *Measurement of the bound-electron g-factor difference in coupled ions*, *Nature* 606  
2863 (2022) pp. 479–483.
- 2864 [6] CDF collaboration, *Observation of top quark production in  $\bar{p}p$  collisions*, *Phys. Rev.  
2865 Lett.* 74 (1995) pp. 2626–2631 [[hep-ex/9503002](#)].
- 2866 [7] D0 collaboration, *Observation of the top quark*, *Phys. Rev. Lett.* 74 (1995)  
2867 pp. 2632–2637 [[hep-ex/9503003](#)].
- 2868 [8] S. W. Herb et al., *Observation of a Dimuon Resonance at 9.5-GeV in 400-GeV  
2869 Proton-Nucleus Collisions*, *Phys. Rev. Lett.* 39 (1977) pp. 252–255.
- 2870 [9] UA1 collaboration, *Experimental Observation of Isolated Large Transverse Energy  
2871 Electrons with Associated Missing Energy at  $\sqrt{s} = 540$  GeV*, *Phys. Lett. B* 122  
2872 (1983) pp. 103–116.
- 2873 [10] DONUT collaboration, *Observation of tau neutrino interactions*, *Phys. Lett. B* 504  
2874 (2001) pp. 218–224 [[hep-ex/0012035](#)].

- 2875 [11] F. Englert and R. Brout, *Broken Symmetry and the Mass of Gauge Vector Mesons*,  
2876 *Phys. Rev. Lett.* 13 (1964) pp. 321–323.
- 2877 [12] P. W. Higgs, *Broken Symmetries and the Masses of Gauge Bosons*, *Phys. Rev. Lett.*  
2878 13 (1964) pp. 508–509.
- 2879 [13] G. S. Guralnik, C. R. Hagen and T. W. B. Kibble, *Global Conservation Laws and*  
2880 *Massless Particles*, *Phys. Rev. Lett.* 13 (1964) pp. 585–587.
- 2881 [14] ATLAS Collaboration, *Observation of a new particle in the search for the Standard*  
2882 *Model Higgs boson with the ATLAS detector at the LHC*, *Phys. Lett. B* 716 (2012)  
2883 p. 1 [[1207.7214](#)].
- 2884 [15] CMS Collaboration, *Observation of a new boson at a mass of 125 GeV with the CMS*  
2885 *experiment at the LHC*, *Phys. Lett. B* 716 (2012) p. 30 [[1207.7235](#)].
- 2886 [16] Particle Data Group collaboration, *Review of Particle Physics*, *PTEP* 2022 (2022)  
2887 p. 083C01.
- 2888 [17] C. N. Yang and R. L. Mills, *Conservation of isotopic spin and isotopic gauge*  
2889 *invariance*, *Phys. Rev.* 96 (1954) pp. 191–195.
- 2890 [18] S. L. Glashow, *Partial Symmetries of Weak Interactions*, *Nucl. Phys.* 22 (1961)  
2891 pp. 579–588.
- 2892 [19] S. Weinberg, *A Model of Leptons*, *Phys. Rev. Lett.* 19 (1967) pp. 1264–1266.
- 2893 [20] A. Salam, *Weak and Electromagnetic Interactions*, *Proceedings of the 8th Nobel*  
2894 *symposium*, Ed. N. Svartholm, Almqvist & Wiksell, 1968, Conf. Proc. C680519  
2895 (1968) pp. 367–377.
- 2896 [21] T. D. Lee and C. N. Yang, *Question of parity conservation in weak interactions*,  
2897 *Phys. Rev.* 104 (1956) pp. 254–258.
- 2898 [22] C. S. Wu, E. Ambler, R. W. Hayward, D. D. Hopper and R. P. Hudson, *Experimental*  
2899 *test of parity conservation in beta decay*, *Phys. Rev.* 105 (1957) pp. 1413–1415.
- 2900 [23] R. L. Garwin, L. M. Lederman and M. Weinrich, *Observations of the failure of*  
2901 *conservation of parity and charge conjugation in meson decays: the magnetic moment*  
2902 *of the free muon*, *Phys. Rev.* 105 (1957) pp. 1415–1417.
- 2903 [24] Y. Nambu, *Quasi-particles and gauge invariance in the theory of superconductivity*,  
2904 *Phys. Rev.* 117 (1960) pp. 648–663.

- 2905 [25] J. Goldstone, *Field theories with « superconductor » solutions*, *Il Nuovo Cimento*  
2906 (1955-1965) 19 (1961) pp. 154–164.
- 2907 [26] LHC Higgs Cross Section Working Group collaboration, *Handbook of LHC Higgs*  
2908 *Cross Sections: 4. Deciphering the Nature of the Higgs Sector*, [[1610.07922](#)].
- 2909 [27] ATLAS Collaboration, *Observation of  $H \rightarrow b\bar{b}$  decays and VH production with the*  
2910 *ATLAS detector*, [ATLAS-CONF-2018-036](#) (2018).
- 2911 [28] CMS Collaboration, *Observation of Higgs Boson Decay to Bottom Quarks*, *Phys.*  
2912 *Rev. Lett.* 121 (2018) p. 121801 [[1808.08242](#)].
- 2913 [29] L. Evans and P. Bryant, *LHC Machine*, *JINST* 3 (2008) p. S08001.
- 2914 [30] The ALICE Collaboration, *The ALICE experiment at the CERN LHC*, *Journal of*  
2915 *Instrumentation* 3 (2008) pp. S08002–S08002.
- 2916 [31] CMS Collaboration, *The CMS experiment at the CERN LHC*, *JINST* 3 (2008)  
2917 p. S08004.
- 2918 [32] The LHCb Collaboration, *The LHCb detector at the LHC*, *Journal of*  
2919 *Instrumentation* 3 (2008) pp. S08005–S08005.
- 2920 [33] ATLAS Collaboration, *The ATLAS Experiment at the CERN Large Hadron Collider*,  
2921 *JINST* 3 (2008) p. S08003.
- 2922 [34] ATLAS Collaboration, *Integrated luminosity summary plots for 2011-2012 data*  
2923 *taking*, (2022). <https://twiki.cern.ch/twiki/bin/view/AtlasPublic/LuminosityPublicResults>.
- 2925 [35] ATLAS Collaboration, *Public ATLAS Luminosity Results for Run-2 of the LHC*,  
2926 (2022). <https://twiki.cern.ch/twiki/bin/view/AtlasPublic/LuminosityPublicResultsRun2>.
- 2928 [36] CERN, *The accelerator complex*, (2012).  
2929 <http://public.web.cern.ch/public/en/research/AccelComplex-en.html>.
- 2930 [37] G. C. Strong, *On the impact of selected modern deep-learning techniques to the*  
2931 *performance and celerity of classification models in an experimental high-energy*  
2932 *physics use case*, [[2002.01427](#)].
- 2933 [38] ATLAS Collaboration, *Atlas track reconstruction – general overview*, (2022).  
2934 <https://atlassoftwaredocs.web.cern.ch/trackingTutorial/idoverview/>.

- 2935 [39] ATLAS Collaboration, *Performance of b-jet identification in the ATLAS experiment*,  
2936 *JINST* 11 (2016) p. P04008 [[1512.01094](#)].
- 2937 [40] ATLAS Collaboration, *Luminosity determination in pp collisions at  $\sqrt{s} = 13 \text{ TeV}$*   
2938 *using the ATLAS detector at the LHC*, *ATLAS-CONF-2019-021* (2019).
- 2939 [41] ATLAS Collaboration, *ATLAS Detector and Physics Performance: Technical Design*  
2940 *Report, Volume 1*, ATLAS-TDR-14; CERN-LHCC-99-014, Geneva (1999).  
2941 <https://cds.cern.ch/record/391176>.
- 2942 [42] ATLAS Collaboration, *Status of the ATLAS Experiment*, Tech. Rep., Geneva (2010).  
2943 <https://cds.cern.ch/record/1237407>.
- 2944 [43] ATLAS Collaboration, *ATLAS Inner Tracker Pixel Detector: Technical Design*  
2945 *Report*, ATLAS-TDR-030; CERN-LHCC-2017-021 (2017).  
2946 <https://cds.cern.ch/record/2285585>.
- 2947 [44] ATLAS Collaboration, *ATLAS Inner Tracker Strip Detector: Technical Design*  
2948 *Report*, ATLAS-TDR-025; CERN-LHCC-2017-005 (2017).  
2949 <https://cds.cern.ch/record/2257755>.
- 2950 [45] ATLAS Collaboration, *The inner detector*, (2022).  
2951 <https://atlas.cern/Discover/Detector/Inner-Detector>.
- 2952 [46] ATLAS Collaboration, *ATLAS Insertable B-Layer: Technical Design Report*,  
2953 ATLAS-TDR-19; CERN-LHCC-2010-013 (2010).  
2954 <https://cds.cern.ch/record/1291633>.
- 2955 [47] B. Abbott et al., *Production and integration of the ATLAS Insertable B-Layer*,  
2956 *JINST* 13 (2018) p. T05008 [[1803.00844](#)].
- 2957 [48] ATLAS Collaboration, *Operation and performance of the ATLAS semiconductor*  
2958 *tracker*, *JINST* 9 (2014) p. P08009 [[1404.7473](#)].
- 2959 [49] ATLAS Collaboration, *Calorimeter*, (2022).  
2960 <https://atlas.cern/Discover/Detector/Calorimeter>.
- 2961 [50] ATLAS Collaboration, *ATLAS Tile Calorimeter: Technical Design Report*,  
2962 ATLAS-TDR-3; CERN-LHCC-96-042, Geneva (1996).  
2963 <https://cds.cern.ch/record/331062>.
- 2964 [51] ATLAS Collaboration, *Muon reconstruction performance of the ATLAS detector in*  
2965 *proton–proton collision data at  $\sqrt{s} = 13 \text{ TeV}$* , *Eur. Phys. J. C* 76 (2016) p. 292

- 2966 [1603.05598].
- 2967 [52] ATLAS Collaboration, *Muon spectrometer*, (2022).  
2968 <https://atlas.cern/Discover/Detector/Muon-Spectrometer>.
- 2969 [53] ATLAS Collaboration, *Performance of the ATLAS trigger system in 2015*, *Eur. Phys. J. C* 77 (2017) p. 317 [1611.09661].
- 2970 [54] ATLAS Collaboration, *The ATLAS Collaboration Software and Firmware*,  
2971 *ATL-SOFT-PUB-2021-001* (2021).
- 2972 [55] T. Cornelissen, M. Elsing, S. Fleischmann, W. Liebig and E. Moyse, *Concepts, Design and Implementation of the ATLAS New Tracking (NEWT)*, .
- 2973 [56] ATLAS Collaboration, *The Optimization of ATLAS Track Reconstruction in Dense Environments*, *ATL-PHYS-PUB-2015-006* (2015).
- 2974 [57] ATLAS Collaboration, *Performance of the ATLAS track reconstruction algorithms in dense environments in LHC Run 2*, *Eur. Phys. J. C* 77 (2017) p. 673 [1704.07983].
- 2975 [58] ATLAS Collaboration, *A neural network clustering algorithm for the ATLAS silicon pixel detector*, *JINST* 9 (2014) p. P09009 [1406.7690].
- 2976 [59] R. Jansky, *Truth Seeded Reconstruction for Fast Simulation in the ATLAS Experiment*, Ph.D. Thesis, Innsbruck U., 2013.  
2977 <https://cds.cern.ch/record/1625231>.
- 2978 [60] ATLAS Collaboration, *Reconstruction of primary vertices at the ATLAS experiment in Run 1 proton–proton collisions at the LHC*, *Eur. Phys. J. C* 77 (2017) p. 332 [1611.10235].
- 2979 [61] ATLAS Collaboration, *ATLAS b-jet identification performance and efficiency measurement with  $t\bar{t}$  events in  $pp$  collisions at  $\sqrt{s} = 13$  TeV*, *Eur. Phys. J. C* 79 (2019) p. 970 [1907.05120].
- 2980 [62] ATLAS Collaboration, *Secondary vertex finding for jet flavour identification with the ATLAS detector*, *ATL-PHYS-PUB-2017-011* (2017).
- 2981 [63] M. Cacciari, G. P. Salam and G. Soyez, *The anti- $k_t$  jet clustering algorithm*, *JHEP* 04 (2008) p. 063 [0802.1189].
- 2982 [64] M. Cacciari, G. P. Salam and G. Soyez, *Fastjet user manual*, *Eur.Phys.J. C*72 (2012)  
2983 p. 1896 [1111.6097].

- 2996 [65] M. Cacciari, G. P. Salam and G. Soyez, *The Catchment Area of Jets*, *JHEP* **04**  
2997 (2008) p. 005 [[0802.1188](#)].
- 2998 [66] ATLAS Collaboration, *Tagging and suppression of pileup jets with the ATLAS*  
2999 *detector*, [ATLAS-CONF-2014-018](#) (2014).
- 3000 [67] ATLAS Collaboration, *Topological cell clustering in the ATLAS calorimeters and its*  
3001 *performance in LHC Run 1*, *Eur. Phys. J. C* **77** (2017) p. 490 [[1603.02934](#)].
- 3002 [68] ATLAS Collaboration, *Jet reconstruction and performance using particle flow with*  
3003 *the ATLAS Detector*, *Eur. Phys. J. C* **77** (2017) p. 466 [[1703.10485](#)].
- 3004 [69] ATLAS Collaboration, *Jet energy scale measurements and their systematic*  
3005 *uncertainties in proton–proton collisions at  $\sqrt{s} = 13\text{ TeV}$  with the ATLAS detector*,  
3006 *Phys. Rev. D* **96** (2017) p. 072002 [[1703.09665](#)].
- 3007 [70] J. M. Butterworth, A. R. Davison, M. Rubin and G. P. Salam, *Jet Substructure as a*  
3008 *New Higgs Search Channel at the Large Hadron Collider*, *Phys. Rev. Lett.* **100** (2008)  
3009 p. 242001 [[0802.2470](#)].
- 3010 [71] ATLAS collaboration, *Measurement of the associated production of a Higgs boson*  
3011 *decaying into  $b$ -quarks with a vector boson at high transverse momentum in  $pp$*   
3012 *collisions at  $\sqrt{s} = 13\text{ TeV}$  with the ATLAS detector*, *Phys. Lett. B* **816** (2021)  
3013 p. 136204 [[2008.02508](#)].
- 3014 [72] ATLAS collaboration, *Performance of jet substructure techniques for large- $R$  jets in*  
3015 *proton-proton collisions at  $\sqrt{s} = 7\text{ TeV}$  using the ATLAS detector*, *JHEP* **09** (2013)  
3016 p. 076 [[1306.4945](#)].
- 3017 [73] ATLAS Collaboration, *In situ calibration of large-radius jet energy and mass in*  
3018 *13 TeV proton–proton collisions with the ATLAS detector*, *Eur. Phys. J. C* **79** (2019)  
3019 p. 135 [[1807.09477](#)].
- 3020 [74] D. Krohn, J. Thaler and L.-T. Wang, *Jets with Variable  $R$* , *JHEP* **06** (2009) p. 059  
3021 [[0903.0392](#)].
- 3022 [75] ATLAS Collaboration, *Variable Radius, Exclusive- $k_T$ , and Center-of-Mass Subjet*  
3023 *Reconstruction for Higgs( $\rightarrow b\bar{b}$ ) Tagging in ATLAS*, [ATL-PHYS-PUB-2017-010](#)  
3024 (2017).
- 3025 [76] ATLAS Collaboration, *Improved electron reconstruction in ATLAS using the*  
3026 *Gaussian Sum Filter-based model for bremsstrahlung*, [ATLAS-CONF-2012-047](#) (2012).

- 3027 [77] ATLAS Collaboration, *Electron efficiency measurements with the ATLAS detector*  
3028       *using the 2015 LHC proton–proton collision data*, **ATLAS-CONF-2016-024** (2016).
- 3029 [78] ATLAS Collaboration, *Performance of missing transverse momentum reconstruction*  
3030       *with the ATLAS detector using proton–proton collisions at  $\sqrt{s} = 13 \text{ TeV}$* , **Eur. Phys.**  
3031       **J. C** **78** (2018) p. 903 [[1802.08168](#)].
- 3032 [79] ATLAS Collaboration, *Observation of  $H \rightarrow b\bar{b}$  decays and  $VH$  production with the*  
3033       *ATLAS detector*, **Phys. Lett. B** **786** (2018) p. 59 [[1808.08238](#)].
- 3034 [80] ATLAS Collaboration, *Observation of Higgs boson production in association with a*  
3035       *top quark pair at the LHC with the ATLAS detector*, **Phys. Lett. B** **784** (2018) p. 173  
3036       [[1806.00425](#)].
- 3037 [81] ATLAS Collaboration, *Search for new resonances in mass distributions of jet pairs*  
3038       *using  $139 \text{ fb}^{-1}$  of  $pp$  collisions at  $\sqrt{s} = 13 \text{ TeV}$  with the ATLAS detector*, **JHEP** **03**  
3039       (2020) p. 145 [[1910.08447](#)].
- 3040 [82] ATLAS Collaboration, *Identification of Jets Containing  $b$ -Hadrons with Recurrent*  
3041       *Neural Networks at the ATLAS Experiment*, **ATL-PHYS-PUB-2017-003** (2017).
- 3042 [83] ATLAS Collaboration, *Deep Sets based Neural Networks for Impact Parameter*  
3043       *Flavour Tagging in ATLAS*, **ATL-PHYS-PUB-2020-014** (2020).
- 3044 [84] ATLAS Collaboration, *Expected performance of the ATLAS  $b$ -tagging algorithms in*  
3045       *Run-2*, **ATL-PHYS-PUB-2015-022** (2015).
- 3046 [85] ATLAS Collaboration, *Optimisation and performance studies of the ATLAS*  
3047        *$b$ -tagging algorithms for the 2017-18 LHC run*, **ATL-PHYS-PUB-2017-013** (2017).
- 3048 [86] ATLAS collaboration, *ATLAS flavour-tagging algorithms for the LHC Run 2  $pp$*   
3049       *collision dataset*, [[2211.16345](#)].
- 3050 [87] P. Nason, *A new method for combining nlo qcd with shower monte carlo algorithms*,  
3051       *Journal of High Energy Physics* **2004** (2004) p. 040–040.
- 3052 [88] S. Frixione, G. Ridolfi and P. Nason, *A positive-weight next-to-leading-order monte*  
3053       *carlo for heavy flavour hadroproduction*, *Journal of High Energy Physics* **2007** (2007)  
3054       p. 126–126.
- 3055 [89] S. Frixione, P. Nason and C. Oleari, *Matching nlo qcd computations with parton*  
3056       *shower simulations: the powheg method*, *Journal of High Energy Physics* **2007** (2007)  
3057       p. 070–070.

- 3058 [90] S. Alioli, P. Nason, C. Oleari and E. Re, *A general framework for implementing nlo*  
3059 *calculations in shower monte carlo programs: the powheg box*, *Journal of High Energy*  
3060 *Physics* **2010** (2010) .
- 3061 [91] NNPDF collaboration, *Parton distributions for the LHC run II*, *JHEP* **04** (2015)  
3062 p. 040 [[1410.8849](#)].
- 3063 [92] ATLAS Collaboration, *Studies on top-quark Monte Carlo modelling for Top2016*,  
3064 *ATL-PHYS-PUB-2016-020* (2016).
- 3065 [93] T. Sjöstrand, S. Ask, J. R. Christiansen, R. Corke, N. Desai, P. Ilten et al., *An*  
3066 *introduction to PYTHIA 8.2*, *Comput. Phys. Commun.* **191** (2015) p. 159  
3067 [[1410.3012](#)].
- 3068 [94] ATLAS Collaboration, *ATLAS Pythia 8 tunes to 7 TeV data*,  
3069 *ATL-PHYS-PUB-2014-021* (2014).
- 3070 [95] R. D. Ball et al., *Parton distributions with LHC data*, *Nucl. Phys. B* **867** (2013)  
3071 p. 244 [[1207.1303](#)].
- 3072 [96] D. J. Lange, *The EvtGen particle decay simulation package*, *Nucl. Instrum. Meth. A*  
3073 **462** (2001) p. 152.
- 3074 [97] ATLAS Collaboration, *The ATLAS Simulation Infrastructure*, *Eur. Phys. J. C* **70**  
3075 (2010) p. 823 [[1005.4568](#)].
- 3076 [98] GEANT4 Collaboration, S. Agostinelli et al., *GEANT4 – a simulation toolkit*, *Nucl.*  
3077 *Instrum. Meth. A* **506** (2003) p. 250.
- 3078 [99] B. R. Webber, *Fragmentation and hadronization*, *Int. J. Mod. Phys. A* **15S1** (2000)  
3079 pp. 577–606 [[hep-ph/9912292](#)].
- 3080 [100] Particle Data Group collaboration, *Review of particle physics*, *Phys. Rev. D* **98**  
3081 (2018) p. 030001.
- 3082 [101] ATLAS Collaboration, *Comparison of Monte Carlo generator predictions for bottom*  
3083 *and charm hadrons in the decays of top quarks and the fragmentation of high  $p_T$  jets*,  
3084 *ATL-PHYS-PUB-2014-008* (2014).
- 3085 [102] Nazar Bartosik, *Diagram showing the common principle of identification of jets*  
3086 *initiated by b-hadron decays*, (2022).  
3087 [https://en.m.wikipedia.org/wiki/File:B-tagging\\_diagram.png](https://en.m.wikipedia.org/wiki/File:B-tagging_diagram.png).
- 3088 [103] ATLAS Collaboration, *Tracking efficiency studies in dense environments*, (2022).

- 3089        <https://atlas.web.cern.ch/Atlas/GROUPS/PHYSICS/PLLOTS/IDTR-2022-03/>.
- 3090 [104] S. Adorni Braccesi Chiassi, *Vector Boson Tagging in the Context of the Search for  
3091 New Physics in the Fully Hadronic Final State*, Ph.D. Thesis, Geneva U., 2021.  
3092 [10.13097/archive-ouverte/unige:158558](https://archive-ouverte.unige:158558).
- 3093 [105] E. Boos et al., *Generic user process interface for event generators*, [[hep-ph/0109068](https://arxiv.org/abs/hep-ph/0109068)].
- 3094 [106] J. Alwall, A. Ballestrero, P. Bartalini, S. Belov, E. Boos, A. Buckley et al., *A  
3095 standard format for Les Houches Event Files*, *Computer Physics Communications*  
3096 **176** (2007) pp. 300–304.
- 3097 [107] K. Hornik, M. Stinchcombe and H. White, *Multilayer feedforward networks are  
3098 universal approximators*, *Neural Networks* **2** (1989) pp. 359–366.
- 3099 [108] D. E. Rumelhart, G. E. Hinton and R. J. Williams, *Learning representations by  
3100 back-propagating errors*, *nature* **323** (1986) pp. 533–536.
- 3101 [109] W. McCulloch and W. Pitts, *A logical calculus of the ideas immanent in nervous  
3102 activity*, *The bulletin of mathematical biophysics* **5** (1943) pp. 115–133.
- 3103 [110] J. Hopfield, *Neural networks and physical systems with emergent collective  
3104 computational abilities*, in *Spin Glass Theory and Beyond: An Introduction to the  
3105 Replica Method and Its Applications*, pp. 411–415, World Scientific, (1987).
- 3106 [111] A. F. Agarap, *Deep Learning using Rectified Linear Units (ReLU)*, *arXiv e-prints*  
3107 (2018) p. [arXiv:1803.08375](https://arxiv.org/abs/1803.08375) [[1803.08375](https://arxiv.org/abs/1803.08375)].
- 3108 [112] S. Elfwing, E. Uchibe and K. Doya, *Sigmoid-Weighted Linear Units for Neural  
3109 Network Function Approximation in Reinforcement Learning*, *arXiv e-prints* (2017)  
3110 p. [arXiv:1702.03118](https://arxiv.org/abs/1702.03118) [[1702.03118](https://arxiv.org/abs/1702.03118)].
- 3111 [113] Y. A. LeCun, L. Bottou, G. B. Orr and K.-R. Müller, *Efficient backprop*, in *Neural  
3112 networks: Tricks of the trade*, pp. 9–48, Springer, (2012).
- 3113 [114] D. P. Kingma and J. Ba, *Adam: A Method for Stochastic Optimization*, *arXiv  
3114 e-prints* (2014) [[1412.6980](https://arxiv.org/abs/1412.6980)].
- 3115 [115] H. Serviansky, N. Segol, J. Shlomi, K. Cranmer, E. Gross, H. Maron et al.,  
3116 *Set2Graph: Learning Graphs From Sets*, *arXiv e-prints* (2020) p. [arXiv:2002.08772](https://arxiv.org/abs/2002.08772)  
3117 [[2002.08772](https://arxiv.org/abs/2002.08772)].
- 3118 [116] P. W. Battaglia, J. B. Hamrick, V. Bapst, A. Sanchez-Gonzalez, V. Zambaldi,  
3119 M. Malinowski et al., *Relational inductive biases, deep learning, and graph networks*,

- 3120        *arXiv e-prints* (2018) p. arXiv:1806.01261 [[1806.01261](#)].
- 3121 [117] M. Zaheer, S. Kottur, S. Ravanbakhsh, B. Poczos, R. Salakhutdinov and A. Smola,  
3122        *Deep Sets*, *arXiv e-prints* (2017) p. arXiv:1703.06114 [[1703.06114](#)].
- 3123 [118] ATLAS Collaboration, *Muon reconstruction performance in early  $\sqrt{s} = 13$  TeV data*,  
3124        **ATL-PHYS-PUB-2015-037** (2015).
- 3125 [119] ATLAS Collaboration, *Electron reconstruction and identification in the ATLAS*  
3126        *experiment using the 2015 and 2016 LHC proton–proton collision data at*  
3127         $\sqrt{s} = 13$  TeV, *Eur. Phys. J. C* **79** (2019) p. 639 [[1902.04655](#)].
- 3128 [120] D. Hwang, J. Park, S. Kwon, K.-M. Kim, J.-W. Ha and H. J. Kim, *Self-supervised*  
3129        *Auxiliary Learning with Meta-paths for Heterogeneous Graphs*, *arXiv e-prints* (2021)  
3130        [[2007.08294](#)].
- 3131 [121] S. Brody, U. Alon and E. Yahav, *How Attentive are Graph Attention Networks?*,  
3132        *arXiv e-prints* (2021) [[2105.14491](#)].
- 3133 [122] A. Vaswani, N. Shazeer, N. Parmar, J. Uszkoreit, L. Jones, A. N. Gomez et al.,  
3134        *Attention Is All You Need*, *arXiv e-prints* (2017) [[1706.03762](#)].
- 3135 [123] D. P. Kingma and J. Ba, *Adam: A Method for Stochastic Optimization*, *arXiv*  
3136        *e-prints* (2014) [[1412.6980](#)].
- 3137 [124] J. Bai, F. Lu, K. Zhang et al., *ONNX: Open neural network exchange*, (2019).  
3138        <https://github.com/onnx/onnx>.
- 3139 [125] ATLAS Collaboration, *Performance of Run 3 HLT b-tagging with fast tracking,*  
3140        *Public b-Jet Trigger Plots for Collision Data*, (2022).  
3141        [https://twiki.cern.ch/twiki/bin/view/AtlasPublic/  
3142        BJetTriggerPublicResults#Performance\\_of\\_Run\\_3\\_HLT\\_b\\_taggi](https://twiki.cern.ch/twiki/bin/view/AtlasPublic/BJetTriggerPublicResults#Performance_of_Run_3_HLT_b_taggi).
- 3143 [126] ATLAS Collaboration, *Neural Network Jet Flavour Tagging with the Upgraded*  
3144        *ATLAS Inner Tracker Detector at the High-Luminosity LHC*,  
3145        **ATL-PHYS-PUB-2022-047** (2022).
- 3146 [127] ATLAS Collaboration, *Jet flavour tagging with GN1 and DL1d. generator*  
3147        *dependence, run 2 and run 3 data agreement studies*, (2023).  
3148        <https://atlas.web.cern.ch/Atlas/GROUPS/PHYSICS/PLOTS/FTAG-2023-01/>.
- 3149 [128] R. Lafaye, T. Plehn, M. Rauch, D. Zerwas and M. Duhrssen, *Measuring the Higgs*  
3150        *Sector*, *JHEP* **08** (2009) p. 009 [[0904.3866](#)].

- 3151 [129] ATLAS Collaboration, *Measurements of  $WH$  and  $ZH$  production in the  $H \rightarrow b\bar{b}$*   
3152 *decay channel in  $pp$  collisions at 13 TeV with the ATLAS detector*, *Eur. Phys. J. C*  
3153 **81** (2021) p. 178 [[2007.02873](#)].
- 3154 [130] ATLAS Collaboration, *Measurement of the associated production of a Higgs boson*  
3155 *decaying into  $b$ -quarks with a vector boson at high transverse momentum in  $pp$*   
3156 *collisions at  $\sqrt{s} = 13$  TeV with the ATLAS detector*, *Phys. Lett. B* **816** (2021)  
3157 p. 136204 [[2008.02508](#)].
- 3158 [131] K. Mimasu, V. Sanz and C. Williams, *Higher order QCD predictions for associated*  
3159 *Higgs production with anomalous couplings to gauge bosons*, *JHEP* **08** (2016) p. 039  
3160 [[1512.02572](#)].
- 3161 [132] ATLAS Collaboration, *Performance of jet substructure techniques for large- $R$  jets in*  
3162 *proton–proton collisions at  $\sqrt{s} = 7$  TeV using the ATLAS detector*, *JHEP* **09** (2013)  
3163 p. 076 [[1306.4945](#)].
- 3164 [133] ATLAS Collaboration, *Measurements of  $b$ -jet tagging efficiency with the ATLAS*  
3165 *detector using  $t\bar{t}$  events at  $\sqrt{s} = 13$  TeV*, *JHEP* **08** (2018) p. 089 [[1805.01845](#)].
- 3166 [134] ATLAS Collaboration, *Calibration of light-flavour  $b$ -jet mistagging rates using*  
3167 *ATLAS proton–proton collision data at  $\sqrt{s} = 13$  TeV*, *ATLAS-CONF-2018-006*  
3168 (2018).
- 3169 [135] ATLAS Collaboration, *Measurement of  $b$ -tagging efficiency of  $c$ -jets in  $t\bar{t}$  events using*  
3170 *a likelihood approach with the ATLAS detector*, *ATLAS-CONF-2018-001* (2018).
- 3171 [136] ATLAS Collaboration, *Flavor Tagging with Track-Jets in Boosted Topologies with the*  
3172 *ATLAS Detector*, *ATL-PHYS-PUB-2014-013* (2014).
- 3173 [137] ATLAS Collaboration, *Identification of boosted Higgs bosons decaying into  $b$ -quark*  
3174 *pairs with the ATLAS detector at 13 TeV*, *Eur. Phys. J. C* **79** (2019) p. 836  
3175 [[1906.11005](#)].
- 3176 [138] S. Alioli, P. Nason, C. Oleari and E. Re, *A general framework for implementing NLO*  
3177 *calculations in shower Monte Carlo programs: the POWHEG BOX*, *JHEP* **06** (2010)  
3178 p. 043 [[1002.2581](#)].
- 3179 [139] ATLAS collaboration, *Measurement of the  $Z/\gamma^*$  boson transverse momentum*  
3180 *distribution in  $pp$  collisions at  $\sqrt{s} = 7$  TeV with the ATLAS detector*, *JHEP* **09**  
3181 (2014) p. 145 [[1406.3660](#)].
- 3182 [140] G. Cullen, N. Greiner, G. Heinrich, G. Luisoni, P. Mastrolia, G. Ossola et al.,

- 3183        *Automated one-loop calculations with GoSam*, *Eur. Phys. J. C* 72 (2012) p. 1889  
3184        [[1111.2034](#)].
- 3185        [141] K. Hamilton, P. Nason and G. Zanderighi, *MINLO: multi-scale improved NLO*,  
3186        *JHEP* 10 (2012) p. 155 [[1206.3572](#)].
- 3187        [142] G. Luisoni, P. Nason, C. Oleari and F. Tramontano,  *$HW^\pm/HZ + 0$  and 1 jet at*  
3188        *NLO with the POWHEG BOX interfaced to GoSam and their merging within*  
3189        *MiNLO*, *JHEP* 10 (2013) p. 083 [[1306.2542](#)].
- 3190        [143] M. L. Ciccolini, S. Dittmaier and M. Krämer, *Electroweak radiative corrections to*  
3191        *associated WH and ZH production at hadron colliders*, *Phys. Rev. D* 68 (2003)  
3192        p. 073003 [[hep-ph/0306234](#)].
- 3193        [144] O. Brein, A. Djouadi and R. Harlander, *NNLO QCD corrections to the*  
3194        *Higgs-strahlung processes at hadron colliders*, *Phys. Lett. B* 579 (2004) pp. 149–156  
3195        [[hep-ph/0307206](#)].
- 3196        [145] G. Ferrera, M. Grazzini and F. Tramontano, *Associated Higgs-W-Boson Production*  
3197        *at Hadron Colliders: a Fully Exclusive QCD Calculation at NNLO*, *Phys. Rev. Lett.*  
3198        107 (2011) p. 152003 [[1107.1164](#)].
- 3199        [146] O. Brein, R. V. Harlander, M. Wiesemann and T. Zirke, *Top-quark mediated effects*  
3200        *in hadronic Higgs-Strahlung*, *Eur. Phys. J. C* 72 (2012) p. 1868 [[1111.0761](#)].
- 3201        [147] G. Ferrera, M. Grazzini and F. Tramontano, *Higher-order QCD effects for associated*  
3202        *WH production and decay at the LHC*, *JHEP* 04 (2014) p. 039 [[1312.1669](#)].
- 3203        [148] G. Ferrera, M. Grazzini and F. Tramontano, *Associated ZH production at hadron*  
3204        *colliders: The fully differential NNLO QCD calculation*, *Phys. Lett. B* 740 (2015)  
3205        pp. 51–55 [[1407.4747](#)].
- 3206        [149] J. M. Campbell, R. K. Ellis and C. Williams, *Associated production of a Higgs boson*  
3207        *at NNLO*, *JHEP* 06 (2016) p. 179 [[1601.00658](#)].
- 3208        [150] L. Altenkamp, S. Dittmaier, R. V. Harlander, H. Rzehak and T. J. E. Zirke,  
3209        *Gluon-induced Higgs-strahlung at next-to-leading order QCD*, *JHEP* 02 (2013) p. 078  
3210        [[1211.5015](#)].
- 3211        [151] B. Hespel, F. Maltoni and E. Vryonidou, *Higgs and Z boson associated production via*  
3212        *gluon fusion in the SM and the 2HDM*, *JHEP* 06 (2015) p. 065 [[1503.01656](#)].
- 3213        [152] R. V. Harlander, A. Kulesza, V. Theeuwes and T. Zirke, *Soft gluon resummation for*

- 3214        *gluon-induced Higgs Strahlung*, *JHEP* 11 (2014) p. 082 [[1410.0217](#)].
- 3215        [153] R. V. Harlander, S. Liebler and T. Zirke, *Higgs Strahlung at the Large Hadron*  
3216        *Collider in the 2-Higgs-doublet model*, *JHEP* 02 (2014) p. 023 [[1307.8122](#)].
- 3217        [154] O. Brein, R. V. Harlander and T. J. E. Zirke, *vh@nnlo – Higgs Strahlung at hadron*  
3218        *colliders*, *Comput. Phys. Commun.* 184 (2013) pp. 998–1003 [[1210.5347](#)].
- 3219        [155] S. Frixione, G. Ridolfi and P. Nason, *A positive-weight next-to-leading-order Monte*  
3220        *Carlo for heavy flavour hadroproduction*, *JHEP* 09 (2007) p. 126 [[0707.3088](#)].
- 3221        [156] M. Czakon and A. Mitov, *Top++: A program for the calculation of the top-pair*  
3222        *cross-section at hadron colliders*, *Comput. Phys. Commun.* 185 (2014) p. 2930  
3223        [[1112.5675](#)].
- 3224        [157] S. Alioli, P. Nason, C. Oleari and E. Re, *NLO single-top production matched with*  
3225        *shower in POWHEG: s- and t-channel contributions*, *JHEP* 09 (2009) p. 111  
3226        [[0907.4076](#)].
- 3227        [158] N. Kidonakis, *Next-to-next-to-leading logarithm resummation for s-channel single top*  
3228        *quark production*, *Phys. Rev. D* 81 (2010) p. 054028 [[1001.5034](#)].
- 3229        [159] N. Kidonakis, *Next-to-next-to-leading-order collinear and soft gluon corrections for*  
3230        *t-channel single top quark production*, *Phys. Rev. D* 83 (2011) p. 091503 [[1103.2792](#)].
- 3231        [160] E. Re, *Single-top Wt-channel production matched with parton showers using the*  
3232        *POWHEG method*, *Eur. Phys. J. C* 71 (2011) p. 1547 [[1009.2450](#)].
- 3233        [161] N. Kidonakis, *Two-loop soft anomalous dimensions for single top quark associated*  
3234        *production with a  $W^-$  or  $H^-$* , *Phys. Rev. D* 82 (2010) p. 054018 [[1005.4451](#)].
- 3235        [162] T. Gleisberg, S. Höche, F. Krauss, M. Schönherr, S. Schumann, F. Siegert et al.,  
3236        *Event generation with SHERPA 1.1*, *JHEP* 02 (2009) p. 007 [[0811.4622](#)].
- 3237        [163] E. Bothmann et al., *Event generation with Sherpa 2.2*, *SciPost Phys.* 7 (2019) p. 034  
3238        [[1905.09127](#)].
- 3239        [164] F. Cascioli, P. Maierhöfer and S. Pozzorini, *Scattering Amplitudes with Open Loops*,  
3240        *Phys. Rev. Lett.* 108 (2012) p. 111601 [[1111.5206](#)].
- 3241        [165] T. Gleisberg and S. Höche, *Comix, a new matrix element generator*, *JHEP* 12 (2008)  
3242        p. 039 [[0808.3674](#)].
- 3243        [166] S. Schumann and F. Krauss, *A parton shower algorithm based on Catani–Seymour*

- 3244        *dipole factorisation*, *JHEP* 03 (2008) p. 038 [[0709.1027](#)].
- 3245    [167] S. Höche, F. Krauss, M. Schönher and F. Siegert, *QCD matrix elements + parton*  
3246        *showers. The NLO case*, *JHEP* 04 (2013) p. 027 [[1207.5030](#)].
- 3247    [168] S. Catani, L. Cieri, G. Ferrera, D. de Florian and M. Grazzini, *Vector Boson*  
3248        *Production at Hadron Colliders: a Fully Exclusive QCD Calculation at NNLO*, *Phys.*  
3249        *Rev. Lett.* 103 (2009) p. 082001 [[0903.2120](#)].
- 3250    [169] J. Butterworth et al., *PDF4LHC recommendations for LHC Run II*, *J. Phys. G* 43  
3251        (2016) p. 023001 [[1510.03865](#)].
- 3252    [170] A. Denner, S. Dittmaier, S. Kallweit and A. Mück, *Electroweak corrections to*  
3253        *Higgs-strahlung off W/Z bosons at the Tevatron and the LHC with Hawk*, *JHEP* 03  
3254        (2012) p. 075 [[1112.5142](#)].
- 3255    [171] A. Denner, S. Dittmaier, S. Kallweit and A. Mück, *HAWK 2.0: A Monte Carlo*  
3256        *program for Higgs production in vector-boson fusion and Higgs strahlung at hadron*  
3257        *colliders*, *Comput. Phys. Commun.* 195 (2015) pp. 161–171 [[1412.5390](#)].
- 3258    [172] ATLAS Collaboration, *Measurement of the Inelastic Proton–Proton Cross Section at*  
3259         $\sqrt{s} = 13\text{ TeV}$  *with the ATLAS Detector at the LHC*, *Phys. Rev. Lett.* 117 (2016)  
3260        p. 182002 [[1606.02625](#)].
- 3261    [173] L. A. Harland-Lang, A. D. Martin, P. Motylinski and R. S. Thorne, *Parton*  
3262        *distributions in the LHC era: MMHT 2014 PDFs*, *Eur. Phys. J. C*75 (2015) p. 204  
3263        [[1412.3989](#)].
- 3264    [174] S. Dulat, T.-J. Hou, J. Gao, M. Guzzi, J. Huston, P. Nadolsky et al., *New parton*  
3265        *distribution functions from a global analysis of quantum chromodynamics*, *Phys. Rev.*  
3266        D93 (2016) p. 033006 [[1506.07443](#)].
- 3267    [175] J. K. Anders and M. D’Onofrio, *V+Jets theoretical uncertainties estimation via a*  
3268        *parameterisation method*, Tech. Rep. ATL-COM-PHYS-2016-044, Geneva (2016).  
3269        <https://cds.cern.ch/record/2125718>.
- 3270    [176] ATLAS Collaboration, *Search for the Standard Model Higgs boson produced in*  
3271        *association with a vector boson and decaying to a pair of b-quarks using large-R jets*,  
3272        ATL-COM-PHYS-2019-1125 (2019).
- 3273    [177] J. Pumplin et al., *New generation of parton distributions with uncertainties from*  
3274        *global qcd analysis*, *JHEP* 07 (2002) p. 012 [[0201195](#)].

- 3275 [178] S. Frixione, E. Laenen, P. Motylinski, C. White and B. R. Webber, *Single-top*  
3276 *hadroproduction in association with a W boson*, *JHEP* 07 (2008) p. 029 [[0805.3067](#)].
- 3277 [179] ATLAS Collaboration, *Measurement of VH, H → bb* production as a function of the  
3278 *vector-boson transverse momentum in 13 TeV pp collisions with the ATLAS detector*,  
3279 *JHEP* 05 (2019) p. 141 [[1903.04618](#)].
- 3280 [180] ATLAS Collaboration, *Evidence for the H → bb* decay with the ATLAS detector,  
3281 *JHEP* 12 (2017) p. 024 [[1708.03299](#)].
- 3282 [181] LHC Higgs Cross Section Working Group, S. Dittmaier, C. Mariotti, G. Passarino  
3283 and R. Tanaka (Eds.), *Handbook of LHC Higgs Cross Sections: 2. Differential*  
3284 *Distributions*, *CERN-2012-002* (2012) [[1201.3084](#)].
- 3285 [182] LHC Higgs Cross Section Working Group, *Handbook of LHC Higgs Cross Sections: 3.*  
3286 *Higgs Properties*, *CERN-2013-004* (2013) [[1307.1347](#)].
- 3287 [183] L. Moneta, K. Belasco, K. Cranmer, S. Kreiss, A. Lazzaro, D. Piparo et al., *The*  
3288 *roostats project*, *arXiv preprint arXiv:1009.1003* (2010) .
- 3289 [184] R. Barlow and C. Beeston, *Fitting using finite Monte Carlo samples*, *Comput. Phys.*  
3290 *Commun.* 77 (1993) pp. 219–228.
- 3291 [185] G. Cowan, K. Cranmer, E. Gross and O. Vitells, *Asymptotic formulae for*  
3292 *likelihood-based tests of new physics*, *Eur. Phys. J. C* 71 (2011) p. 1554 [[1007.1727](#)].
- 3293 [186] J. R. Andersen et al., *Les Houches 2015: Physics at TeV Colliders Standard Model*  
3294 *Working Group Report*, [[1605.04692](#)].

# 3295 List of figures

<small>3296</small>	2.1	The Higgs potential $V(\phi)$ of the complex scalar field singlet $\phi = \phi_1 + i\phi_2$ , with a choice of $\mu^2 < 0$ leading to a continuous degeneracy in the true vacuum states. A false vacuum is present at the origin. . . . .	<small>3297</small> 21
<small>3299</small>	2.2	Higgs boson production cross sections as a function of Higgs mass ( $m_H$ ) at $\sqrt{s} = 13$ TeV [26]. Uncertainties are shown in the shaded bands. At $m_H = 125$ GeV, Higgs boson production is dominated by gluon-gluon fusion, vector boson fusion, associated production with vector bosons, and top quark fusion. . . . .	<small>3300</small> 26
<small>3301</small>	2.3	Diagrams for the four main Higgs boson production modes at the LHC for a Higgs mass $m_H = 125$ GeV at a centre of mass energy $\sqrt{s} = 13$ TeV. . . . .	<small>3302</small> 26
<small>3303</small>	2.4	Higgs boson branching ratios as a function of Higgs mass ( $m_H$ ) at $\sqrt{s} = 13$ TeV [26]. Uncertainties are shown in the shaded bands. At $m_H = 125$ GeV, the Higgs predominantly decays to a pair of $b$ -quarks, around 58% of the time. The leading subdominant decay mode is to a pair of $W$ bosons. . . . .	<small>3304</small> 27
<small>3305</small>	3.1	An overview of the CERN accelerator complex [36]. The LHC is fed by a series of accelerators starting with Linac2 (or Linac4 from 2020). Next are the Proton Synchrotron Booster, the Proton Synchrotron, and finally the Super Proton Synchrotron which injects protons into the LHC. . . . .	<small>3306</small> 30
<small>3307</small>	3.2	The coordinate system used at the ATLAS detector, showing the locations of the four main experiments located at various points around the LHC. The 3-vector momentum $\mathbf{p} = (p_x, p_y, p_z)$ is shown by the red arrow. Reproduced from Ref. [37]. . . . .	<small>3308</small> 31
<small>3309</small>			

3318	3.3 The track parameterisation used at the ATLAS detector. Five coordinates $(d_0, z_0, \phi, \theta, q/p)$ are specified, defined at the track's point of closest approach to the nominal interaction point at the origin of the coordinate system. The figure shows the three-momentum $\mathbf{p}$ and the transverse momentum $p_T$ (defined in Eq. (3.2)). The basis vectors $e_x$ , $e_y$ and $e_z$ are also shown. Reproduced from Ref. [38]. . . . .	33
3324	3.4 Delivered, recorded, and usable integrated luminosity as a function of time over the course of Run 2 [35]. A total of $139\text{ fb}^{-1}$ of collision data is labelled as good for physics, meaning all sub-detector systems were operating nominally. . . . .	35
3328	3.5 Average pile-up profiles measured by ATLAS during Run 2 [35]. . . . .	35
3329	3.6 A 3D model of the entire ATLAS detector [42]. Cutouts to the centre of the detector reveal the different sub-detectors which are arranged in concentric layers around the nominal interaction point. . . . .	36
3332	3.7 A 3D model of the ATLAS ID showing the pixel, SCT and TRT sub- detectors [45]. . . . .	37
3334	3.8 A cross-sectional view of the ATLAS ID, with the radii of the different barrel layers shown [38]. . . . .	38
3336	3.9 A schematic cross-sectional view of the ATLAS IBL [46]. . . . .	39
3337	3.10 The ATLAS calorimeters [49]. The ECal uses LAr-based detectors, while the HCal uses mainly scintillating tile detectors. In the forward region the HCal also includes the LAr hadronic end-caps. . . . .	41
3340	3.11 The ATLAS muon spectrometer [52]. . . . .	43
3341	3.12 Particles (left) which have enough separation will leave charge depositions which are resolved into separate clusters. Sufficiently close particles (right) can lead to merged clusters. Their combined energy deposits are recon- structed as a single merged cluster [57]. . . . .	47
3345	3.13 A sketch of electron reconstruction using the ATLAS detector [77]. Electron reconstruction makes use of the entire ID and the calorimeters. . . . .	52

3347	3.14 An overview of different high and low level taggers used in ATLAS. The low level taggers are IPxD, SV1 and JetFitter, and RNNIP and DIPS [61, 62, 82, 83]. The outputs of these taggers are fed into the high-level taggers DL1, DL1r and DL1d [85, 86]. . . . .	55
3351	4.1 The truth $b$ -hadron decay radius $L_{xy}$ as a function of truth transverse momentum $p_T$ for reconstructed $b$ -jets in $Z'$ events. Error bars show the standard deviation. The pixel layers are shown in dashed horizontal lines. . . . .	59
3354	4.2 Diagram of a typical $b$ -jet (blue) which has been produced in an event alongside two light jets (grey) [102]. The $b$ -hadron has travelled a significant distance (pink dashed line) from the primary interaction point (pink dot) before its decay. The large transverse impact parameter $d_0$ is a characteristic property of the trajectories of $b$ -hadron decay products. . . . .	59
3359	4.3 At lower $p_T$ (left) the decay length of the $b$ -hadron is on average reduced, and the decay tracks are less collimated. At higher $p_T$ (right) the $b$ -hadron decay length increases and the resulting decay tracks are more collimated and have less distance over which to diverge before reaching detector elements. As a result, the ID may be unable to resolve charged depositions from different particles, resulting merged clusters. . . . .	61
3365	4.4 $b$ -hadron decay track reconstruction efficiency as a function of truth $b$ -hadron $p_T$ [103]. Nominal track reconstruction is shown in black, while the track reconstruction efficiency for track candidates (i.e. the pre-ambiguity solver efficiency) is shown in green. For high- $p_T$ $b$ -hadrons, the ambiguity solver is overly aggressive in its removal of $b$ -hadron decay tracks. Suggestions for the improvement of the track reconstruction efficiency in this regime by the loosening of cuts in the ambiguity solver are shown in blue and red. . . . .	62
3372	4.5 Hit multiplicities on the IBL (left) and the pixel layers (right) as a function of the $p_T$ of the reconstructed track for tracks in jets in a $Z'$ sample at $\sqrt{s} = 13$ TeV. Tracks from the weak decay of the $b$ -hadron are shown in red, while fragmentation tracks (which are prompt) are in blue. Baseline tracks are those produced in the standard reconstruction described in Section 3.4.1, while pseudotrack represent the ideal performance of the ATLAS detector and are described in Section 3.4.1. . . . .	63

---

3379	4.6	The fraction of IBL (left) and B-layer (right) hits which are shared on 3380 <i>b</i> -hadron decay tracks as a function of the production radius of the <i>b</i> -hadron 3381      decay product for tracks in jets in a $Z'$ sample at $\sqrt{s} = 13$ TeV. Pseudotacks 3382      represent the ideal performance given the ATLAS detector, see Section 3.4.1.	65
3383	4.7	The average number of good (left) and wrong (right) IBL hits as a function 3384      of <i>b</i> -hadron $p_T$ for tracks using baseline tracking (black) and the modified 3385      version of the outlier removal procedure (red). . . . .	67
3386	4.8	(left) <i>b</i> -hadron decay track $d_0$ pulls ( $d_0/s(d_0)$ ) for baseline and modified 3387      GX2F tracks. (right) The absolute value of the $d_0$ pull as a function of the 3388      truth <i>b</i> -hadron transverse momentum. . . . .	68
3389	5.1	A diagram displaying the logical flow of a single neuron with three inputs 3390 $x_i^j$ . Each input is multiplied by a weight $\theta_j$ , and the resulting values are 3391      summed. A bias term $\theta_0$ is added, and the result $z$ is passed to an activation 3392      function. Each neuron can be thought of as a logistic regression model. . . . .	71
3393	5.2	The output of several common choices for the activation function $g(z)$ of 3394      an artificial neuron. The input $z$ is the output of the dot product between 3395      the activation and the weights, plus a bias term. . . . .	72
3396	5.3	Rate of fake tracks as a function of jet transverse momentum (left) and 3397 $\Delta R(\text{track}, \text{jet})$ (right) for jets in the $Z'$ sample. The rate of fake tracks 3398      increases significantly as a function of $p_T$ , and also increases as the distance 3399      to the jet axis decreases. . . . .	75
3400	5.4	The light-jet efficiency of the low level tagger SV1 for jets in the $Z'$ sample 3401      with $250 < p_T < 5000$ GeV, as a function of <i>b</i> -jet efficiency. The nominal 3402      tracking setup (black) is shown alongside the case where fake tracks which 3403      are not from the decay of a <i>b</i> -hadron are removed. The light-jet efficiency 3404      is decreased, demonstrating that the presence of fake tracks is detrimental 3405      to the algorithm performance. . . . .	76

3406	5.5 (left) Normalised histograms of the fake track classification model output 3407 separated for signal and fake tracks, and further separated by those tracks 3408 which are from the decay of a $b$ -hadron. (right) The ROC curve for all 3409 tracks (solid line) and tracks from the decay of a $b$ -hadron (dashed line). 3410 The plots show tracks in the combined $t\bar{t}$ and $Z'$ testing sample. The model 3411 is able to successfully discriminate between signal and fake tracks, and 3412 shows a very similar performance when looking specifically at tracks from 3413 the decay of a $b$ -hadron. . . . .	79
3414	5.6 (left) Normalised histogram of the $b$ -hadron track identification model 3415 output separated for tracks from the decay of a $b$ -hadron and tracks from 3416 other sources. The two groups are further separated into those tracks which 3417 are fake. (right) The ROC curve for all tracks (solid line). The plots show 3418 tracks in the combined $t\bar{t}$ and $Z'$ testing sample. . . . .	81
3419	5.7 The effect of applying the fake track identification algorithm together with 3420 the $b$ -hadron decay track identification on the jet tagging performance of 3421 SV1 for jets in the $Z'$ sample with $250 \text{ GeV} < p_T < 400 \text{ GeV}$ (left) and 3422 $400 \text{ GeV} < p_T < 1 \text{ TeV}$ (right). The nominal SV1 light-jet rejection (black) 3423 is compared to two working points of fake track removal, labelled “A” (red) 3424 and “B” (orange), which represent two different 2D working points of the 3425 track classification tools. Removal of fake tracks based on truth information 3426 is shown by the green curves. . . . .	82
3427	6.1 Comparison of the existing flavour tagging scheme (left) and GN1 (right). 3428 The existing approach utilises low-level algorithms (shown in blue), the 3429 outputs of which are fed into a high-level algorithm (DL1r). Instead 3430 of being used to guide the design of the manually optimised algorithms, 3431 additional truth information from the simulation is now being used as 3432 auxiliary training targets for GN1. The solid lines represent reconstructed 3433 information, whereas the dashed lines represent truth information [3]. . .	85
3434	6.2 The flow of information through a graph neural network layer for (left) a full 3435 implementation of the layer and (right) a deep sets model [117]. Reproduced 3436 from Ref. [116]. . . . .	88

---

3437	6.3 The inputs to GN1 are the two jet features ( $n_{\text{jf}} = 2$ ), and an array of 3438 $n_{\text{tracks}}$ , where each track is described by 21 track features ( $n_{\text{tf}} = 21$ ). The 3439 jet features are copied for each of the tracks, and the combined jet-track 3440 vectors of length 23 form the inputs of GN1 [3]. . . . .	93
3441	6.4 The network architecture of GN1. Inputs are fed into a per-track initialisa- 3442 tion network, which outputs an initial latent representation of each track. 3443 These representations are then used to populate the node features of a 3444 fully connected graph network. After the graph network, the resulting node 3445 representations are used to predict the jet flavour, the track origins, and 3446 the track-pair vertex compatibility [3]. . . . .	93
3447	6.5 Comparison between the DL1r and GN1 $b$ -tagging discriminant $D_b$ for jets 3448 in the $t\bar{t}$ sample. The 85% WP and the 60% WP are marked by the solid 3449 (dashed) lines for GN1 (DL1r), representing respectively the loosest and 3450 tightest WPs typically used by analyses. A value of $f_c = 0.018$ is used in the 3451 calculation of $D_b$ for DL1r and $f_c = 0.05$ is used for GN1. The distributions 3452 of the different jet flavours have been normalised to unity area [3]. . . . .	98
3453	6.6 The $c$ -jet (left) and light-jet (right) rejections as a function of the $b$ -jet 3454 tagging efficiency for jets in the $t\bar{t}$ sample with $20 < p_{\text{T}} < 250 \text{ GeV}$ . The 3455 ratio with respect to the performance of the DL1r algorithm is shown in 3456 the bottom panels. A value of $f_c = 0.018$ is used in the calculation of $D_b$ 3457 for DL1r and $f_c = 0.05$ is used for GN1 and GN1Lep. Binomial error bands 3458 are denoted by the shaded regions. The $x$ -axis range is chosen to display 3459 the $b$ -jet tagging efficiencies usually probed in these regions of phase space [3].	101
3460	6.7 The $c$ -jet (left) and light-jet (right) rejections as a function of the $b$ -jet 3461 tagging efficiency for jets in the $Z'$ sample with $250 < p_{\text{T}} < 5000 \text{ GeV}$ . The 3462 ratio with respect to the performance of the DL1r algorithm is shown in 3463 the bottom panels. A value of $f_c = 0.018$ is used in the calculation of $D_b$ 3464 for DL1r and $f_c = 0.05$ is used for GN1 and GN1Lep. Binomial error bands 3465 are denoted by the shaded regions. The $x$ -axis range is chosen to display 3466 the $b$ -jet tagging efficiencies usually probed in these regions of phase space [3].	101

---

3467      6.8    The $b$ -jet tagging efficiency for jets in the $t\bar{t}$ sample (left) and jets in the $Z'$ sample (right) as a function of jet $p_T$ with a fixed light-jet rejection of 100 in each bin. A value of $f_c = 0.018$ is used in the calculation of $D_b$ for DL1r and $f_c = 0.05$ is used for GN1 and GN1Lep. GN1 demonstrates improved performance with respect to DL1r across the $p_T$ range shown. Binomial error bands are denoted by the shaded regions [3]. . . . .	102
3473      6.9    The $b$ -jet (left) and light-jet (right) rejections as a function of the $c$ -jet tagging efficiency for $t\bar{t}$ jets with $20 < p_T < 250$ GeV. The ratio to the performance of the DL1r algorithm is shown in the bottom panels. Binomial error bands are denoted by the shaded regions. The $x$ -axis range is chosen to display the $c$ -jet tagging efficiencies usually probed in these regions of phase space [3]. . . . .	104
3479      6.10   The $b$ -jet (left) and light-jet (right) rejections as a function of the $c$ -jet tagging efficiency for $Z'$ jets with $250 < p_T < 5000$ GeV. The ratio to the performance of the DL1r algorithm is shown in the bottom panels. Binomial error bands are denoted by the shaded regions. The $x$ -axis range is chosen to display the $c$ -jet tagging efficiencies usually probed in these regions of phase space [3]. . . . .	104
3485      6.11   The $c$ -jet (left) and light-jet (right) rejections as a function of the $b$ -jet tagging efficiency for $t\bar{t}$ jets with $20 < p_T < 250$ GeV, for the nominal GN1, in addition to configurations where no (GN1 No Aux), only the track classification (GN1 TC) or only the vertexing (GN1 Vert) auxiliary objectives are deployed. The ratio to the performance of the DL1r algorithm is shown in the bottom panels. A value of $f_c = 0.018$ is used in the calculation of $D_b$ for DL1r and $f_c = 0.05$ is used for GN1 [3]. . . . .	106
3492      6.12   The $c$ -jet (left) and light-jet (right) rejections as a function of the $b$ -jet tagging efficiency for $Z'$ jets with $250 < p_T < 5000$ GeV, for the nominal GN1, in addition to configurations where no (GN1 No Aux), only the track classification (GN1 TC) or only the vertexing (GN1 Vert) auxiliary objectives are deployed. The ratio to the performance of the DL1r algorithm is shown in the bottom panels. A value of $f_c = 0.018$ is used in the calculation of $D_b$ for DL1r and $f_c = 0.05$ is used for GN1 [3]. . . . .	106

3499	6.13 A schematic showing the truth track origin and vertex information (left) compared with the predictions from GN1 (right). The diagrams show the truth (left) and predicted (right) structure of a $b$ -jet. The true and predicted origins of the tracks is shown by the coloured circles along the diagonal. The shaded black boxes show the groupings of tracks into different vertices. Vertices reconstructed by SV1 and JetFitter are also marked. Class probabilities $p_b$ , $p_c$ and $p_u$ are rounded to three significant figures. GN1 improves over SV1 and JetFitter by successfully determining the origins and vertex compatibility of all the tracks in the jet with the exception of the truth OtherSecondary track, which is misidentified as pile-up. . . . .	108
3509	6.14 A schematic showing the truth track origin and vertex information (left) compared with the predictions from GN1 (right). The diagrams show the truth (left) and predicted (right) structure of a $b$ -jet. The true and predicted origins of the tracks is shown by the coloured circles along the diagonal. The shaded black boxes show the groupings of tracks into different vertices. Vertices reconstructed by SV1 and JetFitter are also marked. Class probabilities $p_b$ , $p_c$ and $p_u$ are rounded to three significant figures. GN1 improves over SV1 and JetFitter by successfully determining the origins and vertex compatibility of all but one tracks in the jet. . . . .	108
3518	6.15 Heavy flavour vertex finding efficiency as a function of jet $p_T$ for $b$ -jets in the $t\bar{t}$ sample using the exclusive (left) and inclusive (right) vertex finding approaches. The exclusive vertexing approach includes single track vertices while the inclusive approach requires vertices to contain at least two tracks. Efficient vertex finding requires the recall of at least 65% of the tracks in the truth vertex, and allows no more than 50% of the tracks to be included incorrectly. Binomial error bands are denoted by the shaded regions. . .	111
3525	6.16 Heavy flavour vertex finding efficiency as a function of jet $p_T$ for $b$ -jets in the $Z'$ sample using the exclusive (left) and inclusive (right) vertex finding approaches. The exclusive vertexing approach includes single track vertices while the inclusive approach requires vertices to contain at least two tracks. Efficient vertex finding requires the recall of at least 65% of the tracks in the truth vertex, and allows no more than 50% of the tracks to be included incorrectly. Binomial error bands are denoted by the shaded regions. . .	111

3532	6.17 Vertex finding efficiency for other secondary decays as a function of jet $p_T$ for light-jets in the $t\bar{t}$ sample using the exclusive (left) and inclusive (right) vertex finding approaches. The exclusive vertexing approach includes single track vertices while the inclusive approach requires vertices to contain at least two tracks. Efficient vertex finding requires the recall of at least 65% of the tracks in the truth vertex, and allows no more than 50% of the tracks to be included incorrectly. Binomial error bands are denoted by the shaded regions. . . . .	112
3540	6.18 Vertex finding efficiency as a function of jet $p_T$ for light-jets in the $Z'$ sample using the exclusive (left) and inclusive (right) vertex finding approaches. The exclusive vertexing approach includes single track vertices while the inclusive approach requires vertices to contain at least two tracks. Efficient vertex finding requires the recall of at least 65% of the tracks in the truth vertex, and allows no more than 50% of the tracks to be included incorrectly. Binomial error bands are denoted by the shaded regions. . . . .	112
3547	6.19 ROC curves for the different groups of truth origin labels defined in Table 5.1 for jets in the $t\bar{t}$ sample (left) and jets in the $Z'$ sample (right). The FromB, FromBC and FromC labels have been combined, weighted by their relative abundance, into the Heavy Flavour category, and the Primary and OtherSecondary labels have similarly been combined into a single category. The mean weighted area under the ROC curves (AUC) is similar for both samples [3]. . . . .	115
3554	6.20 The $c$ -jet (left) and light-jet (right) rejections as a function of the $b$ -jet tagging efficiency for $t\bar{t}$ jets with $20 < p_T < 250$ GeV, for the looser track selection trainings of GN1. The ratio to the performance of the baseline GN1 model is shown in the bottom panels. A value of $f_c = 0.05$ is used for all models. Binomial error bands are denoted by the shaded regions. . . . .	117
3559	6.21 The $c$ -jet (left) and light-jet (right) rejections as a function of the $b$ -jet tagging efficiency for $Z'$ jets with $250 < p_T < 5000$ GeV, for the looser track selection trainings of GN1. The ratio to the performance of the baseline GN1 model is shown in the bottom panels. A value of $f_c = 0.05$ is used for all models. Binomial error bands are denoted by the shaded regions. . . . .	117

3564	6.22 The HLT light-jet rejection as a function of the $b$ -jet efficiency jets in the $t\bar{t}$ sample with $20 < p_T < 250$ GeV for events with a centre of mass energy $\sqrt{s} = 13.6$ TeV [125]. The ratio to the performance of the DL1d algorithm [86] is shown in the bottom panels. Binomial error bands are denoted by the shaded regions. The purple vertical dashed lines represent the most common working points used for b-tagging. . . . .	118
3570	6.23 The $c$ -jet rejection (left) and light-jet rejection (right) for the upgraded HL-LHC ATLAS detector with $\langle \mu \rangle = 200$ as a function of the $b$ -jet efficiency for jets in the $t\bar{t}$ sample with $20 < p_T < 250$ GeV for events with a centre of mass energy $\sqrt{s} = 14$ TeV [126]. The ratio to the performance of the DL1d algorithm is shown in the bottom panels. Binomial error bands are denoted by the shaded regions. The purple vertical dashed lines represent the most common working points used for b-tagging. . . . .	120
3577	6.24 The $c$ -jet rejection (left) and light-jet rejection (right) for the upgraded HL-LHC ATLAS detector with $\langle \mu \rangle = 200$ as a function of the $b$ -jet efficiency for jets in the $Z'$ sample with $250 < p_T < 5000$ GeV for events with a centre of mass energy $\sqrt{s} = 14$ TeV [126]. The ratio to the performance of the DL1d algorithm is shown in the bottom panels. Binomial error bands are denoted by the shaded regions. . . . .	120
3583	7.1 Diagrams of the signal process (top) and $t\bar{t}$ background (bottom). The object to the right of centre are reconstructed within the large- $R$ jet. For the $t\bar{t}$ background, the large- $R$ jet contains a mistagged $c$ -jet or (less often) a mistagged light-jet. The contribution in the 0-lepton channel results from hadronically decaying $\tau$ lepton, or a electron or muon which is out of the analysis acceptance. For the $t\bar{t}$ background process to be in the signal region, the $b$ -jet on the left hand side must either be not within acceptance, not reconstructed, or not tagged. . . . .	130
3591	7.2 Leading large- $R$ jet mass for the $Z$ and $W + \text{hf}$ processes in the HP SR of the 0-lepton channel [176]. The renormalisation scale $\mu_r$ has been varied by a factor of 0.5 (1DOWN) and 2 (1UP). An exponential function is fitted to the ratio between the nominal and alternate samples. . . . .	142
3595	7.3 Leading large- $R$ jet $m_J$ inclusive in $p_T^V$ for the $V + \text{hf}$ process modelled using both the SHERPA +PYTHIA8 (blue) and MADGRAPH +PYTHIA8 (red) samples [176]. . . . .	143

---

3598	7.4 Leading large- $R$ jet mass distribution for the combined $WZ$ and $ZZ$ processes, inclusive across all signal regions and lepton channels [176]. The renormalisation scale $\mu_R$ has been varied by a factor of 2 (UP) and 0.5 (DOWN). The red and blue curves show the fitted results of the hyperbolic tangent function. . . . .	146
3603	7.5 Comparison of the shapes of the large- $R$ jet mass $m_J$ between SHERPA (Sh221) (black) and POWHEG+PYTHIA8 (PwPy) (red) samples from the $WZ$ and $ZZ$ processes in high and low purity signal regions, integrated over $p_T^V$ regions and the 0- and 1-lepton channels [176]. The dashed green line shows the fitted third order polynomial function and the blue lines show the function after protection is added in the high mass region. . . . .	146
3609	7.6 The $m_J$ post-fit distributions in (top) the 0-, (middle) 1- and (bottom) 2-lepton SRs for (left) $250 \text{ GeV} < p_T^V < 400 \text{ GeV}$ and (right) $p_T^V \geq 400 \text{ GeV}$ . The LP and HP regions are merged for the 0-lepton and 1-lepton channels. The fitted background contributions are shown as filled histograms. The Higgs boson signal ( $m_H = 125 \text{ GeV}$ ) is shown as a filled histogram and is normalised to the signal yield extracted from data ( $\mu_{VH}^{bb} = 0.72$ ), and as an unstacked unfilled histogram, scaled by the SM prediction times a factor of two. The size of the combined on the sum of the fitted signal and background is shown in the hatched band. The highest bin contains the overflow [130]. . . . .	156
3619	7.7 The $m_J$ post-fit distributions in the $t\bar{t}$ control region for (top) the 0-lepton channel and the 1-lepton channel for $250 \text{ GeV} < p_T^V < 400 \text{ GeV}$ and (bottom) the 0-lepton channel and the 1-lepton channel for $p_T^V > 400 \text{ GeV}$ . The background contributions after the likelihood fit are shown as filled histograms. The Higgs boson signal ( $m_h = 125 \text{ GeV}$ ) is shown as a filled histogram on top of the fitted backgrounds normalised to the signal yield extracted from data ( $\mu_{VH}^{bb} = 0.72$ ), and unstacked as an unfilled histogram, scaled by the SM prediction times a factor of 2. The size of the combined statistical and systematic uncertainty for the sum of the fitted signal and background is indicated by the hatched band. The highest bin in the distributions contains the overflow [130]. . . . .	157

3630 7.8  $m_J$  distribution in data after subtraction of all backgrounds except for the  
 3631  $WZ$  and  $ZZ$  diboson processes. The contributions from all lepton channels  
 3632 and signal regions are summed and weighted by their respective values of  
 3633 the ratio of fitted Higgs boson signal and background yields. The expected  
 3634 contribution of the associated  $WH$  and  $ZH$  production of a SM Higgs  
 3635 boson with  $m_H = 125$  GeV is shown scaled by the measured combined  
 3636 signal strength ( $\mu_{VH}^{bb} = 0.72$ ). The diboson contribution is normalised to  
 3637 its best-fit value of  $\mu_{VZ}^{bb} = 0.91$ . The size of the combined statistical and  
 3638 systematic uncertainty is indicated by the hatched band. This error band is  
 3639 computed from a full signal-plus-background fit including all the systematic  
 3640 uncertainties defined in Section 7.3, except for the  $VH/VZ$  experimental  
 3641 and theory uncertainties [130]. . . . .

3642 7.9 Signal strength compatibility test between the (3+1)-POI fit (with the  
 3643 three lepton channels fit separately) and the default (1+1)-POI fit. The  
 3644 compatibility of the three channels is evaluated via a  $\chi^2$  difference test and  
 3645 results in a p-value of 49% [130]. . . . .

3646 7.10 Impact of systematic uncertainties on the fitted  $VH$  signal-strength pa-  
 3647 rameter  $\mu_{VH}^{bb}$  sorted in decreasing order. The boxes show the variations  
 3648 of  $\hat{\mu}$ , referring to the top  $x$ -axis, when fixing the corresponding individual  
 3649 nuisance parameter to its post-fit value modified upwards or downwards by  
 3650 its post-fit uncertainty, i.e.  $\hat{\theta} \pm \sigma_{\hat{\theta}}$ , and repeating the fit. The impact of  
 3651 up- and down-variations can be distinguished via the dashed and plane box  
 3652 fillings. The yellow boxes show the pre-fit impact (top  $x$ -axis) by varying  
 3653 each nuisance parameter by  $\pm 1$ . The filled circles show the deviation of the  
 3654 fitted value for each nuisance parameter,  $\hat{\theta}$ , from their nominal input value  
 3655  $\theta_0$  expressed in standard deviations with respect to their nominal uncer-  
 3656 tainties  $\Delta\theta$  (bottom  $x$ -axis). The error bars show the post-fit uncertainties  
 3657 on  $\hat{\theta}$  with respect to their nominal uncertainties. The open circles show  
 3658 the fitted values and uncertainties of the normalization parameters that are  
 3659 freely floating in the fit. Pre-fit, these parameters have a value of one [176].

3660 7.11 Measured  $VH$  simplified template cross sections times the  $H \rightarrow b\bar{b}$  and  
 3661  $V \rightarrow$  leptons branching fractions in the medium and high  $p_T^{V,t}$  bins [130].

# 3662 List of tables

<small>3663</small>	2.1 The fermions of the SM [16]. Three generations of particles are present. Also present (unlisted) are the antiparticles, which are identical to the particles up to a reversed charge sign. . . . .	15
<small>3664</small>		
<small>3665</small>		
<small>3666</small>	2.2 The bosons of the SM [16]. The photon, weak bosons and gluons are gauge bosons arising from gauge symmetries, and carry the four fundamental forces of the SM. The recently discovered Higgs boson is the only fundamental scalar particle in the SM. . . . .	16
<small>3667</small>		
<small>3668</small>		
<small>3669</small>		
<small>3670</small>	3.1 Overview of the different LHC runs [34, 35]. The average number of interac- tions per bunch-crossing is denoted as $\langle \mu \rangle$ (see Section 3.2.3), and is here averaged over the entire run. The luminosity is the peak instantaneous luminosity. Numbers for Run 3 are preliminary and are only provided to give an indication of expected performance. . . . .	29
<small>3671</small>		
<small>3672</small>		
<small>3673</small>		
<small>3674</small>		
<small>3675</small>	3.2 Quality selections applied to tracks, where $d_0$ is the transverse IP of the track, $z_0$ is the longitudinal IP with respect to the PV and $\theta$ is the track polar angle (see Section 3.2.2 for the IP definitions). Silicon hits are hits on the pixel and SCT layers. Shared hits are hits used on multiple tracks which have not been classified as split by the cluster-splitting neural networks [57]. A hole is a missing hit, where one is expected, on a layer between two other hits on a track. . . . .	46
<small>3676</small>		
<small>3677</small>		
<small>3678</small>		
<small>3679</small>		
<small>3680</small>		
<small>3681</small>		

3682	5.1	Truth origins which are used to categorise the physical process that led to the production of a track. Tracks are matched to charged particles using the truth-matching probability [57]. A truth-matching probability of less than 0.75 indicates that reconstructed track parameters are likely to be mismeasured and may not correspond to the trajectory of a single charged particle. The “OtherSecondary” origin includes tracks from photon conversions, $K_S^0$ and $\Lambda^0$ decays, and hadronic interactions. . . . .	75
3689	5.2	Input features to the fake track classification NN. Basic jet kinematics, along with information about the reconstructed track parameters and constituent hits are used. Shared hits, are hits used on multiple tracks which have not been classified as split by the cluster-splitting neural networks [57], while split hits are hits used by multiple tracks which have been identified as merged, and therefore split. . . . .	77
3695	5.3	Hyperparameter for the track classification model . . . . .	78
3696	5.4	Good and fake track selection efficiencies for the combined $t\bar{t}$ and $Z'$ samples. Two working points are defined, cutting on the NN output at 0.06 and 0.12.	80
3698	5.5	Cut values for the fake and $b$ -hadron decay track MVAs for the two defined working points. Working point “B” cuts more aggressively on the MVA outputs than WP “A”, removing more fake tracks but resulting in an increased loss of signal tracks (which here are all $b$ -hadron decay tracks).	81
3702	6.1	Input features to the GN1 model. Basic jet kinematics, along with information about the reconstructed track parameters and constituent hits are used. Shared hits, are hits used on multiple tracks which have not been classified as split by the cluster-splitting neural networks [57], while split hits are hits used on multiple tracks which have been identified as merged. A hole is a missing hit, where one is expected, on a layer between two other hits on a track. The track leptonID is an additional input to the GN1Lep model [3].	90
3709	6.2	A summary of GN1’s different classification networks used for the various training objectives, adapted from Ref. [3]. The hidden layers column contains a list specifying the number of neurons in each layer. ReLU activation is used through the network [111]. . . . .	95

3713	6.3 The area under the ROC curves (AUC) for the track classification from 3714 GN1, compared to a standard multilayer perceptron (MLP) trained on a 3715 per-track basis. The unweighted mean AUC over the origin classes and 3716 weighted mean AUC (using as a weight the fraction of tracks from the 3717 given origin) is provided. GN1, which uses an architecture that allows track 3718 origins to be classified in a conditional manner as discussed in Section 6.4.3, 3719 outperforms the MLP model for both $t\bar{t}$ and $Z'$ jets. . . . .	114
3720	7.1 Summary of the definitions of the different analysis regions . Signal enriched 3721 regions are marked with the label SR. There are regions with relatively large 3722 signal purity (HP SR) and with low purity (LP SR). Background enriched 3723 control regions are marked with the label CR. The shorthand “add” stands 3724 for additional small- $R$ jets, i.e. number of small- $R$ jets not matched to the 3725 Higgs-jet candidate. The medium and high $p_T^V$ regions are referred to as 3726 $Mp_T^V$ and $Hp_T^V$ , respectively [130]. . . . .	126
3727	7.2 Selections applied to baseline and signal electrons and muons. Signal leptons 3728 are additionally required to satisfy a $p_T > 27$ GeV (25 GeV in the 1-lepton 3729 channel). . . . .	127
3730	7.3 Event selection requirements for the boosted $VH$ , $H \rightarrow b\bar{b}$ analysis channels 3731 and sub-channels [130]. Various channel dependent selections are used to 3732 maximise the signal efficiency and reduce the number of background events 3733 in each analysis region. The $\min[\Delta\phi(\mathbf{E}_T^{\text{miss}}, \text{small-}R \text{ jets})]$ selection is used to 3734 remove jets when the missing transverse momentum $\mathbf{E}_T^{\text{miss}}$ is pointing in the 3735 direction of the Higgs candidate, and the $\Delta\phi(\mathbf{E}_T^{\text{miss}}, \mathbf{E}_{T, \text{trk}})$ is used to reject 3736 events where the calorimeter missing transverse momentum $\mathbf{E}_T^{\text{miss}}$ is not 3737 pointing in the direction of the track-based missing transverse momentum 3738 $\mathbf{E}_{T, \text{trk}}^{\text{miss}}$ . The $\Delta y(V, H_{\text{cand}})$ quantifies the rapidity difference between the 3739 reconstructed vector boson and Higgs candidate ( $H_{\text{cand}}$ ). $m_{\ell\ell}$ refers to the 3740 invariant mass of the two leptons, while $p_T^{\ell_1}$ and $p_T^{\ell_2}$ refer to the $p_T$ of 3741 the first and second leptons, respectively. . . . .	129

3742	7.4 Signal and background processes with the corresponding generators used for the nominal samples [130]. If not specified, the order of the cross-section calculation refers to the expansion in the strong coupling constant ( $\alpha_s$ ). (★) The events were generated using the first PDF in the NNPDF3.0NLO set and subsequently reweighted to the PDF4LHC15NLO set [169] using the internal algorithm in POWHEG-Box v2. (†) The NNLO(QCD)+NLO(EW) cross-section calculation for the $pp \rightarrow ZH$ process already includes the $gg \rightarrow ZH$ contribution. The $qq \rightarrow ZH$ process is normalised using the cross-section for the $pp \rightarrow ZH$ process, after subtracting the $gg \rightarrow ZH$ contribution. An additional scale factor is applied to the $qq \rightarrow VH$ processes as a function of the transverse momentum of the vector boson, to account for electroweak (EW) corrections at NLO. This makes use of the $VH$ differential cross-section computed with HAWK [170, 171]. . . . .	132
3754	7.5 Different sources of uncertainty (i.e. variations in the model) considered for the $V+jets$ background, and the corresponding implementation. For each uncertainty, acceptance and shape uncertainties are derived. . . . .	137
3757	7.6 0-lepton $W+jets$ nominal sample flavour composition and total event yield [176]. $Mp_T^V$ refers to the medium $p_T^V$ region, and $Hp_T^V$ refers to the high $p_T^V$ region (see Table 7.1). . . . .	138
3760	7.7 1-lepton $W+jets$ nominal sample flavour composition and total event yield [176]. $Mp_T^V$ refers to the medium $p_T^V$ region, and $Hp_T^V$ refers to the high $p_T^V$ region (see Table 7.1). . . . .	138
3763	7.8 0-lepton $Z+jets$ nominal sample flavour composition and total event yield [176]. $Mp_T^V$ refers to the medium $p_T^V$ region, and $Hp_T^V$ refers to the high $p_T^V$ region (see Table 7.1). . . . .	139
3766	7.9 2-lepton $Z+jets$ nominal sample flavour composition and total event yield [176]. $Mp_T^V$ refers to the medium $p_T^V$ region, and $Hp_T^V$ refers to the high $p_T^V$ region (see Table 7.1). . . . .	139
3769	7.10 $V+jets$ acceptance uncertainties. $W+jets$ SR and CR uncertainties marked with a superscript † are correlated. The 1L $W+jets$ medium-to-high $p_T^V$ uncertainty marked by * is applied as independent and uncorrelated NPs in both HP and LP signal regions [176]. . . . .	141
3773	7.11 Diboson acceptance uncertainties. All uncertainties except channel extrapolation uncertainties are fully correlated between the $ZZ$ and $WZ$ processes and channels [176]. . . . .	145

---

3776	7.12 Acceptance uncertainties for the $t\bar{t}$ background. The uncertainties on the 0- 3777 and 1-lepton channels are found to be similar, but are conservatively taken 3778 to be uncorrelated. The HP-to-LP SR uncertainty is applied in the HP SR. 3779 The Medium-to-high $p_T^V$ uncertainty is applied in the high $p_T^V$ bin, and is 3780 larger than the computed uncertainty in order to account for the known 3781 mismodelling of the $t\bar{t}$ $p_T$ spectrum. [176]. . . . .	147
3782	7.13 Single-top acceptance uncertainties. Uncertainties are derived in the 1-lepton 3783 channel but applied in a correlated fashion to both the 0- and 1-lepton 3784 channels. The HP-to-LP SR uncertainty is applied in the HP SR. The 3785 Medium-to-high $p_T^V$ uncertainty is applied in the high $p_T^V$ bin. The channel 3786 relative acceptance uncertainty is applied in the 0-lepton channel. [176]. .	148
3787	7.14 Factors applied to the nominal normalisations of the $t\bar{t}$ , $W+\text{hf}$ , and $Z+\text{hf}$ 3788 backgrounds, as obtained from the likelihood fit [130]. The errors represent 3789 the combined statistical and systematic uncertainties. . . . .	154
3790	7.15 Post-fit yields in the 0-lepton channel. Combined statistical and systematic 3791 uncertainties are shown [176]. . . . .	154
3792	7.16 Post-fit yields in the 1-lepton channel. Combined statistical and systematic 3793 uncertainties are shown [176]. . . . .	155
3794	7.17 Post-fit yields in the 2-lepton channel. Combined statistical and systematic 3795 uncertainties are shown [176]. . . . .	155
3796	7.18 Breakdown of the absolute contributions to the uncertainty on the signal 3797 strength $\mu_{VH}^{bb}$ obtained from the (1+1)-POI fit. The average impact repre- 3798 sents the average between the positive and negative uncertainties on $\mu_{VH}^{bb}$ . 3799 The sum in quadrature of the systematic uncertainties attached to the cate- 3800 gories differs from the total systematic uncertainty due to correlations [176]. 3801 . . . . .	163